Universiteit Antwerpen

Doctoral Thesis

Organic aerosol from the oxidation of biogenic organic compounds: a modelling study

Author:
Karl Ceulemans

Promoters:
Dr. Jean-François Müller,
Prof. dr. Magda Claeys

A thesis submitted in fulfilment of the requirements for the degree of Doctor in de wetenschappen: chemie

in the

Faculty of Science, Department of Chemistry

13 October 2014

Cover design: Anita Muys (Nieuwe Mediadienst, Universiteit Antwerpen)

Cover photograph: "Tall Trees in Schwäbisch Gmünd", Matthias Wassermann (`http://www.mawpix.com/`)

ISBN 9789057284649

D/2014/12.293/26

Summary

Aerosols exert a strong influence on climate and air quality. The oxidation of biogenic volatile organic compounds leads to the formation of secondary organic aerosol (SOA), which makes up a large, but poorly quantified fraction of atmospheric aerosols. In this work, SOA formation from α- and β-pinene, two important biogenic species, is investigated through modelling.

A detailed mechanism describing the complex gas phase chemistry of oxidation products is generated, based on theoretical results and structure activity relationships. SOA formation through the partitioning of oxidation products between the gas and aerosol phases is modelled with the help of estimated vapour pressures and activity coefficients. Given the large model uncertainties, validation against smog chamber experiments is essential.

Extensive comparisons with available laboratory measurements show that the model is capable of predicting most SOA yields to within a factor of two for both α- and β-pinene. However, for dark ozonolysis experiments, the model largely overestimates the temperature dependence of the yields and largely underestimates their values above 30 °C, by up to a factor of ten. This model behaviour is improved when additional pathways towards non-volatile products are incorporated. Discrepancies are found between the observed and modelled SOA composition, as the model cannot explain the formation of several observed SOA tracers, and important model SOA species, such as hydroperoxides, await experimental identification.

For β-pinene, uncertainties in key reactions in the newly implemented mechanism are shown to strongly impact ozone and SOA yields. Favouring the ring-opening of the main alkyl radical formed upon β-pinene OH-addition in the model is found to improve both ozone and SOA predictions. Products from bi-peroxy radicals formed in the ozonolysis of β-pinene are found to potentially contribute significantly to SOA.

The model has been used to simulate the long-term photooxidation (ageing) of SOA formed in α-pinene chamber experiments. The model is found to overestimate aerosol concentrations upon SOA ageing by a factor of two or more in many cases, while modelled O/C ratios of aged SOA are also strongly overestimated. Possible causes for these discrepancies include missing gas phase or aerosol photochemistry, and the uncertain impact of wall losses.

Finally, a simple parameterisation has been developed, suitable for use in large-scale models, and capable of reproducing SOA concentrations as simulated by the full model in various conditions.

Samenvatting

Organisch aerosol gevormd bij de oxidatie van biogene organische stoffen: een modelleringsstudie

Aerosolen oefenen een grote invloed uit op het klimaat en op de luchtkwaliteit. De oxidatie van biogene vluchtige organische stoffen leidt tot de vorming van secundair organisch aerosol (SOA), dat een grote, maar slecht gekwantificeerde fractie van atmosferische aerosolen uitmaakt. In dit werk wordt de aerosolvorming als gevolg van de oxidatie van α- en β-pineen, twee biogene stoffen die in grote hoeveelheden door bomen worden uitgestoten, onderzocht door middel van modellering.

Een gedetailleerd mechanisme dat de complexe gasfasechemie van oxidatieproducten beschrijft, werd gegenereerd, gebaseerd op structuur-activiteitsrelaties en theoretische resultaten. SOA-vorming door partitie van oxidatieproducten tussen gas en aerosol wordt gemodelleerd met behulp van geschatte dampdrukken en activiteitscoëfficiënten. Gezien de grote modelonzekerheden is validatie aan de hand van smogkamerexperimenten essentieel.

Vergelijkingen met beschikbare metingen tonen aan dat het model voor α- en β-pineen in de meeste gevallen in staat is om de SOA-concentraties te benaderen tot binnen een factor twee nauwkeurig. Voor donkere ozonolyse overschat het model echter sterk de temperatuursafhankelijkheid van de SOA-vorming, met grote onderschattingen boven 30 °C tot gevolg. Dit kan verbeterd worden door bijkomende reactiepaden naar niet-volatiele producten toe te voegen. Ook zijn er belangrijke afwijkingen tussen de geobserveerde en gemodelleerde samenstelling van het aerosol. Het model blijkt enerzijds niet in staat te zijn om de vorming van verschillende gekende SOA-tracers te verklaren, en anderzijds zijn veelvoorkomende stoffen in het gemodelleerde aerosol, zoals hydroperoxides, nog niet experimenteel geverifieerd.

Voor β-pineen werd aangetoond dat onzekerheden voor enkele cruciale reacties in het nieuwe reactiemechanisme een sterke impact hebben op de vorming van ozon en aerosol in het model. De ringopening van het voornaamste alkylradicaal in de OH-additie van β-pineen blijkt belangrijk te zijn om een redelijke overeenkomst tussen gemodelleerd en geobserveerd ozon en aerosol te bekomen. Biradicalen gevormd tijdens de ozonolyse van β-pineen dragen mogelijk ook sterk bij tot het aerosol.

Het model werd gebruikt voor de simulatie van de langdurige foto-oxidatie (veroudering) van aerosol van α-pineen in smogkamers. We stelden vast dat het model de aerosolconcentraties in dat geval met een factor twee of meer overschat, terwijl de verhouding O/C

eveneens sterk overschat wordt. Mogelijke oorzaken van deze afwijkingen zijn onder andere ontbrekende gas- en aerosolfasechemie, en de onzekere impact van verliezen naar de kamerwanden.

Tot slot werd een simpele parametrisering ontwikkeld voor gebruik in grootschalige atmosferische modellen. Deze is in staat om de aerosolvorming gesimuleerd met het volledige aerosolmodel te reproduceren.

Acknowledgements

I would like to thank everyone who has provided help, advice or support, or shown interest during my work on this dissertation.

First, I want to express my gratitude towards my promoter Dr. Jean-François Müller, for giving me the opportunity to enter into scientific research, and this in an engaging field. Working with him and within the Tropospheric Chemistry Group always happened in a creative and pleasant atmosphere. I also would like to thank him for making my work towards a doctoral degree possible. His guidance and help as advisor throughout my research at the Belgian Institute for Space Aeronomy (BIRA-IASB) and the writing of this dissertation has been invaluable. I have especially appreciated his invariably positive attitude towards research, combined with a great amount of common sense, friendliness, and patience.

I am also very grateful towards my promoter Prof. dr. Magda Claeys, for having accepted the promotership of my doctoral dissertation at the University of Antwerp, and for her continuous guidance throughout the process. Her research and that of her group also provided an important perspective from the observational and experimental side of aerosol science.

I would especially like to thank Prof. dr. Annemie Bogaerts (University of Antwerp), Prof. dr. Piet Van Espen (University of Antwerp), Prof. dr. Bernard Aumont (Université Paris-Est Créteil Val de Marne), Prof. dr. Jean-François Doussin (Université Paris-Est Créteil Val de Marne), Dr. Jean-François Müller (BIRA-IASB), and Prof. dr. Magda Claeys, for their willingness to accept the jury function for this dissertation, and for their interest in my work.

My work has been made possible by financial support from the Belgian Science Policy Office (BELSPO), for which I want to express my gratitude.

Thanks go to the other members of the Tropospheric Chemistry Group at BIRA-IASB. I would like to give special thanks to Steven Compernolle, with whom I have had the pleasure of collaborating closely during this entire research. In particular, his work on vapour pressure and activity coefficient estimation forms an essential part of the aerosol formation model which I have applied, and he has provided numerous other contributions. Special thanks go to Jenny Stavrakou and Maite Bauwens for many stimulating discussions and support. And I gratefully acknowledge Manuel Capouet, who started up the development of the BOREAM model, and introduced me to it upon my arrival at BIRA.

I have had the chance to enjoy numerous enlightening exchanges with other scientists, many within the IBOOT and BIOSOA projects. I am indebted to Prof. dr. Jozef Peeters, Dr. Luc Vereecken and Dr. Thanh Lam Nguyen, whose theoretical calculations form the basis of the chemical mechanisms used in this work, and who provided further insights at numerous occasions. Thanks to Dr. Ariane Kahnt for discussions which provided very useful information on smog chamber experiments, and I would also like to thank her former Leipzig colleagues Dr. Anke Mutzel, Dr. Yoshi Iinuma and Dr. Olaf Böge for making available experimental data on β-pinene oxidation.

I am grateful towards other former colleagues, such as Yves Christophe, Simon Chabrillat, Edith Botek, Sergey Skachko, Cindy Senten, and many others, for the good time I had while sharing an office with them, or during the many lively lunch hour conversations. I would also like to express my appreciation for co-players who tolerated me in their team during the BIRA football matches. Special thanks go to Yves, who invariably was willing to immediately share his great expertise, whenever a Fortran or Linux-related issue turned up, and to Simon, for his many insights into both scientific and non-scientific topics. My work has greatly benefited from the excellent IT-infrastructure at BIRA-IASB, and I thank Vincent Letocart, for his help with various bugs, and Frédéric Counerotte and Fabienne Leclère for hardware and other IT support. I would like to acknowledge many others at BIRA-IASB, with special thanks to Christiane Hizette, for making sure at all times that work at BIRA-IASB can take place under the best of circumstances.

Thanks to Matthias Wassermann (`http://www.mawpix.com/`) for granting me permission to use his image "Tall Trees in Schwäbisch Gmünd" on the cover of my dissertation.

I wish to wholeheartedly thank my family and friends for their continued support during my dissertation work. Many are the people who have listened to my explanations about those tiny particles from gases emitted by trees, without showing the least bit of disinterest, and who have encouraged me to bring this work to a good end. Great thanks go to Marleen and the family Michels-Coenen for their constant support, pep-talks and encouragement. My deepest thanks go to my parents, who have stood behind me the whole time, and have always encouraged me to persevere and follow my interests.

Contents

List of Figures

List of Tables

Abbreviations

AMS	**A**erosol **M**ass **S**pectrometer
BOREAM	**B**iogenic hydrocarbon **O**xidation and **RE**lated **A**erosol formation **M**odel
CI	**C**riegee **I**ntermediate
CMK	**C**yclobutyl **M**ethyl **K**etone
CTM	**C**hemistry **T**ransport **M**odel
EVAPORATION	**E**stimation of **VA**pour **P**ressure of **OR**ganics, **A**ccounting for **T**emperature, **I**ntramolecular, and **N**on-additivity effects (Compernolle et al., 2011)
GECKO-A	**G**enerator for **E**xplicit **C**hemistry and **K**inetics of **O**rganics in the **A**tmosphere (Valorso et al., 2011)
IMAGESv2	**I**ntermediate **M**odel of the **G**lobal and **A**nnual **E**volution of **S**pecies (Stavrakou et al., 2012)
IPCC	**I**ntergovernmental **P**anel on **C**limate **C**hange
IR	Infrared
IUPAC	**I**nternational **U**nion of **P**ure and **A**pplied **C**hemistry
LV-OOA	**L**ow **V**olatility-**O**xygenated **O**rganic **A**erosol (Jimenez et al., 2009)
MBTCA	3-**M**ethyl-1,2,3-**B**utane**T**ri**C**arboxylic **A**cid (Szmigielski et al., 2007)
MCM	**M**aster **C**hemical **M**echanism
MEGANv2.1	**M**odel of **E**missions of **G**ases and **A**erosols from **N**ature version 2.1 (Guenther et al., 2012)
MW	**M**olecular **W**eight
PAN	**P**eroxy **A**cyl **N**itrate

PM10	fraction of **P**articulate **M**atter with diameter below **10** μm
POA	**P**rimary **O**rganic **A**erosol
ppb	**p**arts **p**er **b**illion (for vmr within this work)
ppm	**p**arts **p**er **m**illion (for vmr within this work)
ppt	**p**arts **p**er **t**rillion (for vmr within this work)
RH	**R**elative **H**umidity
SAR	**S**tructure **A**ctivity **R**elationship
SCI	**S**tabilised **C**riegee **I**ntermediate
SIMPOL.1	**SIMP**le group contribution method for predicting vapor pressures and enthalpies of vaporization of multi-functional **O**rganic compounds (Pankow and Asher, 2008)
SMARTS	**SM**ILES (Simplified Molecular Input Line Entry Specification) **AR**bitrary **T**arget **S**pecification (Daylight Inc., 2008)
SMILES	**S**implified **M**olecular **I**nput **L**ine **E**ntry **S**ystem (Weininger, 1988)
SOA	**S**econdary **O**rganic **A**erosol
SV-OOA	**S**emi-**V**olatile-**O**xygenated **O**rganic **A**erosol (Jimenez et al., 2009)
TME	**T**etra**m**ethyl **e**thene
UNIFAC	**UNI**versal quasichemical **F**unctional group **A**ctivity **C**oefficients (Fredenslund et al., 1975)
UV	Ultraviolet
VBS	**V**olatility **B**asis **S**et
vmr	**v**olume **m**ixing **r**atio, a measure of concentration
VOC	**V**olatile **O**rganic **C**ompounds
WHO	**W**orld **H**ealth **O**rganisation

Chapter 1

Introduction

1.1 Context of this study: the role of biogenic secondary organic aerosols in the atmosphere

Due to rapid industrial development, human activities have exerted an increasingly strong influence on the Earth's atmosphere over the last two centuries, giving rise to environmental problems of a global scale. There is now wide agreement on the fact that the rapid rise of the concentrations of greenhouse gases due to anthropogenic emissions, of which CO_2 and methane are the most important ones, has already raised average temperatures, and will lead to an even greater temperature increase by the end of the 21st century, if emissions are not mitigated (IPCC, 2013). The consequences of human-induced global warming have the potential of being detrimental towards many aspects of human society and ecosystems over the globe (IPCC, 2014). A second, largely simultaneous global problem has been the rise of anthropogenic particulate pollution from fossil fuel or biomass combustion by industry, traffic, heating, and cooking. Exposure to this particulate matter (PM) has negative effects on the health of a very large fraction of the world's population (WHO, 2014a). These aerosols also have a large, but still uncertain climatic impact, which is currently estimated to be a cooling effect, thus partly masking the warming of Earth's climate by greenhouse gases (IPCC, 2013).

There is now no place on Earth left which is not affected by some degree of anthropogenic particulate matter, which consists of several types of aerosols, such as soot (also known as black carbon), and primary (directly emitted) or secondary (formed through condensation of vapours) inorganic or organic aerosols (Andreae, 2007). The secondary organic aerosols (SOA) are formed when volatile organic compounds (VOCs) are emitted (for example in car exhaust or during biomass burning), and these VOCs react in

the atmosphere with ozone or radicals, such as the hydroxyl radical (OH) or the nitrate radical (NO_3). The oxidation products are often more condensable than the original VOCs, and might therefore condense onto existing particles, or in some cases form new ones (Seinfeld and Pandis, 2006).

However, before the onset of human air pollution, various natural processes already acted as sources of aerosols, such as mineral dust, sea spray aerosol, volcanic aerosols, particles from natural wildfires, and the secondary organic aerosols due to biogenic VOCs, mainly emitted by vegetation (Andreae, 2007). These biogenic emissions present a large source on a global scale, higher than that of all anthropogenic VOCs combined (Hallquist et al., 2009). Analysis of PM at various locations has shown that SOA is one of its main components (Jimenez et al., 2009). The true magnitude of this aerosol source is still very uncertain, with estimates ranging almost an order of magnitude (IPCC, Working group I, 2014, Hallquist et al., 2009). Recent evidence shows that anthropogenic pollution has the potential to strongly increase the concentration of biogenic SOA (Spracklen et al., 2011). In order to provide better constraints on the overall impact of aerosols on climate and on health, it is crucial to narrow down the uncertainty ranges on the production of biogenic secondary organic aerosols, one of the most important constituents of ambient particulate matter. This requires improving the understanding of the complex oxidation chemistry of VOCs and the physical processes which lead to SOA formation (Hallquist et al., 2009). An important subset of biogenic VOCs are the monoterpenes, 10-carbon-containing hydrocarbons emitted by trees, of which α- and β-pinene are two of the most important members. The formation of SOA from these compounds has received much scientific interest in the last 25 years, and forms the subject of this work.

1.2 Structure of Earth's atmosphere

The major components of the Earth's atmosphere are molecular nitrogen (N_2, 78.08%), molecular oxygen (O_2, 20.95%) and the noble gas argon (Ar, 0.93%) (Jacobson, 2002). The concentrations of other noble gases (neon, helium, krypton, and xenon) are much lower. Among the remaining gases, only water vapour is found at molar concentrations occasionally higher than 1%. Nevertheless, due to their chemical and physical properties, trace gases, such as ozone, carbon dioxide and volatile organic compounds, have a major impact on the atmosphere (Jacobson, 2002, Seinfeld and Pandis, 2006). Additionally, different types of liquid or solid aerosol particles are present.

The atmosphere is divided into several vertical layers, usually defined from the variations of temperature with height (see Fig. 1.1, from Laing and Evans, 2011). Pressure decreases exponentially with height over a large part of the atmosphere (Seinfeld and Pandis,

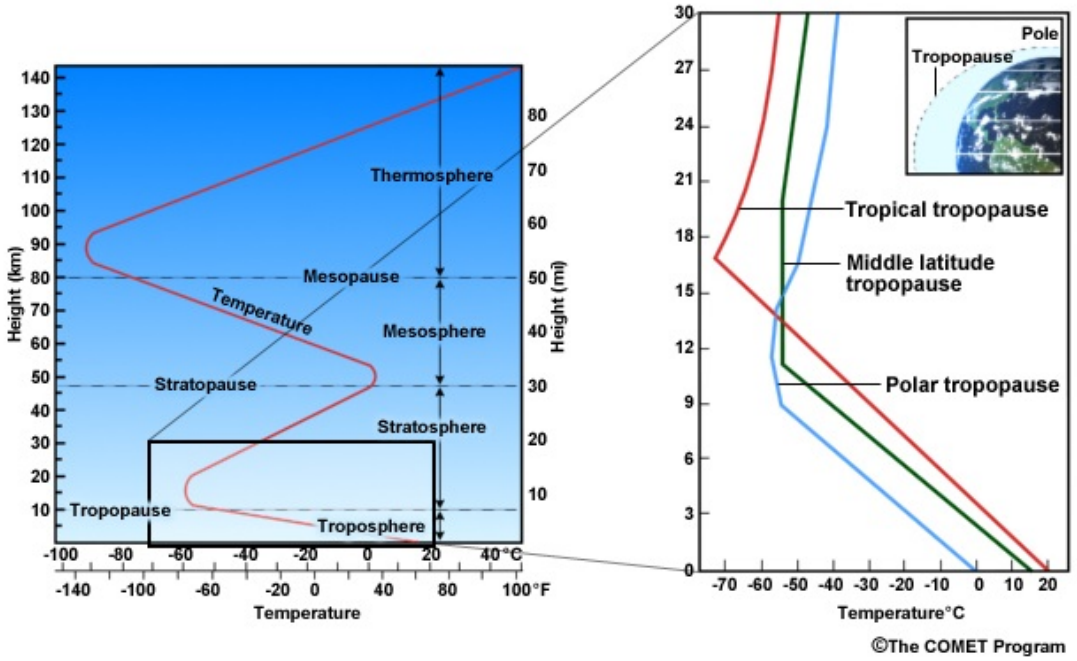

FIGURE 1.1: (a) Standard atmospheric temperature profile (b) height of the tropopause in the tropics, midlatitudes, and poles (Laing and Evans, 2011).

2006). The troposphere is the lowest layer of the atmosphere, and reaches up to the tropopause, which is situated between about 8 km (at the poles) and 15–18 km (above the equator). Within the troposphere, temperature generally decreases with height. Near the tropopause, a minimum temperature is reached (less than 200 K in the tropics). The troposphere is characterised by rapid mixing.

In the next layer, the stratosphere, temperature increases from the tropopause to the stratopause, located between 45 to 55 km, where it reaches a maximum of about 270 K. This vertical gradient is the cause of a very slow vertical mixing in the stratosphere. The cause of the increase in temperature is the absorption of radiation by ozone, which reaches high concentrations in the stratosphere (the ozone layer).

Temperature again decreases with height in the mesosphere, extending from the tropopause up to the mesopause, where a minimum temperature is reached, which is the lowest in the atmosphere. In the next layer, the thermosphere (between the mesopause and about 500 km), absorption of strong short-wave radiation by O_2 and N_2 leads to an increase in temperature with height.

The exosphere, finally, is the outermost layer of the atmosphere, where gas molecules with sufficient energy can escape the Earth's gravity.

This work is concerned with the chemistry of VOCs, released by various processes on the Earth's surface. As a large part of these compounds are short or moderately long-lived, with respect to oxidation processes, they are mostly destroyed before they can reach the stratosphere. Exceptions are long-lived species, such as chlorinated fluorocarbons, which can be transported into the stratosphere, where they can catalyse the destruction of stratospheric ozone, contributing to the ozone hole (Seinfeld and Pandis, 2006).

1.3 Radiative budget of the atmosphere

Of the radiative energy flux received by the Earth (about 1,365 W m^{-2}), about 30% is directly reflected back into space, mostly by clouds and snow or ice (Seinfeld and Pandis, 2006). The rest of the incoming energy is either directly absorbed by gases or aerosols, absorbed by the surface, or reflected by the surface and then absorbed by clouds or aerosols (Seinfeld and Pandis, 2006). Averaged over the Earth's surface and over time, the Earth absorbs about 240 W m^{-2} of solar radiation (Hansen et al., 2011). The Earth's surface and atmosphere also emit thermal infrared (IR) radiation. The different layers of the atmosphere partly reabsorb this IR. The IR radiation emitted into space ensures a (near) balance in incoming and outgoing radiation (Seinfeld and Pandis, 2006). The partial reabsorption of IR radiation by greenhouse gases is the reason why the average temperature of the Earth's surface is about 288 K, instead of about 255 K, which would be the temperature of an Earth without any atmosphere (Jacobson, 2002). This is known as the greenhouse effect. Over long time scales, differences in incoming solar radiation, caused by small variations in the Earth's orbit (known as Milankovitch cycles), combined with feedback effects involving greenhouse gases such as CO_2 and other processes, have contributed to the alternation of ice ages and warmer periods during the past 2.5 million years (Jacobson, 2002, IPCC, Working group I, 2014). The recent rise of greenhouse gases due to anthropogenic activity has caused a radiative imbalance on a much shorter time scale, decreasing the amount of IR radiation escaping to space, and increasing the Earth's average surface temperature (see Section 1.7.3).

1.4 Gas phase chemistry in the troposphere

1.4.1 Inorganic chemistry

As the Earth's atmosphere's main constituents are mostly inert, its chemistry is driven by trace gases. An important class of reactive trace species are the nitrogen oxides, NO and NO_2 (NO_x). NO is formed as a side product during combustion, in soils and in

lightning storms (Jacobson, 2002). Another important reactive species is ozone (O_3), which is formed locally, or, occasionally, transported downwards from the stratosphere.

Under the influence of solar radiation, NO_x and O_3 undergo three mutually-connected reactions:

$$NO + O_3 \rightarrow NO_2 + O_2 \tag{1.1}$$

$$NO_2 + h\nu \rightarrow NO + O \tag{1.2}$$

$$O + O_2 \rightarrow O_3 \tag{1.3}$$

Reaction 1.2, followed by Reaction 1.3, is the only major photochemical source of ozone in the troposphere. Its photolysis is the main primary source of the hydroxyl radical OH, which is the major oxidant for most organic compounds, including the greenhouse gas methane:

$$\begin{aligned} O_3 + h\nu &\rightarrow O_2 + O \\ &\rightarrow O_2 + O(^1D) \end{aligned} \tag{1.4}$$

Here, O is the ground state, and $O(^1D)$ is the first excited state of atomic oxygen. The ground state atomic oxygen quickly recombines with O_2 to ozone. So does part of the excited atomic oxygen, but a second reaction, between $O(^1D)$ and water vapour, forming hydroxyl radicals, is also possible (Seinfeld and Pandis, 2006):

$$H_2O + O(^1D) \rightarrow 2\,OH \tag{1.5}$$

The hydroperoxyl radical HO_2 is formed through the reactions

$$CO + OH \rightarrow H + CO_2 \tag{1.6}$$

$$H + O_2 + M \rightarrow HO_2 + M \tag{1.7}$$

as well as in several organic radical reactions. It can react with NO, with O_3 or with itself:

$$HO_2 + NO \rightarrow NO_2 + OH \tag{1.8}$$

$$HO_2 + O_3 \rightarrow OH + 2\,O_2 \tag{1.9}$$

$$HO_2 + HO_2 \rightarrow H_2O_2 + O_2 \tag{1.10}$$

It follows that the formation of HO_x (OH or HO_2) radicals is a source of ozone in high-NO_x environments, due to the catalytic cycle composed by e.g. Reactions 1.6, 1.7, 1.8, 1.2 and 1.3. In more remote areas, characterised by low NO levels, ozone is destroyed due

to the predominance of Reaction 1.9 over Reaction 1.8. H_2O_2 is a temporary reservoir of HO_x (OH and HO_2), as it can photolyse, or react with OH:

$$H_2O_2 + h\nu \rightarrow 2\,OH \tag{1.11}$$

$$H_2O_2 + OH \rightarrow HO_2 + H_2O \tag{1.12}$$

The termination reaction

$$OH + NO_2 + M \rightarrow HNO_3 + M \tag{1.13}$$

leads to the removal of two radicals, and the formation of nitric acid (Seinfeld and Pandis, 2006). Along with Reaction 1.12, the deposition of HNO_3 and H_2O_2 to the Earth's surface (through either direct contact with the surface, or by solubilisation in water droplets followed by precipitation) is the main sink of HO_x (also NO_x) radicals in the troposphere.

1.4.2 Chemistry of organic species in the troposphere

The reaction of organic compounds with e.g. OH, NO_3 or ozone results in the formation of alkyl radicals, which typically react with O_2 (Seinfeld and Pandis, 2006):

$$R^\bullet + O_2 + M \rightarrow RO_2^\bullet + M \tag{1.14}$$

The subsequent chemistry is summarised in Fig. 1.2, which is taken from Hallquist et al. (2009). The peroxy radicals can react with NO, leading to either alkoxy radicals, or organic nitrates.

$$\begin{aligned} RO_2^\bullet + NO &\rightarrow RO^\bullet + NO_2 \\ &\rightarrow RONO_2 \end{aligned} \tag{1.15}$$

This reaction is dominant in polluted areas, where it contributes to ozone formation (through Reactions 1.2 and 1.3). They can also react with HO_2, forming, depending on the structure, only hydroperoxides, or in some cases peroxy acids or (acyl) alkoxy radicals. A third possibility is reaction with other peroxy radicals, leading either to molecular products, such as alcohols or carbonyl compounds, or alkoxy radicals. The alkoxy radicals undergo unimolecular reactions, such as decomposition, H-shift isomerisation or ring closure, or react with O_2. The formed molecular products are often condensable, and can contribute to secondary organic aerosol (SOA). For a more complete overview, the reader is referred to Chapter 2.

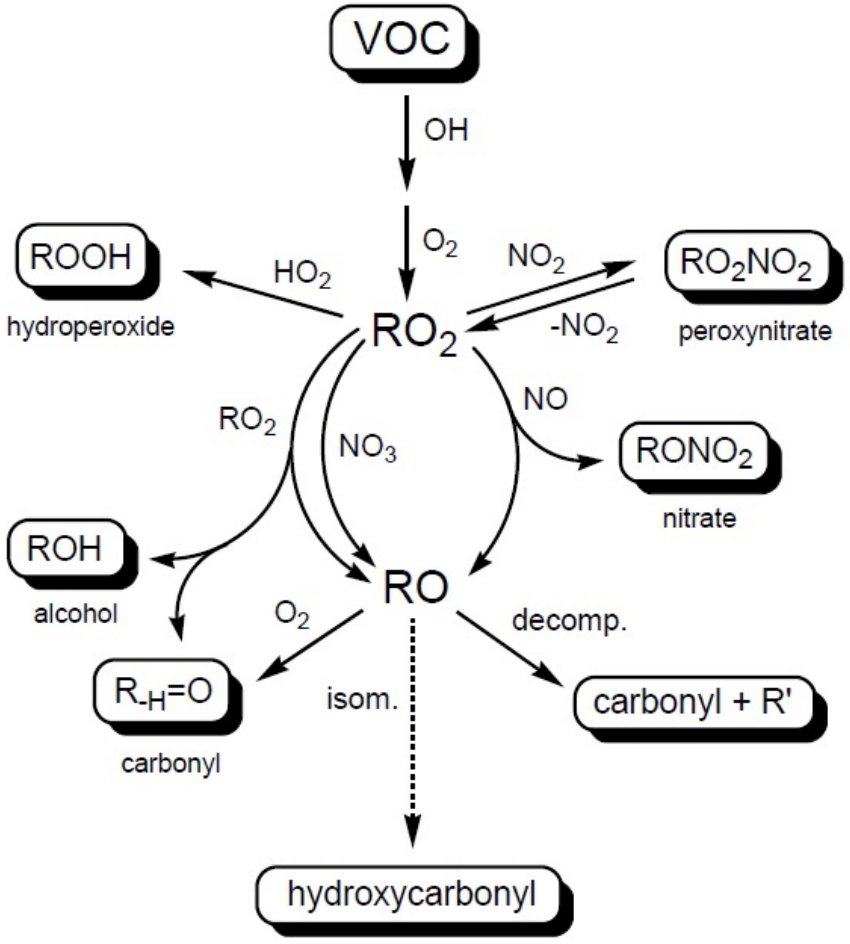

FIGURE 1.2: Simplified schematic of the OH-initiated degradation of generic VOCs to form first-generation products, taken from Fig. 2 in Hallquist et al. (2009).

When concentrations of VOCs are relatively high, compared to NO_x, an increase in NO leads to an increase in ozone production, a condition which is termed "NO_x-limited" (Seinfeld and Pandis, 2006). When NO_x concentrations are high, relative to VOC concentrations, ozone production does not increase with NO_x anymore, as the concentration of RO_2 radicals becomes limited. On the contrary, NO_x increases lead to OH radical removal (through Reaction 1.13) reducing the formation of HO_2 and RO_2 radicals, and therefore net ozone production. This situation is called "VOC-limited".

1.5 Biogenic volatile organic compounds

1.5.1 Biogenic emissions

Living organisms (plants, bacteria, and animals) emit a large number of different organic species into the atmosphere (Hewitt, 1999, Guenther et al., 2012, Guenther, 2013). Methane has the largest emission source, due to methane-generating bacteria, which thrive in anaerobic wet environments, such as wetlands, rice paddies, water reservoirs, and the intestines of ruminants. Methane is also generated in sewage, manure, or landfill. Natural wetlands emit around 200 Tg carbon a^{-1}, globally, while the production from agriculture and waste is estimated to be about equally large (Kirschke et al., 2013). Plant metabolism is a relatively small source (Dueck et al., 2007, Nisbet et al., 2009). Marine plankton is an important source of dimethylsulfide (DMS), with a source of 15–30 Tg per year.

Vegetation represents the largest source for most non-methane biogenic volatile organic compounds (NM-BVOC), emitting thousands of different compounds (Hewitt, 1999, Guenther et al., 2012). These can be primarily subdivided into terpenes (see Section 1.5.2) and oxygenated VOC (OVOC) such as methanol, acetone and 2-methyl-3-buten-2-ol (MBO). Many OVOC are bidirectional, i.e. they are both emitted and taken up by vegetation, e.g. ethanol, acetaldehyde, formaldehyde, acetic acid, and formic acid. Stress-related VOC such as ethene and cis-3-hexenal are emitted predominantly when plants undergo herbivore attack, drought, or damage. Some monoterpenes and sesquiterpenes are also stress-related (Guenther et al., 2012).

1.5.2 Terpenes

A large fraction of biogenic VOC are terpenes, defined by their carbon skeletons derived from multiples of 5-carbon-containing units, with a structure similar to 2-methyl-butane, also referred to as isoprene units (Breitmaier, 2006). The terpenes can additionally contain double bonds, or in some cases oxygenated functional groups. Depending on the number of isoprene units, the terpene is called a hemiterpene (C_5), monoterpene (C_10), sesquiterpene (C_15), etc. More than 40,000 different terpenes are known (Osbourne and Lanzotti, 2009), of which the hemiterpenes, monoterpenes and sesquiterpenes are important as VOCs in the atmosphere. The most important hemiterpene is isoprene (2-methyl-1,3-butadiene).

The biosynthesis of terpenes occurs from isopentenyl pyrophosphate (IPP) and dimethylallyl pyrophosphate (DMAPP) (Eisenreich et al., 2004). Isoprene is formed through

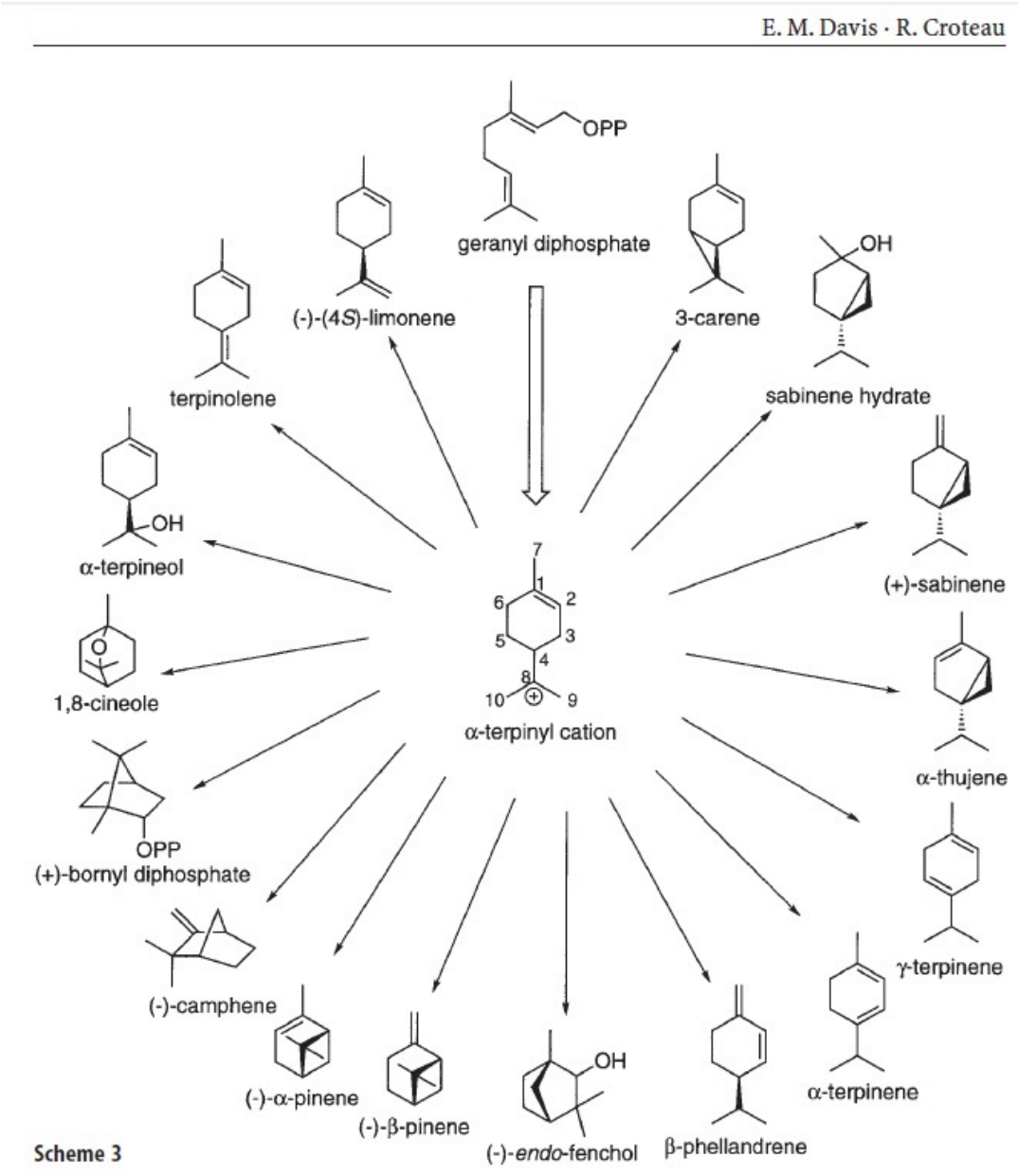

FIGURE 1.3: The biosynthesis of monoterpenes from geranyl diphosphate (Scheme 3 from Davis and Croteau, 2000).

a reaction of DMAPP, mediated by the enzyme isoprene synthase (Miller et al., 2001). Other reactions in plants between DMAPP and IPP lead to geranyl pyrophosphate (alternatively denoted as geranyl diphosphate), which is the precursor to the monoterpenes (Davis and Croteau, 2000). Enzymes called monoterpene synthases regulate the transformation of geranyl pyrophosphate, through the α-terpinyl cation, into various monoterpenes (Fig. 1.3). Not shown are the class of the non-cyclic monoterpenes, such as myrcene and t-β-ocimene, formed through another pathway (Hewitt, 1999).

Some terpenes serve as deterrents against herbivores or pathogens in plants. Certain terpenes, when released upon herbivore attack, attract predators or alert other parts of the same plant and neighbouring plants (Gershenzon and Dudareva, 2007). The oleoresin of trees generally consists of a mixture of mainly mono-, sesqui- and diterpenes, the latter often containing a carboxylic acid group (Martin et al., 2003, da Silva Rodriguez-Corrêa et al., 2012). Upon wounding, the more volatile monoterpenes act as solvent, allowing the mixture to be transported quickly, while the more viscous diterpenes often have toxic properties towards herbivores (Gershenzon and Dudareva, 2007). Isoprene and monoterpenes also play an important role in helping plants cope with temperature and oxidative stress (Vickers et al., 2009).

Terpenes have been collected since antiquity by tapping the oleoresin fluid from trees. The derived pitch was used to water-proof wooden ships (Britannica online, 2013a). One derived product, turpentine, is a solvent of oils and paints (Britannica online, 2013b). α-pinene is its most abundant constituent (40 to 97%) (Haneke and Masten, 2002). Monoterpenes are also widely used in fragranced consumer products (Steinemann et al., 2011).

1.5.3 Terpene emissions

Terpene emissions are highly species-dependent. Factors enhancing emissions are temperature and light, but soil moisture, leaf age, leaf area and CO_2 also play a role (Guenther et al., 2012). There are also indications of history effects of previous temperature and light exposure (Demarcke et al., 2010).

Models for VOC emissions by vegetation, such as MEGAN2.1 (Guenther et al., 2012), need to take into account such complex factors on different scales, by making use of gridded databases of land cover type, and associated distributions of emission factors for common VOCs such as isoprene, monoterpenes, sesquiterpenes, and others. Meteorological analyses are used to deduce light exposure, moisture and temperature, in conjunction with a canopy environment model for estimating the variation of light, temperature and leaf area in the vegetation canopy (Müller et al., 2008).

Results of such global modelling studies indicate that the tropics are the dominant VOC source (about 75%), because of high temperature, light exposure and the presence of strong emitters. Isoprene accounts for roughly 50% of all emitted VOCs, while monoterpenes account for about 15%, or 155 Tg per year (Guenther et al., 2012, Guenther, 2013). The total emission flux of all VOCs was estimated to be about 1000 Tg (or 1 billion tonnes, 1 Gt) per year.

TABLE 1.1: Aerosol characteristics, taken from Table 5.1 of Jacobson (2002).

	Typical diameter	Typical number concentration (particles cm^{-3})	Mass concentration ($\mu g\ m^{-3}$)
Aerosol			
Small	$< 0.2\ \mu m$	10^3–10^6	< 1
Medium	0.20–2.5 μm	1–10^4	< 250
Large	$> 2.5\ \mu m$	$<$ 1–10	< 250
Water droplets			
Fog droplets	10–20 μm	1–500	10^4–10^6
Cloud droplets	10–200 μm	1–1000	10^4–10^7
Drizzle	200 μm–1 mm	0.01–1	10^5–10^7
Raindrops	1–8 mm	0.001–0.01	10^5–10^7

Among the monoterpenes, α-pinene is the most important compound, with 66.1 Tg per year, followed by *t*-β-ocimene (19.4), β-pinene (18.9), limonene (11.4), sabinene (9.0), myrcene (8.7), 3-carene (7.1), camphene (4.0), and others accounting for 17.8 Tg per year. Sesquiterpenes have emissions of about 14.5 Tg per year (Guenther et al., 2012).

1.6 Atmospheric aerosols

An aerosol is defined as a suspension of fine solid or liquid particles in a gas (Seinfeld and Pandis, 2006). Due to their radiation absorption and scattering effects, aerosols can become visible, and exert an influence on the radiative balance of the atmosphere. Clouds, fog, smoke, dust or haze are all well-known types of aerosol. Even when scarcely visible to the eye, aerosols can affect health when inhaled, or contribute to atmospheric processes.

1.6.1 Size distributions

In Table 1.1, typical sizes of different aerosol types are given, based on Jacobson (2002). The diameter of aerosols can range from less than 10 nm up to 100 μm, while the diameter of fog, cloud or rain droplets ranges from 10 μm up to 10 mm. In many cases, the size spectrum of aerosols contains diameter ranges where number concentrations peak; these are referred to as modes (Jacobson, 2002). Aerosol particle distributions can have several of such modes. The nucleation mode contains freshly formed (nucleated) particles, with sizes well below 100 nm.

Nucleation mode aerosols can grow by coagulation and gas condensation, until a new distribution range is reached, the accumulation mode, characterised by a typical diameter range between 100 nm and 2 μm (Jacobson, 2002). Larger particles exist too, but their average atmospheric residence time is limited due to gravitational sedimentation. Other removal processes are wet deposition, due to collisions with falling rain or cloud droplets, or condensational growth into cloud droplets.

1.6.2 Formation of different types of aerosols

Primary aerosols are emitted directly into the air, while secondary particles are formed in the air through homogeneous nucleation of gas phase species or by condensation of vapours onto existing particles (Jacobson, 2002). It should be noted, though, that recent experiments with primary organic aerosols (POA) have shown that their constituents can be semi-volatile, and that upon dilution away from the emission source, this material can partially evaporate, and contribute to SOA (Robinson et al., 2007). Some particles originate from natural processes, while others are of anthropogenic origin.

Important natural sources of primary (mostly organic) aerosols include sea spray aerosols, soil dust and volcanic emissions (ash). They are mostly emitted in the coarse mode. In addition, volcanoes emit sulfur dioxide, which, upon oxidation to H_2SO_4, contributes to secondary inorganic aerosol.

Anthropogenic aerosol emissions include biomass burning, fossil fuel combustion, and industrial processes. These emissions include primary particles (ash and soot, i.e. black carbon particles) and semi-volatile organic species that can lead to SOA (Jacobson, 2002).

Important secondary inorganic aerosols are nitrate, ammonium, and sulfate aerosols. The large quantities of emitted anthropogenic and biogenic VOC undergo oxidation reactions, the products of which are often semi-volatile or condensable. Their ability to partition to already present particles depends on their saturated vapour pressure and the available absorbing and adsorbing material (Pankow, 1994, Seinfeld and Pandis, 2006). SOA is recognised as the major component of PM at many locations (see Section 1.8.1).

Atmospheric particles are often mixtures of several of the above types of aerosol, as seen in Fig. 1.4. They can contain soot (composed of smaller solid beads of elemental carbon, stuck together in clusters), inorganic, biogenic or mineral particles, and amorphous organic material.

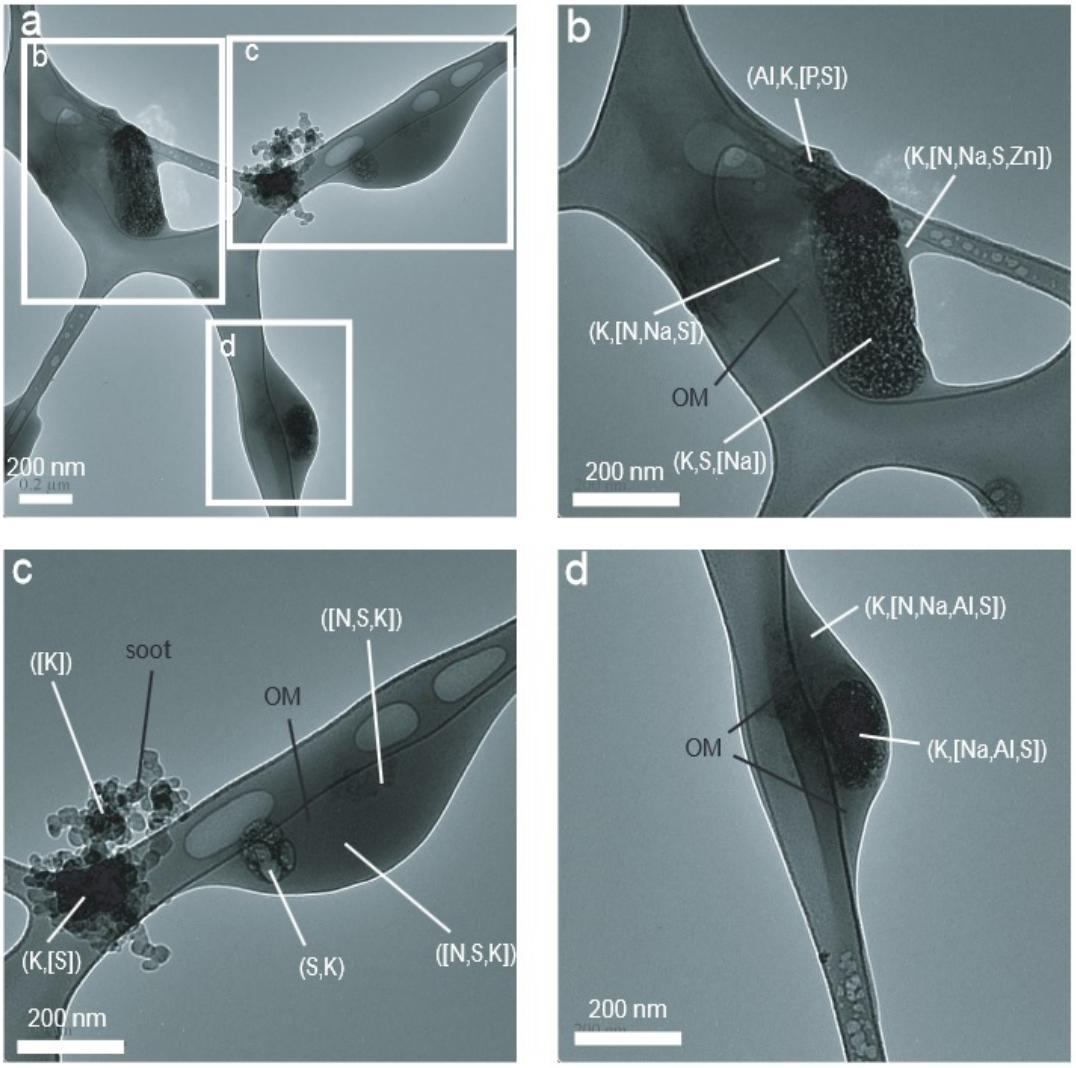

FIGURE 1.4: Morphologies and composition of externally mixed organic matter and soot particles, taken from Adachi and Buseck (2008). Particles were deposited on lacy carbon filters. Samples were obtained in March 2006 over Mexico City. Soot particles have curved graphite layers. OM and the filter, both of which consist of amorphous carbon, have disordered structures. Elements in square brackets are in concentrations < 1 wt%. C, O and Si occur in all particles, and are not indicated separately (Adachi and Buseck, 2008).

1.7 Impact of aerosols

1.7.1 Impact of aerosols on air quality

Already in the Middle Ages, wood and coal burning has been known to cause severe smog episodes in cities such as London (Jacobson, 2002). The Industrial Revolution led to a large increase in coal burning, severely worsening air pollution. The London-type smog is characterised by an accumulation of fuel burning particles (such as soot) and

vapours (such as SO_2) in an inversion layer. The dense haze impairs visibility, blackens or corrodes buildings, and irritates the eyes and lungs (Jacobson, 2002). Besides the chronic exposure, pollution events caused acute spikes in mortality. During the Great Smog event in London in the winter of 1952 to 1953, an estimated 12,000 deaths were related to the pollution (Bell et al., 2003).

Besides this London-type smog, a different type of air pollution is the so-called photochemical smog, which involves the photochemical processing of primary particulate and gaseous emissions. In Los Angeles, for example, almost daily smog episodes could be observed from the start of the twentieth century on, which increased in severity with the increase in automobile traffic (Jacobson, 2002). In the 1950s it was discovered that such episodes are caused by the photochemical processing of a mixture of emitted hydrocarbons and nitrogen oxides. Under sunlight, strong ozone formation takes place, accompanied by the formation of organic peroxides, which cause eye irritation and crop damage, closely resembling the effects of the photochemical smog (Haagen-Smit, 1952). Aerosol formation was also observed, and found to reduce visibility (Haagen-Smit, 1952).

FIGURE 1.5: Smog over Brussels, 14 March 2014. Source: Yahoo News, Geert vanden Wijngaert (`http://news.yahoo.com/photos/layer-smog-covers-city-brussels-friday-march-14-photo-134559650.html`)

Since the eighties/nineties, as health effects became better understood, increasingly strict government controls on particulate matter were implemented and verified through measurement networks in the European Union and the United States. First PM10, and more recently PM2.5 (particulate matter with aerodynamic diameters less than 10 respectively 2.5 μm) limits have been enforced. For example, in the EU, PM10 should not exceed a 24 hour average of 50 μg m^{-3} for more than 35 days (European Union, 2008). Related

pollution control measures have led to decreases of air pollution in the US and Europe. Notwithstanding these downward trends, 91–95% of the EU population remains exposed to PM2.5 concentrations which exceed the WHO safety norms (Guerreiro et al., 2013).

In many other regions, such as China or India, air quality problems have worsened, due to rapid economic development in the last decades, which was not accompanied by adequate pollution controls. Coal burning for power production or heating and increased traffic are main causes (Wang and Hao, 2012). For example, Zhao et al. (2013) found that PM2.5 concentrations were often several hundreds of μg m^{-3} at different locations in China, greatly exceeding the 25 μg m^{-3} norm applicable in Europe.

1.7.2 Health impact of aerosols

That both short- and long-term exposure to fine particulate matter has a significant detrimental impact on health has been shown by a large number of population studies (WHO-Europe, 2013, Pope III, 2011). Such studies find significant correlations between PM10 or PM2.5 and increased hospital admissions or mortality. For long-term exposure, Pope et al. (2009) showed that a 10 μg m^{-3} decrease of PM2.5 leads to a 7.3($\pm$2.4) month increase in life expectancy.

Such estimates of the health impact of PM have been combined with global PM models to estimate the global mortality due to anthropogenic PM. The WHO report that ambient air pollution contributes to about 3.7 million excess deaths globally during 2012 (WHO, 2014a). Additionally, indoor pollution due to indoor fuel burning, mostly in developing nations, contributes to about 4.3 million deaths per year (WHO, 2014b). Together, air pollution is a contributing factor in about one in eight deaths worldwide.

Toxicological studies have shed light on the mechanisms behind these adverse health effects. The smallest particles penetrate deepest into the lung, reaching the alveoli (Valavanidis et al., 2008). Diesel engine exhaust (consisting of black and organic carbon) can cause inflammation of the airways and reduce vascular function and cause myocardial ischaemia, while also mutagenic effects (potentially leading to cancer) have been reported (WHO-Europe, 2013). PM has been shown to enhance plaque formation in the arteries (Sun et al., 2005). A large number of compounds present in PM are able to produce reactive oxygen species (e.g. H_2O_2), and free radicals (e.g. OH and $^{\bullet}O_2^-$), which can cause damage to e.g. DNA (Valavanidis et al., 2008).

Some recent studies have tried to assess the health impact of biogenic SOA. Gaschen et al. (2010) exposed lung cell cultures to SOA from α-pinene and the anthropogenic 1,3,5-trimethylbenzene. This study did not find cytotoxic effects, but more subtle effects

on cell function. McDonald et al. (2010) found that exposure of rats and mice to relatively high concentrations of about 200 μg m^{-3} of SOA from α-pinene did not lead to significant short term health effects. Rohr (2013) concluded that in studies in which humans were subjected to ambient SOA, no specific correlation between health effects and SOA (both biogenic and anthropogenic) has been proven, although there was a relation with POA. It is therefore possible that the health impact of fine PM is dependent on composition, with certain compounds mentioned above clearly adverse to health, and other types of SOA possibly being less harmful, at least at relevant concentrations. There is, however, a lack of epidemiological data on biogenic SOA impact (Rohr, 2013).

1.7.3 Climate change and the impact of aerosols

The global average temperature has increased by about 0.85 °C over the period 1880 to 2012, most probably due to anthropogenic forcings (IPCC, 2013). CO_2 emissions, due to combustion of fossil fuels and deforestation, have strongly increased since the Industrial Revolution, and have totalled between 470 to 640 GtC (gigatonnes carbon) between 1750 and 2011 (IPCC, 2013). The main sinks of CO_2 are uptake by the oceans, leading to ocean acidification, and by terrestrial ecosystems, while about 240 GtC has accumulated in the atmosphere. This has caused atmospheric CO_2-concentrations to rise by 40% since 1750, to a concentration of 391 ppm in 2011, a rise unprecedented in the last 800,000 years (IPCC, 2013).

Due to its greenhouse potential, the excess anthropogenic CO_2 exerts a radiative forcing on the Earth's atmosphere of approximately 1.68 W/m^2 (Fig. 1.6). The second highest anthropogenic radiative forcing is due to methane, and is estimated to be about 0.97 W/m^2. The radiative forcings due to halocarbons (0.23 W/m^2), N_2O (0.17 W/m^2) and CO (0.23 W/m^2) are smaller, but non-negligible.

The effect of aerosols on climate can be divided into a direct effect, through scattering or absorption of sunlight, and an indirect effect on clouds, through the role of aerosols as condensation nuclei (Seinfeld and Pandis, 2006, Myhre et al., 2013, Griffin, 2013). By scattering and reflecting light, aerosols have a cooling effect (Fig. 1.7), because they reflect part of the incoming sunlight back into space. However, aerosols also absorb part of the incoming sunlight. Black carbon is a strong absorber, and therefore contributes to global warming, while SOA and part of the inorganic aerosol are generally much weaker absorbers (Seinfeld and Pandis, 2006). The indirect effect is more complex, and is caused by the ability of aerosol particles to serve as cloud seeds. Higher cloud condensation nuclei numbers lead to clouds with a higher cloud droplet density, which have a higher

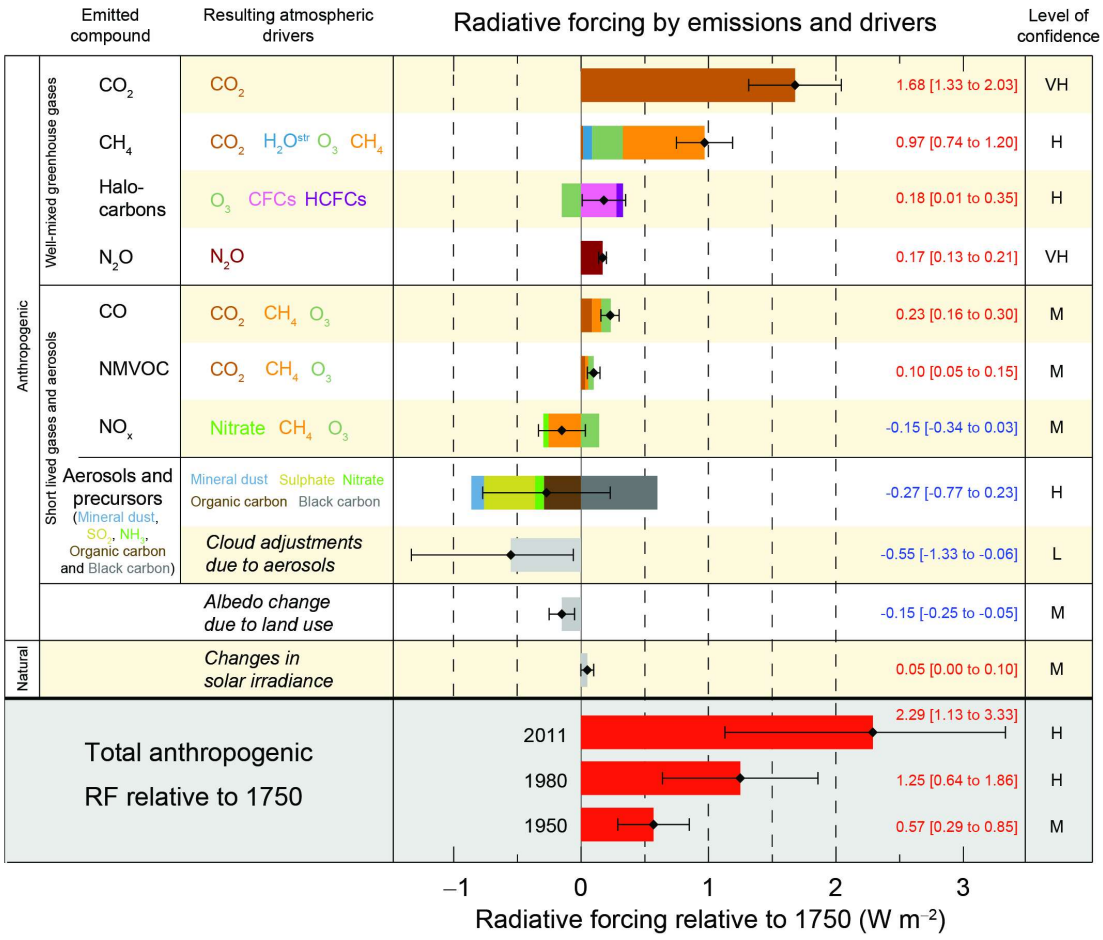

FIGURE 1.6: Radiative forcing estimates in 2011 relative to 1750 and aggregated uncertainties for the main drivers of climate change. Values are global average radiative forcing (RF14), partitioned according to the emitted compounds or processes that result in a combination of drivers. The best estimates of the net radiative forcing are shown as black diamonds with corresponding uncertainty intervals; the numerical values are provided on the right of the figure, together with the confidence level in the net forcing (VH very high, H high, M medium, L low, VL very low). Albedo forcing due to black carbon on snow and ice is included in the black carbon aerosol bar. Small forcings due to contrails (0.05 W m^2, including contrail induced cirrus), and HFCs, PFCs and SF_6 (total 0.03 W m^2) are not shown. Concentration-based RFs for gases can be obtained by summing the like-coloured bars. Volcanic forcing is not included as its episodic nature makes is difficult to compare to other forcing mechanisms. Total anthropogenic radiative forcing is provided for three different years relative to 1750. For further technical details, see IPCC (2013). This is Figure SPM.5 from IPCC (2013).

albedo, and therefore cool the atmosphere more effectively. There is also an effect on cloud lifetime (Seinfeld and Pandis, 2006, Griffin, 2013).

Anthropogenic aerosols have a direct effect for which current estimates range from +0.23 W/m^2 to -0.77 W/m^2, and an indirect effect between -0.06 W/m^2 and -1.33 W/m^2 (Fig. 1.6). Aerosols contribute the largest part of the uncertainty on the total anthropogenic radiative forcing estimate (IPCC, 2013).

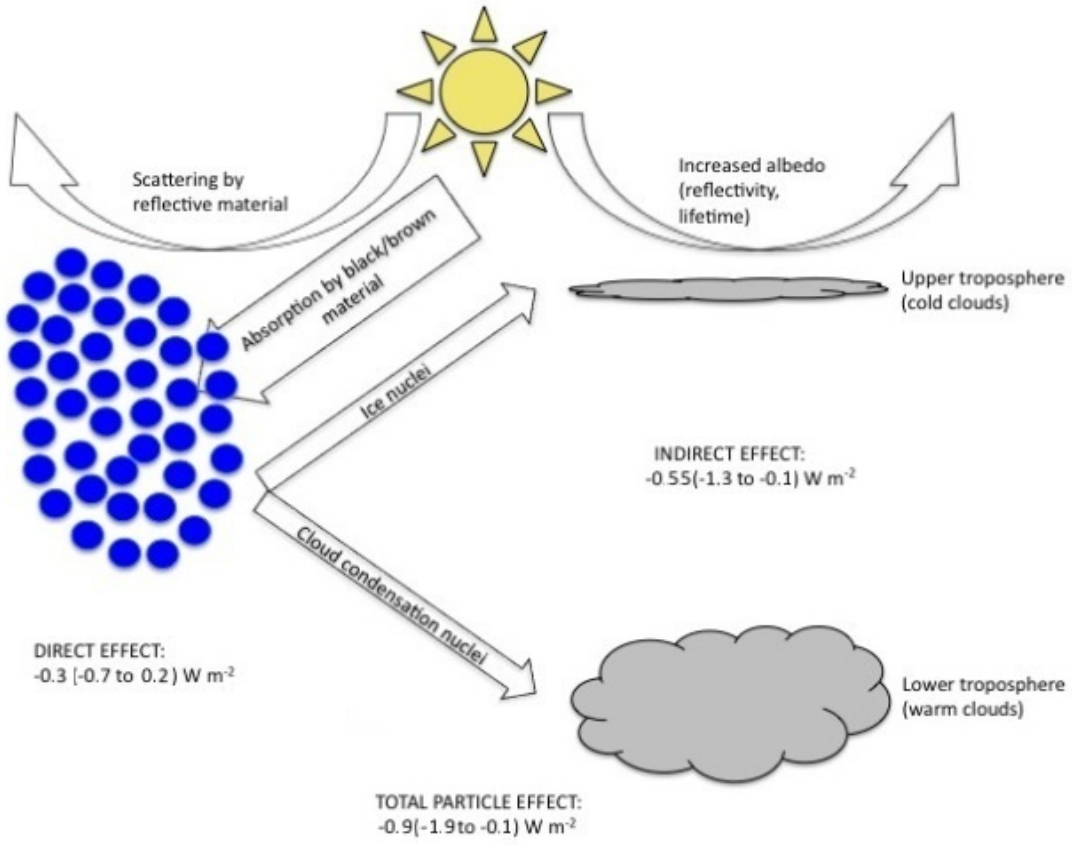

FIGURE 1.7: An illustration and description of the relative magnitude of the direct and indirect effect of particles on radiative forcing of climate. The indicated estimates for the radiative forcings have been updated based on IPCC (2013). ©2013 Nature Education All rights reserved. Taken from Fig. 2 of Griffin (2013)

Given that organic aerosols often make up more than 50% of total aerosol mass, a better understanding of the formation mechanisms and properties of organic aerosols is needed to better represent aerosol radiative forcings, and therefore reduce the uncertainty on climate predictions.

1.8 Secondary organic aerosols

1.8.1 Importance of biogenic SOA: experimental evidence

Measurements of ambient aerosol concentrations and determinations of its constituent fractions have been conducted at a large number of sites across the Earth. It is now possible to distinguish between the inorganic, organic, black carbon, and mineral aerosol fractions (Jimenez et al., 2009).

Fig. 1.8 shows determinations of the composition of sub-micron aerosol particles by aerosol mass spectrometry (AMS) at both rural and urban locations. In many cases,

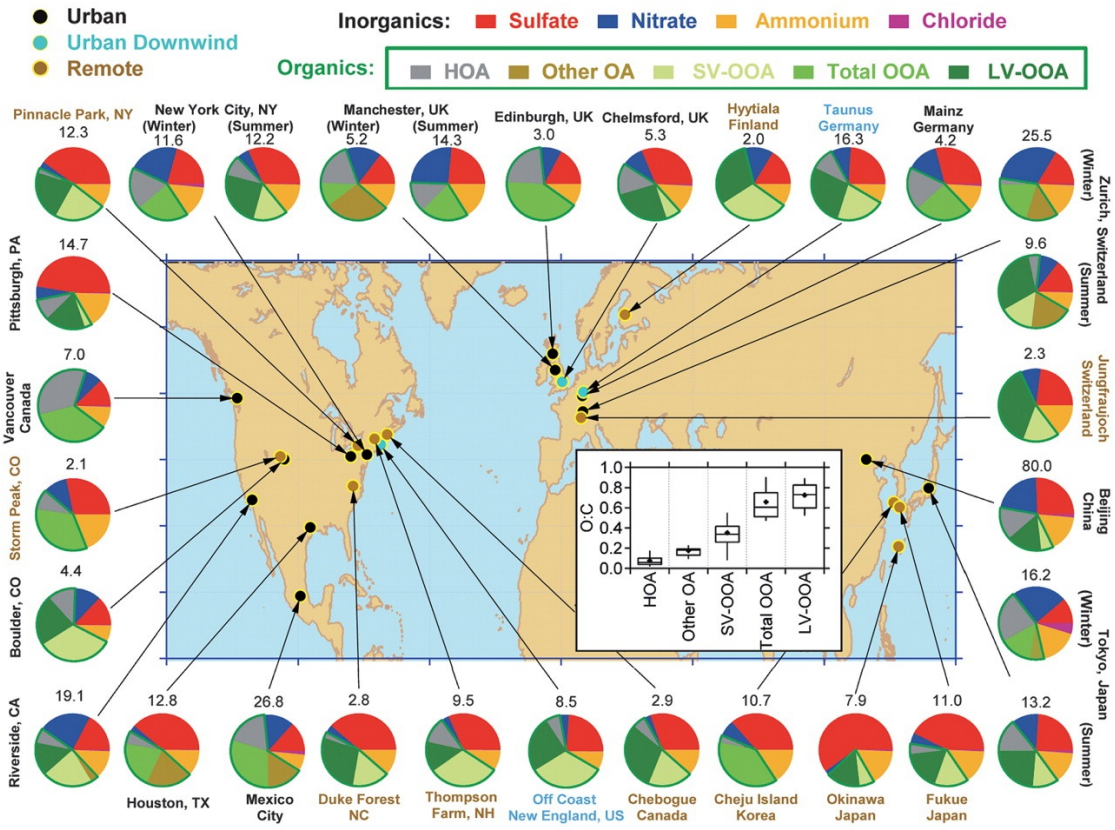

FIGURE 1.8: Total mass concentration (in μg m^{-3}) and mass fractions of nonrefractory inorganic species and organic components in submicrometer aerosols measured through aerosol mass spectrometry (AMS) at multiple surface locations in the Northern Hemisphere (21). In some studies, one oxygenated organic aerosol (OOA) factor was identified, whereas in other locations, two types, SV-OOA and LV-OOA, were identified. Hydrocarbon-like OA (HOA) is a surrogate for urban primary OA, and Other OA includes primary OAs other than HOA that have been identified in several studies, including biomass burning OA (BBOA). (Inset) Distributions of O:C for the OA components identified at the different sites, calculated according to (18). Figure and Caption have been taken from Fig. 1 of Jimenez et al. (2009). Indicated references are included in Jimenez et al. (2009)

the secondary organic fraction makes up more than 50% of the aerosols, and in the most polluted areas, this fraction still exceeds 25%. In some cases, a distinction could be made between semi-volatile and low-volatile organic aerosol (see Section 5.1), showing the possible impact of SOA ageing. Evidence of important contributions of biogenic volatile organic compounds (BVOC) to ambient SOA has been obtained by detection of tracer compounds, such as tetrols, originating from isoprene (Claeys et al., 2004), and pinic acid, norpinic acid, (hydroxy-)pinonaldehyde and pinonic acid (Yu et al., 1999b), and more recently organosulfates (Iinuma et al., 2007, Surratt et al., 2007, 2008, 2010), 3-methyl-1,2,3-butanetricarboxylic acid (MBTCA), terpenylic acid, diaterpenylic acid, diaterpenylic acid acetate and other mostly carboxylic acid containing tracers (Szmigielski et al., 2007, Claeys et al., 2009, Yasmeen et al., 2011, Kristensen et al., 2013) from α-pinene or β-pinene. A large majority of organic molecules in ambient SOA remains

structurally uncharacterised, however.

Chamber experiments on SOA formation present the advantage that initial concentrations and other experimental conditions, such as radiation, temperature and relative humidity (RH), can be controlled and determined more easily than in the real atmosphere. Such experiments have been carried out for biogenic VOC since the late eighties (Hatakeyama et al., 1989). Several VOCs have been identified as important SOA precursors, such as aromatic compounds, mostly of anthropogenic origin (Ng et al., 2007b), and biogenic species such as the monoterpenes (for examples, see references in Sect. 3.2), sesquiterpenes (Ng et al., 2007a), isoprene (Kroll et al., 2006, Hoyle et al., 2011) and dicarbonyls, through cloud or aerosol phase processing (Volkamer et al., 2009). An important parameter is the total organic mass concentration of SOA, M_{O}, from which also the SOA mass yield, defined as $Y = M_{\mathrm{O}}/M_{\Delta\mathrm{VOC}}$ can be derived.

Among the biogenic VOCs, the monoterpenes α- and β-pinene have received much attention. Numerous smog chamber studies have been conducted, aimed at monitoring SOA yields and elucidating the gas phase and aerosol phase composition and chemical mechanisms (see Chapters 3 and 4).

Smog chamber experiments show that various factors can impact SOA yields. Increasing temperature was found to decrease SOA yields (Pathak et al., 2007), as expected from the temperature dependence of saturated vapour pressures of semi-volatile compounds.

Whereas Tsigaridis et al. (2006) only considered ozonolysis as a significant SOA source from monoterpenes, photooxidation experiments, such as Ng et al. (2007a) have shown that high SOA yields are also found in the OH-initiated oxidation of α-pinene, especially under low-NO_x conditions. Griffin et al. (1999) and Fry et al. (2009) have shown that SOA from oxidation by NO_3 leads to particularly elevated SOA yields for β-pinene. It appears therefore that each of the main oxidants of alkenes is of importance for SOA formation.

SOA yields from α-pinene have been shown to decrease with increasing NO_x concentrations (Presto et al., 2005a, Ng et al., 2007a, Capouet et al., 2008). The same is not necessarily true for other VOCs, such as sesquiterpenes (Ng et al., 2007a, Hoyle et al., 2011), for which yields actually increase with increasing NO_x, and for isoprene, for which SOA yields first rise with increasing NO_x/VOC ratios, reaching a maximum, and then decrease (Hoyle et al., 2011).

Measured growth factors show that water can be taken up in significant amounts by SOA (Meyer et al., 2009), although Engelhart et al. (2011) found only slight increases of total aerosol volume due to SOA water uptake from measurements in Crete.

Photochemical ageing can have a strong impact on SOA composition and abundance. Long-term oxidation of semi-volatile compounds by OH was shown to be crucial (Jimenez et al., 2009), influencing SOA concentration, composition and hygroscopicity. A number of recent studies have investigated photooxidative ageing of α-pinene in smog chambers (see Chapter 5).

Isotopic measurements of ambient aerosol samples have recently indicated a positive correlation between anthropogenic pollution and the modern fraction of organic aerosol, which is most likely biogenic SOA (Hoyle et al., 2011). Organic aerosol measurements worldwide seem to indicate the existence of a large anthropogenically-controlled source, which however cannot be explained by fossil carbon emissions (Spracklen et al., 2011, Stavrakou et al., 2013). The observed decrease in SOA yields with increasing NO_x for monoterpenes is at odds with this finding. Suggested explanations are the increasing effect of NO_x on isoprene and sesquiterpene SOA, the impact of acidic particles (which are of anthropogenic origin) on oligomerisation in the SOA, the interaction with already present anthropogenic PM, stimulating absorption of semi-volatile BVOC oxidation products (Hoyle et al., 2011), and the uptake of semi-volatile vapours by water associated with anthropogenic inorganic aerosols (Carlton and Turpin, 2013).

1.8.2 Modelling studies

1.8.2.1 Do we understand SOA formation?

Due to the complexity of VOC oxidation and SOA formation, model simulations are needed for quantitative interpretation of experimental results. Models of variable complexity have been developed for the description of the oxidation of α-pinene, supplemented with a partitioning model (Kamens and Jaoui, 2001, Jenkin, 2004, Capouet et al., 2008, Xia et al., 2008, Valorso et al., 2011), based on the partitioning theory approach of Pankow (1994).

In an ideal model, every gas phase or aerosol phase reaction which the VOC oxidation products can undergo would be represented explicitly, and its rate constant would be known exactly. However, only for the very simplest organic compounds, such as methane, ethane and ethene, have the kinetics of the main oxidation reactions been experimentally investigated (Hallquist et al., 2009). For larger VOCs, the gas phase oxidation spans several generations, leading to a multitude of products, for which kinetic rates and product branching fractions are not known from experiment. Therefore, these kinetic rates need to be inferred based on the reactions of compounds with similar structure, for which experimental data are available (Hallquist et al., 2009, Atkinson et al., 2006). This

has led to the development of so-called structure activity relationships (SARs), which are simple rules to predict kinetic rates of relevant reactions (see Chapter 2). These SARs have been relatively successful when applied to gas phase mechanism generation, but still inherently contain uncertainties. Oxidation products often have a more complex structure than that of the species on which SARs are based, for example because of the presence of multiple functional groups or more complex carbon skeletons. In that case, more advanced theoretical methods, such as quantum-chemical calculations, can sometimes be applied, as for many key reactions in the mechanism of α-pinene (Peeters et al., 2001) and isoprene (Peeters et al., 2009, Peeters and Nguyen, 2012). Such methods are computationally very demanding, however, which limits their applicability to large systems; furthermore, they still have large uncertainties, which are often difficult to quantify (Vereecken and Francisco, 2012).

A similar situation exists for the calculation of the partitioning between gas and aerosol phase, for which the partitioning theory of Pankow (1994) requires the saturated vapour pressures and activity coefficients of the oxidation products. These parameters are also largely estimated from SARs, due to the lack of direct measurements. The situation is even worse for reactions in the SOA phase, which are generally ignored. Another complication is the recent finding that aerosols may not always behave as perfect liquids, but can instead be viscous, preventing efficient mixing and fast equilibration between gas and aerosol phases (Cappa and Wilson, 2011, Shiraiwa et al., 2013a).

Clearly, even the most explicit models have large uncertainties (Hallquist et al., 2009), which inevitably result in large discrepancies between modelled and experimental SOA yields. Extensive comparisons with smog chamber experiments are therefore important in order to estimate their validity. For example, Xia et al. (2008) found that their MCM-based model (Saunders et al., 2003) performed reasonably well at low temperatures and for high aerosol masses, but that it underestimated measured yields by more than a factor of one thousand in case of low measured SOA mass and high temperature. The very detailed model GECKO-A, with ca. 500,000 species (Valorso et al., 2011), was found to overestimate the observed SOA yields for photooxidation experiments of Ng et al. (2007a) by about a factor of two.

Such large deviations from measured SOA yields, and sometimes between different models, indicate that more work is needed to better characterise the impact of mechanistic uncertainties, and possibly disprove or validate newly proposed processes of potential importance. As will be shown in Chapters 3 to 5, the causes of such model discrepancies are not easily identified, and a combination of model errors might be at play. The fact that the majority of oxidation products in the gas phase or SOA has not been experimentally identified (Hallquist et al., 2009) makes model validation difficult. Furthermore, there

is often considerable uncertainty regarding the precise experimental conditions, and especially regarding the possible effects of deposition of vapours or aerosol on the walls (Matsunaga and Ziemann, 2010, Donahue et al., 2012).

1.8.2.2 Modelling SOA formation on the global scale

In order to estimate the extent of aerosol formation in the real atmosphere, models need to account for emissions, chemical transformation, transport, and removal of species. For computational convenience, the atmosphere is generally divided into a number of horizontal and vertical Eulerian grid cells, in which the concentrations of chemical species are calculated based on a simplified representation of chemical, physical and microphysical processes. Meteorological analyses are used to drive the simulation of transport between grid cells (Seinfeld and Pandis, 2006).

To estimate SOA formation in large-scale models, parameterised two-product models have been formulated and based on experimental SOA mass yields (Odum et al., 1996) (see Sect. 6.5). However, smog chamber experiments are often conducted under conditions which differ greatly from the atmosphere: initial VOC loadings are generally much higher, NO_x concentrations might differ, OH-scavengers are often used, and their duration is often relatively short – several hours – while atmospheric photochemical ageing might continue for several days.

A more elaborate parameter model is the 2D-VBS (two-dimensional volatility basis set) model (Jimenez et al., 2009, Donahue et al., 2012), which contains a number of proxy species, spanning different volatilities and O to C ratios. Upon reaction with OH, these proxy species undergo functionalisation and/or decomposition. Its parameters can be optimised against smog chamber experiments. As it contains a representation of additional chemical changes to products, it is better suited for representing SOA ageing.

Global modelling studies on SOA formation have made use of SOA parameterisations for various precursors (see for example Henze et al., 2008, Tsigaridis and Kanakidou, 2007, Farina et al., 2010, Pye and Seinfeld, 2010, Pye et al., 2010, Carlton et al., 2010, Tsigaridis et al., 2014). In such studies, parameterisations for α-pinene SOA are often used for SOA from some or all of the monoterpenes.

Tsigaridis et al. (2014) found that global models still vary greatly in simulated magnitude of POA and SOA. The complexity of the implemented schemes varies between models, in terms of the types of sources implemented (often still very uncertain in magnitude), and the way in which gas-particle partitioning, chemical ageing, multiphase chemistry or aerosol microphysics are treated. This leads to an order of magnitude diversity in

TABLE 1.2: Yearly global production of different types of aerosol, in Tg a^{-1}, based on Tsigaridis et al. (2014) for OA, and on Table 7.1 from IPCC, Working group I (2014). In this last study, the indicated range is the range of the different estimates of the consulted sources.

Type	Minimum	Maximum
POA[a]	34	144
SOA[a]	13	121
monoterpenes[c]	8.7	17.2
isoprene[c]	4.6	14.4
sesquiterpenes[c]	0	3.9
aromatics[c]	1.6	8.6
dicarbonyls and epoxides[c]	0	89
Anthropogenic BC[b]	3.6	6.0
Biomass burning aerosols[b]	29	85.3
Sea spray[b]	1400	6800
Mineral dust[b]	1000	4000
Terrestrial PBAPs[b]	50	1000

[a] From Tsigaridis et al. (2014). [b] From IPCC, Working group I (2014). PBAP stands for primary biological aerosol particle. Note that, although sea spray, mineral dust and PBAPs have high total yearly mass productions, they are often emitted in the coarse mode, and therefore they contribute relatively less to the atmospheric loading than this total production indicates, as they on average undergo more rapid gravitational sedimentation than finer particles do. [c] Range for the studies of Tsigaridis and Kanakidou (2007), Pye and Seinfeld (2010), Farina et al. (2010), Henze et al. (2008) and Lin et al. (2012). Only this last study considered SOA from cloud or aerosol processing of glyoxal, methyl glyoxal or isoprene epoxides. Lin et al. (2012) did not give separate production for traditional monoterpene, isoprene or sesquiterpene SOA. The review of Tsigaridis et al. (2014) did not give specific results for SOA production from the different BVOC for the models included in their study.

vertical organic aerosol distribution between the models. In Table 1.2, an overview is given of global annual production of different types of aerosols. The monoterpenes are found to make up an important, although not dominant contribution to SOA, according to several studies, as isoprene and dicarbonyls are also important biogenic sources.

1.9 Objectives and methodology of this work

The objective of this study is to improve our understanding of the formation mechanisms of organic aerosol from the atmospheric oxidation of biogenic organic compounds. As SOA represents an important fraction of atmospheric aerosols, this can contribute to a better estimate of the impact of aerosols on air quality and climate. The focus lies on SOA from the monoterpenes α- and β-pinene, which are among the most-emitted

biogenic VOCs. As a tool, BOREAM, a model which combines a chemical mechanism and an aerosol formation module, is used to investigate the SOA formation process.

We investigate in how far this model is capable of predicting observed organic aerosol formation under controlled conditions in smog chambers. Important quantities which are compared are SOA mass concentrations, and the concentration of certain gas phase and SOA constituents. These comparisons are meant to explore whether important processes are missing or misrepresented. A particular focus of this work lies on photochemical ageing, i.e. the continued exposure to photolysis and OH radicals, of gas and aerosol compounds, and how well this process is currently reproduced by models.

Another aim is the construction of sufficiently accurate models for SOA formation in regional or global atmospheric models, used to study atmospheric chemistry, air quality or climate. Besides the already discussed problem of the skill of detailed models in reproducing SOA concentrations, another issue is model size. We therefore present a method for deriving a compact parameterisation, suitable for use in large-scale models, but still capable of modelling SOA formation realistically.

In order to achieve the above aims, the development of BOREAM is continued. The model gas phase chemistry and aerosol partitioning mechanisms are brought up to date, a new mechanism for β-pinene is added, and secondary chemistry has been extended using an automatic generation approach, with the aim of modelling SOA ageing. This forms the subject of Chapter 2.

Chapter 3 presents simulations of a number of smog chamber α-pinene experiments. We verify in how far the formation of recently observed specific gas phase and SOA species from α-pinene oxidation is reproduced by the model. In Chapter 4, the new mechanism for β-pinene oxidation is confronted against measurements of gas phase compounds and SOA in smog chambers, and sensitivity tests are conducted in order to estimate the impact of uncertain parameters. In Chapter 5, BOREAM is used for the simulation of recent experiments in which SOA and gas phase compounds from α-pinene are subjected to photochemical ageing. In Chapter 6, a parameterised model is fitted against the detailed mechanism. A novel approach is adopted, appropriate for representing long-term SOA ageing, in close-to-atmospheric conditions. General conclusions and perspectives are presented in Chapter 7.

Chapter 2

Model description

In this Chapter the BOREAM model for monoterpene oxidation and subsequent aerosol formation is described in detail. Gas phase reactions are discussed in Section 2.1. In Section 2.2, the primary chemistry of the two monoterpenes treated in the BOREAM model, α-pinene and β-pinene, is presented. A number of key reactions in these primary chemistry schemes are based on theoretical calculations available in the literature. In Section 2.3, the chemistry of generic species, which represent lumped compounds with similar volatility and carbon number, is defined. In Section 2.4, aerosol processes are discussed, such as the partitioning between gas and aerosol phase, possible heterogeneous or aerosol phase reactions, and wall losses. Section 2.5 shows how the previously discussed parts of the model are implemented with the help of an automatic generation approach. Results obtained with BOREAM are the subject of the next Chapters 3 to 6.

2.1 Gas phase chemistry

For small organic compounds, experimentally derived rate constants and product distributions are available. Most reactions of these small organic species (containing one up to typically three or four carbons) are obtained from recommendations such as the gas-kinetics database of IUPAC (IUPAC, 2014, Atkinson et al., 2006), or from reviewed models such as the MCMv3.2 (Saunders et al., 2003, Jenkin et al., 2012). With some exceptions, such as pinonaldehyde or nopinone, there are few experimental determinations of the reactivity of large oxidation products of α- or β-pinene. For these species, SARs or theoretically derived rates are used, as explained in the next subsections.

2.1.1 OH radical reactions with organic molecules

Reaction with hydroxyl radicals (OH) is one of the most important chemical loss mechanisms for organic molecules in the troposphere (Atkinson et al., 2006). For most hydrocarbons the reaction with OH proceeds by H-abstraction, except for alkenes, for which OH-addition on double-bonded carbon atoms is the major pathway.

2.1.1.1 Addition of OH on double bonds

OH-addition on a double carbon bond is known to result in a pre-reactive complex, where the H of the hydroxyl radical associates with the double bond π-system, followed by rotation of the OH moiety towards either of the carbons (Vereecken and Francisco, 2012). The resulting product is a hydroxy alkyl radical, which can react with O_2 to form a β-hydroxy peroxy radical.

For the OH-addition on double-bonded carbons, the SAR of Peeters et al. (2007) was implemented in BOREAM. In this SAR the rate of addition to a double-bonded carbon a is predicted to depend on the properties of the other carbon b, which will become the position of the alkyl radical after OH-addition. In case of a primary carbon atom b (connected only to the carbon atom a) the rate $k_{\text{prim}} = 0.45 \times 10^{-11}\,\text{cm}^3\,\text{molecules}^{-1}\,\text{s}^{-1}$ is estimated. For secondary and tertiary double bonded carbons the rates are $k_{\text{sec}} = 3.0 \times 10^{-11}\,\text{cm}^3\ \text{molecules}^{-1}\,\text{s}^{-1}$ and $k_{\text{tert}} = 5.5 \times 10^{-11}\,\text{cm}^3\ \text{molecules}^{-1}\,\text{s}^{-1}$. For conjugated dienes, the SAR proposed by Peeters et al. (2007) was implemented, although currently only very few conjugated dienes are present in the BOREAM pinene mechanisms.

This SAR does not take into account the possible influence of oxygenated functional groups near the double bonds. In BOREAM the above SAR is still used in such cases, by lack of more detailed SARs. This assumption likely leads to larger errors compared to the typically small deviations found for non-substituted alkenes by Peeters et al. (2007). The rates for the reactions of α and β-pinene with OH will be discussed in Subsections 2.2.1.1 and 2.2.2.1.

2.1.1.2 H-abstraction by OH

H-abstraction by OH is important for saturated organic compounds, and, although slower than addition on double bonds, it is of importance for some larger alkenes (Vereecken and Francisco, 2012). In BOREAM the SAR of Neeb (2000) is mostly followed for H-abstraction by OH. Another SAR is that of Kwok and Atkinson (1995), used in many models, such as GECKO-A (Aumont et al., 2005, Valorso et al., 2011)

and MCMv3.2 (Jenkin et al., 1997, 2012). The SAR of Neeb (2000) was fitted against experimental rates for about 250 species. It achieves an agreement within 50% for most species in the data set, which is an improvement over the SAR of Kwok and Atkinson (1995). The contributions taken into account for the H-abstraction SAR are given in Table 2.1.

For alkanes, a distinction was made in Neeb (2000) between H-abstractions from carbons containing 3 (primary), 2 (secondary) or 1 (tertiary) hydrogen atoms. The group contributions were derived from data for 41 alkanes, including 12 cyclo-alkanes. They do not take into account effects of ring strain or steric hindrance explicitly, as different types of rings (containing different numbers of carbons or single or double bonds) might induce significantly different effects, and the amount of data was insufficient (Neeb, 2000). This is a problem for many pinene oxidation products, which can contain 1 or 2 rings. Theoretical calculations (Vereecken and Peeters, 2002) did indeed show significant deviations from the SARs of Kwok and Atkinson (1995) and Neeb (2000) for some ring-containing biogenic species.

For carbon atoms bonded to one or more oxygen atoms, H-abstraction group contribution terms were fitted against 26 ethers, 14 alcohols, 7 hydroxy ethers, 5 formates, 3 hydroperoxides, 14 ketones, 5 aldehydes, 2 hydroxy aldehydes, 20 esters and 4 carboxylic acids in Neeb (2000). The group contributions of alcohols and ethers were found to lie close together, and therefore given the same value. Given the low number of experimental data, the abstraction of H from hydroperoxides was also chosen equal to this contribution. A distinction is made between secondary and tertiary hydrogens for these groups. In absence of data for peroxides, we supposed that a peroxide can have a similar effect as a hydroperoxide group. The fastest H-abstraction was found for the aldehydic H. The value obtained by Neeb (2000) (11.5×10^{12} cm^3 molecules^{-1} s^{-1}) is significantly lower than that of Kwok and Atkinson (1995) (20.8×10^{12} cm^3 molecules^{-1} s^{-1}). Given this discrepancy, we adopted an average value, 16.9×10^{12} cm^3 molecules^{-1} s^{-1}. The quantum-chemical calculation of Vereecken and Peeters (2002) for abstraction of the aldehydic hydrogen in pinonaldehyde yielded the same value as the SAR of Kwok and Atkinson (1995).

The group contribution for carbons next to a carbonyl or carboxylic acid group is dependent on the number of hydrogen atoms on this carbon. For primary hydrogen atoms, it is low, $k_{\mathrm{abst}}(\mathrm{C}\mathbf{H}_3\mathrm{C(O)\text{-}X}) = 0.21 \times 10^{-12}$ cm^3 molecules^{-1} s^{-1}. However, for the secondary and tertiary case the group contributions are considerably higher than for the corresponding alkane groups, $k_{\mathrm{abst}}(\mathrm{RC}\mathbf{H}_2\mathrm{C(O)\text{-}X}) = 4.08 \pm 0.87 \times 10^{-12}$ cm^3 molecules^{-1} s^{-1} and $k_{\mathrm{abst}}(\mathrm{R_2C}\mathbf{H}\mathrm{C(O)\text{-}X}) = 11.9 \pm 2.1 \times 10^{-12}$ cm^3 molecules^{-1} s^{-1}, where X = R or H. In the study of Vereecken and Peeters (2002), however, the abstraction of a secondary

TABLE 2.1: Implemented SAR for the rate of H-abstraction by OH in units of 10^{-12} cm^3 $molecules^{-1}$ s^{-1}, based on Neeb (2000). The abstracted **H** is indicated in bold font.

Chemical functionality and BOREAM notation	Notation in Neeb (2000)	k_{298}	A[a]
Alkane			
k_{prim}	$k_{\mathrm{abst}}(\mathrm{RC}\mathbf{H}_3)$	0.21 ± 0.07	-1.5
k_{sec}	$k_{\mathrm{abst}}(\mathrm{R_2C}\mathbf{H}_2)$	1.42 ± 0.06	-1.1
k_{ter}	$k_{\mathrm{abst}}(\mathrm{R_3C}\mathbf{H})$	1.81 ± 0.20	-0.6
Aldehyde			
k_{ald}	$k_{\mathrm{abst}}(\mathrm{RC}\mathbf{H}\mathrm{O})$	16.9[b]	
Ether, alcohol or hydroperoxide			
k_{seth}	$k_{\mathrm{abst}}(\mathrm{RC}\mathbf{H}_2\mathrm{O\text{-}X})\times$ F(X= H, R or OH)[d]	5.32 ± 0.40	0.5
k_{teth}	$k_{\mathrm{abst}}(\mathrm{R_2C}\mathbf{H}\mathrm{O\text{-}X})\times$ F(X= H, R or OH)[d]	6.54 ± 0.90	-1.0
Hydroperoxide or peroxy acid (O-bonded H)			
$k_{\text{H-abst,ROOH}}$	$k_{\mathrm{abst}}(\mathrm{ROO\text{-}}\mathbf{H})$	2.0 ± 0.8	
Alcohol (O-bonded H)			
$k_{\text{H-abst,ROH}}$	$k_{\mathrm{abst}}(\mathrm{RO\text{-}}\mathbf{H})$	0.8 ± 0.7	-0.8
Carboxylic acid (O-bonded H)			
$k_{\text{H-abst,ROH}}$	$k_{\mathrm{abst}}(\mathrm{RC(O)O}\mathbf{H})$	0.8 ± 0.4	
Ester			
$k_{\mathrm{seth}} \times F_{\mathrm{COR}}$	$k_{\mathrm{abst}}(\mathrm{RC}\mathbf{H}_2\mathrm{O\text{-}X})\times$ F(X=C(O)R)	$5.32 \pm 0.40 \times 0.44 \pm 0.06$	0.5
$k_{\mathrm{teth}} \times F_{\mathrm{COR}}$	$k_{\mathrm{abst}}(\mathrm{R_2C}\mathbf{H}\mathrm{O\text{-}X})\times$ F(X=C(O)R)	$6.54 \pm 0.90 \times 0.44 \pm 0.06$	-1.0
$k_{\mathrm{seth}} \times F_{\mathrm{COH}}$	$k_{\mathrm{abst}}(\mathrm{RC}\mathbf{H}_2\mathrm{O\text{-}X})\times$ F(X=C(O)H)	$5.32 \pm 0.40 \times 0.078 \pm 0.22$	0.5
$k_{\mathrm{teth}} \times F_{\mathrm{COH}}$	$k_{\mathrm{abst}}(\mathrm{R_2C}\mathbf{H}\mathrm{O\text{-}X})\times$ F(X=C(O)H)	$6.54 \pm 0.90 \times 0.078 \pm 0.22$	-1.0
Methanoate group			
not considered	$k_{\mathrm{abst}}(\mathrm{ROC(O)\text{-}}\mathbf{H})$	0.012 ± 0.7	
Organic nitrate			
k_{snit}	$k_{\mathrm{abst}}(\mathrm{RC}\mathbf{H}_2\mathrm{O\text{-}X})\times$ F(X=NO_2)	$0.07 \times (5.32 \pm 0.40)$	
k_{tnit}	$k_{\mathrm{abst}}(\mathrm{R_2C}\mathbf{H}\mathrm{O\text{-}X})\times$ F(X=NO_2)	$0.07 \times (6.54 \pm 0.90)$	
$k_{\mathrm{prim}} \times F_{\mathrm{NO_2}}, \ldots$ [c]	$k_{\mathrm{abst}}(\mathrm{RC}\mathbf{H}_3)\times$ F(X=NO_2),...	$0.07 \times (0.21 \pm 0.07)$,...	

[a] A is the exponent in the temperature dependent expressions $k_{\mathrm{OH}}(T) = k_{298}(298\,\mathrm{K}/T)^A$
[b] Value adopted in this work (see text).
[c] This contribution is applied for H-abstraction from unsubstituted carbons in β-position from nitrate groups. [d] The value of the factor F(X= H, R or OH) is 1.

hydrogen on a carbon (C_d) next to a carbonyl in pinonaldehyde was found to have a rate equal to 8.0×10^{-12} cm^3 molecules^{-1} s^{-1} (two times higher), while for the tertiary C_g the H-abstraction rate 2.0×10^{-12} cm^3 molecules^{-1} s^{-1} was more than 5 times lower than in Neeb (2000). In BOREAM these two group contributions have not been considered and the lower group contributions k_{sec} and k_{ter} are used instead. Notwithstanding the deviations between Neeb (2000) and Vereecken and Peeters (2002), it would be of interest to consider the enhancing influence on H-abstraction of neighbouring carbonyl groups in a later model version. The very low contribution for abstraction from methanoate groups in Neeb (2000) is set to zero in BOREAM. Abstraction from methyl ethers or esters has not been implemented, but plays a negligible role in the current BOREAM mechanism.

For organic nitrates, Neeb (2000) considered 16 monofunctional species. It was found that the influence of an organic nitrate group in α-position reduced the H-abstraction rate by a factor $F(X = NO_2) = 0.07$ compared to the group contributions for carbons with other oxygen-containing functional groups, like alcohols or ethers, in α-position. But it was also found that the nitrate groups extended this reducing influence to carbons in β-position, for which a multiplicative factor $F(X = NO_2) = 0.07$ improved agreement for nitrates. This reducing influence is only considered when no other functional group is present on the β-carbon, by lack of data for poly-functional organic nitrates. For organic peroxy acyl nitrate groups, we suppose that the OH-reaction with this group is negligible, based on the IUPAC recommendations for $CH_3C(O)OONO_2$ and $CH_3CH_2C(O)OONO_2$ (IUPAC, 2014).

2.1.1.3 OH oxidation rates for specific biogenic compounds

More detailed experimental and theoretical results are available for a few important pinene oxidation products. The reaction rate of pinonaldehyde with OH was measured by Alvarado et al. (1998) and Nozière et al. (1999), obtaining $48 \pm 8 \times 10^{-12}$ cm^3 molecules^{-1} s^{-1} and $40 \pm 10 \times 10^{-12}$ cm^3 molecules^{-1} s^{-1}, respectively. Vereecken and Peeters (2002) theoretically calculated site-specific H-abstraction rates for pinonaldehyde, pinonic acid and pinic acid. The total reaction rate for pinonaldehyde obtained by Vereecken and Peeters (2002) was 35.2×10^{-12} cm^3 molecules^{-1} s^{-1}, slightly below the experimental values, but above the value given by the SAR of Kwok and Atkinson (1995). Vereecken and Peeters (2002) indicate that the uncertainty for these calculated site-specific H-abstraction rates from individual carbons is difficult to determine, but could be a factor 2 in some cases. In absence of experimental data, in BOREAM we adopted the site-specific rates given in Table 2 in Vereecken and Peeters (2002).

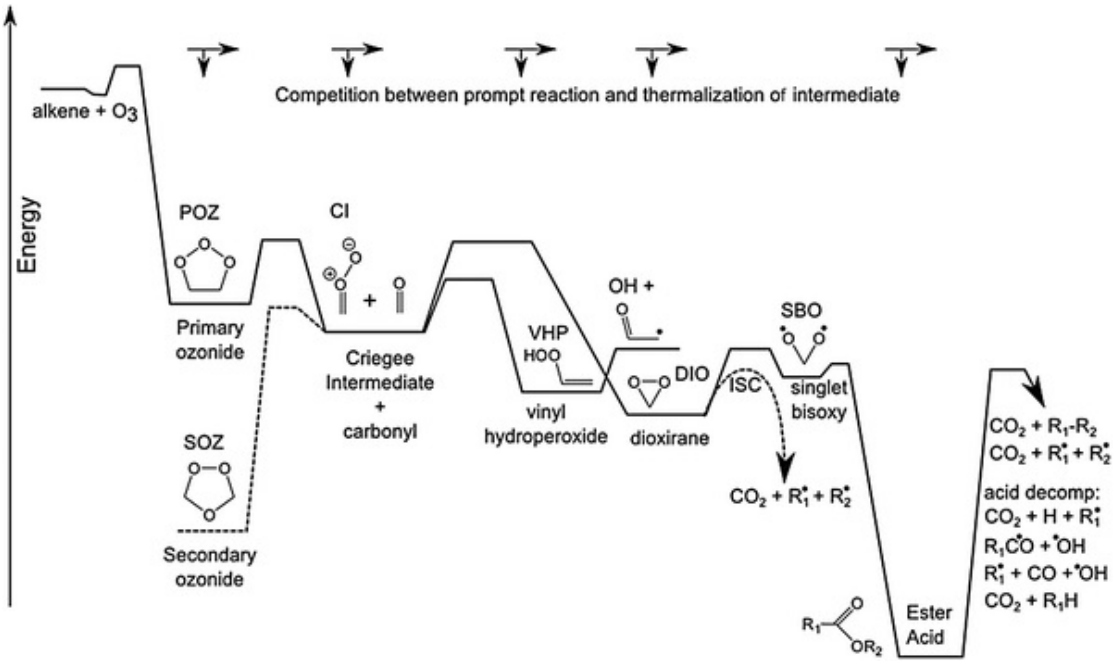

FIGURE 2.1: Reaction scheme for the ozonolysis of alkenes. Reactions in dotted lines are important for thermalised intermediates. This Figure has been taken over without changes from Vereecken and Francisco (2012), Fig. 9.

2.1.2 Reactions of organic molecules with ozone

The reaction of ozone with organic molecules is only of atmospheric interest for species containing double carbon bonds (Atkinson et al., 2006). However, for alkenes it is one of the main oxidation processes together with reaction with OH or NO_3 radicals.

The reaction of alkenes with ozone results in the formation of an unstable primary ozonide (POZ), through addition of the outer oxygen atoms of O_3 on the double-bonded carbon atoms (Vereecken and Francisco, 2012, Donahue et al., 2011a). This reaction is strongly exothermic, and results in a series of relatively weakly bound intermediates, which either quickly decompose or stabilise (Donahue et al., 2011a), see Fig. 2.1. The primary ozonide quickly decomposes through breaking of the original carbon bond, resulting in a so-called Criegee Intermediate (CI) and a carbonyl group (Vereecken and Francisco, 2012, Donahue et al., 2011a). In case the carbon bond on which the ozonolysis addition takes place is non-cyclic, the breaking of the carbon bond leads to a break-up of the original compound into a separate CI and a molecular carbonyl; if the carbon bond was cyclic then the CI functionality and carbonyl group remain on the same product compound. The CI will still contain a large amount of excess energy. It can undergo unimolecular isomerisation into an activated vinyl hydroperoxide (VHP) (Vereecken and

Francisco, 2012, Donahue et al., 2011a) or into a dioxirane (DIO) (Vereecken and Francisco, 2012). Depending on the pressure and temperature, the activated CIs can also partially become thermally stabilised through collisions with the bath gas.

The chemistry of the CIs remains one of the most uncertain parts of the secondary chemistry, and SARs for CI reactions are often based on little or inconsistent data. For α- and β-pinene, relatively few secondary products remain unsaturated, but for terpenes containing multiple double bonds, the ozonolysis of degradation products can be expected to be more important.

2.1.2.1 Ozonolysis reaction rate

The reaction rates of ozone with unsaturated compounds for which no reliable experimental data are available are estimated based on the SAR developed by McGillen et al. (2008), Leather et al. (2010) and McGillen et al. (2011). It takes into account effects of substitutions of carbon atoms or hetero-atomic functional groups around the double-bonded carbon atoms. The reaction rate is given by

$$k_{O_3} = A \cdot \exp \frac{-E_a}{RT} \tag{2.1}$$

(Leather et al., 2010), where the pre-factor A and activation energy E_a are estimated by the expressions $\ln A = -(0.18x + 32.68)$ and $E_a\,(\mathrm{kJ\,mol^{-1}}) = -6.72x + 21.23$, where the so-called index of reactivity $x = yS + I_X$ depends on the total steric effect S and the total inductive effect I_X, and $y = -4.04$ is a constant (Leather et al., 2010). The steric effect S takes into account the reduction of the rate constant of ozone addition due to the fact that substitutions around the carbon atoms of the double bond hinder the addition to the double bond. The presence of bonds in α-, β- and γ-position is taken into account, as described in McGillen et al. (2008) and McGillen et al. (2011), although with a few minor simplifications. For the inductive effect, a number of different types of substitutions given by McGillen et al. (2011), present in α-, β- or γ-position are considered, where the contribution of the substitutions has to be divided by the number of alternative branchings on the way towards the double bonded carbons, as such other branchings are assumed to reduce the inductive effect. McGillen et al. (2011) found that the group contribution method gave good agreement for a large number of compounds in the reaction database compared to previous methods, although considerable discrepancies remain for some compounds. One remaining drawback is also that certain important functional groups, such as nitrates or hydroperoxides, have not been considered, presumably due to lack of data.

2.1.2.2 Initial branching towards different possible CIs

The short-lived primary ozonide undergoes a breaking of the double bond, leaving a carbonyl and CI function on both ends of the broken bond. The branching fraction for the appearance of the CI function on the first or second carbon is obtained from the SAR of Carter (2000), also applied by Laval-Szopa (2003). In this SAR, in case both carbons of a double bond have the same number of substitutions, a 50:50 distribution of the CI function over the two carbon atoms is applied. When there is a difference in substitution, the more-substituted carbon receives the higher branching towards the CI function (0.35:0.65 for $C(H_2)$=C<, 0.30:0.70 for -C(H)=C<, but 0.5:0.5 for $C(H_2)$=C(H)-). However, these branching fractions can be still different in more complex compounds, such as for example β-pinene, where the CI is added predominantly on the endocyclic carbon. Theoretical calculations show that different conformers of the CI (anti or syn with respect to the carbon chain) can have a different chemistry. For the initial ozonolysis of α- and β-pinene this chemistry is elaborated in more detail than for the SAR, and is discussed further on in this Chapter.

2.1.2.3 Reactions of activated CIs

The reactivity of the CIs can be illustrated from Fig.2.1, which is taken over Vereecken and Francisco (2012) (Fig. 9). The CIs can on the one hand undergo a unimolecular isomerisation, either through the formation of an activated vinyl hydroperoxide, which normally decomposes into a carbonyl-bearing alkyl radical and OH, or through formation of a dioxirane, which can, among other reactions, further transform into an ester or acid, or decompose, giving off CO_2 (Vereecken and Francisco, 2012, Donahue et al., 2011a). Whether one or the other channel is chosen depends on the structure, with so-called syn-CI (in which the CI oxygens and a carbon atom, attached to the carbon bearing the Criegee function, are oriented on the same side of the molecule) favouring the H-shift necessary to form the vinyl hydroperoxide. An accurate treatment of the chemistry of CI (and SCI) should therefore include the different types of stereo-isomeric CIs produced. This distinction is not made in the SAR, but it is taken into account in the initial ozonolysis mechanisms. OH yields have been determined experimentally (Atkinson et al., 2006), which give an indication about the contribution of the vinyl hydroperoxide decomposition pathway.

The energetic CIs can also be collisionally stabilised into so-called Stabilised Criegee Intermediates (SCIs), with different reactivity than the original CI. Some small SCIs, e.g. from ethene, are partially stabilised upon formation (Vereecken and Francisco, 2012). For other CIs, the amount of stabilisation is dependent on pressure, with lower pressure

leading to less stabilisation, and higher OH yields (Fenske et al., 2000, Donahue et al., 2011a). The stabilisation fraction tends to increase with the size of the CI, and be lower for CIs originating from the ozonolysis of endocyclic bonds than those from exocyclic bonds, as in the first case all energy remains in the same compound (Donahue et al., 2011a, Vereecken and Francisco, 2012). Due to lack of direct determinations of SCI-stabilisation for many representative compounds, it is still difficult to build a reliable SAR (Laval-Szopa, 2003). In the GECKO-A model, the stabilization has been estimated based on OH-yield measurements, and assumptions on how the SCI-fraction could be related to the OH yield. However, the resulting relation still seems quite inconsistent, with an increase of stabilisation for linear compounds up to 5 carbons, and a sudden drop to almost zero for 6 carbons and above (See Fig. 2.21 in Laval-Szopa, 2003). Therefore, for BOREAM we derived simple relationships for the stabilisation fraction. For endocyclic double bonds, Donahue et al. (2011a) estimates about 0% stabilization for cyclohexene and 15% for α-pinene (based on experimental results), and Nguyen et al. (2009b) found about 75% stabilisation in the case of β-caryophyllene, based on theoretical calculations. These results lead to the simple formula

$$f_{\mathrm{SCI,endo.}} = \begin{cases} 0.12\,\mathrm{nC} - 1.05 & \text{, for nC } \geq 9 \\ 0 & \text{, for nC } < 9 \end{cases} \tag{2.2}$$

with nC the number of carbons in the CI. For exocyclic bonds, we consider the stabilisation of about 37% for the β-pinene 9 carbon CIs (Nguyen et al., 2009a) together with an estimate of about 25% for a 2-carbon CI (based on Laval-Szopa (2003), Table 2.16) in order to obtain the relation

$$f_{\mathrm{SCI,exo.}} = \frac{0.12}{7}\mathrm{nC} + 0.2\,. \tag{2.3}$$

An exception to this trend is the CI from ethene, for which a stabilisation between 30 and 47% has been observed near atmospheric conditions (Atkinson, 1994). The admittedly crude estimates of Eqs. 2.2 and 2.3 should be considered as temporary solutions, awaiting more reliable SARs. They do exhibit at least qualitatively the observed dependence on CI size and the influence of the exo/endocyclicity of the double bond.

The branching between the hydroperoxide channel and the ester channel is assumed identical to that for α-pinene in BOREAM, where the fractions are 74% towards the hydroperoxide channel, and 6% towards the ester channel. Independent of the stabilisation fraction, we will keep the ratio of 74:6 between these channels. We also assume that the ester channel leads to a carboxylic acid. For the hydroperoxide channel, we assume that the position of the radical function will be preferentially on the least-branched carbon if there are two possible branches. In case there is no H available on the adjacent C, then

the branching towards the hydroperoxide channel will be zero. For cases not discussed above (such as an unsaturated carbon or a ketone in α to the Criegee group) we apply the solutions of Laval-Szopa (2003), Fig. 2.21.

2.1.2.4 Reactions of Stabilised Criegee Intermediates (SCI)

The thermally stabilised CI can either undergo unimolecular decompositions, or react with various inorganic compounds, such as water vapour, CO, SO_2, NO_x, HO_x or organic compounds, such as carbonyl compounds or carboxylic acids (Vereecken and Francisco, 2012, Donahue et al., 2012). The bimolecular reaction which is often of most importance in the atmosphere is that with water. Theoretical calculations of Ryzhkov and Ariya (2004) indicate that the reaction with water dimers is considerably faster than that with water monomers, implying a RH dependence, as the fraction of water vapour molecules in the dimer state increases with RH. In the current BOREAM version, the rates of Ryzhkov and Ariya (2004) are used, although more recent calculations by Anglada et al. (2011) found rates of SCI with the water monomer which were 2 orders of magnitude higher than those of Ryzhkov and Ariya (2004), due to a different level of theory (Vereecken and Francisco, 2012). The rates are also found to depend strongly on the level of substitution around the carbon containing the Criegee functionality, and on whether the configuration of the substituents is syn or anti (Ryzhkov and Ariya, 2004, Vereecken and Francisco, 2012). Ryzhkov and Ariya (2004) conducted a theoretical investigation for the reactions of SCIs Me_2COO and MeCHOO (Me stands for the methyl group) with water vapour. For MeCHOO, a large difference was estimated between the rates for the syn- and anti-conformers, the latter reacting the fastest by far ($k_{H_2O} = 1.1 \times 10^{-15}$ cm^3 molecules^{-1} s^{-1} for the monomer and $k_{H_2O} = 5.8 \times 10^{-12}$ cm^3 molecules^{-1} s^{-1} for the dimer). As this SCI features an α-H-atom in syn, exactly as the anti-SCI2 for α-pinene, we adopt these rates. The fraction of water molecules present in the dimer state is estimated based on Chylek and Geldart (1997).

2.1.3 Reactions of organic molecules with NO_3

The reaction with NO_3 is often the dominant oxidant for compounds during night time. During daytime, NO_3 concentrations are strongly depressed due to strong photolysis, although there are situations where it still contributes significantly to daytime photochemistry, mainly near the evening (Geyer et al., 2003).

NO_3 reacts through addition on double bonds or through H-abstraction (Vereecken and Francisco, 2012). H-abstraction is generally negligible, except for aldehydic groups (Kerdouci et al., 2010). For example, for 2,2,4-trimethylpentane and for ethanol, the

measured rate constants k_{NO_3} are 7.50×10^{-17} and 1.8×10^{-15} cm^3 molecules^{-1} s^{-1} (Kerdouci et al., 2010), resulting in e-folding lifetimes of, respectively, 600 days and 25 days, for typical night-time NO_3 concentrations of the order of 20 ppt (Geyer et al., 2003, Geyer, 2000). For aldehydes, recommended values for k_{NO_3} are between 5.6×10^{-16} cm^3 molecules^{-1} s^{-1} for formaldehyde and 2.0×10^{-14} cm^3 molecules^{-1} s^{-1} for pinonaldehyde (Atkinson et al., 2006), leading to e-folding lifetimes of around 82 days and 55 hours. For molecules containing a double bond, reactions are generally faster. For example, for β-pinene the rate is $k_{NO_3} = 2.51 \times 10^{-12}$ cm^3 molecules^{-1} s^{-1} (Atkinson, 1994), resulting in a typical night-time lifetime of about 15 minutes.

In BOREAM only the reactions of NO_3 with aldehydes and alkenes are considered. For small organic compounds, reactions from the MCMv3.2 model (Saunders et al., 2003) are taken. For larger organic compounds, the SAR-method of Kerdouci et al. (2010) is used, which considers all reactions of NO_3, except those with aldehydes. For aldehydes, the approach of Laval-Szopa (2003) is followed, which consists in applying the recommended rate for butanal, $1.7 \times 10^{-12} \exp(-1500/T)$ cm^3 molecules^{-1} s^{-1} (Atkinson, 2007b), for simple aldehydes, $1.4 \times 10^{-12} \exp(-1860/T) \times 0.89$ cm^3 molecules^{-1} s^{-1} for α-keto-aldehydes, and 2.5×10^{-15} cm^3 molecules^{-1} s^{-1} for unsaturated aldehydes (of type -C=C-C=O). In the method of Kerdouci et al. (2010), the impact of a number of possible structures and substitutions is included in the SAR, and it is found that in general the more substituted double bonds are favoured. For the branching between the two carbons of the double bond (which is not given by Kerdouci et al., 2010), following again Laval-Szopa (2003) we adopt the rules proposed by Carter (2000), that in case of an equal number of H-atoms bonded to the carbons, both have the same branching fraction, and that in case of a different number of H-atoms, the least substituted carbon is favoured for addition of NO_3. However, a theoretical study of limonene + NO_3 (Jiang et al., 2009) found a completely opposite trend in the case of the addition on the exocyclic double bond of limonene, where the only possible addition site was the most substituted carbon. Further data are needed to resolve this discrepancy.

2.1.4 Photolysis of organic molecules

Photolysis can be one of the main loss mechanisms for many volatile organic compounds in the atmosphere containing one or more photolabile oxygenated functional groups. In general, photolysis reaction rate coefficients j for a species are calculated using

$$j = \int_{\lambda_1}^{\lambda_2} \sigma(\lambda)\phi(\lambda)I(\lambda)d\lambda \tag{2.4}$$

where $\sigma(\lambda)$ is the absorption cross-section (usually given in units of cm^2), $\phi(\lambda)$ is the quantum yield, which is a coefficient which represents the probability of photolysis upon absorption of a photon, and $I(\lambda)$ is the wavelength-dependent intensity of radiation, expressed in photons cm^{-2} s^{-1} (Section 4.5 of Seinfeld and Pandis, 2006). The units of j are then given in s^{-1}.

Measurements of absorption cross sections or quantum yields are only available for a minority of species, and usually only for relatively small organic species. For larger semi-volatile species we have to make use of SARs based on similarities with species for which data are available. In this work, most of the assumed photolysis rates and product distributions are based on Capouet et al. (2004). We will indicate some important updates and additions, such as for multi-functional carbonyl-containing compounds, for which the impact will be investigated.

For the solar spectrum, the radiation is calculated using the Tropospheric Ultraviolet and Visible Radiation program (TUV) (Madronich, 1993). Photolysis rates are calculated for varying solar zenith angles. For smog chamber experiments various lamps are used. For these lamps, j-values are calculated based on available lamp spectra. For most spectra, relative intensity is given as a function of wavelength. In order to obtain the correct absolute j-values for experiments, we have to make use of a scaling factor, which is calibrated based on one known measured j-value, often that for NO_2.

In general, absorption cross sections are better known than quantum yields. It is often necessary to make extrapolations for the quantum yields based on data at only a few wavelengths, or for different (but structurally related) species. This is also the case for organic species which can undergo multiple reaction channels, for which the individual quantum yields are often unknown, and for which only rough estimates are possible. Below an overview is given of the implemented photolysis reactions.

Tables 2.2 and 2.3 give j-values for small organic and inorganic species used in the model (here for a solar zenith angle of 20°), based on available data for these species. Table 2.4 describes the reactions and j-values for different categories of organic compounds in the model for which no direct determinations of photolytic parameters are available. These tables are updates of the Tables 2.6 and 2.7 given in Capouet (2005).

TABLE 2.2: Photolytic reactions and rates for organic species, based on experimental or theoretical data. We indicate the abbreviation used for the photolysis reaction rate j, and the calculated value for solar irradiation at the surface for a solar zenith angle of 20°, plus the references for absorption cross-sections and quantum yields.

Reaction	Rate notation	$j(s^{-1})$ solar 20°	Note
$CH_2O + h\nu \rightarrow HC^{\bullet}O + H$	$j_{CH_2O,HCO}$	3.7×10^{-5}	a,b
$CH_2O + h\nu \rightarrow CO + H_2$	j_{CH_2O,H_2}	6.3×10^{-5}	a,b
$CH_3CHO + h\nu \rightarrow C^{\bullet}H_3 + HC^{\bullet}O$	j_{d021A}	5.6×10^{-6}	a,b,c
$CH_3CHO + h\nu \rightarrow CH_4 + CO$	j_{d021B}	2.6×10^{-12}	a,b,c
$CH_3CH_2CHO + h\nu \rightarrow CH_3C^{\bullet}H + HC^{\bullet}O$	j_{d031A}	8.8×10^{-6}	a,b,e
$CH_3CH_2CH_2CHO + h\nu \rightarrow CH_3CH_2C^{\bullet}H_2 + HC^{\bullet}O$	j_{d041A}	6.3×10^{-6}	h
$CH_3CH_2CH_2CHO + h\nu \rightarrow CH_2CH_2 + CH_3CHO$	j_{d041B}	1.31×10^{-5}	h
$CH_3CH(CH_3)CHO + h\nu \rightarrow CH_3C^{\bullet}HCH_3 + HC^{\bullet}O$	j_{d042A}	6.9×10^{-5}	f,g
$CH_3CH(CH_3)CHO + h\nu \rightarrow CH_3CH_2CH_3 + CO$	j_{d042B}	8.4×10^{-9}	f,g
$CH_3CH_2CH_2CH_2CHO + h\nu \rightarrow CH_3CH_2CH_2C^{\bullet}H_2 + HC^{\bullet}O$	j_{d051A}	4.3×10^{-6}	h
$CH_3CH_2CH_2CH_2CHO + h\nu \rightarrow CH_3C(H)=CH_2 + CH_3CHO$	j_{d051B}	1.71×10^{-5}	h
$CH_3COCH_3 + h\nu \rightarrow CH_3C^{\bullet}O + C^{\bullet}H_3$	j_{k031}	6.2×10^{-7}	a,e
$CH_3CH_2COCH_3 + h\nu \rightarrow CH_3CH_2C^{\bullet}O + C^{\bullet}H_3$	j_{k041}	3.1×10^{-6}	f,i
$CH_3CH_2CH_2COCH_3 + h\nu \rightarrow CH_3CH_2CH_2C^{\bullet}O + C^{\bullet}H_3$	j_{k051}	4.0×10^{-6}	j
$CH_3CH_2CH_2CH_2COCH_3 + h\nu \rightarrow CH_3CH_2CH_2CH_2C^{\bullet}O + C^{\bullet}H_3$	j_{k061}	3.5×10^{-6}	j,l
CMK + $h\nu \rightarrow$ Cyclobutyl peroxyl + $CH_3C^{\bullet}O$	j_{CMK}	7.7×10^{-6}	k
$CH_3(ONO_2) + h\nu \rightarrow CH_3O^{\bullet} + NO_2$	j_{n011}	1.01×10^{-6}	d,l
$CH_3CH_2CH_2(ONO_2) + h\nu \rightarrow CH_3CH_2CH_2O^{\bullet} + NO_2$	j_{n031}	2.1×10^{-6}	f,l
$CH_3CH(ONO_2)CH_3 + h\nu \rightarrow CH_3CH(O^{\bullet})CH_3 + NO_2$	j_{n032}	3.2×10^{-6}	f,l
$CH_3C(ONO_2)(CH_3)CH_3 + h\nu \rightarrow CH_3C(O^{\bullet})(CH_3)CH_3 + NO_2$	j_{n043}	7.5×10^{-6}	f,l
$CH_3CO(OONO_2) + h\nu \rightarrow CH_3CH_2C(O)O_2 + NO_2$	j_{p021}	8.1×10^{-7}	d,l
$CH_3CH_2CO(OONO_2) + h\nu \rightarrow CH_3CH_2C(O)O_2 + NO_2$	j_{p031}	1.5×10^{-6}	a,l
$CH_3CO(OOH) + h\nu \rightarrow CH_3CO(O^{\bullet}) + OH$	j_{g021}	8.8×10^{-7}	a,l

Continued on Next Page...

Table 2.2 – Continued

Reaction	Rate notation	$j(s^{-1})$ solar 20°	Note
$CH_3OOH + h\nu \rightarrow CH_3O^\bullet + OH$	j_{h011}	6.1×10^{-6}	a,m,l
$CH_2{=}CHCHO + h\nu \rightarrow 0.5\ CH_2{=}CH^\bullet + 0.5\ HC^\bullet O + 0.5\ CH_2{=}CHCH_3 + 0.5\ CO$	j_{ud34}	2.8×10^{-6}	a,n
$CH_2{=}C(CH_3)CHO + h\nu \rightarrow 0.5\ CH_2{=}C(^\bullet)CH_3 + 0.5\ HC^\bullet O + 0.5\ CH_2{=}CHCH_3 + 0.5\ CO$	j_{ud42T}	2.2×10^{-6}	a,o
$CH_2{=}CHC(O)CH_3 + h\nu \rightarrow 0.2\ CH_2{=}CHC^\bullet O + 0.2\ C^\bullet H_3 + 0.6\ CH_3CH{=}CH_2 + 0.6\ CO + 0.2\ CH_3C(O)O_2 + CH_2O + CO$	j_{uk41}	5.2×10^{-6}	a,e
$CH_2(OH)CHO \rightarrow C^\bullet H_2(OH) + HC^\bullet O$	j_{do23A}	1.00×10^{-5}	d,e
$CH_2(OH)CHO \rightarrow CH_3OH + CO$	j_{do23B}	8.5×10^{-7}	d,e
$CHOCHO + h\nu \rightarrow 2\ CO + H_2$	j_{dd21A}	8.1×10^{-5}	a,e
$CHOCHO + h\nu \rightarrow CH_2O + CO$	j_{dd21B}	1.74×10^{-5}	a,e
$CHOCHO + h\nu \rightarrow 2\ HC^\bullet O$	j_{dd21C}	3.4×10^{-5}	a,e
$CHOCHO + h\nu$: sum of all channels	j_{dd21T}	1.32×10^{-4}	
$CH_3COCHO + h\nu \rightarrow CH_3C^\bullet O + HC^\bullet O$	j_{dk33}	2.1×10^{-4}	a,b
Pinonaldehyde $+ h\nu \rightarrow FCH_2 + HC^\bullet O$	$j_{Pinonald.A.}$	7.0×10^{-6}	p,q,s
Pinonaldehyde $+ h\nu \rightarrow$ molecular path	$j_{Pinonald.B.}$	1.90×10^{-5}	p,r
Pinonaldehyde $+ h\nu \rightarrow$ R33 $+ CH_3C^\bullet O$	$j_{Pinonald.C.}$	1.16×10^{-5}	p,r,s
Pinonaldehyde $+ h\nu \rightarrow$ products	$j_{Pinonald.T.}$	3.8×10^{-5}	p,q
$CH_3COCOCH_3 + h\nu \rightarrow 2\ CH_3C^\bullet O$	j_{kk43A}	3.0×10^{-4}	t
$CH_2(ONO_2)CHO + hv \rightarrow CH_2(O^\bullet)CHO + NO_2$	j_{nd21}	1.43×10^{-4}	u
$CH_2(OH)C(CH_3)(ONO_2)CHO + h\nu \rightarrow CH_2(OH)C(CH_3)(O^\bullet)CHO + NO_2$	j_{nd47}	3.3×10^{-4}	x
$CH_2(OH)C(CH_3)(ONO_2)CH(OH)CHO + hv \rightarrow CH_2(OH)C(CH_3)(O^\bullet)CH(OH)CHO + NO_2$	j_{nd5D}	6.5×10^{-5}	y,l
$CH_3COCH_2(ONO_2) + hv \rightarrow CH_3COCH_2(O^\bullet) + NO_2$	j_{nk38}	3.3×10^{-5}	v
$CH_3COCH(ONO_2)CH_3 + hv \rightarrow CH_3COCH(^\bullet)CH_3 + NO_2$	j_{nk45}	4.0×10^{-5}	w
$CH_3COCH(OH)CH_2(ONO_2) + hv \rightarrow CH_3COCH(OH)CH_2(O^\bullet) + NO_2$	j_{nk4A}	1.47×10^{-5}	z,l
$CH_3C(O)CH_2CH(OOH)CH_2CH_3 + hv \rightarrow CH_3C(O)CH_2CH(O^\bullet)CH_2CH_3 + OH$	j_{hk61}	4.2×10^{-4}	α,β

Continued on Next Page...

Table 2.2 – Continued

Reaction	Rate notation	$j(s^{-1})$ solar 20°	Note
$CH_3C(O)CH_2CH_2CH(OOH)CH_3$ + hν→ $CH_3C(O)CH_2CH_2CH(O^{\bullet})CH_3$ + OH	j_{hk62}	1.23×10^{-4}	γ,β
$CH_3COCO(OH)$ + $h\nu$→ CH_3CO + CO_2	j_{ak33}	3.9×10^{-4}	δ

[a]Cross section of Sander et al. (2006)

[b]Quantum yield of Sander et al. (2006)

[c] With pressure-dependence parameters from Horowitz and Calvert (1982).

[d]Cross section of Sander et al. (2011).

[e]Quantum yield of Sander et al. (2011).

[f] Cross section of IUPAC (2014). [g] Quantum yield of IUPAC (2014).

[h] Cross section and quantum yield of Tadic et al. (2001b).[i]Quantum yield of Romero et al. (2005)
[j] Cross section from Martinez et al. (1992). The quantum yield for $CH_3CH_2COCH_3$ is applied.

[k] Cyclobutyl methyl ketone. Cross section from Baldwin et al. (1987), quantum yield for $CH_3CH_2COCH_3$ is applied.[l] Quantum yield is taken to be unity.[m] Cross section of Matthews et al. (2005) for 365–404 nm. [n] Quantum yield of Gardner et al. (1987). [o] Quantum yield taken to be 0.004, based on Pinho et al. (2005).

[p] Cross section of Hallquist et al. (1997) [q] Quantum yield of Pinho et al. (2005) for MEK [r] Quantum yield of Tadic et al. (2001a) for hexanal [s] Notation of radical based on Peeters et al. (2001)

[t] Cross section from Horowitz et al. (2001), quantum-yield from Plum et al. (1983)

[u] Cross section calculated as the sum of those of CH_3CHO and ethyl nitrate, multiplied by the enhancement factor for the interaction of nitrate and carbonyl groups for $CH_3COCH_2(ONO_2)$, i.e. by the ratio of the cross sections for $CH_3COCH_2(ONO_2)$ and (acetone+propyl nitrate). Quantum yield = 1.

[v] Cross section from Barnes et al. (1993), quantum-yield is 0.9, to match j-values of Suarez-Bertoa et al. (2012), see Müller et al. (2014) [w] Cross section from Barnes et al. (1993), quantum yield is 0.75 to match j-values of Suarez-Bertoa et al. (2012)

[x] Cross section calculated as the sum of those of $CH_3CH(CH_3)CHO$) and tert-butyl nitrate, multiplied by the enhancement factor for the interaction of nitrate and carbonyl groups for nk45, i.e. by the ratio of the cross sections for nk45 and (MEK+n032). Quantum yield taken to be unity.

[y] Cross sections taken to be the sum of those of $CH_3C(ONO_2)(CH_3)CH_3$ and $CH_3CH_2CH_2CHO$.
[z] Cross sections taken to be the sum of those of $CH_3CH_2CH_2CH_2(ONO_2)$ and $CH_3CH_2CH_2CHO$.

[α] Based on cross-sections for a 2-hexanone-4-hydroperoxide/3-hexanone-5-hydroperoxide mixture in acetonitrile (Jorand et al., 2000).

[β] We assume that cross-sections in acetonitrile are ca. 3 times lower than in the gas phase in the relevant wavelength range (300–325 nm), based on a comparison for acetone (Jorand et al., 2000).
[γ] Based on cross-sections for $CH_3C(O)CH_2CH_2CH(OOH)CH_3$ in acetonitrile (Jorand et al., 2000).
[δ] Cross sections from Mellouki and Mu (2003), quantum yield of Winterhalter et al. (2001).

TABLE 2.3: Implemented photolytic reactions and photolysis rates for inorganic species, based on experimental or theoretical data. We indicate the abbreviation used for the photolysis reaction rate j, and the calculated value for solar irradiation at the surface for a solar zenith angle of 20°, plus the references for absorption cross-sections and quantum yields.

Reaction	Reaction rate notation	$j(s^{-1})$ solar 20°	Note
$O_3 + h\nu \rightarrow O(^1D) + O_2$	$j_{O_3,O(^1D)}$	3.3×10^{-5}	a,b
$O_3 + h\nu \rightarrow O + O_2$	$j_{O_3,O}$	4.5×10^{-4}	a,b
$NO_2 + h\nu \rightarrow NO + O$	j_{NO_2}	9.6×10^{-3}	a,b
$HONO + h\nu \rightarrow OH + NO$	j_{H,NO_2}	1.57×10^{-3}	c,e
$NO_3 + h\nu \rightarrow NO_2 + O$	$j_{NO_3,O}$	1.98×10^{-1}	a,b
$NO_3 + h\nu \rightarrow NO + O_2$	j_{NO_3,O_2}	2.5×10^{-2}	a,b
$N_2O_5 + h\nu \rightarrow NO_3 + NO_2$	$j_{N_2O_5,NO_2}$	2.4×10^{-9}	c,d
$N_2O_5 + h\nu \rightarrow NO_3 + NO + O$	$j_{N_2O_5,NO}$	3.8×10^{-5}	c,d
$H_2O_2 + h\nu \rightarrow OH + OH$	$j_{H_2O_2}$	7.0×10^{-6}	c,d
$HNO_3 + h\nu \rightarrow OH + NO_2$	j_{HNO_3}	6.5×10^{-7}	f,e
$HNO_4 + h\nu \rightarrow HO_2 + NO_2$	j_{HNO_4,NO_2}	1.04×10^{-5}	a,g
$HNO_4 + h\nu \rightarrow OH + NO_3$	j_{HNO_4,NO_3}	7.2×10^{-6}	a,h

[a] Cross section based on Sander et al. (2006) [b] Quantum yield based on Sander et al. (2006).

[c] Cross section of IUPAC (2014). [d] Quantum yield of IUPAC (2014).

[e] Quantum yield is taken to be unity.

[f] Cross section based on Burkholder et al. (1993).

[g] Quantum yield of this channel is set to 0.59 (from the value at 248 nm, Sander et al., 2006).

[h] Quantum yield of this channel is set to 0.41 (from the value at 248 nm, Sander et al., 2006).

2.1.4.1 Photolysis of monofunctional hydroperoxides, peroxy acids, nitrates and peroxy nitrates

In Table 2.4 the species used to represent photolysis of mono-functional hydroperoxides, peroxy acids, nitrates and peroxy acids in BOREAM are shown. As can be seen, the reference species are relatively small, monofunctional compounds. These rates are also applied to multi-functional compounds containing these groups, as long as interactions between functional groups are not estimated to alter the photolysis parameters when strong interaction effects are believed to occur, such as in the case of a functional group interacting with a carbonyl chromophore (in which case we will apply the SARs described further below, see Sect. 2.1.4.3).

TABLE 2.4: Photolysis rates applied for organic functional groups in BOREAM.

Functional group	Reference compound notation	j used	$j(s^{-1})$ solar 20°
Hydroperoxides	CH_3OOH	j_{h011}	6.1×10^{-6}
Peroxy acids	$CH_3CO(OOH)$	j_{g021}	8.8×10^{-7}
Nitrates	$CH_3CH(ONO_2)CH_3$	j_{n032}	3.2×10^{-6}
Peroxyacyl nitrates	$CH_3CH_2CO(OONO_2)$	j_{p031}	1.55×10^{-6}
Aldehydes	$CH_3CH_2CH_2CH_2CHO$	j_{d051T}	2.1×10^{-5}
(non-multifunctional)	Norrish-type I	j_{d051A}	4.3×10^{-6}
	Norrish-type II[a]	j_{d051B}	1.71×10^{-5}
Ketones (linear,monofunctional)	CH_2=$CHC(O)CH_3$	j_{uk41}	5.2×10^{-6}
Ketones, CMK-like[e]	CMK	j_{CMK}	7.6×10^{-6}
Ketones, cyclic	$CH_3CH_2COCH_3$	j_{k041}	3.1×10^{-6}
Conjugated unsaturated ketones	CH_2=$CHC(O)CH_3$	j_{uk41}	5.2×10^{-6}
Conjugated unsaturated aldehydes	CH_2=$C(CH_3)CH(O)$	j_{ud42T}	5.2×10^{-6}
Aldehyde-ketones (conjugated)	CH_3COCHO	j_{dk33}	2.1×10^{-4}
Di-ketones (conj.)	$CH_3COCOCH_3$	j_{kk43A}	3.0×10^{-4}
Aldehyde-ketones (non-conj.)	Pinonaldehyde	$j_{Pinonald.T.}$	3.8×10^{-5}
Aldehyde-alcohols (conj.)	$CH_2(OH)CHO$	j_{do23A}	1.00×10^{-5}
Keto-carboxylic acid (conj.)[b]	$CH_3COCO(OH)$	j_{ak33}	3.9×10^{-4}
Carbonyl-hydroperoxide (α or β)[c]	2-hexanone-4-hydroperoxide	j_{hk61}	4.2×10^{-4}
Carbonyl-hydroperoxide (γ or δ)[c]	2-hexanone-5-hydroperoxide	j_{hk62}	1.23×10^{-4}
α-carbonyl-nitrates[d]	(1-methyl-2-oxo-propyl)nitrate	j_{nk45}	4.0×10^{-5}
β-carbonyl-nitrates[d]	(2-hydroxy-3-oxo-butyl)nitrate	j_{nk4A}	1.47×10^{-5}

[a] The Norrish-type II pathway is only written if a δ-H is available, and β- and γ-carbons are not cyclic.
[b] Also applied for conjugated keto-peracids.
[c] The current assumption is that interconnecting bonds should not be cyclic. The enhanced photolysis is also applied for similar carbonyl/peroxy acid combinations.
[d] The current assumption is that interconnecting bonds should not be cyclic. The enhanced photolysis is also applied for similar carbonyl/peroxy acyl nitrate combinations.
[e] cyclobutyl methyl ketone

2.1.4.2 Photolysis of carbonyl compounds

For aldehyde groups, in absence of interaction with other groups in the molecule, the photolysis rates calculated for pentanal are used, based on the absorption cross section and quantum yields measured by Tadic et al. (2001b). Two reaction channels are open. In the so-called Norrish-type I photolysis, two radicals are produced following cleavage of the α-β-bond. In Norrish-type II photolysis, an H-atom is abstracted by the photolytically activated aldehydic oxygen atom, from the carbon in δ-position. This leads to a recombination in which the β-γ-bond breaks, a double bond is formed between the γ- and δ-atom, and the abstracted H-atom shifts back to the β-carbon, leading to acetaldehyde (Tadic et al., 2011). A second possible channel for Norrish-type II photolysis is cyclisation between the α- and δ-carbon. Tadic et al. (2001b) found that Norrish-type I and Norrish-type II accounted for about 20% and 80% of the reactions, respectively.

There is a considerable variation in calculated j-values for the individual ketones (Table 2.2). j-values increase with size for linear ketones (2-propanone, 2-butanone, 2-pentanone and 2-hexanone), while the j-value of the 6-carbon cyclic compound cyclobutyl methyl ketone (CMK) is still considerably higher than that of 2-hexanone. In α-pinene photooxidation, many important products have more than 6 carbons, and many of these compounds are multi-functional or contain one or more rings. It can be expected that the photolysis rate of these species will be higher than these of 3–6 carbon linear ketones. In the model, the j-value of methyl vinyl ketone (MVK), which lies between the rate of linear ketones and that of CMK for atmospheric radiation, is adopted as the generic photolysis rate for ketones.

Experiments on the largest ketones show evidence for a contribution from both the Norrish-I and Norrish-II processes (Ausloos, 1961, McMillan et al., 1964), although exact quantum yields were not determined for the reaction branching. Laval-Szopa (2003) assumed a 30:70 ratio between these processes based on some experimental evidence (see their Table 2.13, note 8). In BOREAM, a similar ratio has been assumed (20:80) whenever Norrish-type II decomposition is possible. For the Norrish-type I process, it has been assumed that the bond attaching the largest carbon chain to the ketone-bearing carbon is broken, based on the product distribution of butanone. In the MCMv3.2 model (Saunders et al., 2003), the Norrish-type II reactions have not been considered.

For molecules containing the structure of cyclobutyl methyl ketone, we use the values obtained for this compound. In this case the bond between the cyclobutyl ring and the ketone is broken preferentially, resulting in two radicals (Baldwin et al., 1987).

For cyclic ketones, there is still a lack of consistent data on absorption cross sections, quantum yields and product distributions (Calvert et al., 2011). Awaiting further, more

relevant data, the photolysis rate of the linear 2-butanone has been adopted. The product distribution is different from that of the linear ketones. For cyclohexanone, three product distributions have been observed, namely 5-hexenal (I), cyclopentane + CO (II), or pentene + CO (III) (Calvert et al., 2011). Scala and Ballan (1972) state that reactions I and II have quantum yields of approximately 0.2 and 0.8, respectively. However, other data presented by (Calvert et al. (2011) in Fig. IX-E-12 show pentene as an important product. For other cyclic ketones in general no clear conclusion emerges regarding the product distribution. We have assumed that the cycloalkane + CO pathway is dominant (90% yield) and that the formation of an unsaturated aldehyde has a 10% yield.

When more than one carbonyl function is present in the same molecule, significant enhancement effects occur, justifying separate SARs. In the case of conjugated carbonyl functions, we apply the photolysis rates of methylglyoxal (for aldehyde-ketones) or diacetyl (for α-diketones). For cyclic diketones, the photolysis rate of diacetyl is used, although recent measurements of the absorption cross section of α-cyclohexanedione by Mukhopadhyay et al. (2011) indicate that its photolysis rate could be even higher. Based on this study, the CO elimination pathway (leading to pentanone for α-cyclohexanedione) is assumed to be the main pathway.

In the case of non-conjugated keto-aldehydes, we have considered the enhancement effects of the ketone-aldehyde combination, which have been observed for pinonaldehyde. For those compounds, distinct photolysis rates are used for the radical decomposition of the ketone and of the aldehyde group, and for the molecular decomposition. It should be noted that the molecular photolytic decomposition products currently implemented in BOREAM still await direct experimental confirmation. For the molecular decomposition channel of other non-conjugated keto-aldehydes, if possible a Norrish-type II decomposition is applied, occurring in two thirds of the cases on the aldehyde group and in one third of the cases on the ketone group. More experimental data are required to allow a refinement of these assumptions for the fate of keto-aldehydes.

2.1.4.3 Photolysis of carbonyl nitrates and carbonyl hydroperoxides

Individual carbonyl compounds tend to have relatively low quantum yields for near-atmospheric radiation. For radiation above 320 nm, for example, it falls below 0.1 for formaldehyde or acetaldehyde (Atkinson et al., 2006), while for methyl ethyl ketone a value of around 0.34 has been found (Atkinson et al., 2006). Mono-functional nitrates have a quantum yield near unity, but their absorption cross sections for near-atmospheric radiation are comparatively low (Atkinson et al., 2006), leading to relatively low j-values (see Table 2.4). When the ketone and nitrate groups are adjacent, the cross sections

are known to be much larger than the cross sections of either monofunctional nitrates or monofunctional ketones (Barnes et al., 1993). Quantum yield data were not directly available from Barnes et al. (1993), but it is assumed in BOREAM that α-ketone nitrates, like alkyl nitrates, have a quantum yield near unity, and that the main photolysis channel is breaking of the O-NO_2 bond. As discussed in Müller et al. (2014), the photolysis rates measured by Suarez-Bertoa et al. (2012), combined with absorption cross sections obtained from Barnes et al. (1993), imply that quantum yields are near unity. Müller et al. (2014) applied this result to α- and β-ketone and aldehyde compounds, and showed that using the faster photolysis rates for these compounds improved agreement with measurements during isoprene NO_x photooxidation experiments of Paulot et al. (2009).

A near-unity quantum yield has been observed before for a multi-functional compound, such as, first theoretically and later on experimentally, for the major HPALD (hydroperoxide aldehyde) products proposed by Peeters et al. (2009) in the isoprene OH mechanism. Like other conjugated carbonyls (e.g. MACR, methacrolein), the HPALDs have a considerably larger cross section compared to the corresponding monofunctional aldehyde species (Peeters and Müller, 2010). For this compound, the main channel was proposed to be dissociation of the O-OH bond. It seems plausible that a similar process can lead to near-unity quantum yields for multi-functional carbonyls containing either a hydroperoxide or a nitrate group.

Jorand et al. (2000) found experimentally that 2,5-, 2,4- and 3,5-hexylketohydroperoxides have strongly enhanced absorption cross sections in acetonitrile solution, compared to monofunctional ketones and hydroperoxides, especially in the near-visible UV-spectrum, which is most relevant for tropospheric photolysis. A near-quantum yield is supposed, and calculated photolysis rates are given in Table 2.2.

In BOREAM, we have now introduced the increased photolysis rates discussed above in the cases of combinations of a carbonyl group with a nitrate group (both alkyl nitrates and acyl peroxy nitrates, although for the latter group this is purely based on analogy, as no direct measurements exist yet) or a hydroperoxide or peroxy acid group. As the precise mechanisms of the absorption cross section and quantum yield enhancement effect in multi-functional compounds is currently not yet fully understood, and the results of Jorand et al. (2000) suggest that the effects decrease with the intramolecular distance of the groups, we have only applied this rate enhancement if the groups are deemed sufficiently close in the molecule (see Table 2.4).

For compounds in which the groups are more distant, the effect has not been considered. Furthermore, the effect has not been considered in case any of the bonds in between the groups is cyclic, as ring strain effects might affect the cross section or quantum yield enhancement, in ways which are currently difficult to estimate. Therefore, the current

implementation is conservative, awaiting further experimental results. If this effect were also valid for cyclic structures, then a considerable number of additional species might see their photolysis rate strongly enhanced in the oxidation mechanism of α- and β-pinene. The possible impact will require further investigation. In Chapter 5, the possible impact on SOA ageing of the current implementation is investigated and compared with simulations without the newly calculated enhanced carbonyl-hydroperoxide and carbonyl-nitrate photolysis.

2.1.5 Alkyl radical reactions

For most alkyl radicals, addition of O_2 is the dominant fate at atmospheric O_2 concentrations and pressures (Atkinson, 2007a). These reactions have high rate constants in the troposphere and are implemented as instantaneous in BOREAM. For aliphatic alkyl or acyl alkoxy radicals, the resulting peroxy radicals are thermally stabilised in the majority of cases. For allyl radicals formed after OH-addition on isoprene, the peroxy radicals formed after addition of O_2 are less stable than usual, making decomposition and interconversion between different peroxy radicals possible (Peeters et al., 2009). In some cases, particularly energetic alkyl radicals can undergo unimolecular decompositions, such as ring opening, which was found to be an important pathway for α-pinene and β-pinene oxidation (see Subsections 2.2.1.1 and 2.2.2.1), but it is not yet possible to provide a general SAR for this type of reaction.

For radicals containing other substitutions in α-position, it is found that the excess energy available will lead to prompt decomposition (Vereecken and Francisco, 2012), yielding a carbonyl plus an inorganic radical. This is the case when the α-substituent is a hydroperoxide, alcohol or nitrate group. Similar SARs are also being used in the MCM model (Jenkin, 2004) and in the GECKO-A model (Laval-Szopa (2003), Table 2.1). For a number of special cases we follow Laval-Szopa (2003), such as for the structures R-O-C$^{\bullet}$=O and R(=O)-C$^{\bullet}$=O. For an alkyl radical on a carbon which also bears a peroxide bond, we suppose decomposition of the peroxide oxygen-oxygen bond, as for the alkyl radical resulting from radical ROO6R1O in the β-pinene low-NO_x OH-oxidation mechanism (Vereecken and Peeters, 2012). We summarise the SARs implemented in BOREAM in Table 2.5.

2.1.6 Peroxy radical reactions

Most peroxy radicals in the troposphere originate from the addition of triplet oxygen molecules to alkyl radicals or acyl alkyl radicals, although they can also be formed in other ways, such as H-abstraction from hydroperoxide or peroxy acid groups. The class

TABLE 2.5: Implemented reactions for alkyl radicals. Reactions are supposed to occur instantaneously.

Reaction	Note
$RC^{\bullet} + O_2 \rightarrow RCO_2^{\bullet}$	a
$RC^{\bullet}(=O) + O_2 \rightarrow RC(=O)O_2^{\bullet}$	a
$RC^{\bullet}(ONO_2) + O_2 \rightarrow RC(=O) + NO_2$	b
$RC^{\bullet}(OOH) + O_2 \rightarrow RC(=O) + OH + O_2$	b
$RC^{\bullet}(OH) + O_2 \rightarrow RC(=O) + HO_2$	a
$R\text{-}O\text{-}C^{\bullet}=O + 2\ O_2 \rightarrow R\text{-}(O\text{-}O^{\bullet}) + CO_2 + O_2$	c
$R\text{-}C(=O)\text{-}C^{\bullet}=O \rightarrow R\text{-}C^{\bullet}=O + CO$	c
$R\text{-}O\text{-}O\text{-}C^{\bullet}\text{-}R' \rightarrow R\text{-}O^{\bullet} + O{=}C\text{-}R'$	d

[a] Atkinson (2007a) [b] Vereecken and Francisco (2012)
[c] Laval-Szopa (2003) [d] Vereecken and Peeters (2012)

of peroxy radicals is often represented by the abbreviation "RO2". Although radicals, therefore shorter-lived than molecular species, they are generally longer-lived than alkyl radicals or alkoxy radicals. In the troposphere they mainly react with NO, NO_2, NO_3, HO_2 or other RO_2 (Vereecken and Francisco, 2012). NO_x reactions are often dominant in regions which undergo the influence of human activities, while the reactions with HO_2 or cross-reactions with other peroxy radicals are usually dominant in more remote areas.

The implementation of the SARs for peroxy radicals presented in the following subsections largely follows the approach adopted in Capouet et al. (2004), Capouet (2005) and Capouet et al. (2008).

2.1.6.1 Reactions of peroxy radicals with NO

For the reaction of peroxy radicals with NO, two product channels are considered: one main channel leading to an alkoxy radical (RO) and NO_2, which has the highest branching fraction, and a channel leading to a stable organic nitrate ($RONO_2$).

$$RO_2 + NO \rightarrow RO^{\bullet} + NO_2 \tag{2.5}$$

$$RO_2 + NO \rightarrow RONO_2 \tag{2.6}$$

The overall reaction rate for organic peroxy radicals containing more than two carbon atoms is given by $k_{NO+RO2} = 2.54 \times 10^{-12} \exp(360/T)$ cm^3 molecules^{-1} s^{-1}, following Saunders et al. (2003). For acyl peroxy radicals containing more than two carbon atoms, the rate constant for $C_2H_5C(O)O_2 + NO$ is adopted: $k_{NO+RO3} = 6.7 \times 10^{-12} \exp(340/T)$ cm^3 molecules^{-1} s^{-1} (Atkinson et al., 2006). The nitrate yields of acyl peroxy radicals

and of RO_2 with 2 or less carbons are assumed to be negligible, and for other peroxy radicals the SAR of Arey et al. (2001) is followed, which gives an increasing nitrate yield with increasing carbon number.

2.1.6.2 Reactions of peroxy radicals with NO_2

Based on experimental data (Atkinson et al., 2006), the reaction of peroxy radicals with NO_2 has been deemed unimportant (Jenkin et al., 1997, Capouet et al., 2004), as the resulting peroxy nitrates are strongly unstable at room temperature (Tyndall et al., 2001). For acyl peroxy radicals, the reaction with NO_2 follows the Troe expression, which is used for trimolecular reactions in which molecules within the bath gas take part (Tyndall et al., 2001). However, for atmospheric reactions, Atkinson et al. (2006) recommend the use of the high pressure limit rate, which is $1.1 \times 10^{-11}\,\mathrm{cm^3\,molecules^{-1}\,s^{-1}}$ for $CH_3C(=O)O_2$ (Tyndall et al., 2001).

The resulting peroxy acyl nitrates (PANs) can undergo thermal decomposition back to the acyl peroxy radical and NO_2, for which the recommended rate $k_{\mathrm{PAN}} = 5.4 \times 10^{16} \exp(-13830/T)\ \mathrm{s^{-1}}$ (over the range 300–330 K, Atkinson et al., 2006) is used, also outside the temperature range. The decomposition in a liquid organic phase is currently not considered by most models, including BOREAM, but Roberts (2005) (Table 1) showed that at 298 K, PAN has a decomposition rate of the order of $5 \times 10^{-5}\ \mathrm{s^{-1}}$ in *n*-octanol, about 6 times slower than the gas phase decomposition, resulting in a lifetime of about 5.5 hours. Also, the decomposition in an aqueous phase could be significantly faster (Roberts, 2005).

2.1.6.3 Reactions of peroxy radicals with NO_3

For the reaction

$$\mathrm{RO_2 + NO_3 \rightarrow RO + NO_2 + O_2}, \tag{2.7}$$

rates recommended by the IUPAC gas kinetics database (IUPAC, 2014) are used: for peroxy radicals, this is the rate for $CH_3CH_2O_2 + NO_3$, $2.3 \times 10^{-12}\ \mathrm{cm^3\ molecules^{-1}\ s^{-1}}$, and for acyl peroxy radicals $4.1 \times 10^{-12}\ \mathrm{cm^3\ molecules^{-1}\ s^{-1}}$, for $CH_3C(O)O_2 + NO_3$.

2.1.6.4 Cross-reactions of peroxy radicals

Cross-reactions of peroxy radicals have two main product channels, one leading to two alkoxy radicals and one leading to molecular products containing an -OH and an =O

group, generally written as

$$\mathrm{RO_2 + R'O_2 \rightarrow RO^\bullet + R'O^\bullet + O_2} \tag{2.8}$$

$$\begin{aligned} \mathrm{RO_2 + R'O_2} \quad \rightarrow \quad & a\,\mathrm{ROH} + a\,\mathrm{R'_{-H}{=}O} + \\ & (1-a)\,\mathrm{R_{-H}{=}O} + \\ & (1-a)\,\mathrm{R'OH} + \mathrm{O_2} \end{aligned} \tag{2.9}$$

(Vereecken and Francisco, 2012). The reaction has the tetroxide $\mathrm{RC(H}_m\mathrm{)OOOOC(H}_n\mathrm{)R'}$ as an intermediate, although theoretical investigations are not yet conclusive on the precise mechanism for Reactions 2.8 and 2.9. Experimental data show that self-reaction rates increase from tertiary to primary peroxy radicals, with radical size, and when substitutions, with such groups as β-hydroxy, α-carbonyl or acyl, are present (Orlando and Tyndall, 2012, Capouet et al., 2004). Product branchings also depend on structure, with tertiary peroxy and acyl peroxy radicals not following channel 2.9 in self-reactions (Orlando and Tyndall, 2012). Reactions between acyl peroxy radicals and primary or secondary alkoxy radicals can lead to a branching towards carboxylic acid for the acyl peroxy radical, which is about 10% for $\mathrm{CH_3O_2}$ + $\mathrm{CH_3C(O)O_2}$ (Orlando and Tyndall, 2012).

Implementing the self- and cross-reactions of peroxy radicals presents a mechanistic challenge, as explicit implementation would lead to a quadratic increase of equations with the number of peroxy radicals. A solution consists in grouping peroxy radicals of similar reactivity, and tracking their abundances through counter species. Reactions between explicit peroxy radicals and the peroxy radical class counter species can then mimic the cross-reaction with real peroxy radicals. This method has been pioneered by Madronich and Calvert (1990) and Jenkin et al. (1997). For BOREAM, the implementation was discussed in Capouet et al. (2004). The peroxy radicals are divided according to the presence of substitutions. Those peroxy radicals without any relevant substitutions in α- or β-position are assigned to classes of alkyl peroxy radicals R1R, R2R and R3R, according to whether the peroxy function is primary, secondary or tertiary (based on the number of hydrogen atoms). Peroxy radicals with a β-hydroxy function are assigned to classes R1H, R2H and R3H, and "multi-functional" peroxy radicals (which are taken to include α-carbonyl, α-hydroxy, and other combinations of functional groups in α- or β-position deemed relevant) are classed into R1O, R2O and R3O (which were R1M, R2M and R3M in Capouet et al., 2004). Together with the acyl peroxy radicals (RO3) this gives ten classes, for which self-reaction rates are estimated, based on extrapolations

of the available experimental data (see Table 2.6). As for some classes experimental data are very scarce, the assignment of the self-reaction and cross-reaction rates still has a large degree of uncertainty.

TABLE 2.6: Self-reaction rates of peroxy radical classes. The adopted values are taken over from Capouet et al. (2004), except for those for R3O and RO3, which are different, but still compatible with experimental evidence.

Peroxy class	k_{self} (in cm^3 molecules^{-1} s^{-1})	Peroxy class	k_{self} (in cm^3 molecules^{-1} s^{-1})
R1R	4.0×10^{-12}	R1O	1.5×10^{-11}
R2R	4.0×10^{-13}	R2O	1.0×10^{-11}
R3R	1.0×10^{-16}	R3O	5.0×10^{-14}
R1H	8.0×10^{-12}	RO3	1.7×10^{-11}
R2H	3.0×10^{-12}		
R3H	5.0×10^{-14}		

It can be shown by analysis of the kinetic equations that if two species A and B have practically identical reactivity towards one another and to themselves, that then the rate for the interreaction $k_{\text{A+B}} = 2k_{\text{A,self}} = 2k_{\text{B,self}}$. For RO_2 species, with self-reaction rates which can differ by a large factor (Orlando and Tyndall, 2012), a reasonable assumption is that their interreactivity might be approximated by the geometric average of the self-reactivity. These two observations lead to the assumption by Madronich and Calvert (1990) of $k_{\text{RO}_2,\text{R'O}_2} = 2\sqrt[2]{k_{\text{self,RO}_2} \cdot k_{\text{self,R'O}_2}}$ for the cross-reaction rates between different peroxy radicals, when no experimental data are available. For the reaction between peroxy radicals and acyl peroxy radicals, the rate 1.0×10^{-11} cm^3 molecules^{-1} s^{-1} is adopted, as most measured rates fell within the range 1.0–1.25×10^{-11} cm^3 molecules^{-1} s^{-1} (Capouet et al., 2004).

Table 2.7 (taken from Capouet et al., 2004) shows the branching fractions for the reaction of peroxy radicals with a peroxy radical counter. The branchings are discussed in Capouet et al. (2004). In addition to the class characteristics, also the impact of cyclicity on the branching is taken into account for the explicit peroxy radical.

2.1.6.5 Reactions of peroxy and acyl peroxy radicals with HO_2

For most alkyl peroxy radicals, reaction with HO_2 leads to a hydroperoxide and O_2 (Reaction 2.10), through an intermediate state in which the hydrogen of HO_2 is transferred

TABLE 2.7: Branching fractions for self- and cross-reactions of peroxy radicals. The Table is taken from Table 1 in Capouet et al. (2004).

For primary/secondary peroxy radicals	
+ prim.*/sec. → 0.50 RO + 0.25 R(−H)=O + 0.25 ROH	*a*
+ tert. → 0.7 RO + 0.3 R(−H)=O	*b*
+ acyl → 0.86 RO + 0.14 R(−H)=O	*c*
For tertiary peroxy radicals	
+ prim./sec. → 0.7 RO + 0.3 ROH	*b*
+ tert. → RO	*d*
+ acyl → RO	*d*
For acyl peroxy radicals	
+ prim./sec. → 0.86 RC(O)O + 0.14 RC(O)OH	*c*
+ tert. → RC(O)O	*d*
+ acyl → RC(O)O	*d*
For cyclic peroxy radicals	
+ prim./sec. → 0.3 RO + 0.35 R(−H)=O + 0.35 ROH	*e*
+ tert. → 0.7 RO + 0.3 R(−H)=O	*b*
+ acyl → 0.86 RO + 0.14 R(−H)=O	*c*

∗ Read "+ prim.", etc., as "RO_2 + primary R'O_2"
[a] For cross reactions of primary and secondary RO_2 radicals, Atkinson (1994) suggests a constant ratio of 45 ± 20% for the oxy-forming route at 298 K from the few available data of self-reactions.[b] No experimental data. Values assumed. [c] Based on the measurement of Horie and Moortgat (1992) for the reaction of $CH_3C(O)O_2$ at 298 K. [d] Only one reaction path can occur. [e] Based on the measurement of the self-reaction of c-$C_6H_{11}O_2$ by Rowley et al. (1992).

to the oxygen of the peroxy radical (Vereecken and Francisco, 2012). For some substituted peroxy radicals (such as acyl peroxy radicals) one or two other channels might be available (Reactions 2.11 and 2.12), which occur through an intermediate complex between HO_2 and the (acyl) peroxy group, in which the hydrogen of HO_2 temporarily bonds with the acyl oxygen, and the other oxygens form a tetroxide group. This intermediate leads to either an alkoxy radical, OH and O_2, or a carboxylic acid and O_3 (Vereecken and Francisco, 2012).

$$RO_2 + HO_2 \rightarrow ROOH + O_2 \tag{2.10}$$

$$RO_2 + HO_2 \rightarrow RO^{\bullet} + OH + O_2 \tag{2.11}$$

$$RC(O)O_2 + HO_2 \rightarrow RC(O)OH + O_3 \tag{2.12}$$

For non-acyl peroxy radicals, the total reaction rate parameterised by Jenkin et al. (1997) is used:

$$k_{\mathrm{RO_2,HO_2}} = 3.0 \times 10^{-13} \exp(1250/T) \times [1 - \exp(-0.34\, n)]\ \mathrm{cm^3\ molecules^{-1}\ s^{-1}}, \quad (2.13)$$

where n is the number of carbons.

For acyl peroxy radicals the rate is based on a recommended expression for $CH_3C(O)O_2$ of Atkinson et al. (2006),

$$k_{\mathrm{R(O)O_2,HO_2}} = 5.2 \times 10^{-13} \exp(980/T)\ \mathrm{cm^3\ molecules^{-1}\ s^{-1}}, \quad (2.14)$$

valid over the temperature range 250–400 K.

For acyl peroxy radicals, the branching fractions assigned in BOREAM to Reactions 2.10 (leading to peroxy acids and O_2), 2.11 (leading to an alkoxy radical and OH) and 2.12 (leading to a carboxylic acid and O_3) are 0.41, 0.46, and 0.13, respectively. These values are nearly identical to the recommendations of IUPAC (2014) (0.41 ± 0.2, 0.44 ± 0.2 and 0.15 ± 0.1) for CH3C(O)O_2, based among others on Jenkin et al. (2007) and Hasson et al. (2004), which have been adopted in the MCMv3.2 model update (Jenkin et al., 2012).

For α-carbonyl peroxy radicals, besides Reaction 2.10 also Reaction 2.11 can occur. The branching fractions for α-carbonyl peroxy radicals adopted in BOREAM are 0.85 and 0.15 respectively, based on Dillon and Crowley (2008) for $CH_3C(O)CH_2OO$. Note that the branching fractions for another compound, $CH_3C(O)CH(OO)CH_3$, were found to be quite different (0.42 ± 0.1 for the hydroperoxide channel) by another group (Hasson et al., 2012).

Large uncertainty still exists for the product branching fractions of β-hydroxy peroxy radicals reacting with HO_2. Dillon and Crowley (2008) did not observe OH-formation for $CH_3CH(OH)CH(O_2)CH_3$ + HO_2, with an upper limit of 0.06 for its yield. The α-pinene photooxidation study Eddingsaas et al. (2012b) did however observe tentative evidence for a high yield from Reaction 2.11 for the primary β-hydroxy peroxy radicals formed in the α-pinene + OH mechanism. They observed a high pinonaldehyde yield under low-NO_x and relatively high HO_2 conditions, which in current mechanisms is only possible if the β-hydroxy peroxy radicals can partly form alkoxy radicals + OH. In BOREAM we have set the branching fractions of channels 2.10 and 2.11 to 50:50 for these β-hydroxy peroxy radicals, which was found to give better agreement with the observed distribution of hydroperoxides and pinonaldehyde in Eddingsaas et al. (2012b)

(see Sections 3.3.1 and 5.2.2.2). These branching fractions have also been preliminarily adopted for all β-hydroxy peroxy radicals counting more than 5 carbon atoms.

2.1.6.6 Unimolecular reactions of peroxy radicals

H-shift in peroxy radicals is usually assumed to be too slow to compete against bimolecular reactions, but for certain functionalised radicals, H-shift of hydrogens with a double bond or an alcohol, aldehyde or hydroperoxide group in α-position was found to be competitive through quantum-chemical calculations (Vereecken et al., 2007, Vereecken and Peeters, 2012). Examples can be seen in the α-pinene + OH mechanism (see Sect. 2.2.1.1) and in the β-pinene + OH mechanism (Vereecken and Peeters, 2012). Peeters et al. (2009) and Peeters and Müller (2010) estimated that H-shifts in the Z-δ-hydroxy peroxy radicals from isoprene are of major importance at low-NO_x conditions, and play a large role in explaining observed OH recycling. However, due to limited experimental data, this process is not considered for secondary products.

Peroxy radical ring closure is important for some double-bond containing peroxy radicals under low-NO_x conditions (Vereecken and Peeters, 2004), resulting in peroxides, as in the pinene + OH mechanisms (Figs. 2.3 and 2.9). A generally applicable SAR is not yet available.

2.1.7 Alkoxy radical reactions

Alkoxy radicals are major products of peroxy radical reactions, and are also formed during the photolysis of hydroperoxides and organic peracids. Lifetimes of alkoxy radicals are generally very short, as they typically undergo three types of fast processes: bimolecular reaction with O_2, unimolecular decomposition or H-shift isomerisation (Orlando et al., 2003, Atkinson et al., 2006, Atkinson, 2007b, Vereecken and Francisco, 2012).

Table 2.8: Reactions of alkoxy radicals.

Reaction	Type
$RCHO^{\bullet} + O_2 \rightarrow RC{=}O + HO_2$	bimolecular H-abstraction by O_2
$RCCH(O^{\bullet})R' \rightarrow RC^{\bullet} + R'C(=O)H$	unimolecular decomposition (carbon bond scission)
$RC(H)CCCH(O^{\bullet}) \rightarrow RC^{\bullet}CCCH(OH)$	unimolecular H-shift isomerisation

In the case of decomposition, depending on whether the carbon bond is cyclic or acyclic, either one carbonyl-containing alkyl radical, or an alkyl radical and a molecular carbonyl product will be produced. For H-shift isomerisation, through vibrational bending of the alkoxy radical, cyclic intermediates are formed, in which the alkoxy radical oxygen approaches a carbon atom in the carbon chain of the molecules, allowing an H-shift (Vereecken and Francisco, 2012). A distinction is made based on the number of non-H-atoms in the cyclic intermediate to indicate the H-shift type, in this case a 1,5-H-shift is shown in Table 2.8. The resulting alkyl radicals can either react with O_2 to form peroxy radicals, or decompose.

The variability of measured rates for reactions of alkoxy radicals with O_2 is usually less than that of the rates of unimolecular decomposition or H-shift isomerisation, which can vary by many orders of magnitude (Vereecken and Francisco, 2012). Due to this fact, one of these three types of reactions is often dominant, reducing the impact of uncertainty on the estimation of the rates on the final outcome.

Experimental rates for alkoxy radicals (with 2 or more carbons) reaction with O_2 lie between 6 and 20×10^{-15} cm^3 molecules^{-1} s^{-1} around 298 K (Atkinson et al., 2006, Atkinson, 2007b). In BOREAM, the temperature-dependent rate $k_{\mathrm{RO+O_2}} = 8.9 \times 10^{-14} \exp(-550/T)$ cm^3 molecules^{-1} s^{-1} is adopted, which equals 14×10^{-15} molecules^{-1} cm^3 s^{-1} at 298 K. Atkinson (2007b) recommend $k_{\mathrm{RO+O_2}} = 2.5 \times 10^{-14} \exp(-300/T)$ cm^3 molecules^{-1} s^{-1} (equal to 9×10^{-15} cm^3 molecules^{-1} s^{-1} at 298 K) for primary or secondary alkoxy radicals, which might also be applicable to cyclic alkoxy radicals, based on cyclohexoxy. The difference between these adopted values is not expected to have a large influence, given the lower importance of this reaction compared to decomposition and H-shift isomerisation.

For alkoxy radical decompositions, Atkinson (2007b) proposed a SAR based on experimental results. However, for this SAR few data were available which could be used to estimate the influence of functional groups on the decomposition rate. In Vereecken and Peeters (2009), energy barrier heights were calculated using quantum-chemical calculations based on the B3LYP/6-31G(d,p) level of theory. This was done for a number of compounds containing most functional groups relevant for atmospheric chemistry, such as alcohol, carbonyl, nitrate, hydroperoxide, ether, peroxide. Also, compounds containing double bonds and 3 to 6-membered rings were considered. A SAR was constructed based on these calculated values, see Tables 3, 4 and 5 in Vereecken and Peeters (2009). For the peroxy acyl nitrates, which were not considered by Vereecken and Peeters (2009), we have currently supposed that they exert the same influence as nitrates, when present in β-position of the alkoxy radical function. The groups reduce or increase the energy

barrier compared to that of the reference compound:

$$E_b = E_b(\mathrm{CH_3CH_2O^\bullet}) + \sum_s (F_s \times N(s)), \tag{2.15}$$

where F_s are the group contributions and $N(s)$ is the number of times these groups are present. For barriers below 7 kcal/mol, a correction function was fitted by Vereecken and Peeters (2009) in order to obtain more accurate estimates.

The estimated energy barriers (E_b) were then used by Vereecken and Peeters (2009) in a formula for the kinetic rate of decomposition, based on transition state theory:

$$k_{\mathrm{RO,decomp.}} = L \times 1.8 \times 10^{13} \times \left(\frac{T}{298\mathrm{K}}\right)^{1.7} \times \exp\left(\frac{-E_b}{RT}\right) \mathrm{s}^{-1} \tag{2.16}$$

In this formula, L is the degeneracy (the number of identical bond scissions possible). This SAR was implemented in BOREAM (also used in the GECKO-A model since Aumont et al., 2013). The SAR still has its limitations, as discussed by Vereecken and Peeters (2009), such as the method of calculation of the energy barriers, which is still not of the highest level of theory available, and the lack of experimental data which can serve as a benchmark. The SAR method also does not yet address the interactions between functional groups (Vereecken and Peeters, 2009), which are possible in the multi-functional compounds that make up secondary organic aerosols.

For H-shift isomerisation there are fewer experimental rate determinations available than for decomposition (Vereecken and Francisco, 2012). Theoretical calculations need to take into account rotational and vibrational degrees of freedom of the possible reactant structures, while also the effect of quantum-tunnelling has to be taken into account. It is found that 1,5-H-shifts are usually most favourable, while 1,6-H-shifts and 1,7-H-shifts can sometimes also have non-negligible rates (Vereecken and Francisco, 2012, Vereecken and Peeters, 2010, Atkinson, 2007b). Due to the limited availability of experimental results, experimentally-based SARs have been derived mostly only for aliphatic alkoxy radicals, although effects of the presence of alcohol or carbonyl functions have been considered, based on the analogy with H-abstraction by OH (Atkinson, 2007b). Vereecken and Peeters (2010) devised a SAR based on calculated H-abstraction rates for a wider range of compounds, considering also ether, hydroperoxide and nitrate groups, and effects of double bonds, but not the peroxy acyl nitrate group. This SAR has been implemented in BOREAM, as it covers the widest range of compounds relevant for SOA formation. One drawback of the method is that the set on which the SAR is based contained mostly linear compounds. Ring strain and steric hindrance will make transposing this SAR to cyclic compounds, which are of major importance for α- and

β-pinene oxidation, problematic (Vereecken and Peeters, 2010). In the primary mechanisms for α- and β-pinene, H-shifts in cyclic compounds occur frequently, as was shown by quantum-theoretical calculations (Fantechi et al., 2002, Capouet et al., 2008, Vereecken and Peeters, 2012). Therefore, it was decided to apply the SAR to cyclic compounds in BOREAM if the atom chain between the alkoxy radical oxygen and the carbon providing the H for H-shift contains at most one cyclic bond, as it can be assumed that in that case the rotations and bending necessary in order to obtain the cyclic transition state for H-shift are still possible, and similar to those occurring in the linear compounds for which the SAR was derived. If two or more cyclic bonds are present within the span of the H-shift, then we assume that strain or steric hindrance is too strong and prevents H-shift. In reality, such H-shifts are sometimes possible, if the geometry of the molecule is favourable.

Alkoxy radicals can also undergo other unimolecular reactions. Unimolecular ring closure between an alkoxy radical and a double bond was studied by Vereecken and Peeters (2004) and was found to be important for the primary chemistry of α and β-pinene. A general SAR was not yet derived though, and therefore this process is not yet considered for secondary products in BOREAM. For α-unsaturated alkoxy radicals and α-ether-bonded alkoxy radicals the treatment of Laval-Szopa (2003) is followed.

2.2 Primary chemistry of monoterpenes

2.2.1 α-pinene gas phase oxidation mechanism

In this subsection the primary chemistry of α-pinene in the BOREAM model is described. It was first used in the modelling studies Capouet et al. (2004) and Capouet et al. (2008), and with some further adaptations in Ceulemans et al. (2010) and Ceulemans et al. (2012). The primary gas phase mechanism is largely based on theoretical calculations and SARs. For the reaction rates of α-pinene and some major oxidation products such as pinonaldehyde, available experimental kinetic data were also used. To aid the discussion, the 10 carbon atoms in α-pinene are named from a to j, as indicated in Fig. 2.2, following Capouet et al. (2008).

2.2.1.1 α-pinene oxidation by OH

The rate constant chosen for the reaction of α-pinene with OH is $1.21 \times 10^{-11} \exp(444/T)$ cm^3 $molecules^{-1}$ s^{-1} (IUPAC, 2014). The theoretical work of Peeters et al. (2001) forms the basis of the primary OH-oxidation mechanism, with additions provided by Vereecken

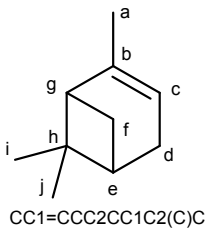

FIGURE 2.2: α-pinene with lettering of carbon atoms, used to describe the primary chemistry in the text.

et al. (2007). The implementation in BOREAM has been discussed in Capouet et al. (2004) and Capouet et al. (2008). An overview is given in Fig. 2.3.

Reaction of OH with α-pinene was predicted to occur mostly through addition on the double-bonded carbons, with each addition accounting for about 44%. The main H-abstraction channel was found to account for about 9%. The other H-abstractions together represent an additional 3%, but were replaced by the main H-abstraction channel. In the case of the OH-addition on carbon *c*, the resulting activated alkyl radical P1OH (notation of Peeters et al., 2001) can either stabilise, add O_2 and continue the usual peroxy radical chemistry, or undergo a ring-opening. In this last case, after addition of O_2, two stereo-isomeric peroxy radicals are formed, one in which the OH-group is in syn-position with the O_2 group (40%), and one in anti-configuration (60%). Those stereo-isomers are predicted to undergo different chemistry (Vereecken et al., 2007). The anti-conformer of the peroxy radical undergoes an H-shift isomerisation, competitive with bimolecular reactions, leading to formation of a hydroperoxide group. For the syn-conformer, a ring-closure of the peroxy radical competes with bi-molecular reactions with for example NO, leading to an alkoxy radical, which itself can also undergo ring closure. The β-OH-alkyl radicals (thermal P1OH and P2OH) react with O_2, forming peroxy radicals, which after reaction with NO result in two alkoxy radicals. In both these β-OH-alkoxy radicals (RO23 and RO28), the bond between the carbons with the alcohol and alkoxy group will be broken after unimolecular decomposition. The resulting α-OH-alkyl radicals add O_2, forming α-OH-peroxy radicals. Under normal conditions, the latter decomposes to pinonaldehyde in both channels, although under very high-NO_x conditions, it can also react bimolecularly.

The reaction mechanism of OH-oxidation of pinonaldehyde is based on Fantechi et al. (2002) and Peeters et al. (2001), and together with its photolysis mechanism is shown in Fig. 2 of Capouet et al. (2004). Note that a recent study of Chacon-Madrid et al. (2013) found a relatively high norpinonaldehyde yield in photooxidation experiments (around

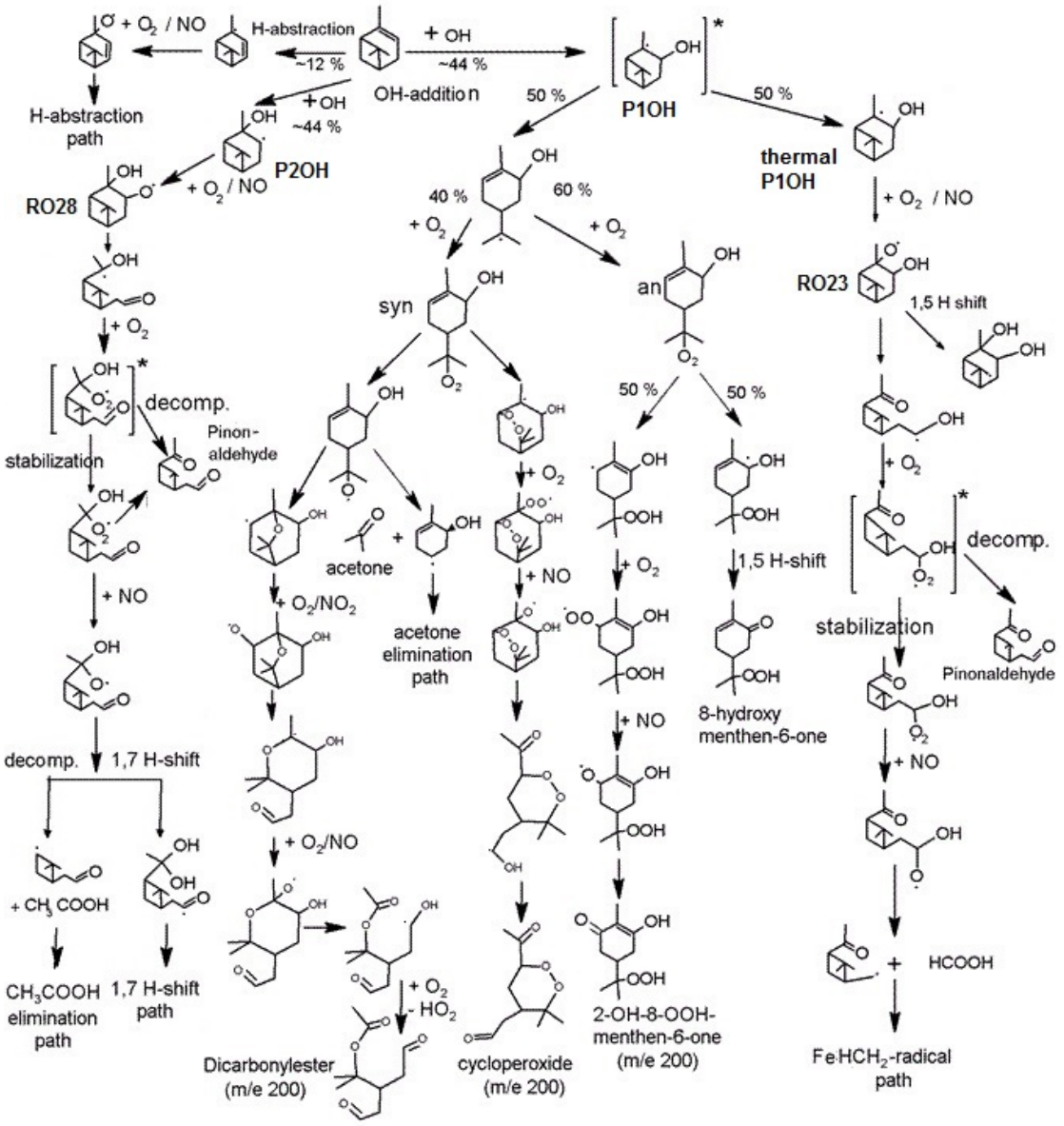

FIGURE 2.3: The initial steps of the mechanism of the oxidation of α-pinene by OH, used in BOREAM. The relative reaction branching fractions are shown in percent. The addition of O_2 to alkyl radicals and subsequent chemistry of peroxy radicals is simplified in this figure, only showing the continuation of the radical chain to alkoxy radicals through the reaction with NO, although the complete peroxy radical chemistry is present in BOREAM. Continuations of radical pathways not shown can be found in Peeters et al. (2001) and Vereecken et al. (2007).

50%), while the channel leading to this compound in BOREAM has a branching fraction of only about 25%.

2.2.1.2 α-pinene ozonolysis

For ozonolysis, the total rate constant used in BOREAM is $1.01 \times 10^{-15} \exp(-732/T)$ cm^3 $molecules^{-1}$ s^{-1}. This rate is 5–10% less than the recent update by IUPAC (2014), but well within the experimental uncertainty range.

The description given below for the chemistry in BOREAM after the reaction with O_3 has been taken over mostly from Ceulemans et al. (2010) and from Capouet et al. (2008), with minor updates. Fig. 2.4 provides an overview of the current mechanism.

The ozonolysis of α-pinene leads to the formation of two Criegee Intermediates in equal proportions (Ma et al., 2007): CI1, with a secondary Criegee functionality ($RC(CH_3)OO$), and CI2, with a primary Criegee functionality (RC(H)OO).

Activated CIs can either decompose (yielding OH) or be collisionally stabilised. The yield of Stabilised Criegee Intermediates (SCIs) is constrained by the measured pinonaldehyde yield in α-pinene ozonolysis experiments, assuming that pinonaldehyde is produced exclusively through the reaction of SCIs with water vapour. The experimental range is 15–40 % (Berndt et al., 2003, Tillmann et al., 2010). In Capouet et al. (2008) an SCI yield of 13.5% was assumed (9% SCI2 yield and 4.5% SCI1 yield).

Both isomers CI1 and CI2 have anti- and syn-conformers. Theoretical calculations (Nguyen, T. L., personal communication) indicate that only one of the CI isomers/conformers undergoes substantial collisional stabilisation, namely the anti-CI2, for which a 1,4-H-shift is impossible, whereas the other three conformers decompose fully via fast 1,4-H-shifts while still activated. The overall yield of anti-CI2 is estimated to be 30%, of which a large fraction can be stabilised, estimated to be about two-thirds in order to account for the ca. 20% observed pinonaldehyde yield from the very fast reaction with water (see below). The model has been adapted accordingly, i.e. CI2 (produced with a 50% branching fraction) is stabilised for 40%, and CI1 is not stabilised at all. Other pathways previously considered (Capouet et al., 2008) remain identical, but are scaled to preserve stoichiometric balance.

The bimolecular reactions of the SCI, especially with water vapour, have been described in Subsection 2.1.2.4. The anti-CI2 from α-pinene lacks a β-H-atom in syn to the OO-function, and therefore cannot decompose via 1,4-H-shift but only follow the slower ester channel or be stabilised (see above, Nguyen et al., personal communication). For the anti-SCI2, an exact decomposition rate was not available, but for similar reasons

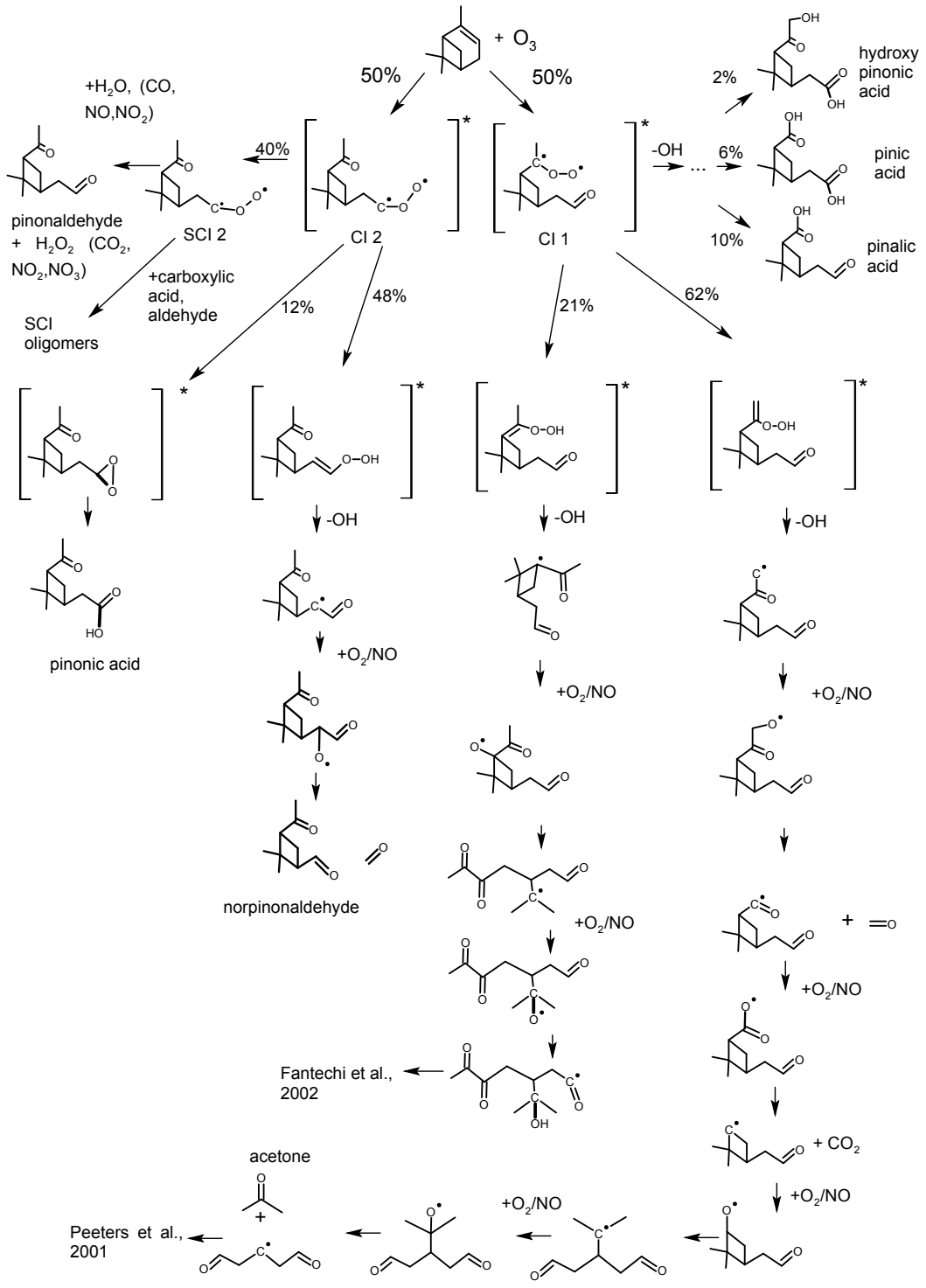

FIGURE 2.4: The ozonolysis mechanism of α-pinene in BOREAM. The relative reaction branching fractions are shown in percent. The production of pinic, pinalic and hydroxy pinonic acid has not been elucidated mechanistically, but was added based on experimental yields, and is modelled in BOREAM as a direct production from CI1.

as for the excited CI, its decomposition is assumed to be slow compared to bimolecular reactions, and therefore ignored.

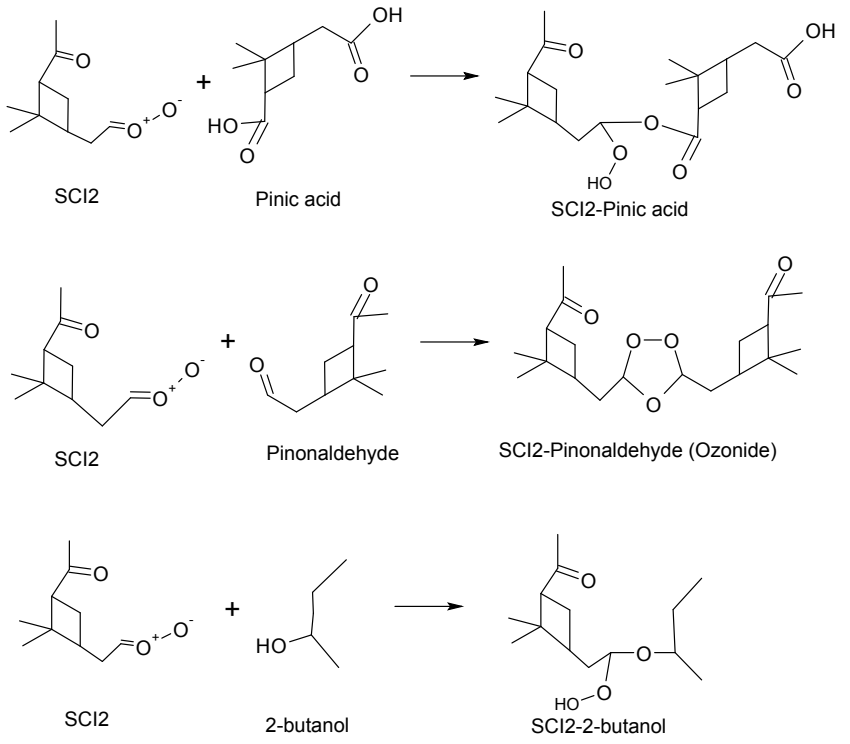

FIGURE 2.5: Possible reactions between Stabilised Criegee Intermediates from α-pinene ozonolysis with pinic acid, pinonaldehyde and 2-butanol.

Several previous modelling studies of α-pinene ozonolysis have considered the possibility of SCI reactions with organic molecules (Bonn et al., 2007, Kamens and Jaoui, 2001). Recent chamber studies (Tolocka et al., 2006, Heaton et al., 2007) have observed a rapid formation of oligomer products from α- and β-pinene ozonolysis, which were believed to be similar to the reaction products of SCI with carboxylic acids or carbonyls. These reactions yield high molecular mass hydroperoxides made of two monomers bonded through an oxygen atom, or secondary ozonides (Fig. 2.5). Tobias and Ziemann (2001) measured relative rates for reactions between SCI and alcohols, carbonyls, carboxylic acids and water vapour for the SCI from tetradecene ozonolysis. For the reactions of SCI with carbonyls we adopt the absolute rate measured by Fenske et al. (2000) for CH_3CHOO + $CH_3CH{=}O$ (10^{-12} molecules^{-1} cm^3 s^{-1}). The rates for SCI reactions with carboxylic acids (6.30×10^{-12} molecules^{-1} cm^3 s^{-1}) and with alcohols (2.22×10^{-14} molecules^{-1} cm^3 s^{-1}) are obtained from the relative rates of Tobias and Ziemann (2001).

The main pathway for the CIs is transformation into an unstable unsaturated hydroperoxide, which decomposes into a 2-oxo-alkyl radical and OH. In the case of CI2, this

pathway leads eventually to norpinonaldehyde as a major stable product. The other Criegee's hydroperoxide leads to two alkyl radicals which undergo several consecutive radical reactions, yielding stable semi-volatile products. In addition, CI2 undergoes the so-called ester-channel, with the ester decomposing quickly into pinonic acid. The yield of pinonic acid from CI2 is taken to be 12%, higher than in Ma et al. (2007).

It is known that α-pinene ozonolysis yields several carboxylic acids, most importantly pinic, hydroxy pinonic and pinalic acid (Yu et al., 1999a, Iinuma et al., 2004, Ma et al., 2007), for which explicit formation routes are still unknown (Capouet et al., 2008). Laboratory experiments (Ma et al., 2007) have indicated that pinic acid is produced exclusively from CI1. In BOREAM, these carboxylic acids are assumed to be produced through CI1, with total yields of 3% for pinic acid, 1% for hydroxy pinonic acid and 5% pinalic acid, based on yields measured by Yu et al. (1999a).

2.2.1.3 α-pinene oxidation by NO_3

The reaction with NO_3 proceeds at a rate taken as $k_{NO_3} = 1.19 \times 10^{-12} \exp(490/T)$ molecules^{-1} cm^3 s^{-1} in BOREAM (IUPAC, 2014). The reaction is supposed to occur exclusively by addition on the double bond, with 65% addition on carbon *c*, and 35% on carbon *b*. The resulting peroxy radicals can lead to alkoxy radicals, which upon decomposition give pinonaldehyde. It should be noted that this mechanism has not received the same theoretical attention as those for OH or O_3, therefore it appears likely that possibly important reaction pathways are still ignored.

2.2.1.4 α-pinene oxidation by O(^{3}P)

In BOREAM, α-pinene + O(^{3}P) (reaction rate: 3.2×10^{-11} molecules^{-1} cm^3 s^{-1}, Pinho et al., 2007) is assumed to have α-pinene oxide as the main product (77%), based on Pinho et al. (2007).

2.2.2 β-pinene gas phase oxidation mechanism

After α-pinene, β-pinene is perhaps the second-most investigated monoterpene in atmospheric chemistry, and both its ozone formation and secondary organic aerosol potential have been studied in both laboratory and modelling studies. Therefore, the BOREAM model has been extended with a mechanism for β-pinene oxidation by its main oxidants, OH, O_3 and NO_3, based on the same principles as for α-pinene. In the next Sections we will discuss the main aspects of these mechanisms.

For oxidation by OH, the mechanism in BOREAM is based on the theoretical study of Vereecken and Peeters (2012), and for ozonolysis it is based on the theoretical work of Nguyen et al. (2009a). The mechanism of β-pinene oxidation by OH and O_3 in the MCM was previously used in modelling studies by Jenkin (2004) and Pinho et al. (2007). Large differences exist between the MCM mechanism and the mechanisms of Nguyen et al. (2009a) and Vereecken and Peeters (2012), as will be seen in this section.

2.2.2.1 β-pinene oxidation by OH

In Vereecken and Peeters (2012) the initial OH-addition and H-abstraction by OH for β-pinene, and subsequent radical reactions of alkyl, alkoxy and peroxy radicals, were characterised by means of quantum-theoretical calculations. Other reactions in the primary chemistry mechanism are based on widely used SARs, such as for the bimolecular reactions of peroxy radicals. The secondary chemistry of the oxidation products was generated based on SARs described earlier in this Chapter.

For the initial OH-reaction, several results for the total reaction rate near atmospheric pressure are available (Fig. 2.6). Temperature-dependent rates were determined experimentally by Gill and Hites (2002) ($1.47 \times 10^{-11} \exp(467\text{K}/T)$ cm^3 molecules^{-1} s^{-1}, which equals 7.05×10^{-11} cm^3 molecules^{-1} s^{-1} at 298 K) and Montenegro et al. (2012), and theoretically by Dash and Rajakumar (2013). Measurements at single temperatures were obtained by Davis et al. (2005), Atkinson et al. (1986), Winer et al. (1976) and Dash and Rajakumar (2013).

No direct experimental determinations of the site-specific rates are available to our knowledge. Vereecken and Peeters (2012) called into question part of the theoretical results for the OH addition on β-pinene by Fan et al. (2005), indicating that higher-level calculations would be needed, but did not provide these yet. Instead, Vereecken and Peeters (2012) used the SAR of Peeters et al. (2007) to determine the site-specific rates of OH-addition on β-pinene. The main pathway was found to be the addition of OH on carbon C_a (see Fig. 2.7), with a branching fraction of 83.3%, while the other addition on carbon C_b was found to have a branching fraction of only 6.8% (Table 2.9). H-abstraction from carbons C_c and C_d was found to account for 5.9% and 3.0% of total rate, based on quantum-chemical calculations, while abstraction from other carbons was minor. The sum of all OH-reactions was found to be 6.6×10^{-11} cm^3 molecules^{-1} s^{-1}. A reanalysis using different interpolation schemes for the strain- and ring-enhanced abstractions led to higher abstraction rates, which gave a total reaction rate of 7.1×10^{-11} cm^3 molecules^{-1} s^{-1}. No clear preference was given by Vereecken and Peeters (2012) for any of the two sets of branching fractions (in BOREAM the first series is used). The

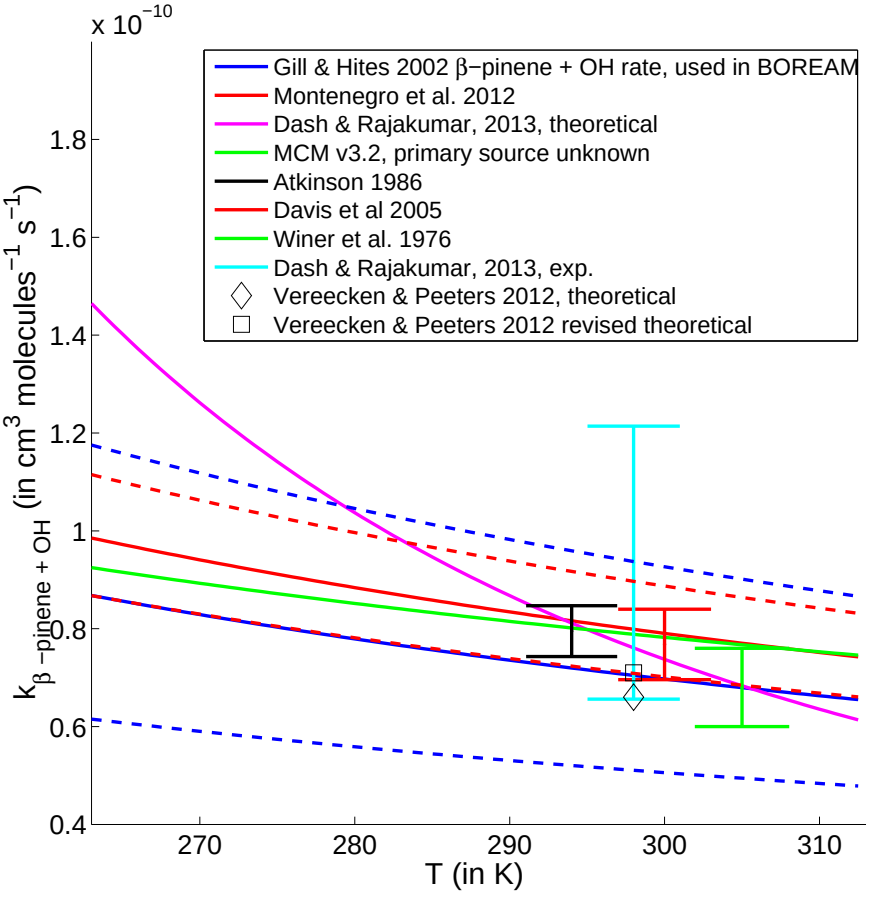

FIGURE 2.6: Overview of experimental and theoretical values for $k_{\beta\text{-pinene,OH}}$ at different temperatures. The temperature-dependent rates of Gill and Hites (2002) and Montenegro et al. (2012) are given together with the given uncertainty range in dashed lines, in the same colour. The single-temperature data points with error bars are legend entries 5 to 8.

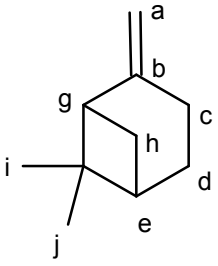

FIGURE 2.7: β-pinene with lettering of carbon atoms

above mentioned temperature-dependent rate of Gill and Hites (2002) has been adopted as the total OH reaction rate in the standard BOREAM scheme. In the MCMv3.2, the rate $2.38 \times 10^{-11} \exp(357\,\mathrm{K}/T)$ cm^3 molecules^{-1} s^{-1} is used. Most results are situated between 7.0 to 8.5×10^{-11} cm^3 molecules^{-1} s^{-1}. The value 7.05×10^{-11} cm^3 molecules^{-1} s^{-1} used in BOREAM at 298 K is about 12% lower than that of the MCMv3.2 (7.9×10^{-11} cm^3 molecules^{-1} s^{-1}). The main difference for the branching fractions is that in the current MCMv3.2, H-abstractions by OH have not been considered for β-pinene (Table 2.9).

TABLE 2.9: Branching fractions (in percent) for the initial OH oxidation of β-pinene in Vereecken and Peeters (2012) (used in BOREAM), a possible variation in these branching fractions given by Vereecken and Peeters (2012) using a different methodology, and in the MCMv3.2 model (Saunders et al., 2003).

Site	k_{site} Vereecken and Peeters (2012)	k_{site} Vereecken and Peeters (2012) (alternative)	k_{site} MCMv3.2
OH-addition			
C_a	83.3	77	92.4
C_b	6.8	6	7.6
H-abstraction			
C_a	0.0	0	0
C_c	5.9	11	0
C_d	3.0	3	0
C_e	0.0	0	0
C_g	0.0	0	0
C_h	0.2	2	0
C_i	0.4	0	0
C_j	0.4	0	0

For the reactions of the primary radicals formed after OH reaction, we rely on the theoretical calculations of Vereecken and Peeters (2012). We give a brief overview of the main aspects of the mechanism, which has been completely implemented in BOREAM. We briefly discuss the most important differences with the MCMv3.2 mechanism, see Fig. 2.8.

After addition of OH on the main addition site C_a, an activated alkyl radical, **actBPINOH1** (following the notation of Vereecken and Peeters, 2012), is formed, which either stabilises to a less energetic alkyl radical, **BPINOH1**, or undergoes a ring opening reaction, which after addition of O_2 leads to the peroxy radical **R1OO**. In the MCMv3.1, discussed in Pinho et al. (2007), it was already assumed that **actBPINOH1** can undergo a prompt ring opening, in analogy with the similar ring opening in the α-pinene mechanism, proposed by Nozière et al. (1999) and Peeters et al. (2001). The

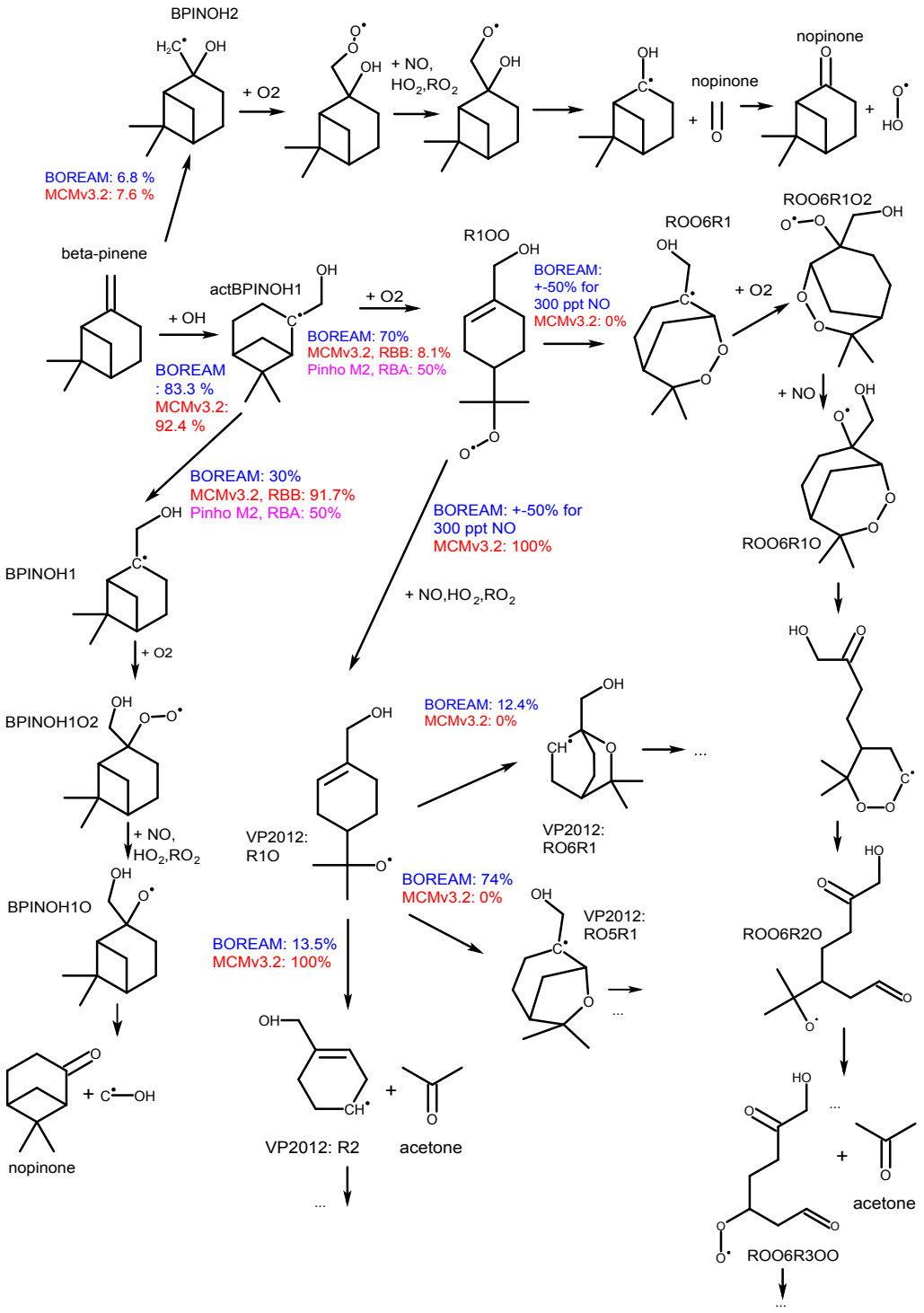

FIGURE 2.8: First steps in the β-pinene OH addition reaction mechanism of Vereecken and Peeters (2012). The branching fractions of the main reaction pathways are compared with those assumed in the MCMv3.2. For the activated radical **actBPINOH1**, the branching fractions in sensitivity tests in BOREAM (RBA and RBB) and mechanism 2 of Pinho et al. (2007) are given. Names are based on Vereecken and Peeters (2012) (VP2012). For peroxy-radicals, only the pathway to the alkoxy radical is shown. Further radical chemistry can be found in Vereecken and Peeters (2012).

ring opening branching fraction was set to 8.1%, based on the yield of acetone, as it was thought that decomposition into radical **R2** and acetone was the main fate of the alkoxy radical **R1O** formed after reaction of **R1OO** with NO. Based on quantum-chemical calculations, however, Vereecken and Peeters (2012) estimated a much higher yield (70%) for the ring opening reaction. The alkoxy radical **R1O** is now predicted to also undergo two different alkoxy radical ring closure reactions, leading to a 5-membered oxygen-containing ring with a 74% yield, and a 6-membered oxygen-containing ring with a 12.4% yield. This leaves the acetone-producing channel of **R1O** with a yield of only 13.5%, which multiplied by the initial branching fraction towards **R1OO** is consistent with the reported acetone yields. The main channel in the MCM mechanism leads to the peroxy radical **BPINOH1O2**, with a branching fraction of 91.7%, while in Vereecken and Peeters (2012) this channel has a branching fraction of only 30%. It should be noted though that Pinho et al. (2007) also considered a test in which **actBPINOH1** has 50:50 branching fractions towards **R1OO** and **BPINOH1** (mechanism 2). Another difference, of importance under low-NO_x conditions, is that **R1OO** undergoes a ring closure isomerisation towards **ROO6R1**, which becomes of equal importance as the **R1O**-channel at NO concentrations of around 300 ppt, and which leads to oxygenated peroxides.

The main fate of the peroxy radical **BPINOH1O2** is reaction with NO under high-NO_x conditions, leading to the alkoxy radical **BPINOH1O**, which decomposes into nopinone and formaldehyde. As pointed out by Vereecken and Peeters (2012), the higher branching fractions of the **R1OO** channel in the new mechanism leads to nopinone yields which are more consistent with experimental data. Pinho et al. (2007) proposed H-shift isomerisations for **BPINOH1O** (in their β-pinene mechanism 3), which were not confirmed by Vereecken and Peeters (2012).

In Vereecken and Peeters (2012) the H-abstraction by OH at sites C_c and C_d produces the radicals **CR1OO**, **CR2OO** and **DR1O**. These channels lead to a complex chemistry yielding mostly unsaturated oxygenated primary products which, upon reaction with ozone or OH leads to a large variety of semi-volatile oxygenated species, which can contribute to SOA. The relatively minor H-abstractions from sites C_h, C_i and C_j are predicted to have yields below 1%, and are currently not treated in BOREAM.

2.2.2.2 β-pinene ozonolysis

Several kinetic studies of the reaction rate of β-pinene with ozone have been conducted experimentally and theoretically (Fig. 2.9). The rate recommended by Atkinson (1994) is 1.5×10^{-17} cm^3 molecules^{-1} s^{-1} at 298 K, with an estimated uncertainty of about 35%. The laboratory study of Khamaganov and Hites (2001) derived a rate which increases

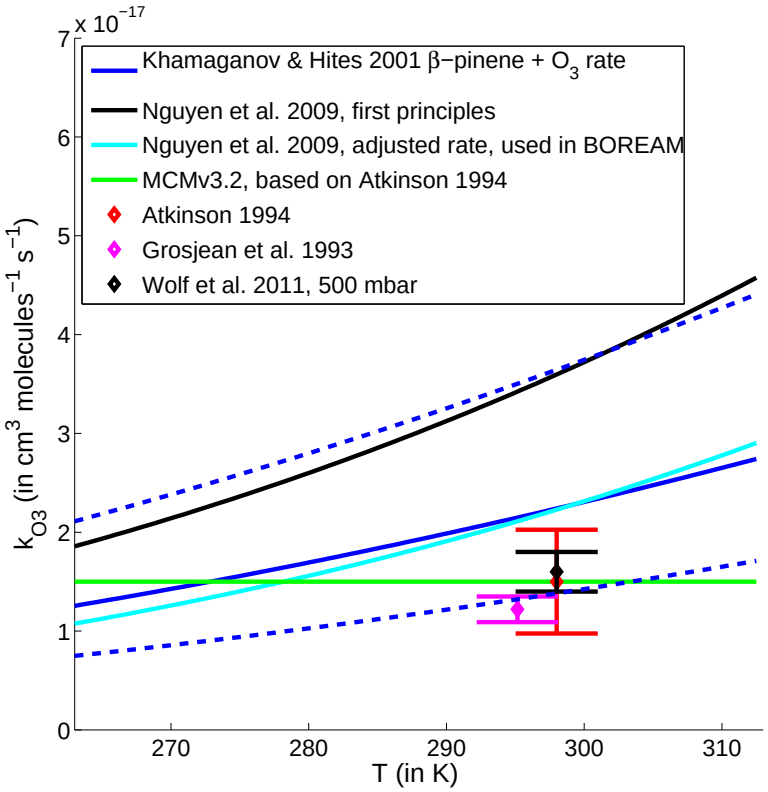

FIGURE 2.9: β-pinene ozonolysis rates determined by experiment or theory. The temperature-dependent rate determined experimentally by Khamaganov and Hites (2001) is given in solid blue, together with the uncertainty range in dashed blue lines. The theoretically determined rate of Nguyen et al. (2009a) (solid black) was adjusted to match Khamaganov and Hites (2001) (cyan), which is the current rate in the standard BOREAM mechanism. Experimental values around 298 K were determined by Atkinson (1994), Grosjean et al. (1993) and Wolf et al. (2011), the first of which has served as the source for the currently temperature-independent rate in the MCMv3.2 model (Saunders et al., 2003) (green).

with temperature, equal to around $2.2 \times 10^{-17}\,\mathrm{cm^3\,molecules^{-1}\,s^{-1}}$ at 298 K, considerably higher than the recommendation of Atkinson (1994), although also with a large uncertainty range. The values obtained at 292 K by Grosjean et al. (1993) and at 298 K by Wolf et al. (2011) seem to be more in line with the Atkinson (1994) recommendation. Nguyen et al. (2009a) determined a temperature dependent rate constant theoretically, with a temperature dependence similar to Khamaganov and Hites (2001), but higher overall. As there are quite significant uncertainties in the theoretical calculations, an adjusted temperature-dependent rate based on the experimental result of Khamaganov and Hites (2001) is adopted ($1.15 \times 10^{-22} T^{2.66} \exp(-888/T)\,\mathrm{cm^3\,molecules^{-1}\,s^{-1}}$) in the current "standard" BOREAM mechanism. Although the value of Atkinson (1994) (which has been adopted in the MCM) at 298 K is a factor 0.67 lower than that adopted in BOREAM, the new temperature-dependent rate recommendation by the IUPAC Panel is close to the rate adopted in BOREAM (IUPAC, 2014). It is worth noting that the

ozonolysis rate of β-pinene is about 4 to 5 times lower than that for α-pinene, while its reaction rate with OH is about 2 times higher.

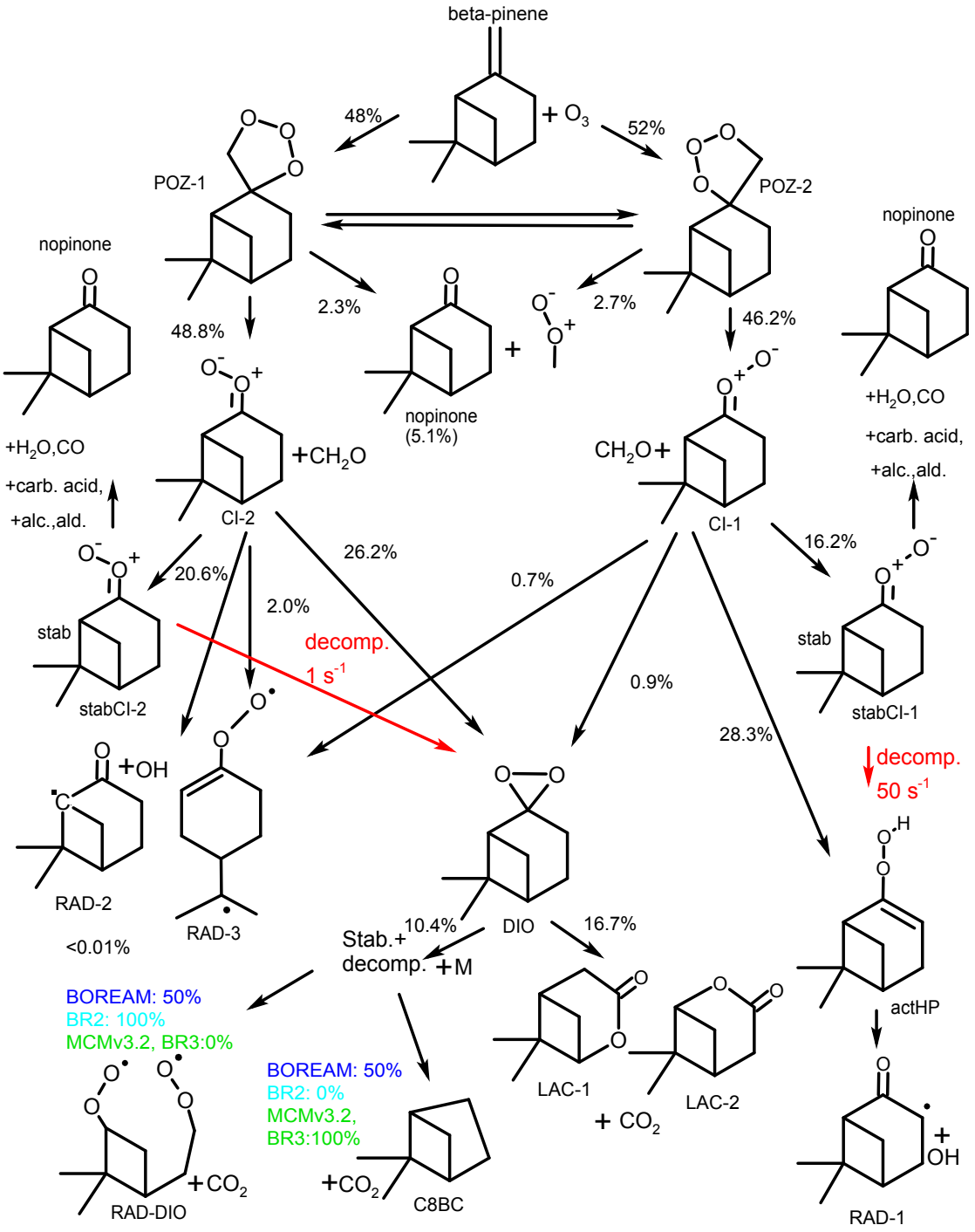

FIGURE 2.10: β-pinene ozonolysis mechanism, adopted from Nguyen et al. (2009a). Some additional important pathways discussed by Nguyen et al. (2009a) have been added to the scheme, such as the decomposition of the stabilised Criegee intermediates **CI-1** and **CI-2**, and the as yet quite uncertain pathways from the dioxyrane **DIO** (see text for details).

For the primary ozonolysis chemistry (Fig. 2.10) the theoretical study of Nguyen et al.

(2009a) was used. Upon reaction, two primary ozonides are formed with about equal yields, which can interconvert, and which only differ in the orientation of the oxygens of the primary ozonide groups with respect to the carbon skeleton of the molecule. These primary ozonides rapidly decompose, to either nopinone and a one carbon activated Criegee Intermediate (CI), with a yield of about 5%, or to stereo-isomeric activated Criegee intermediates CI-1 (with a yield of 48.8 %) and CI-2 (46.2%). According to Nguyen et al. (2009a), these CIs can either be thermally stabilised to the stabilised Criegee intermediates **SCI-1** or **SCI-2**, or they can undergo further isomerisations which depend on the structure. In previous mechanisms, such as those used by Jenkin (2004) and Pinho et al. (2007), the distinction between **CI-1** and **CI-2** was not explicitly taken into account. The hydrogen atom closest to the Criegee-functionality is more easily abstracted through intramolecular H-shift for **CI-1** than for **CI-2**, as the H-shift was found to be much less favourable from the tertiary carbon atom (with a 95% branching fraction for **CI-1** against less than 0.01% for **CI-2**) (Nguyen et al., 2009a). For **CI-1** this leads to an activated hydroperoxide **HP**, which quickly decomposes to OH and radical **RAD-1**, which undergoes a complex further radical chemistry before reaching stable molecular products.

CI-2 was found by Nguyen et al. (2009a) to lead to a dioxirane **DIO**, which can either isomerise to two different lactones, with a branching fraction which was not yet resolved by the calculations (assumed 50%/50% in BOREAM), but with a total yield from β-pinene ozonolysis of 16.7%, or be converted into a triplet bisoxyradical. The fate of this bisoxyradical was not resolved either, although Nguyen et al. (2009a) suggest it will decompose into CO_2 and either a bi-alkyl radical **RAD-DIO** (to our knowledge for the first time proposed by Jaoui and Kamens, 2003), or a bicyclic alkane, containing a 5-membered ring (**C8BC** in the MCMv3.2 mechanism), but a quantification of yields was not made. In the MCM model, the compound **C8BC** has a total yield from β-pinene ozonolysis of 19.8% (Saunders et al., 2003), suggesting it is considered the main product of the isomerisation of the dioxirane, as lactones and the biradical **RAD-DIO** were not yet considered in the MCM. In BOREAM, the production of either product **RAD-DIO** or **C8BC** has been left as a possibility, and in the standard mechanisms these products have been assigned a preliminary relative branching fraction of 50%/50%. In two model variations, named BR2 and BR3, the relative branching fraction towards the biradical **RAD-DIO** is set to 100% or 0%. As a bicyclic alkane, the compound **C8BC** should stand out from other oxidation products of β-pinene, and measurement of its yield (or its absence) in a smog chamber experiment could help to resolve this part of the mechanism. Both **CI-1** and **CI-2** were found to lead to another biradical **RAD-3** by Nguyen et al. (2009a), for which a preliminary mechanism was proposed, and which was implemented in BOREAM. The bi-peroxy radicals have been implemented in BOREAM based on

the SARs for mono-peroxy radicals. For the cross reactions of bi-peroxy radicals with peroxy radicals, we have also made use of the peroxy radical counters for the different peroxy radical classes.

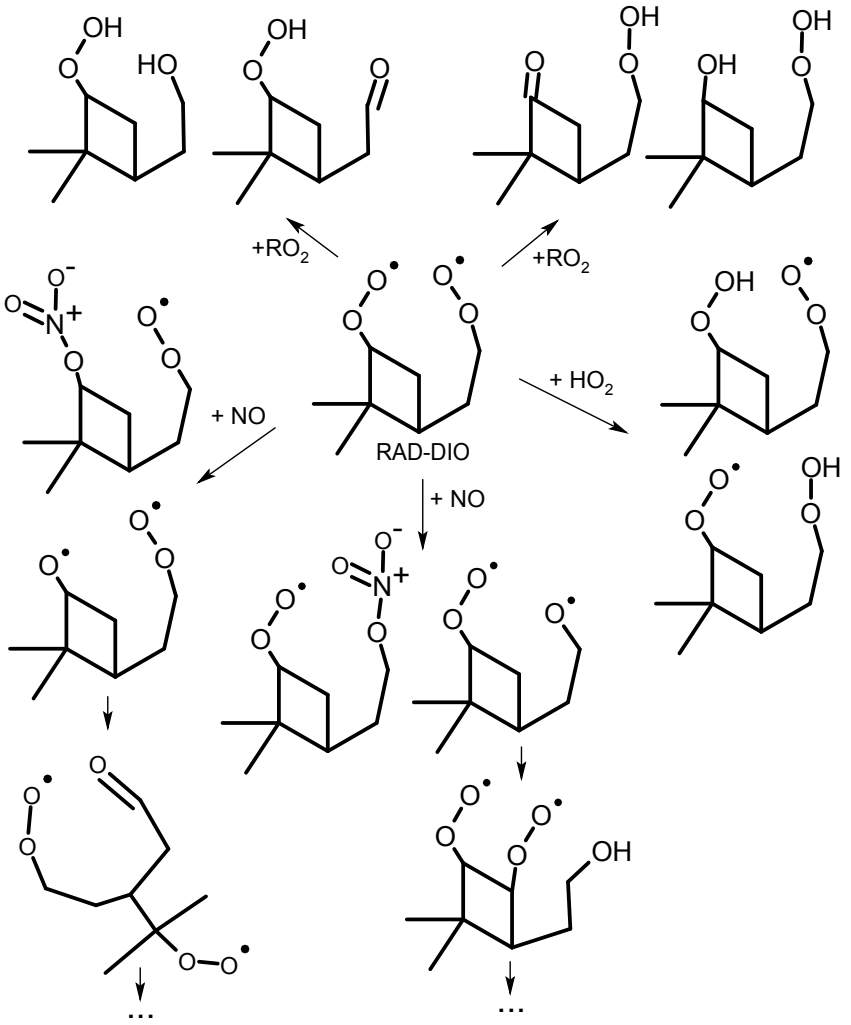

FIGURE 2.11: Simplified scheme of the possible reactions of the biradical **RAD-DIO**.

A similar mechanism has been implemented in BOREAM for **RAD-DIO**, for which a simplified scheme is shown in Fig. 2.11. The proposed chemistry for the biradicals remains highly speculative, as it relies on SARs for mono-peroxy and mono-alkoxy radicals, which are applied to bi-peroxy or alkoxy-peroxy radicals, which could possibly undergo other complex isomerisation which remain unknown. Due to its complexity, the biradical chemistry is generated automatically, (ignoring some minor alkoxy radical pathways), until only molecular compounds or mono-radicals are present, which can then be treated using the regular SARs for the secondary chemistry. The treatment of the biradicals originating from **RAD-DIO** leads to about 1250 chemical reactions in BOREAM. The

biradical chemistry leads to a large variety of multi-functional compounds, which can be of importance for both gas phase chemistry and SOA formation.

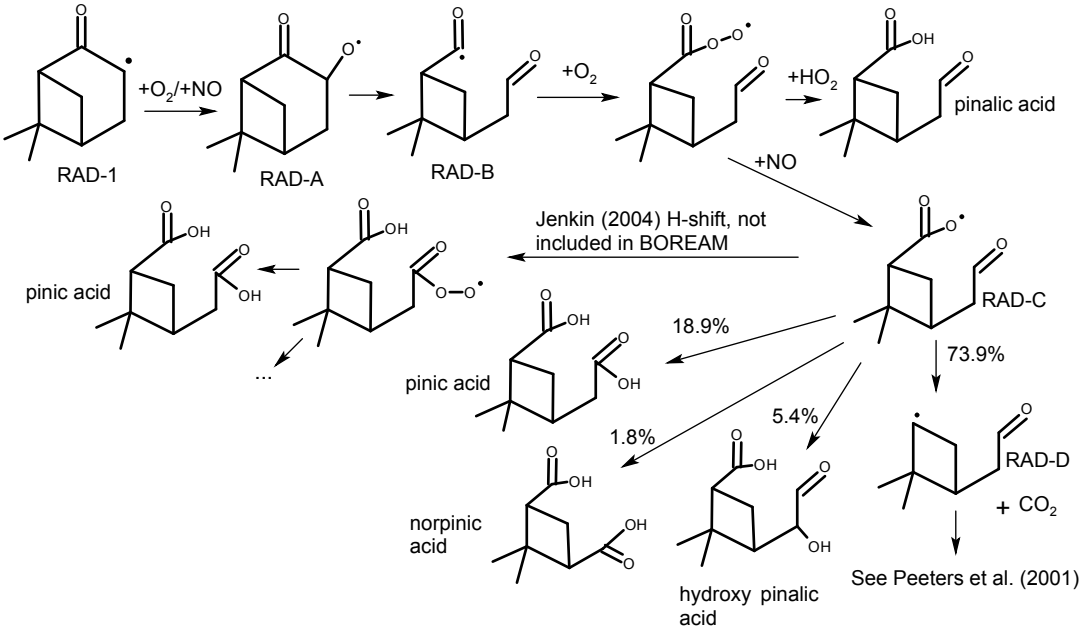

FIGURE 2.12: Reaction mechanism for **RAD-1** in BOREAM, based on Nguyen et al. (2009a). The not-implemented pathway proposed by Jenkin (2004) towards pinic acid is shown. Instead, in BOREAM a direct production of pinic, norpinic and hydroxypinalic acid has been implemented from radical **RAD-C**.

The reaction mechanism for **RAD-1**, based on Nguyen et al. (2009a), is shown in Fig. 2.12. The pathway proposed by Jenkin (2004) towards pinic acid is also shown. In Nguyen et al. (2009a) this pathway was estimated to be negligible compared to the decomposition of **RAD-C**. However, Yu et al. (1999a) and Ma and Marston (2008) both found significant yields of pinic and other acids, which have structures suggesting that they could be formed from **RAD-C**. Since the precise formation mechanism remains unknown, a direct production of pinic, norpinic and hydroxypinalic acid (a structural isomer of the hydroxy norpinonic acid reported by Yu et al. (1999a), that would have been difficult to distinguish from this last compound, but which can be formed from **RAD-C**) has been implemented from **RAD-C** in BOREAM, with yields chosen in order to approach the total yields towards these acids reported in Yu et al. (1999a). As this direct production likely does not correctly reflect the true dependence to experimental conditions, and since pinic acid is the single most important species present in the SOA, this introduces significant uncertainty into the BOREAM simulations of SOA formation in β-pinene ozonolysis.

SCI-1 and **SCI-2** can both decompose, with rates estimated to be about 50 and 1 s^{-1} by Nguyen et al. (2009a), although these rates were suggested to be very uncertain.

The product distribution of these decompositions has been assumed to be identical to that of the decomposition of the activated CIs in BOREAM. Competing with this are bimolecular reactions (see Section 2.1.2.4). The reaction of water monomers and dimers is implemented following the calculated rates by Ryzhkov and Ariya (2004) for Me_2COO, which are more than an order of magnitude slower than those for anti-MeCHOO (used for the α-pinene SCI), but which could still contribute significantly. The reaction with water vapour is assumed to lead to nopinone and H_2O_2, as we assume that the formed α-hydroxy hydroperoxides decompose quickly, although this assumption requires experimental confirmation. Reactions with CO, NO and NO_2 also leads to nopinone. The reactions of **SCI-2** with about 25 carboxylic acid and aldehyde species, leading to SCI oligomers, have been implemented, similarly as for α-pinene. Also in this case the absolute reaction rates are very uncertain.

2.2.2.3 β-pinene oxidation by NO_3

The rate recommended by Atkinson (1994) is used for the reaction with NO_3: $2.51 \times 10^{-12}\,cm^3\,molecules^{-1}\,s^{-1}$. The reaction mechanism following NO_3-addition has been less studied than the OH- and ozone-initiated mechanisms, and data are lacking on the product distributions. Following the SAR for NO_3 addition adopted in BOREAM, we assume that NO_3 is added exclusively on the exocyclic double-bonded carbon. After reaction with NO, the resulting peroxy radical yields an alkoxy radical, in which a carbon bond decomposes, breaking the 6-membered ring. Fry et al. (2009) also proposed that this initial alkoxy radical might undergo H-shift isomerisations, leading to low-volatility compounds. Three previous β-pinene + NO_3 SOA studies (Hallquist et al., 1999, Griffin et al., 1999, Fry et al., 2009) all found relatively high SOA yields, higher than in the case of α-pinene, and also higher than for β-pinene OH addition. This suggests that more pathways towards multifunctional species could be present, perhaps similar to the Vereecken and Peeters (2012) OH-addition ring opening, although this is speculative. Given the large uncertainty, we will not focus on the NO_3 mechanism, although in several smog chamber experiments considered in Chapter 4, NO_3 contributes significantly to β-pinene oxidation.

2.2.2.4 β-pinene oxidation by $O(^3P)$

For β-pinene + $O(^3P)$ the reaction rate 2.7×10^{-11} $molecules^{-1}$ cm^3 s^{-1} is adopted. The product distribution follows Pinho et al. (2007), see Fig. 2.13.

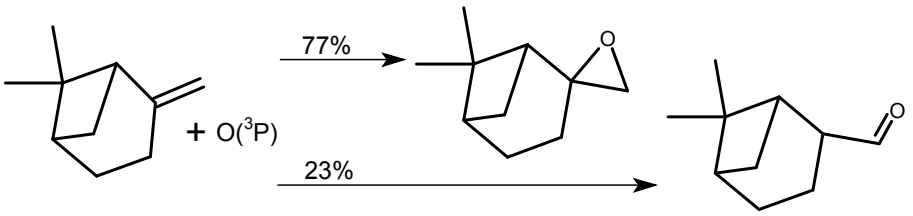

FIGURE 2.13: Reaction mechanism for β-pinene + O(^{3}P).

2.2.2.5 Chemistry of nopinone

Nopinone (also called pinaketone) is a major primary product of both β-pinene OH-oxidation and ozonolysis. Nopinone itself is expected to mainly react with OH or undergo photolysis in the gas phase. Two experimental determinations of the reaction rate with OH are available in the literature: $1.7 \pm 0.2 \times 10^{-11}$ molecules^{-1} cm^3 s^{-1} (Calogirou et al., 1999, adopted in BOREAM) and $1.43 \pm 0.37 \times 10^{-11}$ molecules^{-1} cm^3 s^{-1} (Atkinson and Aschmann, 1993). Product branchings in BOREAM are based on Lewis et al. (2005), who performed quantum-chemical calculations of the rates of the possible H-abstractions by OH using a density-functional transition-state calculation. Although their absolute rate is about a factor of two too low, we rely on the relative branching obtained in this study (Fig. 2.14). For the photolysis of nopinone, due to lack of specific data, we have applied the standard SAR for cyclic ketones to nopinone.

2.3 Generic chemistry

The generic chemistry system was introduced in Capouet et al. (2008), and further extended in Ceulemans et al. (2010, 2012). Generic species are used to represent classes of lumped multi-functional compounds. In the current version of the model, generic species are defined by their carbon number (from 10 down to 6) and by one explicit functional group. Other functional groups are not explicitly specified, although they have an impact on the volatility and reactivity of the compound. Therefore, the generic species are further subdivided into 11 volatility classes. Each class represents lumped organic compounds, which have a "parent compound" (the molecule resulting from replacement of the explicit functional group by one or more hydrogen atoms) with a saturated liquid vapour pressure $p^0_{\mathrm{L,parent}}$ falling within a given volatility class range. For the highest volatility class, indicated by the letter "a", $p^0_{\mathrm{L,parent}} > 10^{-1}$ Torr at 298 K. Class "b" contains species with 10^{-1} Torr $> p^0_{\mathrm{L,parent}} > 10^{-1.5}$ Torr, etc., and for the lowest volatility class "k", $p^0_{\mathrm{L,parent}} < 10^{-5.5}$ Torr.

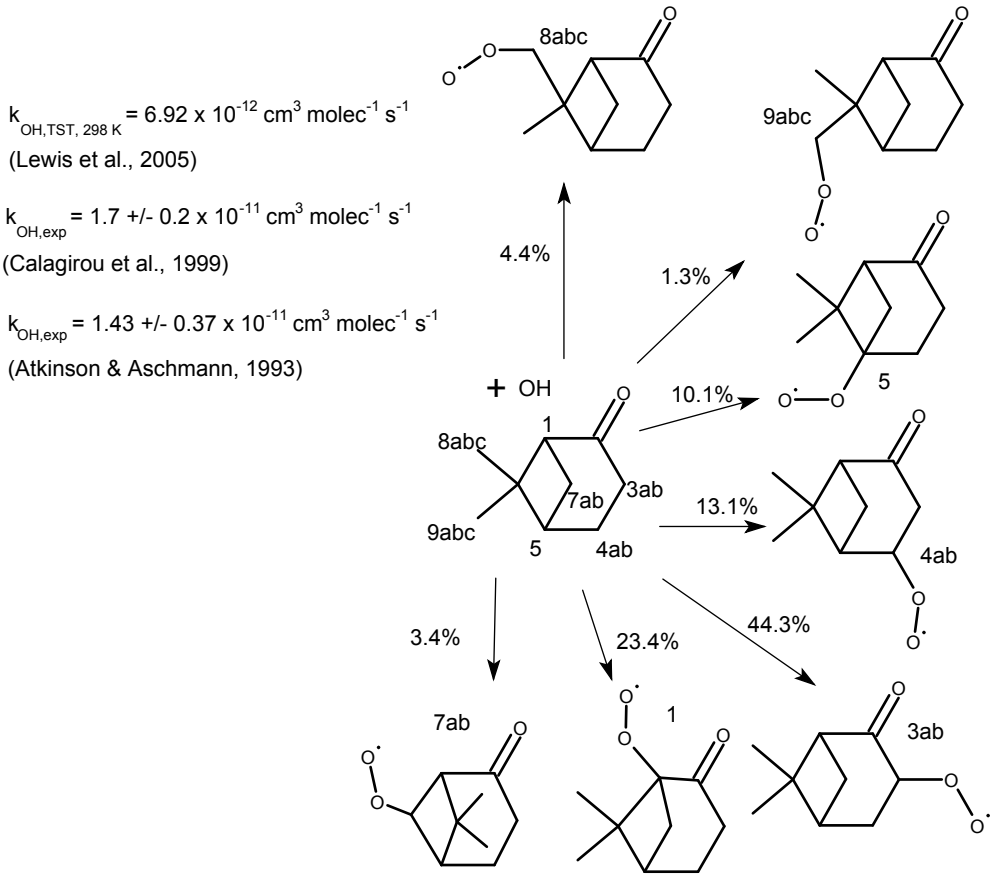

FIGURE 2.14: Hydrogen abstractions by OH from nopinone (Lewis et al., 2005). Product branchings are based on the calculated rates using DFT/transition state theory. For the absolute rate, the experimental value of Calogirou et al. (1999) was used in BOREAM.

In the model, the vapour pressure of a non-radical generic species is determined by the contribution of its explicit group (previously based on Capouet and Müller, 2006, now based on EVAPORATION) and the representative volatility class vapour pressure $p^0_{\mathrm{L,LX}}$, taken to be equal to the geometric mean of the vapour pressure range for each class at 298 K, e.g. $10^{-1.25}$ Torr for class "b", and $10^{-0.75}$ Torr for class "a" and $10^{-5.75}$ Torr for class "k". In our notation, a generic species name consists of the prefix "LX", the carbon number, the vapour pressure class symbol, and the explicit functional group. In total there are 55 classes (5 carbon numbers times eleven vapour pressure classes), besides the generic products with less than 6 carbon atoms, which are not considered for SOA formation, and lumped into a special generic class (with prefix "SX"). Each class includes 13 gas phase species: 3 radical species (alkoxy, peroxy and acyl peroxy) and 10 molecular species, and their chemistry is described by 86 reactions for each class (see Section A.1 in the Appendix).

Molecular generic compounds can react with the OH radical or undergo photolysis. The rates of reactions involving the explicitly represented functional group are obtained through structure activity relationships, as for the explicit molecular products. In order to account for the reactivity of the implicit part of the generic compounds, we base our assumption on the fact that generic species with lower vapour pressures are more functionalised, and therefore generally more reactive. On the basis of simple assumptions, described in Appendix A, the OH-reactivity and photolysis rates have been assigned. Whereas reactions such as photolysis or alkoxy-radical decomposition lead to a loss of carbon atoms or functional groups, other reactions might add functional groups to the implicit part of the molecule. In each case, the product of the reaction is assigned to the appropriate carbon number/volatility class.

TABLE 2.10: Illustration of generic alkoxy radical reactions included in BOREAM. R2R and RO3 denote peroxy radical counters (Capouet et al., 2004). The rates of these reactions are detailed in the Appendix.

LX10iO + O_2 →	LX10iCHO + HO_2 (1)
LX10iO →	0.60 LX9hO2 + 0.60 R2R + 0.20 LX9fO3 + 0.20 RO3 + 0.20 LX9bCHO + 0.20 OH + CH_2O (2.a)
LX10iO →	LX9dO2 + R2R + HCOOH (2.b)
LX10iO →	LX7bO2 + R2R + acetone (2.c)
LX10iO →	0.60 LX10kO2 + 0.60 R2R + 0.20 LX10kO3 + 0.20 RO3 + 0.20 LX10gCHO + 0.20 OH (3)

The generic alkoxy radicals can undergo three types of reactions (Table 2.10): reaction with O_2, leading to a carbonyl function (1), decomposition (2) or H-shift isomerisation (3). The reaction with O_2 usually has a reaction rate of typically 3-8 $\times 10^4$ s^{-1}. Three types of possible decomposition are considered: decomposition into an alkyl radical and CH_2O (which can occur for primary explicit peroxy radicals); formic acid elimination, (possible for explicit peroxy radicals containing an alcohol group); and acetone elimination. Other types of decomposition, for example breaking of a ring structure, are not considered. The branching fraction estimates are based on the reactions of the explicit alkoxy radicals present in BOREAM (see Capouet et al., 2004, 2008). It is found that decomposition is the most frequently occurring reaction, with H-shift isomerisation the second-most important fate. Decomposition of alkoxy radicals is favoured by the presence of oxygenated functional groups, and often more so than H-shift isomerisations, for which the rate can even be decreased due to presence of certain functional groups (Vereecken and Peeters, 2009, 2010). It is therefore assumed that lower volatility generic compounds, which generally represent more functionalised species, have a higher branching towards decomposition. Among the decompositions, type (2.a) (Table 2.10) is most common. The implicit part of the generic species changes upon decomposition or H-shift

isomerisation. In particular, the product generally belongs to a different volatility class than the reactant. This is illustrated with two examples from Table 2.10.

In Reaction (2.c), the reactant loses three carbon atoms and one alcohol functionality, leading to an expected increase of $p^0_{\mathrm{L,parent}}$ of 3.5 orders of magnitude (Capouet and Müller, 2006). Since one vapour pressure class spans a $\log(p^0_{\mathrm{L,parent}})$ range of 0.5, the product in our example moves up 7 volatility classes, from class "i" to class "b". On the other hand, for H-shift isomerisation (Reaction (3) in Table 2.10) the alkoxy radical abstracts an H-atom from another carbon, leading to a hydroxy alkyl radical (Vereecken and Peeters, 2010). This radical can react with oxygen, forming a peroxy radical ("LX10kO2"), which becomes the explicitly represented group. The alcohol function is included in the implicit part of the generic species, reducing its volatility, so that it moves from class "i" to the lowest vapour pressure class "k". When the alkyl radical contains a primary carbonyl function, it forms an acyl peroxy radical ("LX10kO3") after reaction with oxygen. If instead it contains an α-hydroperoxide, nitrate or alcohol function, it will decompose into an aldehyde. The implicit part of the generic species then loses a functional group, so that the product volatility is increased ("LX10gCHO"). For peroxy and acyl peroxy radicals, the same scheme is used as for their explicit counterparts. All generic alkyl peroxy radicals are assumed to have the reactivity of secondary alkyl peroxy radicals.

The fact that the precise structure of the generic compounds is not defined makes it difficult to determine certain molecular properties, such as elemental composition (determining molecular mass and O to C ratio), or activity coefficients. To address this issue, we determined, for each generic species, a small number of different explicit structures, having the same estimated saturated vapour pressure, carbon number and explicit functional group. These proxy structures are then used to determine the contribution of generic compounds to elemental composition and activity coefficients. This is clearly a crude approximation, but at least it takes into account the fact that generic species with lower vapour pressures tend to be more oxygenated.

The generic chemistry scheme contains the implicit representation of a very large number of chemical reactions which the further generation products are expected to undergo. It is based on choices for rate constants, made on the basis of analogy with other mechanisms, such as the explicit primary chemistry of α-pinene. The assumed reactivity of the generic species remains, however, among the largest sources of uncertainty in our model. This uncertainty is explored through sensitivity tests presented in Sections 3.2 and 6.4.5.

2.4 Aerosol physics and chemistry

2.4.1 Representation of the aerosol particles

The physical representation of the aerosol phase is kept very simple in BOREAM. The focus is laid on chemical processes leading to the condensation of VOC oxidation products and the subsequent growth of aerosol. In the current model version, the number concentration of aerosol is fixed during the entire simulation, and all particles are assumed to have an identical diameter, which is variable throughout the experiment. Aerosol processes such as particle formation and coagulation are not represented. In the real world, particles are distributed over a range of different diameters, which vary through nucleation, coagulation, condensation and deposition, as was shown in Section 1.6.1. However, in most cases the aerosol particle diameters in smog chamber experiments are distributed in a well-defined mode around a variable peak diameter. If the diameter of the single diameter distribution used in BOREAM is close enough to the peak diameter of the real aerosol distribution, then the average difference between the real diameters and the single value adopted in the model will be limited.

In many smog chamber experiments, after the initial particles have formed and coalesced to a certain size (say above 10 nm), absorptive partitioning of condensable species is the dominant process of aerosol growth. As will be seen in Subsection 2.4.2, the equilibrium between aerosol and gas phase concentrations depends on the total mass of the absorbing organic material (Pankow, 1994) as long as adsorption processes may be deemed unimportant. Even if the number and diameter distribution of the particles in the model is biased, as long as the total absorbing mass is still correct, then also the equilibrium that is reached between gas phase and aerosol phase will be correct, according to absorptive partitioning. Other processes are however dependent on the surface area of the aerosol particles. Examples are the kinetic rates of uptake and escape of molecules between gas and aerosol phase, which can be of importance when equilibrium has not been reached. As will be seen in the next section, processes such as particle deposition on chamber walls and heterogeneous chemical processes taking place at the surface of aerosol particles are dependent on the aerosol surface. Therefore, if the modelled average diameter deviates much from the real particle diameter distribution, there could be substantial errors in the parameterised effects of these processes.

Organic compounds are represented in the model through separate species in the gas phase and in the aerosol phase. This allows kinetic modelling of the partitioning. Aerosol particles in BOREAM are assumed to be liquid and perfectly mixed, and they have an identical composition. Recent research has indicated that this assumption might

not always hold. Zobrist et al. (2008) showed that under certain circumstances (low temperatures, low relative humidity, high molecular weight compounds) aerosol particles show properties which correspond more to glasses than to perfect liquids, due to high viscosity. Virtanen et al. (2010) showed that in smog chamber experiments and in real atmospheric biogenic SOA, some particles bounced off surfaces upon impact, which is evidence of an amorphous solid state, compared to a perfect liquid state, which would lead to particles sticking on the surface. Such high viscosity will hinder mixing, causing concentration differences within the aerosol particles, which in turn could have a strong impact on partitioning (Virtanen et al., 2010).

BOREAM currently does not contain a representation of particle nucleation, although many experiments start from nucleation, i.e. no seed particles are used. According to the partitioning theory of Pankow (1994), a non-zero initial absorbing mass is required in order to allow the onset of partitioning. In such cases it is assumed in BOREAM that the initial particles have a small diameter (equal to 7.5 or 10 nm), and a particle number typical of that which was observed during the course of the experiment. Particles typically grow to sizes of one hundred or several hundreds of nm. The mass of the initial particles used to set off partitioning is then generally negligible compared to the total organic mass of the aerosols, and therefore the impact of the initial particle number and diameter on final SOA mass is expected to be small. However, at the onset of the simulation, the deviations between the model and the experiment could be much larger. This mostly plays a role in very short experiments, such as for example in von Hessberg et al. (2009) in Chapter 4, or when the aerosol mass is very low, as in some experiments at high temperature (see for example the experiments of Pathak et al., 2007, in Chapter 3).

If seed particles are used in the experiments, the reported amount of particles is introduced at the start of the experiment in BOREAM. In the case of inorganic seed at relatively low relative humidity, these seeds are expected to be solid, and the partitioning of organic vapours to the seed aerosol should follow adsorptive, instead of absorptive partitioning (Pankow, 1994). However, data on the physical parameters needed to represent the adsorption of organic vapours on inorganic surfaces is lacking. Initially in BOREAM the hypothesis was adopted that the total inorganic mass could be included in the absorptive mass of absorptive partitioning. This unrealistic enhancement of the absorptive mass might lead to overestimations of the organic aerosol mass. Cocker III et al. (2001) showed that the presence of inorganic seed did not enhance absorbed organic mass compared to nucleation experiments. Therefore, in an alternative setting, we assume a low initial aerosol diameter and mass, similar to the assumption for nucleation. This allows the onset of partitioning to the aerosol phase, which in reality is made possible through the adsorption process. This model deficiency will mostly only play a

role at the early stages of smog chamber experiments, before absorption becomes the dominant partitioning process.

2.4.2 Partitioning between gas phase and aerosol phase

The partitioning between aerosol and gas phase makes use of the absorption theory of Pankow (1994), in which the equilibrium constant $K_{p,i} = C_{p,i}/C_{g,i} \cdot M_O^{-1}$ determines the ratio of the particle and gas phase concentration of species i, which is also dependent on the total absorbing organic aerosol mass concentration M_O (in μg m^{-3}). This partitioning constant can be calculated through the formula

$$K_{p,i} = \frac{760 \cdot RT \cdot f_{\text{om}}}{\text{MW}_{\text{om}} \cdot 10^6 \cdot \gamma_i \cdot p^0_{L,i}} \tag{2.17}$$

where R is the gas constant (atm m^3 K^{-1} mol^{-1}); T is temperature (K); MW_{om} is the molecular weight of the absorbing medium (g mol^{-1}); f_{om} is the weight fraction of organic matter in the total aerosol; γ_i is the activity coefficient of compound i in the particulate phase; $p^0_{L,i}$ is its subcooled saturated vapour pressure (here in Torr), and 760 (Torr atm^{-1}) and 10^6 (μg g^{-1}) are unit conversion factors.

The partitioning of a species X between the gas phase and the organic aerosol (OA) is modelled kinetically through a condensation and evaporation reaction, based on the method proposed by Kamens et al. (1999):

$$\text{X} + \text{OA} \rightarrow \text{X}_p + 2\,\text{OA} : k_{\text{on},i} \tag{2.18}$$

$$\text{X}_p \rightarrow \text{X} - \text{OA} : k_{\text{off},i}. \tag{2.19}$$

The forward condensation rate k_{on} is parameterised following Lelieveld and Crutzen (1991), Capouet et al. (2008):

$$k_{\text{on}} = \frac{\text{MW}_{\text{om}}}{\rho N_{\text{Avo}}} \times \left(\frac{a^2}{3D_g} + \frac{4a}{3\omega\gamma} \right)^{-1}, \tag{2.20}$$

where MW_{om} is the average molecular weight of the absorbing organic material, ρ is its density, a is the particle radius, D_g is the diffusivity in the gas phase (based on Fuller et al., 1969), ω is the mean gas phase molecular speed, and γ is the dimensionless mass accommodation coefficient, which expresses the probability of uptake upon collision. A value of 0.3 has been assumed, based on the value deduced by Bowman et al. (1997), although the precise value of γ remains highly uncertain. The desorption reaction rate is calculated through

$$K_{p,i} = \frac{k_{\text{on},i} \cdot N_{\text{Avo}}}{\text{MW}_{\text{om}} \cdot 10^{12} \cdot k_{\text{off},i}}. \tag{2.21}$$

The methods for estimating the saturated vapour pressures and activity coefficients of compounds in the aerosol phase are discussed in the next sections.

2.4.2.1 Vapour pressure estimation

The EVAPORATION method (Compernolle et al., 2011) is used to estimate the saturated liquid vapour pressure $p^0_{L,i}$ as a function of temperature for the semi-volatile species in BOREAM. In this method, contributions from the carbon skeleton, the functional groups and intramolecular interactions between groups, occurring in multi-functional compounds, are taken into account. A comparison with other recent group contribution methods (Capouet and Müller, 2006, Pankow and Asher, 2008, Nannoolal et al., 2008) against compounds of the experimental data set used for the fitting showed that the deviations are lowest for the EVAPORATION method. The largest deviations were obtained for diacids. For hydroperoxides, peroxy acids and peroxy acyl nitrates, only few saturated vapour pressures are known, and almost none for multi-functional species, such that the uncertainties on their group contributions in all methods are expected to be important.

The results presented in Chapters 3 and 6 were obtained by using the earlier and simpler method of Capouet and Müller (2006) (as described in Ceulemans et al., 2010, 2012). EVAPORATION was applied in the simulations described in Chapters 4 and 5, both in the mechanism generation and for estimation of vapour pressures of explicit model species. Although the use of either EVAPORATION or the method of Capouet and Müller (2006) leads to some quantitative differences, the differences between these two methods are small enough that the main conclusions remain unchanged.

2.4.2.2 Activity coefficient calculation

The activity coefficients γ_i are calculated at each model time step using the method described in Compernolle et al. (2009), covering most relevant atmospheric functional groups. This is an adapted version of UNIFAC (Fredenslund et al., 1975), as formulated by Hansen et al. (1991), and with some parameters determined by Raatikainen and Laaksonen (2005). Water uptake is also considered by the model.

As described above, the calculation of activity coefficients for generic species relies on the use of proxy compounds. It is acknowledged that the choice of the proxy molecules implies some arbitrariness, as the true composition of the generic species classes is not known, and can vary from experiment to experiment.

2.4.3 Heterogeneous and aerosol phase chemistry

Heterogeneous and aerosol phase chemistry can have an important impact on SOA composition, for example through the formation of oligomers (Hallquist et al., 2009, Ziemann and Atkinson, 2012). Although the formation of peroxy hemiacetals through reactions of aldehydes and hydroperoxides was investigated using BOREAM (Capouet et al., 2008), their rates remain quite uncertain, and these reactions are not considered in the standard version. Recent work by Shiraiwa et al. (2013b) showed, however, that upon addition of tridecanal to oxidation products of dodecane, SOA mass increased strongly due to peroxyhemiacetal formation, which modelling with the KM-GAP model suggested occurs at the particle surface. Even without extra addition of aldehydes, this process could be of importance. Other oligomer forming reactions, such as hemiacetal formation, aldol condensation, esterification and polymerisation were shown to occur in SOA under the influence of acid catalysis (Jang et al., 2002, Ziemann and Atkinson, 2012), but at reaction rates which are still poorly characterised (see the review of Ziemann and Atkinson, 2012).

Organosulfates have recently been identified by several groups as important aerosol constituents, both in lab and ambient aerosols (Iinuma et al., 2007, Surratt et al., 2007, 2008, 2010, Eddingsaas et al., 2012a, Hansen et al., 2014). They are presumably formed in the aerosol phase from biogenic VOC oxidation products which interact with acidic inorganic seed, containing H_2SO_4. Their formation may take place through reactions between alcohol or carbonyl groups (Surratt et al., 2007) or epoxide groups (Iinuma et al., 2007) with H_2SO_4. The kinetics of these reactions are still poorly understood, which has prevented inclusion of organosulfate formation in the BOREAM model, but consideration in future model versions is certainly desirable. The importance of organosulfates seems to be restricted to experiments with acidic seed, however (Eddingsaas et al., 2012a), so this omission is less important for most experiments considered in this work.

Other studies have focused on OH-oxidation of the aerosol phase (Smith et al., 2009). This process is neglected, as sensitivity tests indicate that it has only a minor impact on SOA yields due to kinetic limitations under atmospheric conditions (Hildebrandt et al., 2010). However, for long term SOA ageing it could still be of importance.

In previous modelling studies, the photolysis of species in the aerosol phase was generally ignored, due to lack of data, and because the further chemistry of radical products in the aerosol is poorly understood. Several studies (Walser et al., 2007, Pan et al., 2009) have shown that the photolysis of oxygenated organic compounds in the particulate phase is far from negligible. In Mang et al. (2008) the photolysis of carbonyls in limonene SOA was

investigated, and estimates of the quantum yield and absorption spectra for the carbonyl compounds in the SOA led to an estimated lifetime of about 6 hours for a zenith angle of 20°. The present model version includes aerosol phase photolysis, with identical j-values and product distributions as in the gas phase, due to lack of experimental data on aerosol phase absorption cross sections and quantum yields. The inclusion of photolysis of aerosol species is justified in view of the above evidence that most species which photolyse in the gas phase, also do so in the liquid phase, although the precise impact of the phase (gas vs. aerosol) on absorption cross sections and quantum yields remains largely unknown. The most important simplification in the current implementation of photolysis in the aerosol is the fact that we take the same product distribution as for gas phase photolysis, meaning that the products are assumed to appear in the gas phase. This is probably a large deviation from the true chemical fate, especially for radical species which are expected to react with other molecules or radicals in the liquid organic phase, through reactions which might be specific to the aerosol phase. Tests with BOREAM show, however, that even with the present formulation, aerosol photolysis has a significant effect on SOA yields in experiments of sufficiently long duration. Therefore, notwithstanding the limitations of the present aerosol photolysis mechanism, its inclusion should still be more realistic than a complete omission of this possibly important process. Most previous SOA studies, using either detailed mechanisms, such as the MCMv3.2 model (Saunders et al., 2003) or GECKO-A (Valorso et al., 2011), or parameterised models such as the VBS model (Jimenez et al., 2009, Donahue et al., 2012), have not considered the photolysis of SOA species.

2.4.4 Wall loss processes

Wall losses can have very important effects on final suspended SOA masses, either through particle deposition or transfer of vapours to the wall, which otherwise might have partitioned to the aerosol phase (Park et al., 2001, Pierce et al., 2008, Hallquist et al., 2009, Matsunaga and Ziemann, 2010, Donahue et al., 2012). Many experimental studies have attempted to quantify the amount by which particulate or gas phase wall losses affect reported yields. Neglecting wall losses in the analysis of experimental data could lead to a serious underestimation of SOA yields.

Wall losses are often estimated by fitting an exponential decay function to the time-dependent decreasing SOA concentration in the chamber. This implicitly assumes a time-independent wall loss rate, and a constant SOA concentration had wall losses not been present (therefore assuming that chemistry and partitioning have reached an equilibrium). This assumption has been applied in many previous studies, such as Presto et al. (2005b,a), Pathak et al. (2007, 2008) and Pfaffenberger et al. (2013).

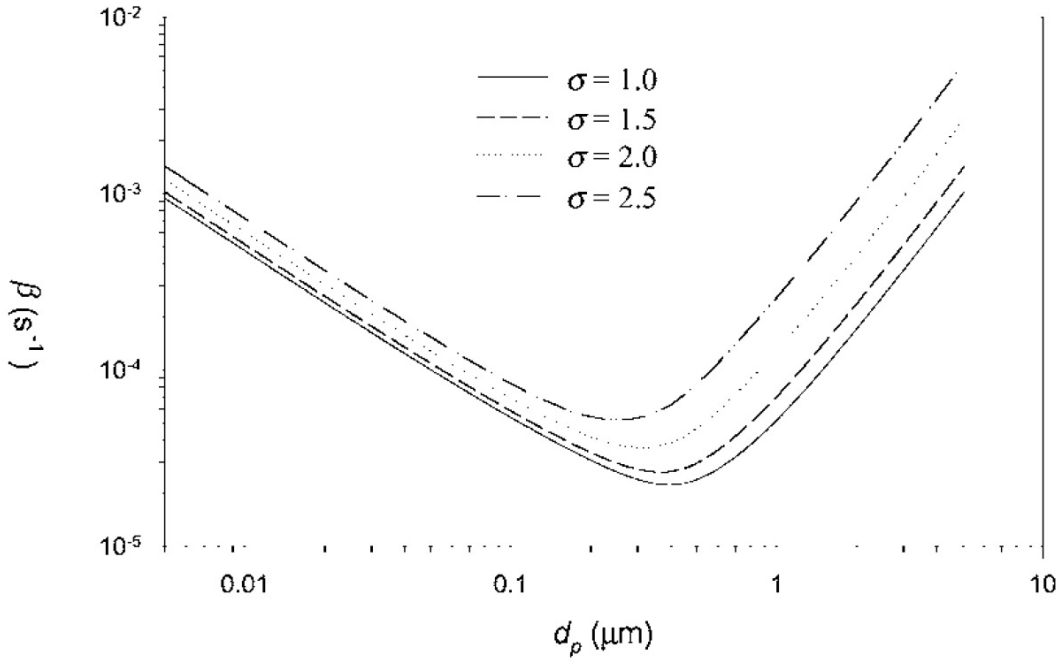

FIGURE 2.15: Typical dependencies of wall loss rates (β, in s^{-1}) on diameter (d_p), on a log/log scale, in Fig. 2, taken from Park et al. (2001).

However, it has long been known that particulate wall losses are dependent on particle size — i.e. on diameter for spherical particles (Crump et al., 1982, Park et al., 2001, Keywood et al., 2004). In Park et al. (2001), wall losses were studied both experimentally (using inorganic particles) and theoretically, taking into account the effects of diameter distributions in the aerosol phase. From Fig. 2.15, it can be seen that for very small diameters (below 10 nm), the logarithm of the wall loss deposition rate β decreases linearly with respect to the logarithm of the diameter, until around 200–300 nm this linear dependence breaks down, and a minimum is reached around 300 to 400 nm. For higher diameters, a linear increase of the logarithm of β in function of the logarithm of the diameter sets in. Therefore, wall losses could be significantly faster at the start of the experiment, when diameters are smaller, than near the end of the experiment. This can cause an underestimation of wall losses for experiments assuming a constant wall loss rate. Measured SOA was corrected by Ng et al. (2007a) and Eddingsaas et al. (2012a) based on wall loss rate measurements for different diameters by Keywood et al. (2004).

SOA particles deposited to the walls during the course of a smog chamber experiment remain in contact with the air in which the semi-volatile VOC oxidation products are present, therefore it can be assumed that particles on the wall continue to participate in gas/particle phase partitioning (Hildebrandt et al., 2009, Donahue et al., 2012). Just as

suspended particles grow due to the partitioning of organic vapours, these vapours also partition to wall-deposited particles, causing these to grow as well, at the expense of the suspended particles. As argued by Hildebrandt et al. (2009), this transfer of semi-volatile vapours to wall-deposited particles represents a third wall loss process, together with the loss through direct deposition of particles to the wall (be it with a diameter-dependent or independent rate), and the direct deposition of gas phase vapour molecules on the wall surface. Wall losses estimated by fitting an exponential decay function to observed suspended SOA mass concentration do not take into account the above described additional loss of organic material to the wall, leading to an underestimation of true experimental wall losses.

In BOREAM, we have chosen to conduct a first simulation neglecting wall losses, and obtain the SOA mass concentration $M_{O,\text{total}}$ from this simulation. The estimated diameters are tracked in this simulation. In a second simulation, the number of particles deposited to the wall, $N_{\text{dep.}}$, is calculated, using a diameter-dependent rate based on Park et al. (2001). We also assume that wall-deposited particles participate in gas/particle partitioning, just like the suspended particles, and therefore wall-deposited and suspended particles have the same average diameters, similarly as in Donahue et al. (2012) and Hennigan et al. (2011). We then calculate the mass concentration of the wall-deposited particles as $M_{O,\text{total}} \times N_{\text{dep.}}/N_{\text{total}}$, where N_{total} is the total number of particles, both suspended and deposited on the wall. Note that recent studies have taken advantage of the use of inorganic seed particles, in order to infer wall losses from the observed ratio of inorganic seed to organic material in the particles (Henry and Donahue, 2012).

The quantitative impact of gas phase wall losses has even more uncertainty than particle wall losses. McMurry and Grosjean (1985) showed that certain gas phase species are deposited in significant amounts onto the Teflon walls of smog chambers. Most studies on SOA formation from monoterpenes do not provide quantitative estimates of possible gas phase deposition rates to walls during the experiments. Given the lack of quantitative data this process has not been implemented yet in such cases.

There are indications that the material which makes up the wall surface is important in determining the wall loss rate. Salo et al. (2011) reported important wall losses of carboxylic acids to the aluminium wall of the AIDA chamber, which have been implemented in BOREAM (see Chapter 5). Matsunaga and Ziemann (2010) studied the partitioning of gas vapours (alkanes, alkenes, 2-alcohols and 2-ketones) to the walls of a small Teflon chamber, providing proof that this process is of importance, and cannot easily be ignored. They suggested that this process occurs according to an equilibration process, similar to the partitioning of semi-volatile species between the absorbing aerosol mass and the gas phase. For 10-carbon containing molecules, only a small fraction

(±5%) partitioned to the wall, but for 2-alcohols and 2-ketones with 12 or 13 carbons, this fraction rose to about 20% and 50% respectively (Matsunaga and Ziemann, 2010). For monoterpene oxidation, semi-volatile compounds partitioning to the SOA are mostly multifunctional, and have larger atomic mass and lower volatility than the 13-carbon compounds found to partition to the wall. As suggested by Matsunaga and Ziemann (2010), more experimental data on different relevant compounds will be needed before the true impact of gas phase wall losses can be estimated. This gas phase equilibration to the Teflon walls has been implemented in a recent aerosol chemistry and physics model, ADCHAM (Roldin et al., 2014) and in the KM-GAP model (Shiraiwa et al., 2013b), although the used deposition rates also remain highly uncertain in these models.

Especially for long-duration SOA ageing smog chamber experiments, wall losses can have large effects. In a SAPHIR chamber experiment (Salo et al., 2011), suspended SOA yields after one day were less than one seventh of the estimated SOA yields corrected for wall loss of particles. Donahue et al. (2012) found similar wall losses for ageing experiments modelled with the 2D-VBS model. The problem with such large wall losses is that their uncertainties can eclipse differences in actual SOA formation between the experiment and models. In Chapter 5 we will estimate wall losses in α-pinene SOA ageing experiments modelled with BOREAM.

2.5 Model implementation

In this Section some more technical points of the implementation of BOREAM are discussed. We will describe how the chemical information on compounds is stored, how secondary chemistry equations are generated, and how the chemical mechanism is used to calculate the time evolution of the concentration of species and aerosol.

2.5.1 Chemical species representation and naming convention

During both the implementation and simulation of chemical mechanisms, it is necessary to have the information on the structure of the considered chemical compounds available, and to store this information for later use. A great number of data structures and tools has been devised with this aim within the field of cheminformatics, which combines methods from computer science and chemistry (Wild, 2009). When dealing with detailed chemical mechanisms, such techniques are necessary so that rate constants or thermodynamic properties can be estimated based on structure. For large models, mechanism generation based on an automatic approach which makes systematic use of coded

Table 2.11: Carbon atom connection matrix and organic functional group matrix, for the molecule shown in Fig. 2.16 .

1	1	0	0	0	0	0	0	4	0	0
1	1	1	0	0	0	1	0	0	0	0
0	1	1	0	1	1	0	0	9	0	0
0	0	0	1	0	0	0	0	10	5	0
0	0	1	0	1	0	0	0	0	0	0
0	0	1	0	0	1	0	0	0	0	0
0	1	0	0	0	0	1	1	0	0	0
0	0	0	0	0	0	1	1	8	5	0

Table 2.12: Functional group matrix entries, with their number coding in BOREAM.

Functional group	Group structure	code
Alkyl radical	$^{\bullet}$	1
Alkoxy radical	-O$^{\bullet}$	2
Peroxy radical	-O-O$^{\bullet}$	3
Alcohol	-OH	4
Carbonyl	=O	5
Hydroperoxide	-O-OH	6
Nitrate	-ON(=O)=O	7
Peroxy nitrate	-OON(=O)=O	8
Ether bond, on 1st C	-O-	9
Ether bond, on 2nd C	-O-	10
Peroxide bond, on 1st C	-O-O-	11
Peroxide bond, on 2nd C	-O-O-	12
Nitrite	-O-N=O	50

chemical structure is superior to hand-writing equations, for reasons of speed, reliability, reproducibility, and maintenance (Aumont et al., 2005).

2.5.1.1 Connection tables and functional group matrix

Chemical structure can be represented in the form of a connection table, a data structure which has been used since the onset of cheminformatics. Aumont et al. (2005) used a connection table to represent chemical species in the GECKO-A model (Valorso et al., 2011). This approach has been used in BOREAM, since the model version used in Ceulemans et al. (2010). In this approach, a carbon bond matrix represents the carbon backbone structure (see Table 2.11). In a second matrix the presence of oxygenated functional groups is given for each carbon atom (Aumont et al., 2005).

The coding system for the functional group matrix used in BOREAM is shown in Table 2.12. Oxygenated bonds within the carbon backbone structure, such as ether or peroxide bonds, are indicated on both carbon atoms connected to the ether or peroxide oxygen.

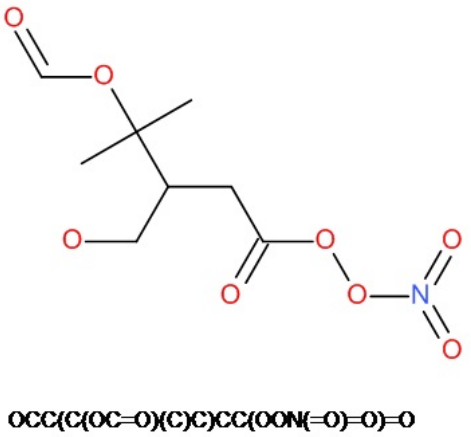

FIGURE 2.16: Example of the structure of a multi-functional compound, present in β-pinene SOA, for which the carbon bond matrix and functional group matrix are given in Table 2.11 .

The carbon bond matrix and functional group matrix for an example species (Fig. 2.16) is shown in Table 2.11. In the carbon matrix on the left, the off-diagonal elements indicate the presence of carbon bonds (1, 2 or 3 for single, double, or triple bonds). In the functional group matrix, each row can contain up to 3 non-zero numbers, of which the meaning is indicated in Table 2.12.

The functional group matrix allows efficient searching of SAR groups. For some applications, such as the determination of cycles within a molecule or for naming systems such as SMILES, a full connection matrix indicating all bonds between non-hydrogen atoms explicitly is more useful, and therefore also used in BOREAM.

Stereochemistry is not stored explicitly in BOREAM. When a distinction between different geometric configurations is important, and leads to different reaction rates, we use a flag indicating whether the compound is in a syn- or anti-configuration, for example. Similarly, another flag is used to distinguish between activated or stabilised radicals. Also, since partitioning is modelled kinetically, the gas-phase and aerosol-phase compounds are distinguished by a flag.

2.5.1.2 Naming and canonicalisation of species representation

Most models require a naming convention for chemical species. In BOREAM the SMILES notation is used (Weininger, 1988). A SMILES (Simplified Molecular Input Line Entry System) name is a character string indicating the atoms and bonds contained in a molecule. Atoms connected to one another are written next to each other, and brackets are used to indicate branches in the molecular structure, while numbers at both ends

of connected cyclic atoms can be used to represent ring structures (see for example the SMILES name for α-pinene in Fig. 2.2). Hydrogen atoms are generally ignored, but if necessary they can be indicated, for example in order to allow the representation of radicals. There are also extensions which allow the representation of stereo-information, but in BOREAM no use is made of these for now.

The same molecule can be represented by a large number of valid SMILES-names, depending on the order in which one decides to step through the molecule. A canonicalisation procedure, proposed by Weininger et al. (1989), assigns ascending numbers to non-symmetric atoms in the molecule, which are determined by various structural criteria. A depth-first search is then performed, in which branches are walked through first or later, depending on the aforementioned ordering. A canonicalisation based on this algorithm was implemented in BOREAM and its mechanism generator through a number of Fortran subroutines, in order to make sure that each molecule can be uniquely identified by means of this canonical SMILES. Some drawbacks to the canonized SMILES system remain. One is that various implementations differ in the details of the canonicalisation implementation, due to some ambiguity in the original description of the algorithm. This has led to different canonical SMILES being used in models or software packages. Some community-wide cheminformatics projects, such as Open Babel (O'Boyle et al., 2011) provide standardised implementations. A second drawback is that in some rare cases, the canonicalisation of Weininger et al. (1989) can still fail (O'Boyle, 2012). Since 2006, there is also a IUPAC-endorsed canonical naming system, named InChi (IUPAC, 2011), which is based on a rigorous canonicalisation algorithm, but which is less intuitive than the SMILES naming system. For the species in BOREAM, the SMILES canonicalisation is sufficient. Both notation systems remain widely used in the chemistry community. Recently O'Boyle (2012) has shown how the InChi canonicalisation can be used to produce rigorously canonical SMILES.

2.5.2 Chemical mechanism generation

The BOREAM mechanism is built up starting from the explicit chemical mechanisms discussed in Sections 2.1 and 2.2. For the further reactions of the products generated in these chemical mechanisms, we rely on the SARs to determine the relevant reactions. The approach used in this generation is adopted from Aumont et al. (2005), of which Figs. 1 and 2 give a good overview of the adopted algorithm. First, a list is made of the species which are produced in the primary chemistry, but which have not been treated yet in the mechanism. For each of these compounds, the chemical equation generator selects the appropriate SARs, and adds their reactions to the mechanism. Reaction products which have not been treated yet are added to the to-do list of species

to be treated. This process is continued until all possible products have been treated. However, this will lead to mechanisms with millions of chemical compounds, as a large number of combinatorially possible molecular configurations can be produced through the continued gas phase oxidation. Aumont et al. (2005) showed that for n-alkanes the order of magnitude of the number of compounds in the explicitly generated mechanisms by GECKO-A increased linearly with alkane size, and already reached more than 10^6 for n-octane. Extrapolating this to n-decane, of the order of 10^8 species might be produced. Given the larger complexity of the structure of the monoterpenes, this number might be a lower limit. The number of chemical equations is approximately an order of magnitude higher than the number of species. Such vast models would be computationally very expensive to generate, and even more difficult to solve.

In the GECKO-A model, this problem has been addressed by the lumping of species which have relatively low yields and which are sufficiently similar in reactivity and volatility (Valorso et al., 2011). Additionally, nearly non-volatile species were excluded from the mechanism. For α-pinene, this led to mechanisms with around 5×10^5 species. The continuity equation of the chemical compounds was solved using the Two-step solver (Verwer, 1994, Verwer et al., 1996, Valorso et al., 2011).

In BOREAM, the KPP preprocessor and solver are used, which have more severe limitations on the number of species, but the generic chemistry scheme discussed previously made it possible to reduce the number of species to acceptable levels. In the latest model version, aimed towards the simulation of ageing experiments, this is performed in the following way. The chemical equation generator is used to determine the reactions of the non-treated primary products of the mechanism. In a first step, the newly formed secondary products that still have to be treated are substituted by the appropriate generic species. These reactions are added to the primary chemistry scheme, and this first model version is subsequently used in BOREAM to simulate a number of different α-pinene oxidation experiments in various conditions. In these simulations, the reaction fluxes through each equation are estimated. These reaction fluxes are used to determine which equations contribute most to the production of generic species. This ranking is then used to design a new, extended version of the BOREAM mechanism. The explicit products formed in the reactions which contribute most to the generic compound production are added to the list of BOREAM species, and the mechanism generator is used to write their reactions in this new version. Several iterations of this procedure are required to significantly reduce the contribution of generic species to the gas phase chemistry and SOA. For α-pinene, this procedure was applied 5 times, after which version 6 is obtained. Afterwards, a number of unused equations in the generic chemistry were dropped, and a small number of additional compounds, which previously were substituted by generic species, were still included explicitly. This led to a mechanism (version 7) with 91,070

equations and 10,493 species. At that stage, the current limitations of the KPP-solver are reached.

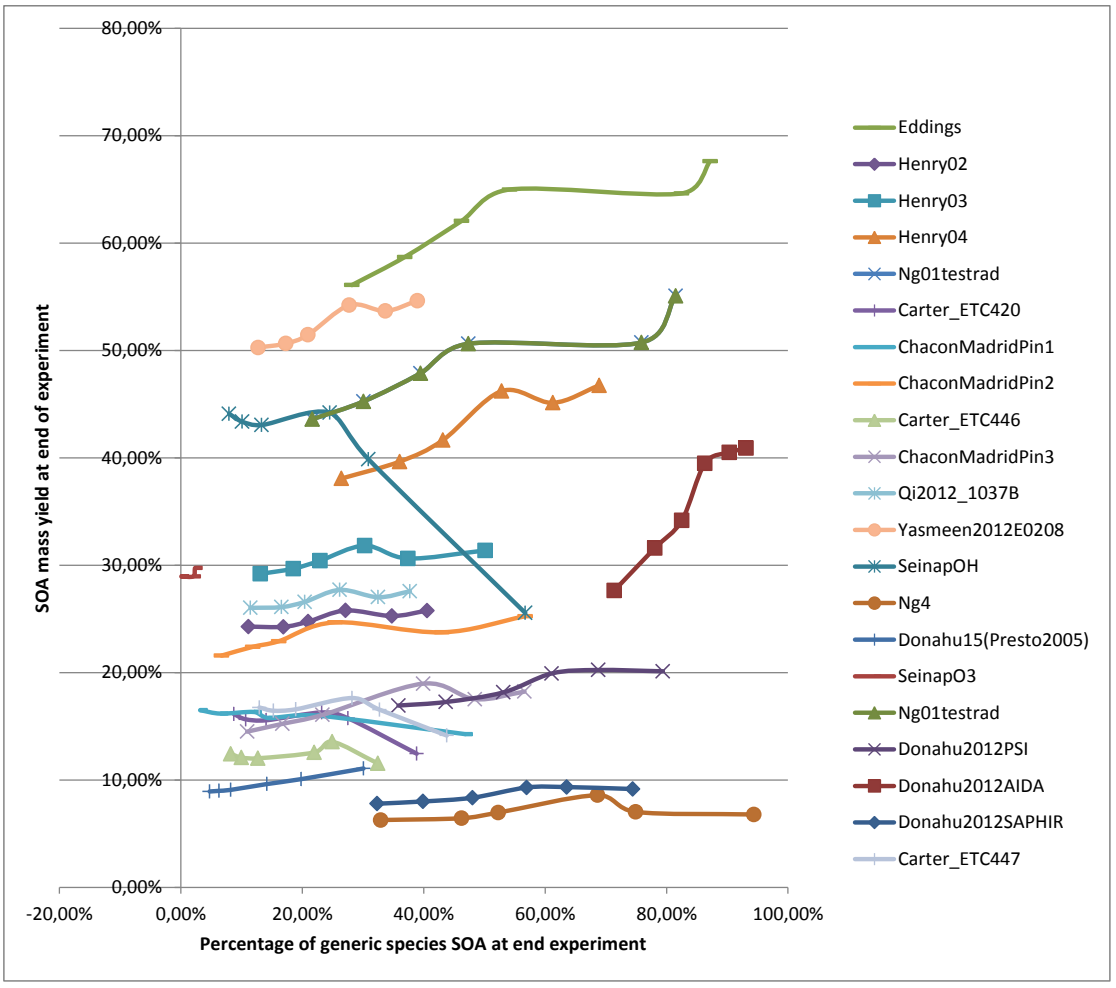

FIGURE 2.17: Simulated SOA mass yield at the end of each experiment versus percentage of generic species in the SOA, for the first six versions of BOREAM (see Table 2.13, see the text for details) and for the experiments labelled on the right (see Chapters 3 and 5 for details on these experiments). The highest (lowest) percentage of generic species is always achieved by version 1 (version 6).

For the simulations of the α-pinene oxidation experiments with the different BOREAM mechanism versions (1 to 6), the relative contribution of generic species to total SOA and the SOA mass yield calculated at the end of each test simulation is shown in Fig. 2.17 for the different model version iterations during the mechanism generation. These experiments will be discussed in more detail in Chapter 5.

As shown by Fig. 2.17, a strong reduction of the generic contribution to SOA was achieved when moving from version 1 to 6, in most cases reducing this contribution from 50–90% to 10–30%. Some variation is seen in the SOA yields between different ageing versions (of the order of 10% in absolute yield in most cases), but when moving from version 4 to 6, this variation is relatively mild for most experiments. This can be

TABLE 2.13: Number of species and equations for the iteratively extended BOREAM versions for α-pinene SOA ageing.

BOREAM ageing version	1	2	3	4	5	6	7
Number of species	3286	4103	5116	6471	8114	10401	10493
Number of equations	22116	31131	39449	51722	67103	89123	91070

seen as evidence that the generic chemistry does not tend to cause very large deviations compared to more explicit mechanisms. These deviations are probably smaller than other uncertainties on the modelled SOA yields, caused by for example uncertainties in the primary chemistry or in the SARs for explicit compounds, for which evidence is found in simulations of experiments in which the number of generic species is limited (see Chapters 3 and 4).

It should be noted that Chapters 3 and 6 made use of two other, earlier BOREAM versions, described in Ceulemans et al. (2010) and Ceulemans et al. (2012), which treated ageing less extensively, and contained higher contributions of generic species. In these versions, the primary products were treated using the SARs, but for most compounds, the formed secondary products were substituted with generic compounds. These previous versions therefore largely correspond to the current version 1. In the previous versions, only for specific primary products with important yields, such as pinonaldehyde, was the secondary chemistry implemented more explicitly. This is mainly of importance for Chapter 6, as this considers the parameterisation of long-term ageing scenarios. However, the main focus in Chapter 6 is the method for parameterising SOA, and we expect that its results would remain at least qualitatively applicable when using updated mechanism versions.

For β-pinene, a similar iterative model extension was applied as for α-pinene, leading to a mechanism containing 54,355 equations and 6,738 species. This mechanism was applied for the simulations presented in Chapter 4, and is found able to keep contributions of generic species to SOA within reasonable bounds (at most around 20%) for the simulated experiments.

The BOREAM mechanism extension described in this section strongly reduces the impact of uncertainties associated to the use of generic compounds. This probably presents a reasonable approach towards achieving the most explicit mechanism possible within given computational constraints, as only reactions which have the largest impact are treated explicitly. Compared to the mechanism of GECKO-A in Valorso et al. (2011), this mechanism might still be inferior in its level of detail, but its number of species is about 50 times lower.

2.5.3 Chemical equation solver

In order to solve the set of differential equations governing the concentrations of the chemical compounds, the KPP-2.1 kinetic pre-processor and solver are used (Sandu and Sander, 2006, Sandu et al., 2003). The Rosenbrock algorithm has been chosen among the choices of available solvers. This solver is suitable for solving stiff equation systems (i.e. systems containing strongly different time scales, such as is the case for gas phase chemistry systems). KPP reads in the chemical mechanism and generates the corresponding Fortran routines constituting the solver.

One drawback of KPP is that it has not been designed for very large systems. Below 10,000 equations, the pre-processing phase is still fast, and takes only several minutes. However, for larger mechanisms, both computation time and memory use increase rapidly with increasing number of species and equations. By making a few minor changes to the preprocessor, we were able to compile the above mentioned version of about 90,000 equations and 10,500 species with a peak memory requirement of about 24 GB. This is due to the use of several full matrices of size (number of equations) times (number of species), used to represent the stoichiometric coefficients of species in the equations. This problem can be mitigated by rewriting the program using a sparse matrix approach, but this work has currently not been undertaken yet. As mentioned above, another solution could be a transition to the two-step solver, for which Valorso et al. (2011) have proven its ability to solve very large systems.

Chapter 3

Modelling of α-pinene oxidation

In this Chapter, a number of dark ozonolysis and photooxidation smog chamber experiments using α-pinene as precursor are investigated using the BOREAM model. An evaluation of the modelled production of a number of detected oxidation products is also presented.

3.1 Simulation of dark ozonolysis experiments

In the present section, we evaluate BOREAM against a large set of dark ozonolysis experiments available from the literature. Due to absence of light and use of OH-scavengers in the majority of ozonolysis experiments, these comparisons provide a test of the first generation chemistry in the model. We aim to evaluate the impact of possible uncertainties in the gas-phase mechanism and in the estimation of thermodynamic properties of condensable compounds, with the temperature dependence of the modelled SOA yields as a particular focus. The results have been obtained using the BOREAM version described in Ceulemans et al. (2010).

3.1.1 Ozonolysis experiments considered

Table 3.1 summarises the dark ozonolysis experiments simulated in this work. OH-scavengers were used in most experiments in order to keep ozone as the dominant oxidant of α-pinene. Scavenging OH radicals also limits the extent to which primary ozonolysis products are further oxidised. Most studies used 2-butanol (BUT2OL) or cyclohexane (CHEX). The majority of experiments were conducted at low relative humidity (RH). In most cases only an upper limit for RH in the experiments is given, e.g. 10% in Pathak

TABLE 3.1: Simulated dark ozonolysis experiments for α-pinene. G is the geometrically averaged ratio of modelled to observed yields (Section 3.1.2).

Study	#	VOC (ppb)	T (K)	RH (%)	scavenger	G
Iinuma et al. (2004)	9	100	291–296	41–52	no	2.54
Ng et al. (2006)	1	186	292	4.1	CHEX	0.67
Presto et al. (2005a)	21	15–235	295	N.A.	BUT2OL	1.57
Shilling et al. (2008)	1	10	298	40	BUT2OL	0.39
Song et al. (2007)	17	5.9–81	300–302	<1	CHEX	0.86
Cocker III et al. (2001)	47	12–227	300–302.5	<2,14–57	BUT2OL	1.1
Camredon et al. (2010)	2	159–180	293–297	0.33	CO	0.97
Yu et al. (1999a)	3	59–107	306–308	N.A.	BUT2OL	0.57
Griffin et al. (1999)	6	16.7–65	303–310	5	BUT2OL	0.134
Hoffmann et al. (1997)	5	41–168	319–322	N.A.	no	0.34
Pathak et al. (2007)	37	3.7–115	273–313	<10	BUT2OL	0.86

et al. (2007), 1% for Song et al. (2007). Values below these limits were used in the simulations.

The modelled SOA formation is evaluated by comparison with reported experimental SOA mass yields. In some cases, wall losses are taken into account for the estimation of experimental SOA yields, such as in Presto et al. (2005a) and Pathak et al. (2007).

Both seeded and non-seeded experiments were considered. Since partitioning is based on absorption in our model, a non-zero initial absorptive mass M_O is needed to start up the partitioning. In some experiments, however, SOA formation is initiated by nucleation or adsorption onto non-absorbing seed aerosols, processes which are not explicitly modelled. Instead we suppose that a small amount of initial organic aerosol is formed, which plays the role of an absorptive seed. We acknowledge that in such cases the choice of the initial absorbing aerosol mass can be rather arbitrary, and that more explicit modelling of nucleation or adsorption would be desirable.

For non-seeded experiments, nucleation is assumed to occur rapidly after the onset of the experiment. The initial particle diameter is set to 10 nm (the approximate detection limit in most smog chamber studies). The initial particle number is set to 20,000/cm^3, a typical value for α-pinene ozonolysis experiments (see for example Cocker III et al., 2001).

The type of seed utilised can differ. In Cocker III et al. (2001), dry or aqueous inorganic seed was used. In Song et al. (2007), hydrophobic organic seed was tested. It was found that dry inorganic or hydrophobic seed did not influence SOA yields significantly, and therefore it probably did not contribute to the absorbing phase. For these experiments, we use the same initial conditions as for pure nucleation.

In Pathak et al. (2007), however, dry inorganic seed was sometimes found to strongly enhance SOA yields, especially when SOA yields were low in absence of seed. We conclude that the adsorbing effect of the seed plays an important role for these experiments. In this case, we have included the seed mass in the initial M_O, as a proxy for the adsorption taking place on the dry inorganic seed.

In Presto et al. (2005a), SOA produced in a previous experimental run was used as seed, which we used as initial absorbing mass.

In many experiments, the initial seed mass is small in comparison with the final SOA mass, hence its influence on final SOA yields will be small. In some cases however, the seed might play a significant role, possibly not well represented by the model.

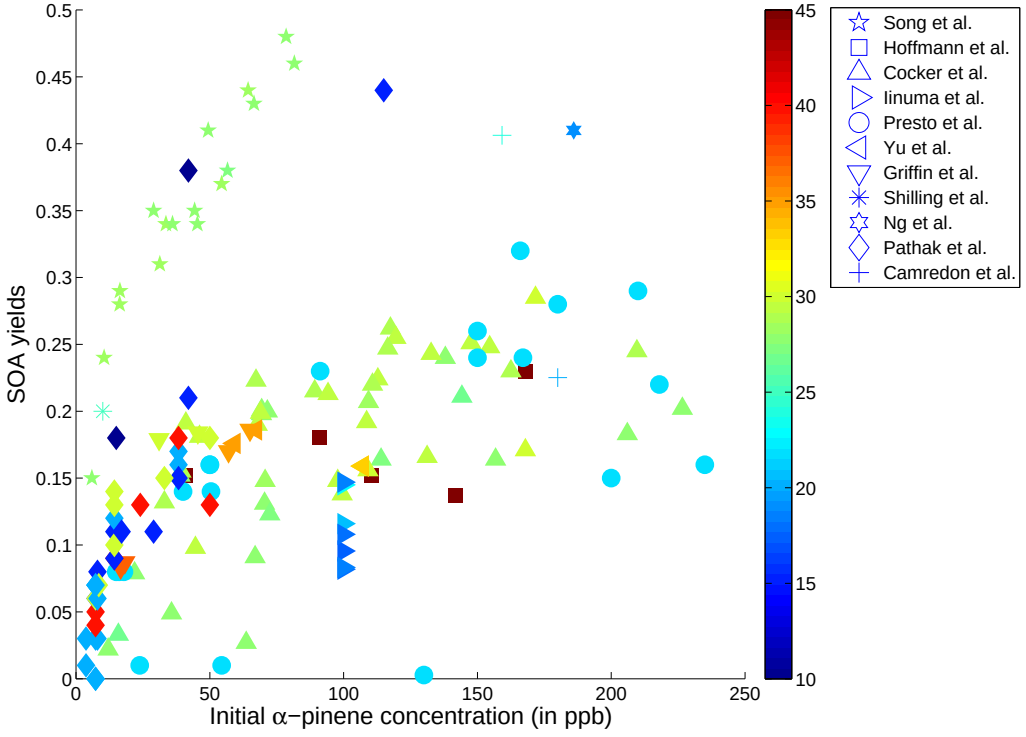

FIGURE 3.1: Experimental SOA yield for α-pinene dark ozonolysis experiments, in function of initial α-pinene concentration and temperature (in °C, colour code).

Figure 3.1 provides an overview of experimental SOA mass yields from α-pinene dark ozonolysis experiments. As expected from the absorptive theory (Pankow, 1994), higher yields are often found at higher initial α-pinene concentrations and lower temperatures. However, the variability of SOA yields is large, even for similar concentrations and temperatures. In particular, the yields from Song et al. (2007) and Pathak et al. (2007) are generally higher than those from other experiments conducted under similar conditions.

3.1.2 Model performance and temperature dependence of modelled SOA yields

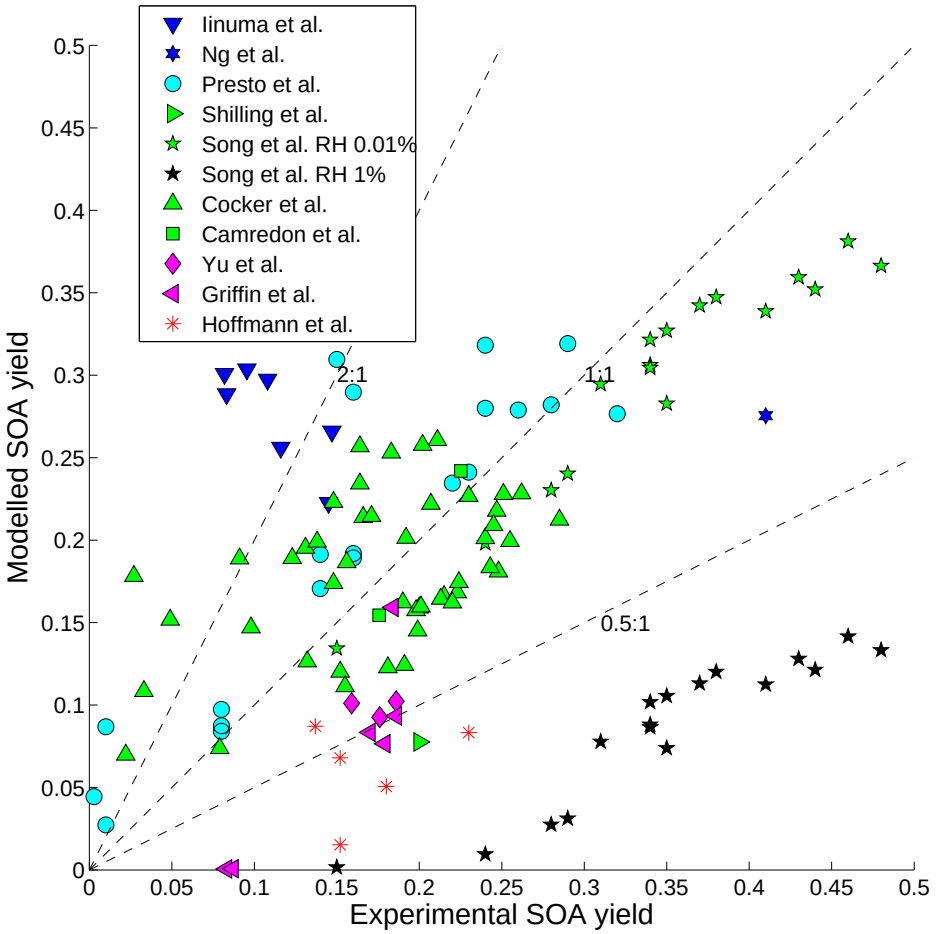

FIGURE 3.2: Modelled versus experimental SOA yields for the dark ozonolysis experiments listed in Table 3.1 (except those of Pathak et al., 2007).

The modelled maximum SOA mass yields are compared to the corresponding experimental values in Fig. 3.2 for all experiments (Table 3.1), excluding those of Pathak et al. (2007). The colour of each symbol indicates the temperature range of the experiment, with blue for the lowest temperatures (below 20°C) and red for the highest temperatures (above 40°C). The results for Pathak et al. (2007) are given separately in Fig. 3.3.

For each series of experiments in Table 3.1, the geometrically averaged ratio of modelled to observed yields,

$$G = \left(\prod_{i=1}^{n} Y_{\mathrm{mod},i} / Y_{\mathrm{exp},i} \right)^{1/n} \tag{3.1}$$

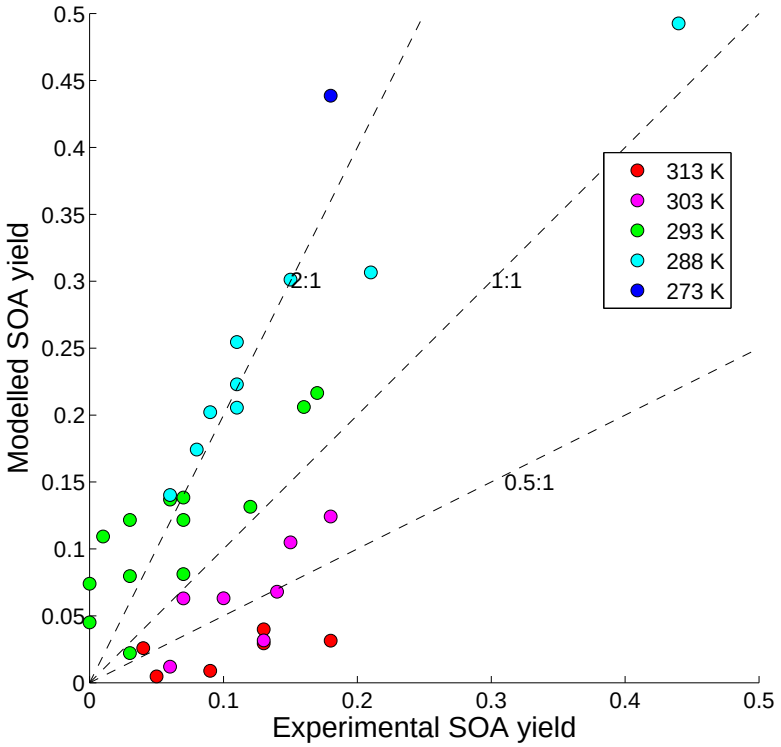

FIGURE 3.3: Modelled versus experimental SOA yields for the simulated dark ozonolysis experiments from Pathak et al. (2007). The water vapour concentration is supposed to be 73 ppm (below the experimental upper limit of 10% RH).

is given as a measure for overall model bias. Complementary measures of the agreement between model and observations are provided by

$$G_{\text{abs}} = \exp\left[(1/n) \cdot \sum_{i=1}^{n} |\ln(Y_{\text{mod},i}/Y_{\text{exp},i})|\right] \tag{3.2}$$

which we will refer to as the average model discrepancy factor. Over- and underestimations can cancel out in the average ratio defined by Eq. 3.1, but not in the discrepancy factor given by Eq. 3.2.

The model is found to reproduce the majority of SOA yields to within a factor of two (Figs. 3.2 and 3.3). The largest underestimations are found for the experiments of Griffin et al. (1999) and Hoffmann et al. (1997), performed at the highest temperature (with average model/data ratios of 0.13 and 0.34, see Table 3.1.) For the experiments by Song et al. (2007), although relative humidity was reported to be low (< 1%), the model results are found to be strongly dependent on the precise assumed value, with drastically improved model performance at very low RH (0.01%) due to SCI oligomerisation, as discussed in Sect. 3.1.3.

The largest overestimations of the SOA yield are found for the experiments by Iinuma et al. (2004) (factor $G = 2.54$), and for some experiments from Cocker III et al. (2001).

In this last study, the use of aqueous inorganic seed was found to slightly lower SOA formation, possibly due to activity effects of inorganic species, which are not present in the model.

Both Fig. 3.2 and 3.3 suggest a dependence of the model/data bias on temperature, with most overestimations occurring at the lower end of the temperature range, and the worst model underestimations occurring at the highest temperatures. This is especially clear for the experiments of Pathak et al. (2007) (Fig. 3.3), with overestimations often exceeding a factor of two below 20 °C, whereas large underestimations are found at higher temperatures, with G values of 0.65 and 0.22 at 30 °C and 40 °C, respectively. The worst overestimations are found for experiments 6, 8, 16, 17 and 18 from Pathak et al. (2007) conducted at 20 °C, with experimental yields of 0–3%. However, Pathak et al. (2007) indicated that these low yields were due to large wall losses of semi-volatile products in these experiments, which might therefore not be appropriate for evaluating the model performance.

The worst underestimations of the SOA yield occur for experiments 1 ($Y_{\mathrm{model}} = 0.0089$ versus $Y_{\mathrm{exp}} = 0.09$) and 10 (0.0048 versus 0.05), which were performed without seed at 40 °C. The low modelled SOA yields are due to the near-absence of initial aerosol mass M_0, and the strong increase of the saturated vapour pressures with temperature: about an order of magnitude per 20°C increase in the case of pinic acid and other typical SOA components (Capouet and Müller, 2006). Under such conditions, the ratio $C_{p,i}/C_{g,i} = K_{p,i} \cdot [M_0]$ is very low for all but the most condensable species in the model. For these experiments, the dominant components of the modelled SOA are pinic and hydroxypinonic acid, and SCI oligomers. For experiments with higher yields (e.g. experiment 13 from Pathak et al., 2007), a number of multifunctional hydroperoxides and alcohols formed in the hydroperoxide channel of the CI also contribute to SOA, whereas the SCI oligomers are unimportant.

In Fig. 3.4, observed and modelled yields in unseeded experiments from Pathak et al. (2007) are compared. The initial concentrations were identical in the simulations of these experiments (ozone 1500 ppb, α-pinene 7.3 ppb, water vapour 73 ppm). In contrast with the weak temperature dependence seen in the observations, the yields of the standard BOREAM model (the second bar from the left at each temperature) decrease strongly with temperature.

The performance of the model is further examined in Table 3.2, which provides the geometrically averaged ratios of modelled to observed yields at the different temperatures. The average ratio G is close to unity for the entire data set, i.e. the model is unbiased in an average sense. The strong temperature dependence of the modelled yield is one of

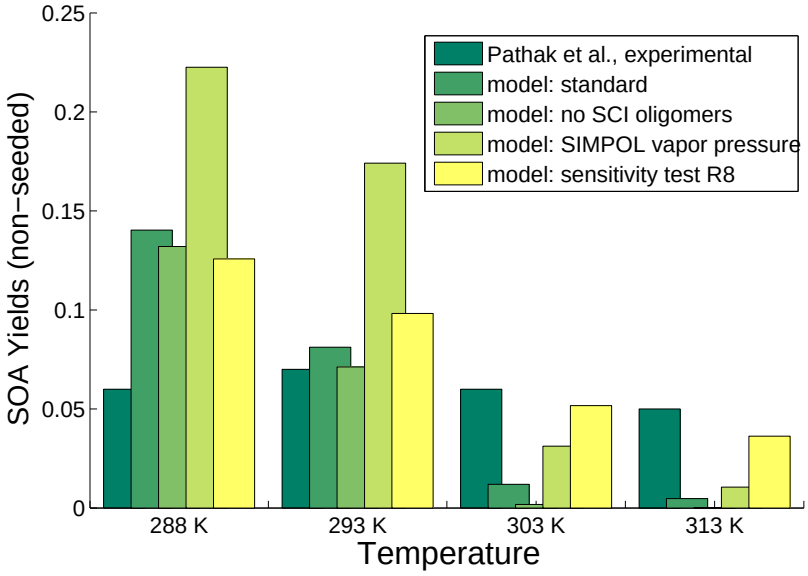

FIGURE 3.4: Experimental and modelled SOA yields at several temperatures for experiments 11, 7, 12 and 10 in Pathak et al. (2007). Results from a selection of the performed sensitivity tests are also shown.

TABLE 3.2: Geometrically averaged ratios of modelled to observed SOA yields for the Pathak et al. (2007) experiments at different temperatures, and for several model sensitivity tests. STD: standard mode; R1: without SCI oligomers; R2: vapour pressures from SIMPOL; R3: vapour pressures from Myrdal and Yalkowsky (1997) with Nannoolal et al. (2004) boiling point; R4: vapour pressures of Nannoolal et al. (2008) with Nannoolal et al. (2004) boiling point; R5: ideality assumed; R6: with addition of unvolatile product; R7: modified T-dependence of vapour pressures; R8: combination of R6 and R7. G and G_{abs} are defined in Section 3.1.2.

	STD	R1	R2	R3	R4	R5	R6	R7	R8
273 K	1.95	1.37	2.36	0.84	1.94	1.98	2.0	1.06	1.17
288 K	1.90	1.59	2.93	0.73	1.92	2.28	2.14	1.40	1.61
293 K	1.37	1.18	2.64	0.38	1.40	1.20	1.84	1.12	1.59
303 K	0.49	0.29	1.42	0.089	0.48	0.37	0.82	0.61	0.95
313 K	0.20	0.034	0.69	0.012	0.22	0.154	0.58	0.41	0.82
G	0.86	0.49	1.83	0.18	0.87	0.78	1.30	0.86	1.24
G_{abs}	2.17	3.2	2.31	5.5	2.16	2.7	1.79	1.63	1.46

the main causes for the average discrepancy G_{abs} of 2.17 for the model with standard settings.

3.1.3 Sensitivity analysis

We explore the sensitivity of modelled SOA to key model assumptions related to the gas-phase mechanism and the partitioning of condensable products.

The impact of oligomer products formed in the reactions of SCI with large molecular products is strongly RH-dependent, since their yields are determined by the competing reaction of SCI with water vapour. When RH humidity is above 1%, most SCI react with water vapour. At very low RH however, the SCI oligomers can contribute significantly to SOA mass. Given the large uncertainties associated with the different SCI reactions, a sensitivity simulation is performed, neglecting the formation of oligomers from SCI (simulation R1). The results (Table 3.2 and Fig. 3.4) show that these reactions have a large impact on the yields for experiments by Pathak et al. (2007), in particular at high temperature when the modelled SOA yields are low, improving the model agreement significantly (from a factor 0.034 to 0.20) at 40 °C, although not removing underestimations entirely. At lower temperatures or higher initial VOC concentrations, the relative increase of the SOA yields due to SCI oligomers is less pronounced.

The partitioning of α-pinene products depends on their thermodynamic properties: the saturated vapour pressures and the activity coefficients, as explained in Section 2.4.2. These properties are not directly measured for the vast majority of compounds present in SOA, and their estimation is very uncertain. In addition, the gas-phase ozonolysis mechanism might lack chemical pathways leading to the formation of very condensable compounds, as suggested by the severe underestimation of SOA yields at low initial α-pinene concentration (Capouet et al., 2008, Xia et al., 2008).

We further investigate the sensitivity of modelled SOA yields to (1) the choice of the vapour pressure estimation model, (2) the activity coefficients, (3) the temperature dependence of vapour pressures. In addition, the impact of possible additional ozonolysis pathways leading to the formation of highly condensable compounds is also explored.

Besides the method of Capouet and Müller (2006), used in the standard version of the model, we tested the SIMPOL method (Pankow and Asher, 2008) (run R2 in table 3.2), the Myrdal and Yalkowsky (1997) vapour pressure method in combination with the method of Nannoolal et al. (2004) for boiling point estimation (R3), and the Nannoolal et al. (2008) vapour pressure method in combination with the method of Nannoolal et al. (2004) for boiling point estimation (R4).

The SIMPOL method (R2) increases SOA yields significantly compared with the base case (see Fig. 3.4). This is due to the lower vapour pressures which this method predicts for important products of ozonolysis, compared with Capouet and Müller (2006). SOA yields are increased over the entire temperature range, and the temperature dependence of the yields remains too strong in comparison with the observations. On average, the SOA yields are overestimated by a factor $G = 1.8$. The average discrepancy factor (G_{abs}) is 2.3 for this run, similar to the base case.

The simulation R3 (based on Myrdal and Yalkowsky, 1997) results in lower model SOA yields compared to the standard case, especially at high temperature, where yields are more strongly underestimated. The modelled yields are underestimated at all temperatures in this run, with a G value of 0.18. Finally, the simulation based on vapour pressures of Nannoolal et al. (2008) (run R4) gives results which are quite in line with those from the standard run using the vapour pressure method of Capouet and Müller (2006).

In simulation R5, the method of Capouet and Müller (2006) is used, but the activity coefficients are all set to one (Table 3.2), i.e. the aerosol is assumed to be an ideal mixture. This has only a minor effect at low temperature, but leads to a decrease of the yields at high temperature, as can be seen in Fig. 3.4 and Table 3.2. As a consequence, the average discrepancy factor (G_{abs}=2.7) is increased.

The results of these simulations (R2–R5) demonstrate the importance of accurate prediction methods for the thermodynamic properties of α-pinene products. However, the choice of the prediction method appears to have only little effect on the temperature dependence of the modelled yields. Therefore, we test also the effect of an additional production pathway of very condensable products, which would be present in the particulate phase at all temperatures considered. This test is justified by the large uncertainties of the gas phase mechanism. In addition, it might possibly represent the effect of highly condensable compounds produced by particulate phase or heterogeneous reactions. Such reactions are still largely unexplored and have not been represented in the standard model due to the current lack of reliable kinetic data and knowledge of reaction pathways.

Simulation R6 therefore includes the production of a completely unvolatile product in the ozonolysis of α-pinene, with a yield of 2.5%. The results (Table 3.2) show significantly higher yields (a factor of 3), and therefore much less underestimation at the highest temperature, whereas the yields at low temperatures are only slightly increased.

An alternative solution for improving the modelled temperature dependence is explored in run R7, which includes an artificial decrease of the temperature dependence of the saturation vapour pressure. More precisely, we subtract $0.04 \cdot (T - 298\mathrm{K})$ from the

contribution of each functional group to $\log p^0_{L,i}$ in the method of Capouet and Müller (2006). This results in a lowering of vapour pressure above 298 K, and an increase below 298 K.

Compared to the base case, the simulation R7 improves the model results at all temperatures. The average bias remains essentially unchanged, but the average discrepancy factor G_{abs} is lowered to a value of 1.6.

Finally, the run R8 combines R6 and R7, leading to the best performance among all sensitivity simulations, with G_{abs} equal to 1.46. Even in this run, however, SOA yields are significantly overestimated at 15–20 °C.

It should be stressed that the modified temperature dependence of the vapour pressures is probably not very realistic. It would require a lowering of the enthalpy of vaporisation for all compounds, for which there is no direct justification. Therefore, the improved performance of runs R7 and R8 should be considered with caution. A further possibility would be a temperature dependence of chemical pathways leading to the formation of less volatile products at high temperature. This remains speculative; no such process has been identified yet.

3.2 Model comparison against photooxidation smog chamber experiments

Previous simulations of α-pinene photooxidation (Capouet et al., 2008) and dark ozonolysis (see Section 3.1) smog chamber experiments showed that the BOREAM SOA mass yields generally fall within a factor two of the experimental data. For dark ozonolysis, larger discrepancies were found at high temperatures (above 30 °C) and at low VOC loadings and no seed. In this section, the BOREAM model (using the model version described in Ceulemans et al., 2012) is evaluated, with a focus on photooxidation experiments, and on experiments in which secondary chemistry through OH-oxidation or photolysis takes place.

An overview of the simulated experiments is given in Table 3.3. All experiments made use of a light source. Most experiments also included a considerable quantity of NO_x, with NO_x/VOC ratios of the order (or larger) than unity, except the first experiment of Ng et al. (2007a), which was conducted under very low-NO_x conditions, and three among the six Presto et al. (2005a) experiments considered. For experiment 1 in Ng et al. (2007a), unknown quantities of NO_x, H_2O_2 and O_3 were present at the start of the experiment, which were constrained using the measurements of α-pinene and O_3

TABLE 3.3: Photooxidation smog chamber experiments simulated with the full BOREAM model.

Experiment	Initial VOC (ppb)	NO_x (ppb)	T (K)	NO_2 photolysis j-value (in s^{-1})	Exp. SOA mass yield	Model SOA mass yield
Ng et al. (2007a)						
Exp. 1	13.8	(0.7)	298	$5.5{\cdot}10^{-3}$	0.379	0.592
Exp. 4	12.6	938	299	$7.0{\cdot}10^{-3}$	0.066	0.070
Ng et al. (2006)						
Exp. 3/9/2005	108	95	293	$1.1{\cdot}10^{-3}$	0.26	0.298
Presto et al. (2005a)						
Exp. 12	20.6	11	295	$3.0{\cdot}10^{-2}$	0.065	0.066
Exp. 15	205	6.5	295	$3.0{\cdot}10^{-2}$	0.304	0.331
Exp. 19	156	6	295	$3.0{\cdot}10^{-2}$	0.251	0.284
Exp. 25	10.8	20	295	$3.0{\cdot}10^{-2}$	0.026	0.019
Exp. 26	152	9	295	$3.0{\cdot}10^{-2}$	0.224	0.278
Exp. 27	15	14	295	$3.0{\cdot}10^{-2}$	0.057	0.040
Takekawa et al. (2003)						
Exp. 1	100	53	283	$4.0{\cdot}10^{-3}$	0.312	0.390
Exp. 2	81	43	283	$4.0{\cdot}10^{-3}$	0.317	0.360
Exp. 3	55	30	283	$4.0{\cdot}10^{-3}$	0.275	0.307
Exp. 4	196	102	303	$4.0{\cdot}10^{-3}$	0.133	0.249
Exp. 5	146	80	303	$4.0{\cdot}10^{-3}$	0.119	0.224
Exp. 6	93	54	303	$4.0{\cdot}10^{-3}$	0.066	0.187
Nozière et al. (1999)						
Exp. 17	305	3500	298	$3.5{\cdot}10^{-4}$	0.073	0.067
Exp. 18	1488	3300	298	$3.5{\cdot}10^{-4}$	0.306	0.314
Exp. 19	980	4090	298	$3.5{\cdot}10^{-4}$	0.219	0.178
Exp. 20	330	3755	298	$3.5{\cdot}10^{-4}$	0.079	0.102
Hoffmann et al. (1997)						
Exp. 3	72	203	315	$8.3{\cdot}10^{-3}$(solar)	0.078	0.105
Exp. 4	19.5	113	315	$8.3{\cdot}10^{-3}$(solar)	0.016	0.085
Exp. 5	53.0	206	324	$8.3{\cdot}10^{-3}$(solar)	0.037	0.038
Exp. 6	94.5	135	321	$8.3{\cdot}10^{-3}$(solar)	0.086	0.068
Exp. 7	87.4	125	321	$8.3{\cdot}10^{-3}$(solar)	0.108	0.101
Exp. 8	95.5	124	316	$8.3{\cdot}10^{-3}$(solar)	0.102	0.101
Exp. 9	94.6	122	316	$8.3{\cdot}10^{-3}$(solar)	0.089	0.101

for this experiment, provided in Valorso et al. (2011), following the approach of this last study. For experiment 4 in Ng et al. (2007a), the HONO concentration and an unknown OH-source were constrained similarly, based on α-pinene and NO_x data (see again Valorso et al., 2011). For the low-NO_x scenario, reasonable agreement is reached for ozone production (Fig. B.2 in the Appendix). For the high-NO_x experiment, reproducing the observed α-pinene decay is possible only when an additional OH-source is included, possibly due to reactions on walls, as proposed by Valorso et al. (2011). Reasonable agreement is obtained with measured NO and NO_2 concentrations (Fig. B.4 in the Appendix). Note that, as OH exposure was considerable in the experiments of Ng et al. (2007a), these experiments will also be investigated in Chapter 5, using the BOREAM version extended for SOA ageing. The results obtained with that version remain similar for the gas phase.

In addition, the simulated ozone production has been evaluated against the measured $D(O_3 - NO) = ([O_3] - [O_3]_{initial}) - ([NO] - [NO]_{initial})$, a measure for ozone production, in three experiments of Carter (2000). The BOREAM model shows good agreement or

slight overestimation of ozone production for these experiments (Figs. B.5a to B.5c in the Appendix).

In Ng et al. (2007a) an aerosol density of 1.32 g cm^{-3} was measured, which was used in the derivation of the experimental mass yields based on the measured aerosol volume concentrations. A density of 1.25 g cm^{-3} was used by Ng et al. (2006). In all other studies considered, the reported mass yields were obtained by multiplying the measured volume concentrations by an assumed aerosol density of 1.0 g cm^{-3}. Since this estimate is likely too low, in view of the measurement of Ng et al. (2007a), we have multiplied the reported SOA mass yields by a factor of 1.32.

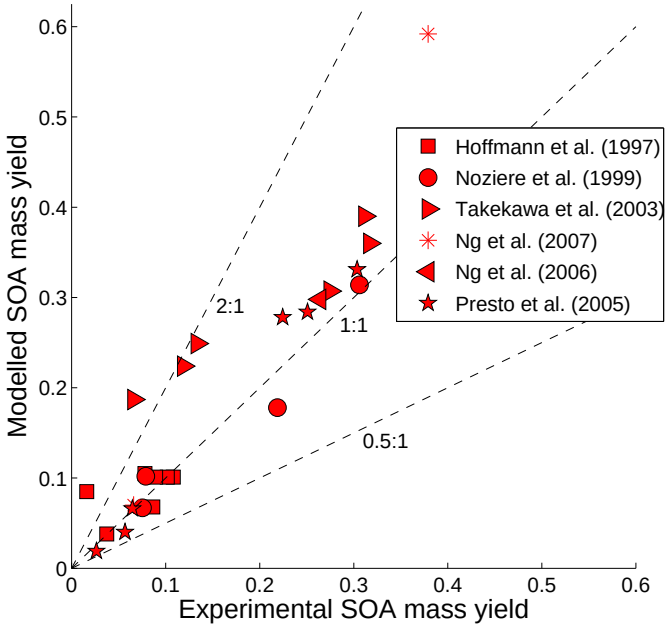

FIGURE 3.5: Measured versus modelled aerosol mass yields for the α-pinene photooxidation smog chamber experiments reported in Table 3.3.

In Fig. 3.5, SOA mass yields from smog chamber experiments are compared with calculated yields using BOREAM. For most experiments, the SOA yields are reproduced to within a factor of 2. In some experiments, such as Takekawa et al. (2003) and Hoffmann et al. (1997), there is a considerable ozone production, so that part of the α-pinene undergoes ozonolysis. A small part of the large overestimations (about a factor of 2) found for three experiments of Takekawa et al. (2003) might be related to uncertainties regarding the yield of carboxylic acids, such as pinic and hydroxy pinonic acid, which are formed in α-pinene ozonolysis, but for which the formation mechanism is not well understood (Ceulemans et al., 2010). Their production yield is held fixed in the model, although it is very probably dependent on photochemical conditions, e.g. the NO_x abundance. Pinic

acid is found to represent about 8% of the SOA in the experiments of Takekawa et al. (2003) at 303 K. Most species in the modelled SOA for the experiments of Takekawa et al. (2003) bear a peroxy acetyl nitrate (PAN) group. Uncertainties regarding the formation and decomposition of such species could therefore be responsible for part of the model overestimates. The model reproduces the SOA decrease with increasing NO_x concentrations, as seen from the comparison of experiments 1 and 4 of Ng et al. (2007a), for which the time evolution is given in Fig. 3.6. The SOA yield in the low-NO_x experiment 1 of Ng et al. (2007a) is overestimated by the model, a result which was also obtained in Valorso et al. (2011). Overall, the model results agree reasonably well with the experimental values, considering the theoretical and experimental uncertainties.

Fig. 3.6 shows the sensitivity of calculated SOA to changes in the values of key parameters in the generic chemistry scheme of the BOREAM model, such as the assumed value for k_{LX}, the reactivity towards OH (see Table A.3 in Appendix A), and the photolysis rate j_{LXALD} of the generic part of the generic species (see Table A.2 in Appendix A). The tests show that their impact on simulated SOA mass yields is limited for both the low- and high-NO_x experiments 1 and 4 of Ng et al. (2007a). Variations in the branching ratios of alkoxy radicals towards decomposition and H-shift isomerisation have a larger impact on predicted SOA in the high-NO_x case. Assuming that a large fraction (50% or 100%) of alkoxy radicals undergoes H-shift isomerisation leads to a large increase of predicted SOA yields (although these assumptions are most likely too high, as an evaluation of the SARs for a representative number of alkoxy radicals in the model shows). A main reason for the higher sensitivity of SOA yields to the branching of alkoxy radicals under high-NO_x conditions is simply the fact that alkoxy radicals are much more frequently formed at high NO_x than at low NO_x.

Addressing the uncertainty of the generic chemistry scheme would require a more explicit characterisation of the generic species corresponding to the different generic species classes, for example with the help of a self-generating mechanism approach such as used in Valorso et al. (2011). Structure activity relationships for alkoxy radicals, such as those in Vereecken and Peeters (2009) and Vereecken and Peeters (2010), can then be applied to a number of representative explicit alkoxy radicals in the model, in order to obtain a more thorough estimate of the average branching fractions of alkoxy radicals, which can then be applied for generic species.

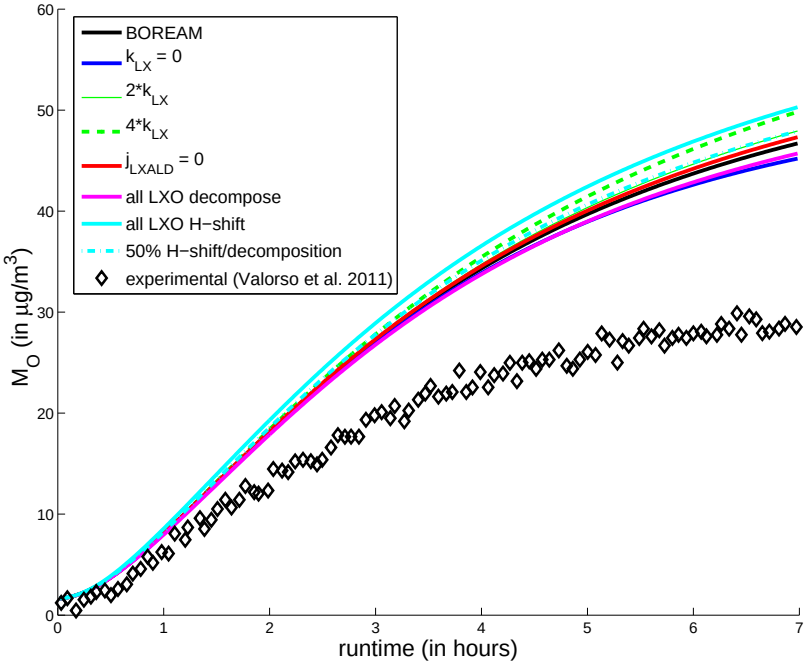

(A) Exp. 1, Ng et al. (2007a)

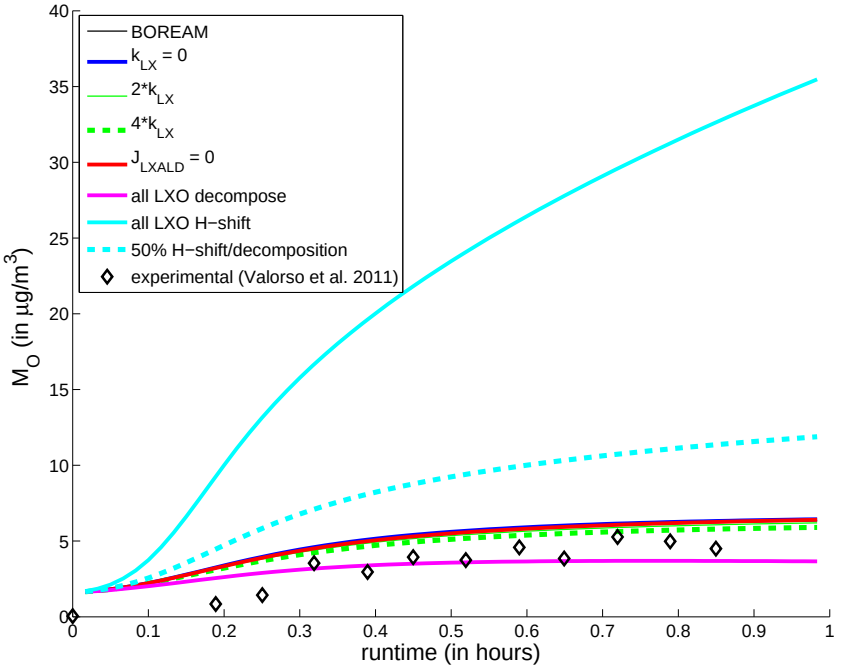

(B) Exp. 4, Ng et al. (2007a)

FIGURE 3.6: Organic aerosol evolution in Experiments 1 (low-NO_x) and 4 (high-NO_x) of Ng et al. (2007a), based on data presented in Valorso et al. (2011). Shown are standard BOREAM results (black lines), as well as sensitivity tests varying key parameters of the generic chemistry, including the assumed reaction constant with OH of the generic part of generic species classes, k_{LX}, the j-value j_{LXALD} of this generic part, and the branching ratios of generic alkoxy radicals (denoted LXO).

3.3 Model investigation of pathways leading to specific observed products

This section discusses the simulation of a number of specific compounds observed in laboratory experiments.

3.3.1 Hydroperoxides and pinonaldehyde

Reasonable agreement was obtained for a number of reported first generation products observed in the gas phase in experiments by Eddingsaas et al. (2012b). The observed pinonaldehyde under low-NO_x implies a novel pathway for the reaction of specific β-hydroxy peroxy radicals with HO_2 leading to alkoxy radicals and OH (see Section 2.1.6.5). Including this pathway in BOREAM with a 50% channel ratio leads to a reasonable agreement with observations (Fig. 3.7), although the gas phase concentration of the main products is somewhat overestimated. It should be noted that the carbon balance of this experiment was not completely closed. In the model, main SOA products are hydroperoxides, such as the various isomers of the hydroxy dihydroperoxide of mass 218. Despite their detection in the gas phase, no hydroperoxide products have been reported by Eddingsaas et al. (2012a) for the SOA, even though their low vapour pressure suggests that they should partition to the SOA phase. It should be noted that Reinnig et al. (2009) tentatively identified hydroperoxides and peroxy acids in the SOA produced in the ozonolysis of α- and β-pinene, although these authors indicate that further identification using other techniques are needed to confirm these results.

3.3.2 Simulation of organic acid tracer compounds

This subsection briefly discusses the formation in BOREAM of α-pinene SOA tracer species which have been observed both in smog chamber experiments and in the ambient atmosphere (Szmigielski et al., 2007, Claeys et al., 2009, Yasmeen et al., 2012, Eddingsaas et al., 2012a, Kristensen et al., 2013). As can be seen in Table 3.4, the oxidation of α-pinene as implemented in BOREAM in a low-NO_x experiment of Yasmeen et al. (2012) leads to only ppt levels of 8- and 10-hydroxy pinonic acid, norpinic acid and diaterpenylic acid for an initial α-pinene concentration of 258 ppb. Model pathways towards terpenylic, diaterpenylic acid acetate (Claeys et al., 2009) and MBTCA were found to have very low yields in the studied experiment, the reason being that the multigeneration chemistry needed to form those compounds generally takes longer than the time scale of the experiment, and involves a number of unfavourable reaction branchings.

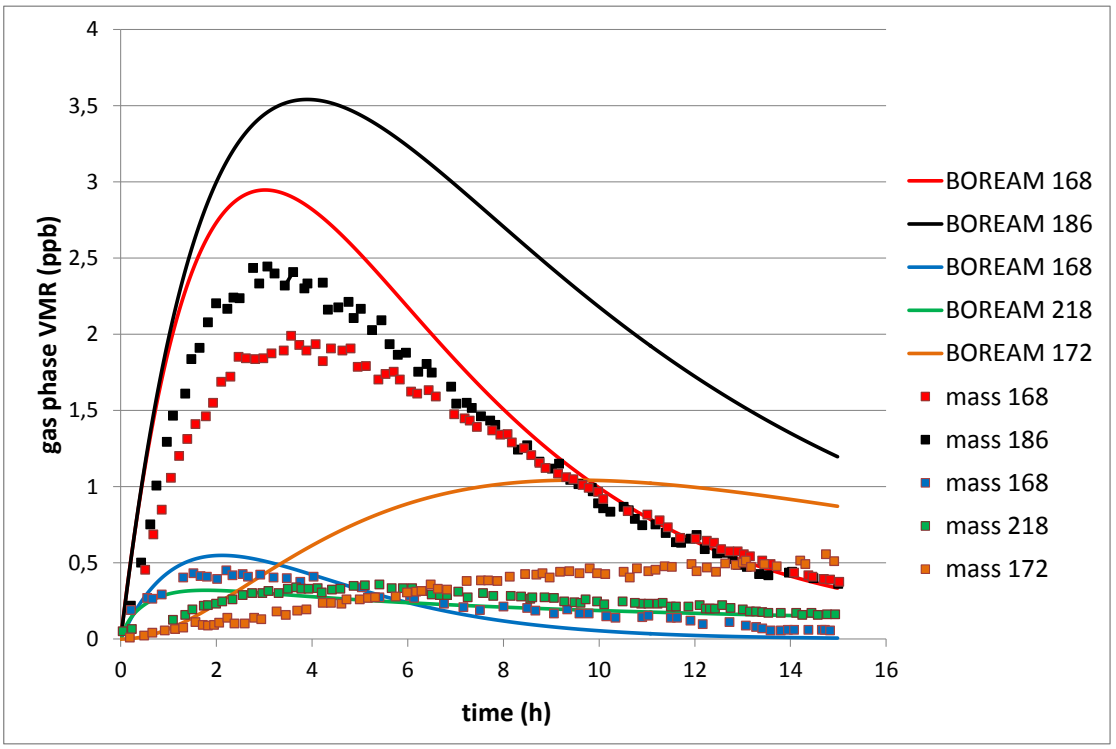

FIGURE 3.7: BOREAM simulation of the 20 ppb α-pinene low-NO_x experiment of Eddingsaas et al. (2012b), which is experiment 7 in Table 5.1. The different masses are m168 (red): pinonaldehyde, m186(black): hydroxy hydroperoxides, m218 (green): hydroxy dihydroperoxides, m172 (orange): hydroperoxide product of pinonaldehyde oxidation, m168 (blue): hydroperoxide from the H-abstraction channel of α-pinene (Eddingsaas et al., 2012b).

The pathways towards terpenylic acid are shown in Fig. 3.8, on which the reaction fluxes (the amount of compound produced at each reaction step, in this case taken over the duration of the entire experiment) are indicated. From the initial 258 ppb of α-pinene, only a minuscule flux reaches terpenylic acid. The main reasons are the unfavourable competition of other pathways, such as the peroxy radical ring closure, and the need for two further OH-oxidation steps of molecular products, which have longer lifetimes than the duration of the experiment. The exact yields of the reported tracers were not quantified by Yasmeen et al. (2012), but their detection likely implies that their yields were considerably higher than the BOREAM-calculated values. It should be noted that Eddingsaas et al. (2012a) also report detection of terpenylic acid in non-negligible amounts, both under low- and high-NO_x conditions. In a recent study (Kristensen et al., 2014), terpenylic acid was found to account for 1 to 4% of SOA in α-pinene photooxidation experiments, and for 1 to 2% of SOA in ozonolysis.

High observed MBTCA yields were found in both high-NO_x (Szmigielski et al., 2007, Eddingsaas et al., 2012a) and low-NO_x conditions (Yasmeen et al., 2012, Eddingsaas et al., 2012a). Müller et al. (2012) observed a yield of the order of 1% MBTCA in low-NO_x pinonic acid oxidation. Kristensen et al. (2014) found that MBTCA reached

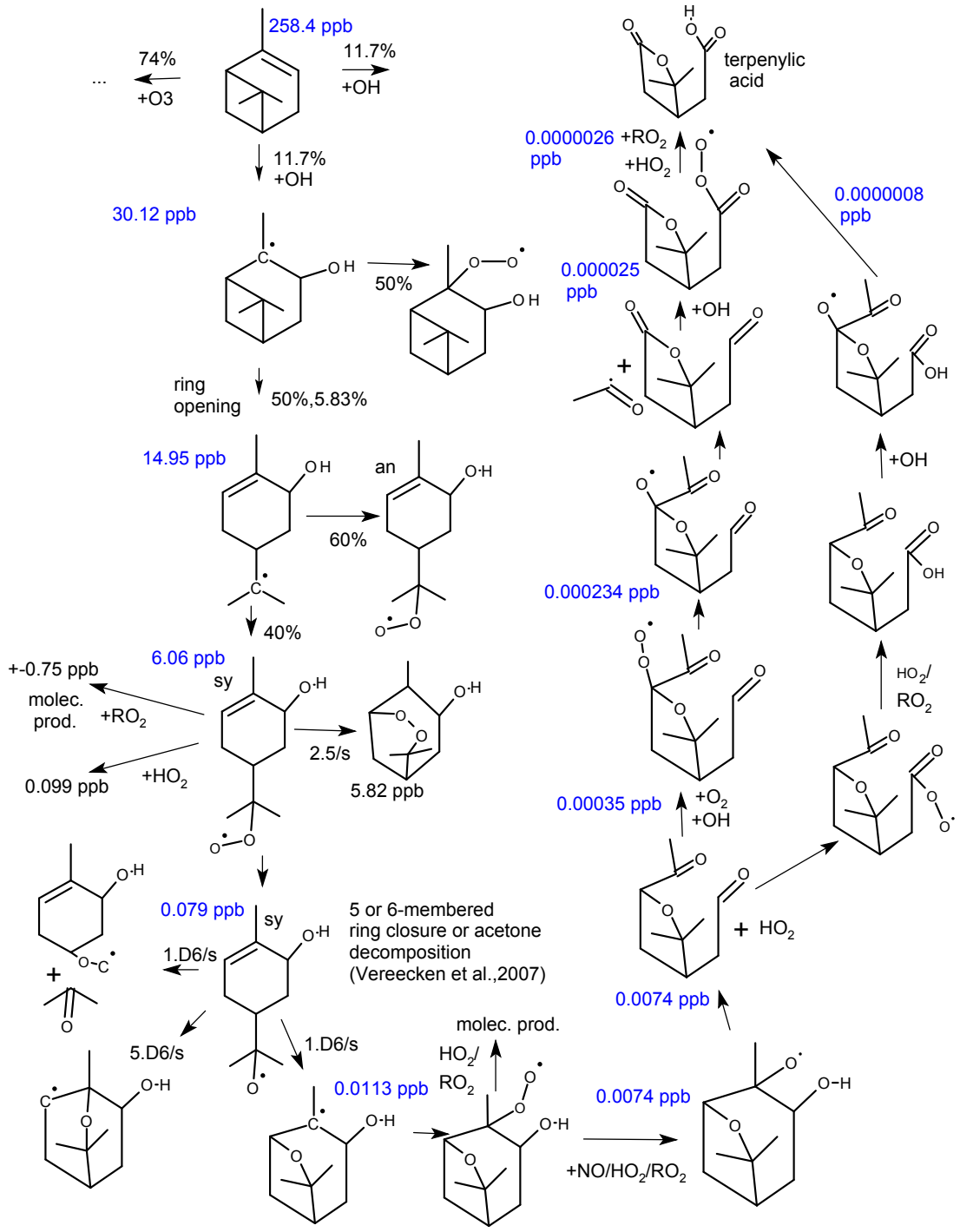

FIGURE 3.8: BOREAM pathways, with reaction fluxes indicated, towards terpenylic acid, for experiment E0208 of Yasmeen et al. (2012)

Table 3.4: Calculated concentrations of tracers in experiment E0802 in Yasmeen et al. (2012).

Name	BOREAM (ppt)
8-Hydroxypinonic acid	29
10-Hydroxy pinonic acid	2.2
Diaterpenylic acid	73
Norpinic acid	11
Terpenylic acid	0.003
Diaterpenylic acid acetate	< 0.001
MBTCA (conventional chem.)	< 0.001
MBTCA (direct pathway Müller et al., 2012)	2.8

2 to 5% of SOA in high-NO_x OH-oxidation experiments, while for ozonolysis, MBTCA concentrations were much smaller. In Praplan et al. (2012), succinic acid is formed from cyclobutyl methyl ketone, in a reaction scheme which is presumably similar to that for the formation of MBTCA from pinonic acid. Simulations with BOREAM show that conventional reaction pathways underestimate succinic acid formation by 2–3 orders of magnitude at low-NO_x. A possible alternative pathway involving a shift of an aldehyde H in a peroxy radical could generate succinic peracid in significant amounts, but it does not operate at high-NO_x. Similar pathways for MBTCA from pinonic acid have negligible yields (see Table 3.4). Even the pathway of Müller et al. (2012) leads to only ppt-levels of MBTCA. Therefore the production of important acidic tracer species such as MBTCA and terpenylic acid remains unexplained from a mechanistic point of view.

3.4 Conclusions

The simulation by BOREAM of a large number of α-pinene dark ozonolysis experiments is found to reproduce the measured SOA yields to within a factor of 2 or less in most cases, a promising result given the large uncertainties in the oxidation mechanism and the estimation of partitioning coefficients. However, the strong decrease of the modelled yields with temperature contrasts with the much weaker temperature dependence exhibited by the observations. As a consequence, model overestimations of up to a factor 2 are found at low temperature, whereas underestimations by up to an order of magnitude are found at high temperature (> 30 °C), in particular when initial VOC concentrations are low. The temperature dependence of the model bias was also reported in previous modelling studies based on the MCM mechanism (Jenkin, 2004, Xia et al., 2008). Even larger

underestimations were found by Xia et al. (2008) for high temperature dark ozonolysis experiments from Pathak et al. (2007).

The formation of oligomer products from the reactions of SCI with carboxylic acids is found to contribute significantly to SOA in the case of low yield α-pinene experiments performed at very low relative humidity. In such cases, the model agreement was greatly improved when these reactions were taken into account. However, their formation is expected to be negligible under atmospheric conditions.

The saturated vapour pressure estimation is found to be of great importance. For example, the use of SIMPOL (Pankow and Asher, 2008) increased SOA yields by a factor three in the case of high-temperature experiments by Pathak et al. (2007), whereas the Myrdal and Yalkowsky (1997) method (with Nannoolal et al. (2004) boiling point) decreased SOA yields by up to an order of magnitude, and Nannoolal et al. (2008) gave yields which were very similar to our base case using Capouet and Müller (2006). The temperature dependence of the SOA yields is largely overestimated in all cases.

The calculation of activity coefficients (non-ideality of SOA mixture) is found to slightly improve the model agreement in low yield experiments, compared to a sensitivity simulation assuming ideality. As shown by Compernolle et al. (2009), non-ideality has a large impact at high relative humidity due to its strong influence on the modelled water uptake.

The model performance in terms of temperature dependence is improved when additional ozonolysis pathways are assumed to form highly condensable products, or when the temperature dependence of vapour pressures is decreased. However, such a reduction of temperature sensitivity of saturated vapour pressures is very likely unrealistic, given the constraints provided by saturated vapour pressure measurements at different temperatures (e.g. for pinic acid). It appears therefore more likely that highly condensable species are missing in the model, with formation pathways which could possibly be temperature dependent. These compounds could be produced in the gas phase, or through heterogeneous or particle-phase processes.

Evaluation against a large number of photooxidation smog chamber experiments shows that most experimental SOA mass yields can be reproduced to within a factor 2. Uncertainties in the generic chemistry were found to have only a small impact on SOA for low-NO_x experiments. At high NO_x, the branching ratios towards decomposition or H-shift isomerisation adopted for alkoxy radicals are found to have a possibly large influence on SOA. Evaluation against photooxidation experiments in which more extensive SOA ageing takes place is deferred to Chapter 5.

Finally, serious discrepancies are found between modelled and experimentally observed SOA composition. For the low-NO_x photooxidation experiment of Eddingsaas et al. (2012a), the gas phase formation of hydroperoxide products and pinonaldehyde can be reproduced qualitatively, but the model predicts large concentrations of hydroperoxides in the SOA, which most experimental studies have not yet been able to confirm. On the other hand, many experimental studies report the formation of a number of SOA tracer species containing one or more carboxylic acid groups. Currently, the BOREAM mechanism does not provide an explanation for their relatively large observed yields. This could also have important implications for the modelling of SOA yields, as these tracers, and other possible oxidation products involved in the chemical pathways towards them, might possibly account for part of the very condensable compounds invoked to explain the higher-than-modelled yields in high temperature dark ozonolysis experiments. It should be reminded though, that the total amount of identified SOA species still make up only a small fraction of the total SOA.

Chapter 4

Modelling of β-pinene oxidation

In this Chapter, BOREAM is confronted with β-pinene smog chamber experiments available in the literature. Section 4.1 gives an overview of experimental studies on β-pinene. Section 4.2 discusses previous mechanism developments and modelling studies, while the BOREAM β-pinene mechanism itself was already discussed in Section 2.2.2. In Section 4.3, a number of uncertainties in the BOREAM mechanism are summarised, and several sensitivity tests are presented. The simulation results are discussed in Sections 4.4 and 4.5. Finally, Section 4.6 will summarise the conclusions which can be drawn from these simulations.

4.1 β-pinene smog chamber studies

One of the first smog chamber studies on SOA formation due to oxidation of monoterpenes was Hatakeyama et al. (1989). For β-pinene ozonolysis, this study obtained yields of CO_2 ($27 \pm 2\%$), formaldehyde ($76 \pm 2\%$) and nopinone ($40 \pm 2\%$), and an SOA yield of about 13%. Arey et al. (1990) investigated the formation of gas phase products due to β-pinene oxidation by OH in the presence of NO_x, and obtained a nopinone yield of $30 \pm 4.5\%$. In Zhang et al. (1992), very low SOA yields were reported from the photooxidation of pinenes in presence of NO_x, from below 1% to maximum 5%, but it might be suspected that experimental problems, such as wall losses, dilution or SOA measurement issues might have contributed to the low values obtained. The experiments of Hoffmann et al. (1997), Griffin et al. (1999) and Fry et al. (2009) showed that relatively high yields resulted from the oxidation of β-pinene by OH and NO_3, higher than in the case of α-pinene.

The study of Yu et al. (1999a) was the first to identify several important products in the SOA, such as pinic acid, norpinic acid and several other carboxylic acids, lumped hydroxy pine ketones and 3-oxo-pina-ketone. Nopinone was found to be mainly confined to the gas phase. It should be noted that the carbon balance was below 50% (Yu et al., 1999a), as in all experiments the detection was biased towards compounds for which current detection methods were available, such as carboxylic acids. Jaoui and Kamens (2003) studied both gas and aerosol phase composition too, and quantified the yield of about 15 products, mainly carboxylic acids, carbonyl or alcohol-group bearing species. Ma and Marston (2008) confirmed the formation and determined yields of several carboxylic acids, such as pinic acid, norpinic acid, pinalic-3-acid, pinalic-4-acid and norpinalic acid, and possibly 4-OH-pinalic-3-acid, but these products only formed a fraction of the total SOA species, which remain mainly structurally undetermined. Iinuma et al. (2007) reported the detection of organosulfates in β-pinene ozonolysis experiments using acidic inorganic seed.

Docherty and Ziemann (2003) observed a strong influence of OH-scavengers on β-pinene ozonolysis SOA yields. Several later studies, such as Pathak et al. (2008), studied the temperature dependence of SOA yields. von Hessberg et al. (2009) investigated the effects of humidity and temperature in a flow tube experiment, in which the reaction time is only 40 s. Other studies included investigations of the mass spectral fragmentation (Kostenidou et al., 2009), volatility (Lee et al., 2011) and real refractive indices (Kim et al., 2010) of SOA generated from β-pinene ozonolysis.

In comparison with α-pinene, the oxidation of β-pinene by OH has received somewhat less attention. Besides the already mentioned OH studies, Carter (2000) studied the gas phase formation of ozone and several organic species, such as formaldehyde and nopinone, during high-NO_x photooxidation. Larsen et al. (2001), using UV-initiated β-pinene oxidation, saw the formation of pinic acid, norpinic acid and OH-pinonic acid. Wisthaler et al. (2001) quantified gas phase yields for acetone ($13 \pm 2\%$) and nopinone ($25 \pm 3\%$) at high-NO_x conditions. Jaoui and Kamens (2003) performed photooxidation experiments in presence of NO_x with sunlight, and identified products, which were often similar to those detected in β-pinene ozonolysis. Auld and Hastie (2011) identified several masses corresponding to nitrates for photooxidation experiments in presence of NO_x, although the precise structures and yields were not determined. Very few studies under low-NO_x conditions have been performed. Larsen et al. (2001) used H_2O_2 as an OH source, but did not report any SOA mass yields. To our knowledge, the only experiment for which SOA mass and yield times series are available is an experiment of the LEAK group (Ariane Kahnt, personal communication, 2014). Also, the ageing of β-pinene SOA has been studied much less extensively than for α-pinene.

4.2 Previous mechanism development and modelling of β-pinene oxidation

Among the earliest models for the gas phase chemistry of β-pinene oxidation, is the SAPRC model of Carter (2000), which is a parameterised model in which the oxidation by OH, O_3, $O(^3P)$ or NO_3 leads to a number of inorganic radicals, organic molecular products and a number of operators, used to represent the further chemistry of peroxy and alkoxy radicals in a simplified way. Product yields were optimised in order to reproduce VOC decay and the formation of ozone and a few organic products in smog chamber experiments. Whereas SAPRC could reproduce ozone formation reasonably well in the case of α-pinene, ozone formation and VOC decay were less well reproduced in the case of β-pinene (Carter, 2000).

Jenkin et al. (2000) proposed a mechanistic pathway towards pinic acid, in the hydroperoxide channel of the Criegee intermediate formed in the β-pinene ozonolysis mechanism (see Fig. 2.12 and Subsection 2.2.2.2), as also occurs in the α-pinene mechanism. The crucial step in this mechanism was a hypothetical 1,7-H-shift of an acyl alkoxy radical, leading to pinic acid. However, quantum-chemical calculations showed that the competing decomposition of the acyl alkoxy radical is much more favourable (Nguyen et al., 2009a). Since then, no alternative credible pathway has been proposed for the relatively high observed pinic acid yields from α- and β-pinene.

Jaoui and Kamens (2003) proposed a mechanism for β-pinene ozonolysis, of which some main pathways agree with the more recent mechanism of Nguyen et al. (2009a), which forms the basis for the BOREAM β-pinene mechanism (see Section 2.2.2.2). Jaoui and Kamens (2003) did not rely on detailed quantum-chemical calculations. The OH-mechanism proposed by Jaoui and Kamens (2003) does not yet include the possible ring-opening or ring-closure of peroxy or alkoxy radicals, which are main features of the Vereecken and Peeters (2012) mechanism.

The β-pinene ozonolysis and OH-oxidation mechanism in the MCMv3.2 model was presented in Jenkin (2004) and Pinho et al. (2007), and has already been discussed and compared with the current BOREAM mechanism in Section 2.2.2. Jenkin (2004) modelled SOA formation in two experiments of Yu et al. (1999a) and one of Jaoui and Kamens (2003). A major outcome of the study was that the estimated saturated vapour pressures had to be decreased by 2 orders of magnitude, in order to obtain a reasonable agreement with the observed SOA yields. This might point towards deficiencies in their vapour pressure estimation method, for which more recent alternatives can now be used, and possibly to a too low production of condensable products. Pinho et al. (2007)

investigated VOC consumption and formation of ozone, nopinone and formaldehyde for the photooxidation experiments of Carter (2000), and obtained a good agreement for 2 out of 3 modelled experiments. They also considered several variations on the standard MCM mechanism. Comparisons of these experiments with the BOREAM model will be presented hereafter in this chapter.

Chen and Griffin (2005) designed a 16-reaction condensed model, making use of the operator method introduced by Carter (2000), but with additional detail, and including a production of condensable species. Comparisons were made with gas phase measurements in photooxidation experiments using solar light (Griffin et al., 1999), although the good agreement found for VOC consumption and O_3 was likely obtained due to an ad hoc adjustment of the photolysis rates. For SOA, a good agreement with measurements was possible only if the estimated saturated vapour pressures were decreased by a factor of one thousand. This might again be partly explained by the use of less suitable vapour pressure estimation methods and by missing products in the mechanism.

Our BOREAM mechanism is based on the theoretical studies of Nguyen et al. (2009a) and Vereecken and Peeters (2012) (see Chapter 2). Vereecken and Peeters (2012) performed some limited modelling with an implementation of the new mechanism in a version of the MCM model, and verified the yields of products such as acetone, nopinone and formaldehyde against literature values, but did not perform further model comparisons against experiments. In the next sections, the BOREAM model performance will be evaluated for gas phase chemistry and SOA formation, and sensitivities to some critically uncertain reaction rates in the mechanism will be investigated.

4.3 Uncertainties in the current BOREAM β-pinene oxidation mechanism

The reaction rates calculated using quantum-chemical methods have a considerable uncertainty, which is often difficult to quantify (Nguyen et al., 2009a, Vereecken and Peeters, 2012). Typical uncertainties can in some cases be of the order of a factor of 2 (such as for the rate of the initial H-abstractions by OH) (Vereecken and Peeters, 2012). For most reactions in the mechanism, direct experimental reaction rate measurements are lacking. The SARs used to estimate rate constants also carry uncertainties that are difficult to estimate. In order to assess the importance of mechanistic uncertainties, we will undertake sensitivity tests to estimate the impact of variations in key reaction rates in the primary mechanism. The true uncertainty of the simulation results is probably larger than the uncertainty range suggested by these sensitivity tests. Further advances in

theoretical and experimental determinations of rate constants and product distributions will be necessary in order to increase the reliability of the model.

In this study we use the mechanism detailed in Section 2.2.2 as the standard mechanism. The impact on gas phase chemistry and SOA formation is investigated through some variations of important reaction rates or reaction branchings in this standard mechanism, given in Table 4.1, or by tests of assumptions made in previous studies (Jenkin, 2004, Pinho et al., 2007).

TABLE 4.1: BOREAM β-pinene mechanism variations tested in this chapter.

Code	Type
STA	Standard BOREAM β-pinene mechanism, described in Section 2.2.2.
RBA	Test in which **actBPINOH1** has 50:50 radical branching fractions towards **R1OO** and **BPINOH1**, instead of 70:30 (see Fig. 2.6).
RBB	Test in which **actBPINOH1** has 8:92 radical branching fractions towards **R1OO** and **BPINOH1**, instead of 70:30 (see Fig. 2.6).
BR2	Test in which the branching fractions towards the biperoxy radical **RADDIO** or the bicyclic alkane **C8BC** are set to 100:0, instead of 50:50, as in the standard mechanism.
BR3	Test in which the branching fractions towards the biperoxy radical **RADDIO** or the bicyclic alkane **C8BC** are set to 0:100, instead of 50:50, as in the standard mechanism. This corresponds to the branching in the current MCMv3.2 model.
O31	Test in which the β-pinene ozonolysis rate has been scaled down by a factor of 0.673, leading to a value of 1.5×10^{-17} cm^3 molecules^{-1} s^{-1} at 298 K, matching the recommendation of Atkinson (1994).
O32	Same as RBA, but with the β-pinene ozonolysis rate scaled down by a factor of 0.673.

4.4 Model simulations of photooxidation and ozonolysis experiments: gas-phase chemistry

In this section, BOREAM is confronted with β-pinene oxidation experiments for which measurements of gas phase compounds are available. Note that in some photooxidation experiments (Carter, 2000), ozone contributes more to the oxidation of β-pinene than OH, while in some dark ozonolysis experiments (Exp. 14/04/2011, Kahnt, 2012), when no OH scavenger is used, OH contributes significantly (see Table 4.2). Also, in some cases O(^{3}P) contributes up to about 25% of the total loss, such as for ETC442 in Carter (2000).

TABLE 4.2: Initial β-pinene concentration (VOC_i) and simulated amount of β-pinene oxidised at the end of the experiment (in ppb), and VOC_{OH}, VOC_{O_3}, VOC_{NO_3} and $VOC_{O(^3P)}$, the percentages of β-pinene oxidised by the 4 oxidants considered, for simulations with the standard mechanism (using $j_{NO_2} = 0.351$ min^{-1} in the case of Carter, 2000).

experiment	VOC_i	$-\Delta VOC$	VOC_{OH}	VOC_{O_3}	VOC_{NO_3}	$VOC_{O(^3P)}$
Carter (2000)						
ETC434	957	932	31.6	52.7	10.5	5.2
ETC435	282.5	262.2	39.0	41.1	15.9	4.1
ETC442	274.3	99.1	45.3	25.9	3.6	25.1
Böge (2009)						
07/03/2008	103.2	25.1	92.7	6.8	0.8	2.8
28/04/2008	99.5	19.3	89.6	7.2	0.7	2.6
Hoffmann et al. (1997)						
β-pinene + OH	95	95	51.1	20.3	22.7	5.8
Kahnt (2012)						
14/04/2011	100	38	35.8	64.2	0.0	0.0

The experiments of Carter (2000) were previously modelled by Carter (2000), using the condensed SAPRC-model, and by Pinho et al. (2007), using the detailed MCM model version 3.1. For three experiments (ETC434, ETC435 and ETC442), β-pinene, nopinone, formaldehyde and $D(O_3 - NO)$ (defined as ($[O_3]_{final}$ - $[NO]_{final}$) - ($[O_3]_{initial}$ - $[NO]_{initial}$)), which is a measure of the potential for ozone formation, were given and compared with simulations. Figs. 8 and 9 of Pinho et al. (2007) show that β-pinene decomposition and $D(O_3 - NO)$ were reproduced quite well, except for the last part of ETC434, where $D(O_3 - NO)$ was systematically underestimated.

The spectrum of the UV lamps (Carter et al., 2005) has been scaled based on the given range of the photolysis rates of NO_2, 0.251 to 0.351 min^{-1} (Pinho et al., 2007), as those rates were believed to vary between experiments (Carter, 2000), even though the same lamps were used. Two simulations were performed with BOREAM, using photolysis rates corresponding to either the lower or the higher end of the radiation intensity range of the lamps, shown in dashed and solid lines respectively on Figs. 4.1 and 4.2. Simulations by Pinho et al. (2007) (scenario 1) are given in black.

Comparison of the standard run using higher radiation values (blue solid line) with the measurements (black diamonds) shows that its performance is variable (see Table 4.3). In experiment ETC434, ozone formation and β-pinene decay are overestimated (by about 25% on average). For experiment ETC435, ozone formation is underestimated during the first 3.5 hours, and overestimated afterwards, while for ETC442, ozone formation and β-pinene consumption are persistently underestimated (by about 30% and 40%,

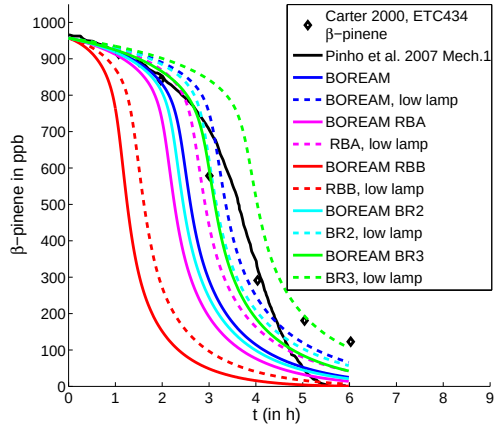

(A) β-pinene for ETC434 of Carter (2000)

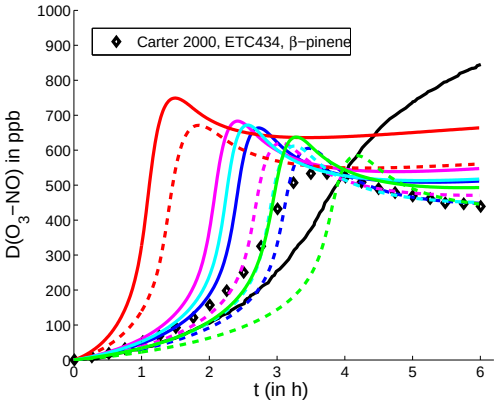

(B) $D(\mathrm{O_3} - \mathrm{NO})$

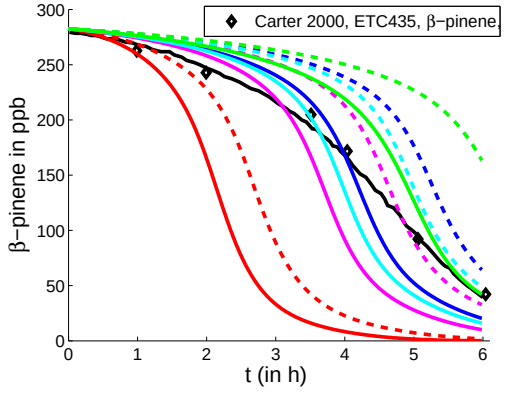

(C) β-pinene for ETC435 of Carter (2000)

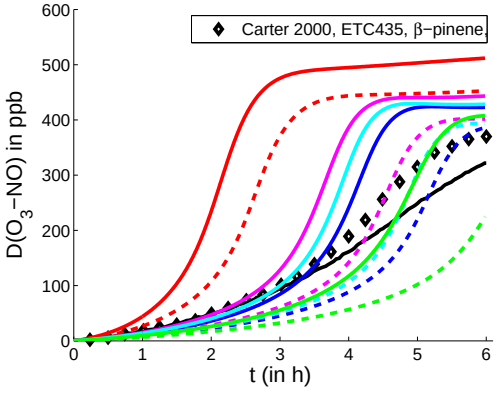

(D) $D(\mathrm{O_3} - \mathrm{NO})$

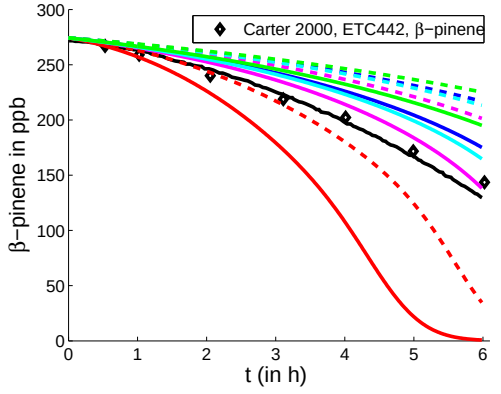

(E) β-pinene for ETC442 of Carter (2000)

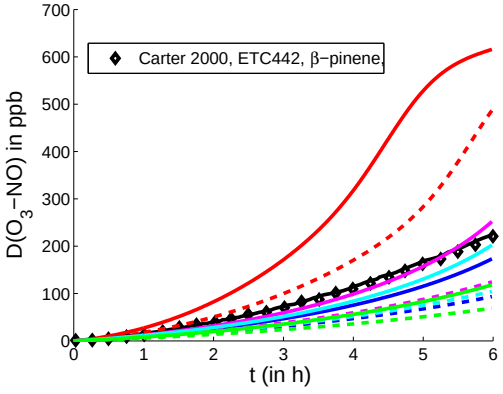

(F) $D(\mathrm{O_3} - \mathrm{NO})$

FIGURE 4.1: Simulations of experiments ETC434, ETC435 and ETC442 (Carter, 2000, Pinho et al., 2007) for β-pinene and $D(\mathrm{O_3} - \mathrm{NO})$. Black diamonds are experimental values, the black solid line represents Mechanism 1 of Pinho et al. (2007) (with branching of 8.1% towards **R1OO**). BOREAM simulations are conducted for both the high and low value of $j_{\mathrm{NO_2}}$ given by Pinho et al. (2007) (solid and dashed). Standard BOREAM simulations are given in blue. Sensitivity tests for the main radical branching fractions in the OH-oxidation mechanism, between **R1OO**/**BPINOH1**, are given in magenta (RBA, 50%/50%) and red (8.1%/91.9%, RBB). Tests BR2 and BR3 are shown as cyan and green lines.

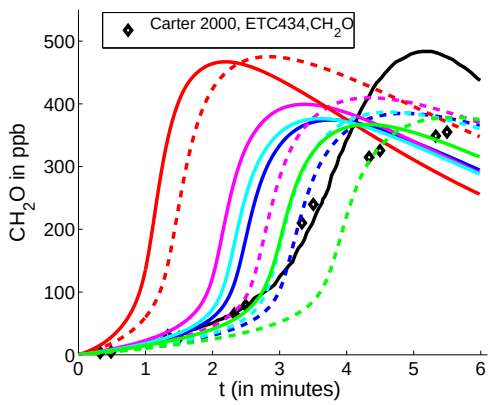

(A) CH_2O for ETC434 of Carter (2000)

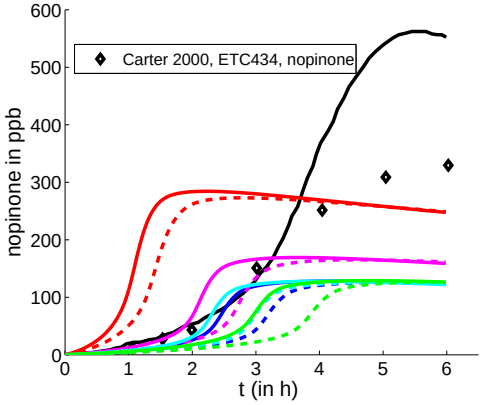

(B) ETC434 nopinone

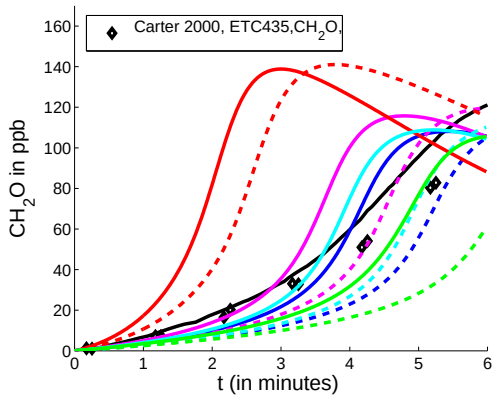

(C) CH_2O for ETC435 of Carter (2000)

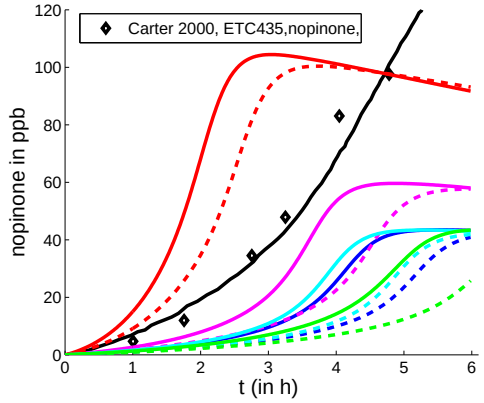

(D) ETC435 nopinone

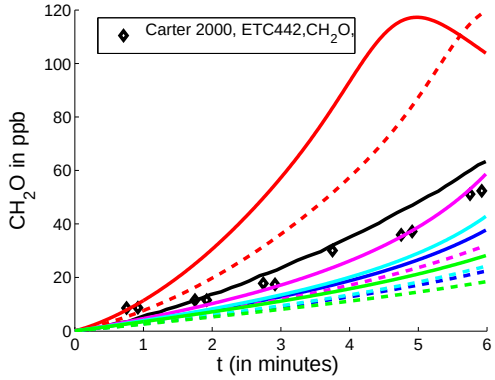

(E) CH_2O for ETC442 of Carter (2000)

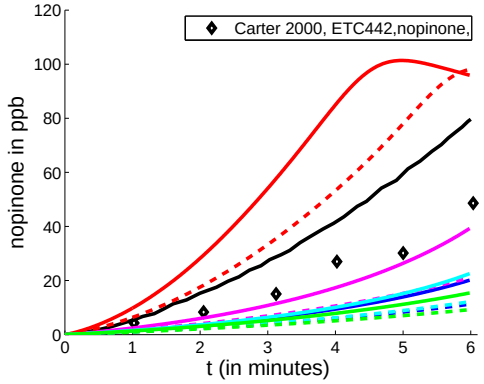

(F) ETC442 nopinone

FIGURE 4.2: As Fig. 4.1, for formaldehyde and nopinone.

TABLE 4.3: The mean relative deviations (MRD, defined as $\overline{(C_{\mathrm{mod}} - C_{\mathrm{exp}})/C_{\mathrm{exp}}}$, where C_{exp} and C_{mod} are the experimentally determined and modelled concentrations, and the average is taken over all data points from one hour after the start until the end of the experiment, and over the three experiments ETC434, ETC435 and ETC442 of Carter (2000)) and mean absolute relative deviations (MARD, defined as $\overline{|C_{\mathrm{mod}} - C_{\mathrm{exp}}|/C_{\mathrm{exp}}}$), in percent, for different mechanism variations for β-pinene experiments of Carter (2000). "hl" and "ll" stand for high lamp and low lamp strength, meaning that the higher or lower end of the radiation intensity range was chosen, corresponding to $j_{\mathrm{NO_2}} = 0.351$ min^{-1} or 0.251 min^{-1}.

Scenario	-Δ β-pinene		$D(\mathrm{O_3} - \mathrm{NO})$		$\mathrm{CH_2O}$		nopinone	
	MRD	MARD	MRD	MARD	MRD	MARD	MRD	MARD
STA hl	-8	29	-2	26	0	36	-57	57
STA ll	-46	48	-38	39	-36	41	-73	73
RBA hl	19	42	24	32	39	49	-24	32
RBA ll	-28	37	-21	29	-12	33	-52	52
RBB hl	205	205	194	193	258	260	267	269
RBB ll	110	115	98	98	172	172	152	153
BR2 hl	0	32	9	28	12	41	-54	54
BR2 ll	-40	43	-31	34	-30	40	-71	71
BR3 hl	-29	32	-28	33	-24	32	-66	66
BR3 ll	-58	58	-54	56	-51	53	-78	78
O31 hl	-50	50	-43	51	-51	51	-77	77
O31 ll	-69	69	-64	69	-69	69	-85	85
O32 hl	-34	37	-26	38	-29	34	-57	57
O32 ll	-61	61	-53	59	-55	56	-73	73

respectively). There is a considerable decrease in ozone formation when assuming lower lamp intensities, leading to better agreement for experiment ETC434, but worsening the underestimation of ozone production for the other two experiments. The simulations of Pinho et al. (2007) seem to reproduce the observed concentrations more closely, except in experiment ETC434. The observed decrease, which is qualitatively reproduced by BOREAM, is caused by formation of SOA, likely not taken into account in Pinho et al. (2007). SOA formation causes an important fraction of organic compounds to condense, decreasing the reactivity in the gas phase, and by consequence the potential for ozone formation. SOA formation was strongest in ETC434, as initial VOC concentrations were much higher than in the other two experiments.

As explained in Section 2.2.2, the MCM β-pinene OH mechanism differs strongly from the more recent mechanism of Vereecken and Peeters (2012), regarding the fate of a number of important radicals. Here, we focus our analysis on differences for the major compounds formed in the early steps of the mechanism. In scenario RBA, the branching of reactions of **actBPINOH1** towards **R1OO** and **BPINOH1** is changed from 70:30 to 50:50, which is still very likely within the uncertainty of the quantum-chemical calculations of Vereecken and Peeters (2012). This change increases ozone formation. For

the higher lamp intensity, this improves agreement with experiment ETC442 for ozone (to a deviation of about 10%), but it leads to overestimations of about 50% and 35% for experiments ETC434 and ETC435. In scenario RBB, the branching of reactions of **actBPINOH1** towards **R1OO** and **BPINOH1** is set to 8:92, as in the current MCM model, and scenario 1 of Pinho et al. (2007). This sharply increases ozone formation, which becomes strongly overestimated in all cases, from about 160% for experiment ETC442, up to 220% for experiment ETC435. Surprisingly, the difference of BOREAM results with the simulations of Pinho et al. (2007) is strongly increased in RBB, even though **actBPINOH1** undergoes the same reactions in both mechanisms. This is explained by the large difference between the respective mechanisms for the products of **actBPINOH1**. Also differences in the SARs and photolysis rates between the MCM model and BOREAM might contribute to this important difference in ozone formation between the two models. Clearly, the uncertainty in the reaction branching for **actBPINOH1** has important consequences for ozone formation.

The comparisons for formaldehyde and nopinone are shown in Fig. 4.2. In the standard mechanism, formaldehyde is overestimated in ETC334 by 35% on average, underestimated by about 35% for ETC442, and underestimated before 3.5 hours after the start, and overestimated afterwards, for ETC435. Formaldehyde production is larger in mechanism RBA than in the standard mechanism, leading to overestimations for ETC434 and 435, and good agreement for ETC442. Nopinone formation is consistently too low for most scenarios, by more than a factor of 2 in most cases, and only in scenario RBA in the case of high photolysis rates is the underestimation more moderate. In scenario RBB, nopinone formation is overestimated by about 100% to 400%, depending on the experiment and the lamp intensity. Nopinone is produced mostly in the minor OH addition channel (towards **BPINOH2**) and in the **BPINOH1** channel (see Fig. 2.6). However, the minor CI + formaldehyde and SCI + H_2O channels of the ozonolysis mechanism also contribute.

The sensitivity tests for the branching fraction of the biperoxy radicals and the bicyclic alkane in the decomposition of the lactones are shown in cyan and green in Figs. 4.1 and 4.2. Increasing the yield of peroxy biradicals (BR2) is found to increase ozone formation, while the scenario in which only bicyclic alkanes are produced (BR3) decreases it. Neither of these scenarios lead to a markedly better model agreement for all three experiments, with underestimations of $D(O_3 - NO)$ in all cases for ETC442.

In Fig. 4.3, the results of two additional tests, O31 and O32, are shown for experiment ETC434. In those tests, the previous simulations STA and RBA were altered by adopting the lower rate for β-pinene ozonolysis recommended by Atkinson (1994), which is also used in the MCMv3.2, and by Pinho et al. (2007), down from the higher value in the

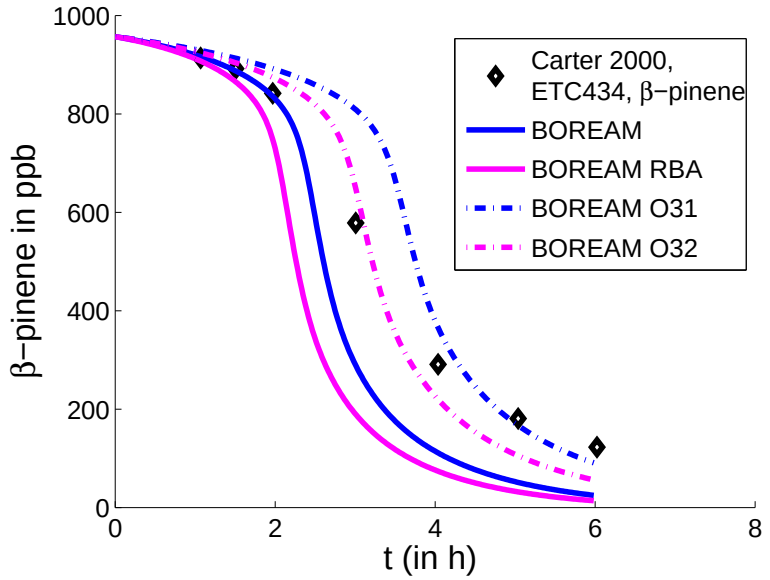

(A) β-pinene for ETC434 of Carter (2000)

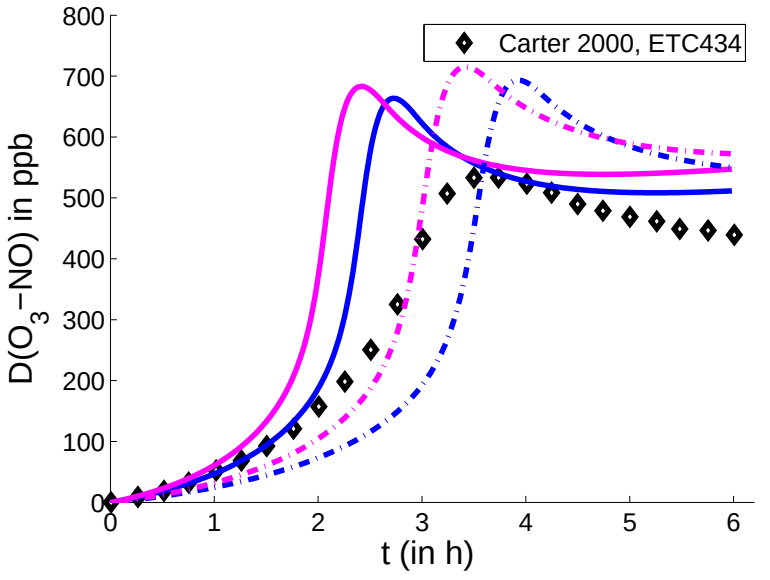

(B) $D(O_3 - NO)$

FIGURE 4.3: Simulations of gas phase chemistry of Experiment ETC434 (Carter, 2000, Pinho et al., 2007) for β-pinene and $D(O_3 - NO)$. Black diamonds are experimental values. BOREAM simulations are conducted for the high range value of j_{NO_2} given by Pinho et al. (2007). Standard BOREAM simulations are given in blue solid lines, while these for scenario RBA are given in solid magenta. Sensitivity tests O31 and O32, in which the O_3 reaction rate is lowered to $1.5 \times 10^{-17}\,cm^3\,molecules^{-1}\,s^{-1}$ (as recommended by Atkinson (1994) at 298 K, and used in the MCM model), but which are otherwise identical to STA and RBA, are given in dash-dotted lines.

TABLE 4.4: Mean relative deviations (MRD) and mean absolute relative deviations (MARD, see Table 4.3 for the definitions) between experimental and modelled concentrations, averaged over the two β-pinene photooxidation experiments (7/3/2008 and 28/4/2008) in the LEAK chamber (Böge, 2009), for different mechanism variations. Values are shown in percent.

Scenario	-Δ β-pinene		O_3		NO		$NO_2 + CH_3ONO$	
	MRD	MARD	MRD	MARD	MRD	MARD	MRD	MARD
STA	-28	-10	56	56	29	29	-3	3
RBA	-9.5	12	92	92	16	16	10	10
RBB	66	66	295	295	-24	24	52	52

standard BOREAM mechanism, based on Nguyen et al. (2009a) (see Section 2.2.2.2). Lowering the ozonolysis rate is found to delay both the β-pinene decay and ozone formation. Whereas the standard mechanism overestimates β-pinene consumption in ETC434, the O31 simulation underestimates it for most of the experiment. With respect to the RBA mechanism, which overestimates β-pinene consumption, scenario O32 markedly improves the agreement with the observations. For ETC435 and ETC442, however, these tests worsen the underestimations of β-pinene decay and $D(O_3 - NO)$.

Overall, Table 4.3 shows that no tested scenario offers a clear improvement in comparison with the measured values over the STA high lamp scenario, with only the RBA hl and BR2 hl achieving similar agreement, i.e. about 30% mean absolute relative deviation for β-pinene, $D(O_3 - NO)$ and formaldehyde, and about 50% underestimation of nopinone.

BOREAM is also confronted against two experiments (07/03/2008 and 28/04/2008) performed in the LEAK chamber (Iinuma et al., 2004), available in the Eurochamp database (Böge, 2009). These experiments made use of Osram-Eversun UV-lamps, for which a relative spectrum was found in Petrovič et al. (2012). Directly measured photolysis rates were not available, so the calculated rates were scaled by a factor chosen in order to provide a reasonable match with β-pinene, O_3, ozone and NO_x, leading to $j(NO_2) = 5.54 \times 10^{-3}$ s^{-1}. This introduces some additional uncertainty in the simulations. β-pinene (103.2 and 100 ppb), NO (99.5 and 99.8 ppb) and CH_3ONO (8.3 ppb and 11.8 ppb) were introduced at the start of the experiments. Comparison of simulations and measurements suggests that some additional NO (ca. 18 ppb) was added during the first 6 minutes of the experiment on 07/03/2008.

Table 4.2 shows that β-pinene is mainly oxidised by OH in these experiments. Figures 4.4a and 4.4b and Table 4.4 show BOREAM simulation results for the mechanisms STA, RBA and RBB. As previously, ozone production and β-pinene consumption are increased for the last two scenarios. Scenario RBA gives the best match for the measured β-pinene evolution, but leads to an increased overestimation of ozone (with about 120% and 60%

on average for LEAK 7/3/2008 and 28/4/2008, respectively). In Scenario RBB, ozone is strongly overestimated. No tested scenario reproduces all measured gas phase compounds simultaneously. The uncertainty on the photolysis rates complicates the analysis, as not all possible scalings of the radiation have been tested.

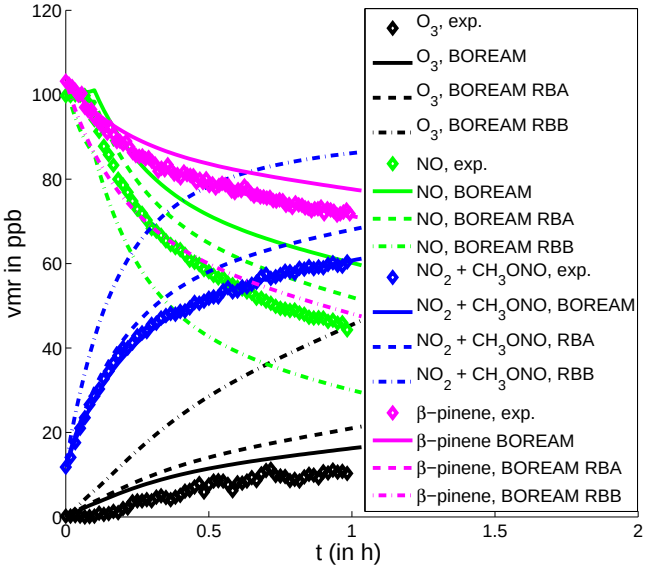

(A) LEAK 7/3/2008, β-pinene, O_3, NO and NO_y

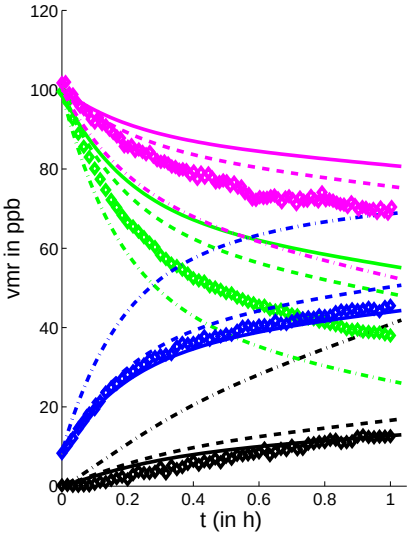

(B) LEAK 28/4/2008, β-pinene, O_3, NO and NO_y

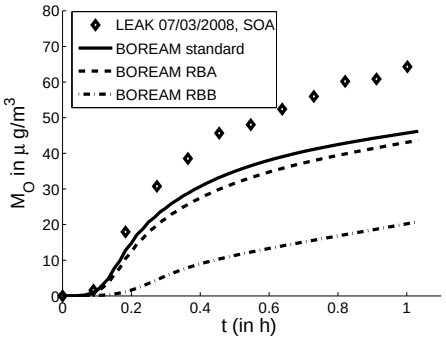

(C) LEAK 7/3/2008, SOA

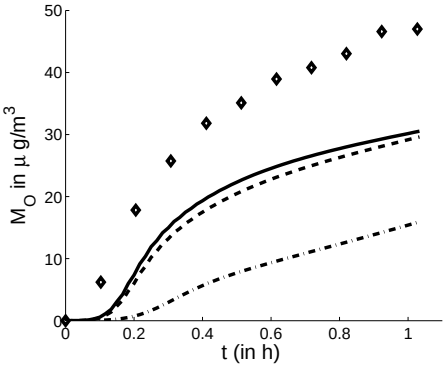

(D) LEAK 28/4/2008, SOA

FIGURE 4.4: Simulated and observed temporal profiles for the LEAK chamber (Iinuma et al., 2007) experiments on 7/3/2008 and 28/04/2008 (Böge, 2009), available in the EUROCHAMP database (EUROCHAMP - EU 7th FP Infrastructure Initiative, 2014). Given are measurements and simulations for β-pinene, O_3, NO, the sum NO_2 + CH_3ONO and SOA. Simulations were performed with the standard β-pinene mechanism and for the test simulations RBA and RBB (see text).

The β-pinene photooxidation experiments of Hoffmann et al. (1997) and Griffin et al. (1999) made use of solar light. Given the unavailability of photolysis rate measurements, the fact that the radiation actinic flux was variable due to changes in local time and cloudiness, introduces a potentially large uncertainty in the calculation. In Hoffmann

et al. (1997) and Chen and Griffin (2005) a time-variable scaling factor for the radiative fluxes was adjusted in order to minimise the difference in measured and modelled O_3 and NO. The obvious flaw of this approach is that it assumes that model discrepancies are only due to photolysis rates. In BOREAM, the photolysis rates are calculated based on the solar zenith angle, which is simulated for the location and time using a publicly available algorithm (Roy, 2009, Reda and Andreas, 2008), but no adjustment for cloudiness is applied, due to lack of data. Fig. 4.5 shows the comparisons for the photooxidation experiment of Hoffmann et al. (1997). β-pinene consumption is modelled reasonably well by both the standard version and the RBA scenario. Ozone is overestimated during the first hour, and is better reproduced by the standard run than by the RBA scenario. The RBB scenario again leads to an ozone production which is far too large. NO_x is less well reproduced by the standard and RBA simulations, with underestimations for NO_2 and overestimations for NO. Similar results are obtained for the photooxidation experiments of Griffin et al. (1999).

4.5 Model simulations of smog chamber experiments: secondary organic aerosol

In this section we evaluate the ability of BOREAM to simulate SOA formation during β-pinene oxidation. We distinguish between dark ozonolysis and photooxidation experiments. For many of the considered experiments, these are, to our knowledge, the first simulations performed with a detailed chemical aerosol formation model.

4.5.1 Dark ozonolysis experiments

Similarly to Pathak et al. (2007) for α-pinene, Pathak et al. (2008) performed a number of dark β-pinene ozonolysis experiments in order to estimate the impact of initial VOC concentration, temperature and seed on SOA yields. These experiments were conducted with an OH-scavenger, ensuring that ozone was the main oxidant, and that secondary chemistry due to OH was of limited importance. Simulated and measured aerosol yields are compared in Fig. 4.6. Two different hypotheses were tested regarding the influence of the initial inorganic seed on SOA. In the first scenario, we assumed that the inorganic seed does not contribute to the total absorbing mass. In order to account for the limited amount of organic compounds which can be adsorbed on its surface (a process expected to play a significant role in the early stage of the experiment, when organic aerosol mass is close to zero), a small initial organic aerosol mass is supposed, estimated from the measured number of particles and assuming a diameter of 7.5–10 nm. This is enough to

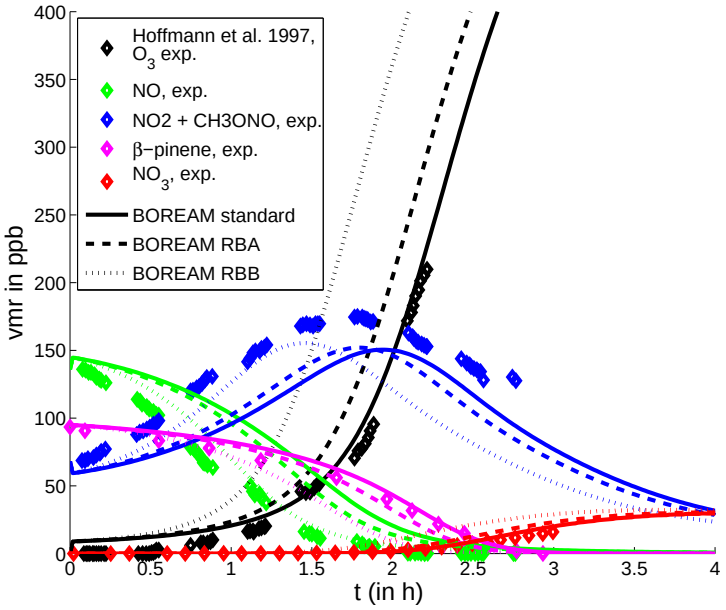

(A) Hoffmann et al. (1997), O_3, NO, NO_2, β-pinene, and NO_3

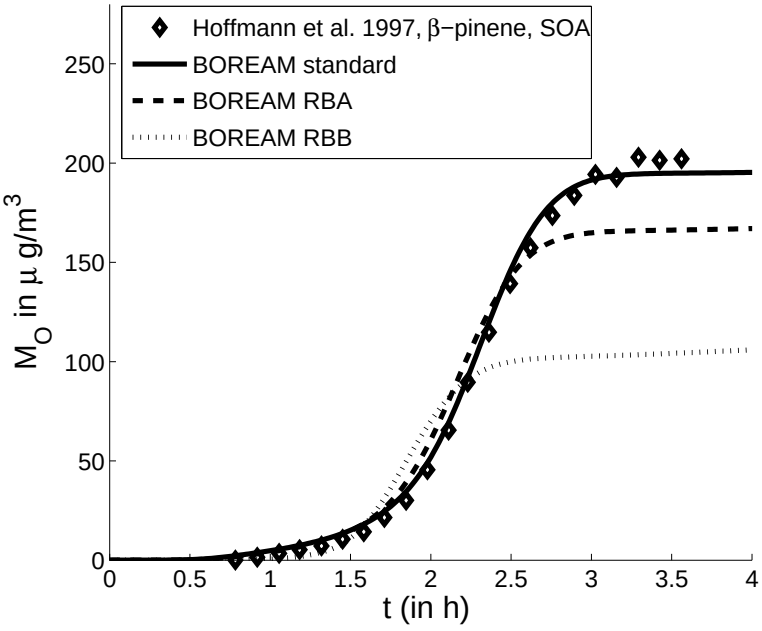

(B) Hoffmann et al. (1997), β-pinene photoox.; SOA

FIGURE 4.5: Simulations and measurement for the β-pinene photooxidation experiment of Hoffmann et al. (1997), using solar radiation. For the calculation of the photolysis rates for simulations, it was assumed that the experiment started at 10:30 am, and that there was no cloud cover. Given are measurements and simulations for O_3, NO, NO_2, β-pinene, and NO_3 (for which the values are given in ppt instead of ppb in this graph) and SOA. Simulations were performed with the standard β-pinene mechanism and test simulations RBA and RBB (see text).

allow the initial aerosol growth to take off, but in most cases small enough to ensure that its contribution to total aerosol mass can be neglected during most of the course of the experiment. In the second scenario, the inorganic aerosol is assumed to fully contribute to the absorbing aerosol mass, strongly increasing this last quantity's initial value.

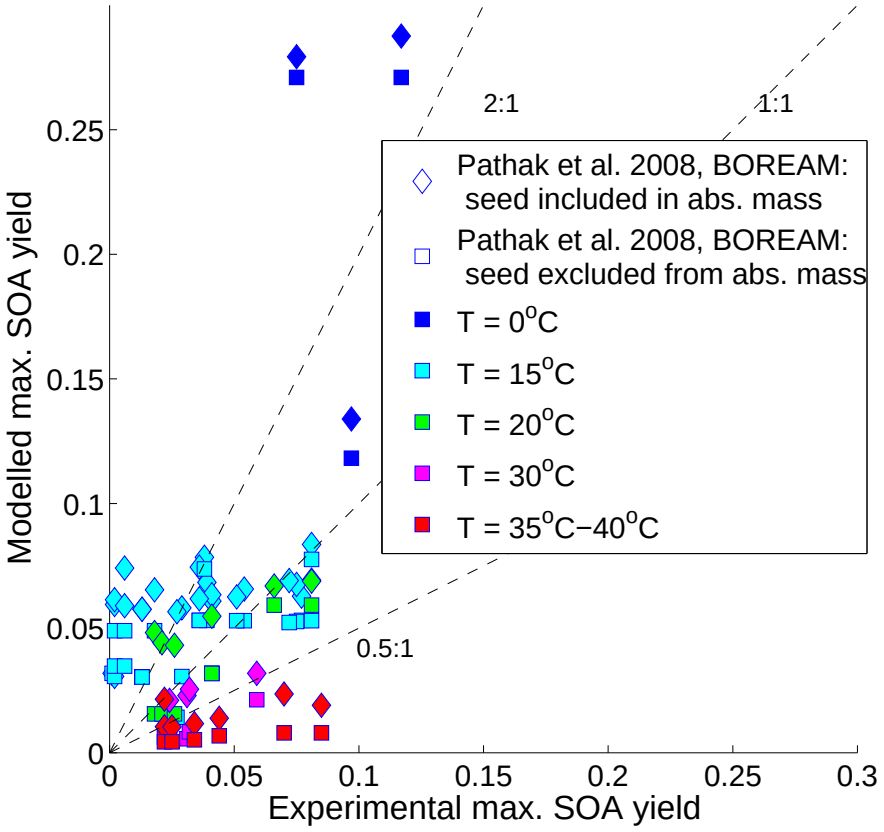

FIGURE 4.6: Overview of simulated versus measured SOA concentrations for β-pinene ozonolysis experiments of Pathak et al. (2008).

It can be observed from Fig. 4.6 that temperature has a strong influence on the model performance. At the lowest temperatures (0 and 15 °C) the simulated yield are often overestimated by more than a factor two, whereas at the highest temperatures (30 and 40 °C) most yields are underestimated by more than a factor two. The choice for the treatment of seed particles is seen to have a strong impact at high temperatures, but it does not fundamentally affect the picture of the temperature dependence. In Fig. 4.7, the time-evolution of SOA in five experiments at different temperatures exhibits the same pattern. The two sensitivity tests BR2 and BR3, producing respectively more or less biradicals in the stabilisation channel of the dioxirane **DIO**, are shown to increase or decrease the SOA yields, but do not remedy the problem of the SOA temperature-dependence of the model.

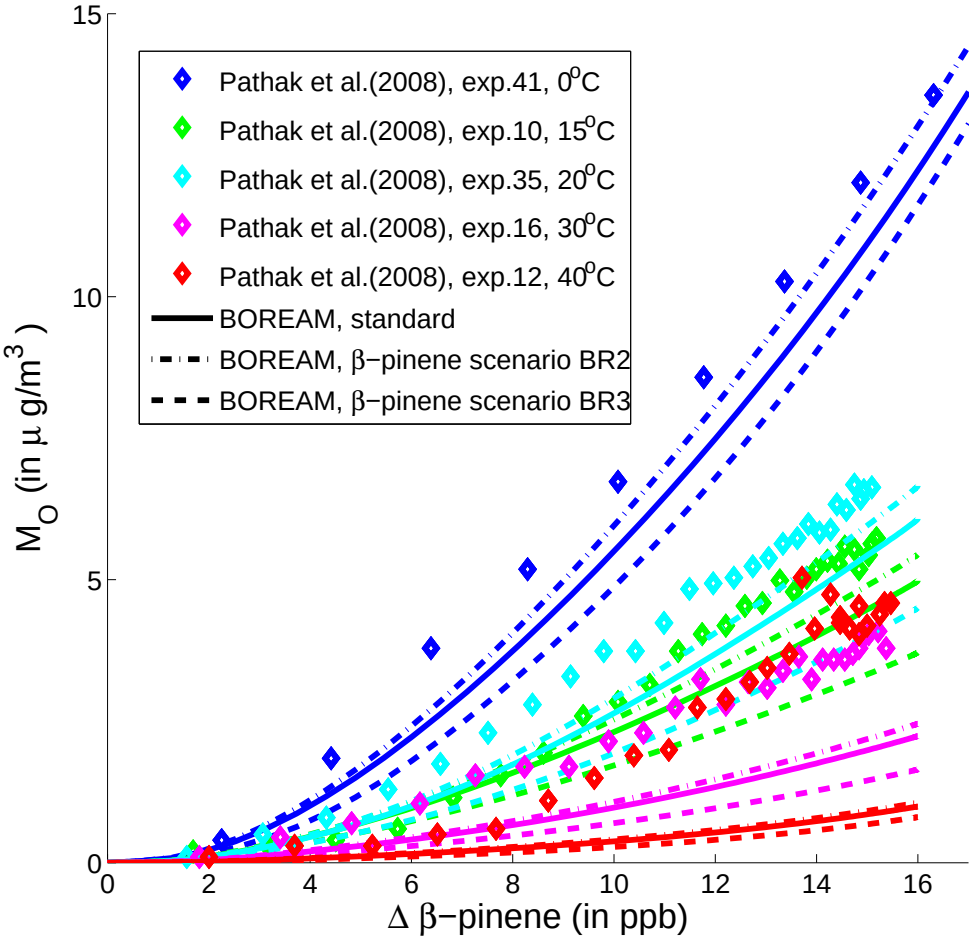

FIGURE 4.7: Simulations with the BOREAM standard, BR2 and BR3 (with respectively 50%, 100% and 0% of biradicals produced in the stabilisation channel of the dioxirane **DIO**) of five experiments at different temperatures between 0 °C and 40 °C in Pathak et al. (2008).

The temperature dependence of the model performance is similar to that found in Section 3.1.2 for α-pinene dark ozonolysis in Pathak et al. (2007). There the analysis suggested that the observations can be explained by a combination of a decreased temperature-dependence of the partitioning constant and formation of an additional amount of very condensable material. The similar SOA yield temperature dependence for β-pinene suggests the same conclusion here. The extra condensable material needed to increase the yields at high temperatures could be due to oligomerisation reactions, currently not represented in BOREAM, or to missing gas-phase pathways. The uncertainty around the production of pinic acid, which is one of the main SOA constituents, could play a role. The decreased temperature-dependence of partitioning constants is more difficult to rationalise. The EVAPORATION method was used here for vapour pressure

estimation, which was found to give similar results as the Capouet-Müller method (Capouet and Müller, 2006) in Chapter 3. We do not know of any indication for such a decreased temperature dependence of vapour pressures. Another possibility could be a temperature-dependence of the reaction branchings of the SCI. An enhanced decomposition rate of SCI at higher temperature would decrease the yield of the quite volatile nopinone, while increasing the importance of the hydroperoxide channel (with production of for example pinic acid) or the biradical channels, leading to more condensable species.

Another comprehensive study on β-pinene dark ozonolysis was performed by von Hessberg et al. (2009), where the ozonolysis took place in a laminar flow tube, and concentrations were measured at a point in the flow which corresponded to about 40 s of reaction time. Therefore, it can be expected that the BOREAM model, due to its single diameter mode and constant aerosol number, and the absence of explicit coagulation and nucleation representations, should not model this early SOA formation well. The standard BOREAM model indeed strongly underestimates the yields, with more than two thirds of the calculated yields being underestimated by more than a factor of 3 (see Fig. 4.8a). A simulation in which practically instantaneous equilibration is achieved between gas and aerosol shows a much better agreement between model and experiment (see Fig. 4.8b). This shows that kinetic limitations play a large role at this time scale. In the standard mechanism, the mass accommodation factor is set to 0.3. Tests using a value of unity increased some of the yields, but overall strong underestimations remained. In BOREAM the number of aerosol particles was set based on the values measured by von Hessberg et al. (2009) at 40 s. Due to coagulation, aerosol numbers might have already strongly decreased before 40 s, causing a model underestimation of aerosol surface. However, as for Pathak et al. (2008), it cannot be excluded that other factors cause a large model uncertainty, reflected in the observed deviations.

For a number of additional experiments, the model performance in reproducing the SOA yield is shown in Fig. 4.9. The majority of experimental SOA mass yields is reproduced to within a factor of 2, but as previously (for Griffin et al. (1999), Yu et al. (1999a) and Kim et al. (2010)) the yields are sometimes underestimated by more than a factor of 2 above 25 °C. There are also some yield overestimations by a factor 2 or more for experiments at or near room temperature, such as for some experiments of Kahnt (2012), Lee et al. (2011) and Kostenidou et al. (2009). Overall, the temperature dependence of the bias is less pronounced than in Pathak et al. (2008), in part because the initial VOC concentrations were higher in several experiments. Indeed, experiments with the higher initial VOC have higher concentrations of condensable species, and therefore generally higher SOA mass, which in turn enhances condensation. Therefore, any model overestimation of the

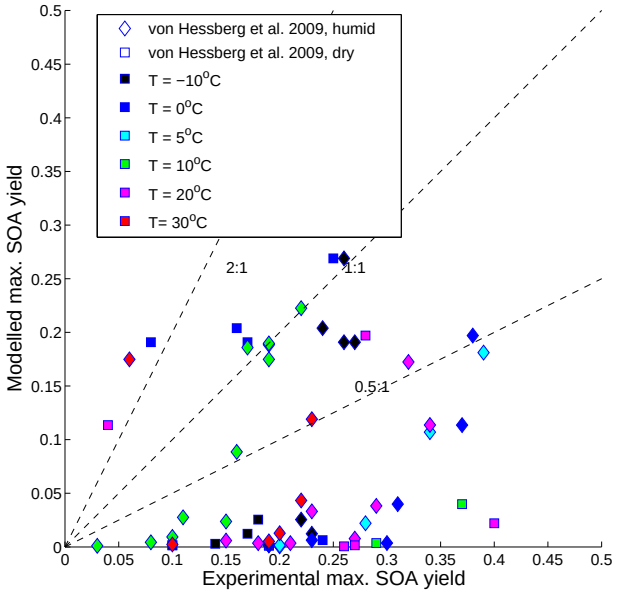

(A) standard BOREAM simulations

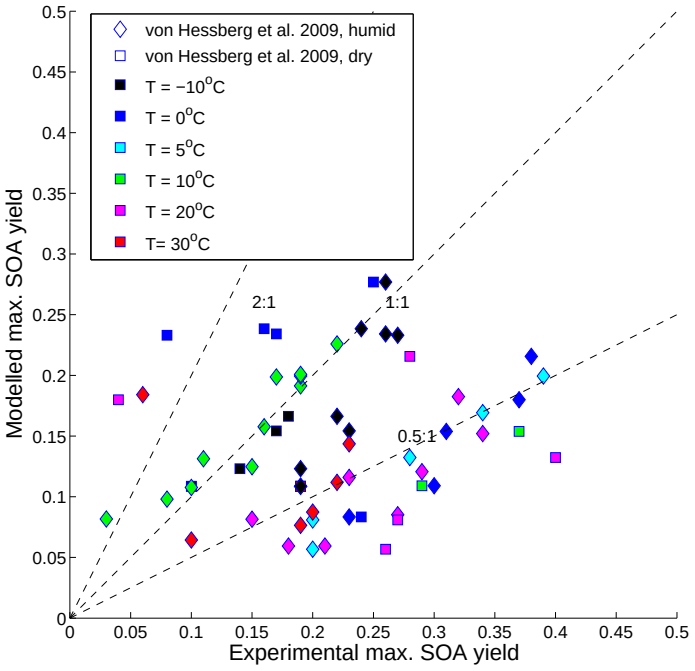

(B) BOREAM with very fast partitioning equilibration

FIGURE 4.8: Overview of simulated versus measured SOA yields for β-pinene ozonolysis flow-tube experiments of von Hessberg et al. (2009). Results are shown for (A) the standard model, and (B) a simulation assuming instantaneous partitioning between the gas and aerosol phase.

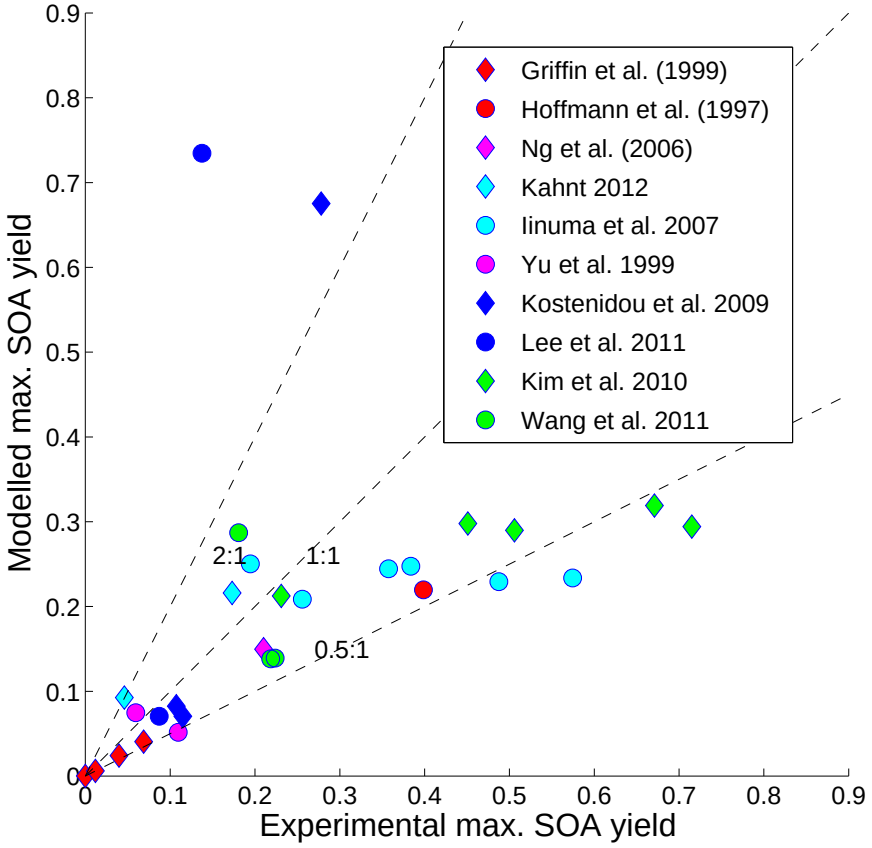

FIGURE 4.9: Simulated versus measured SOA yields for β-pinene ozonolysis experiments (besides Pathak et al. (2008) and von Hessberg et al. (2009)).

saturated vapour pressures at higher temperatures will then prevent fewer species from partitioning to the SOA than if the absorbing mass were lower.

4.5.2 OH-oxidation experiments

In Fig. 4.10 the BOREAM SOA yields are compared with measurement values in β-pinene photooxidation experiments. All experiments except one (LEAK, 13/08/2012) were conducted with NO_x. Time profiles of SOA concentrations are shown in Figs. 4.4c and 4.4d for the high-NO_x experiments in the LEAK chamber (Böge, 2009), in Fig. 4.5b for the photooxidation experiment using solar light of Hoffmann et al. (1997), and in Fig. 4.11 for the low-NO_x 13/08/2012 experiments conducted in the LEAK chamber (TROPOS, Leipzig Atmospheric Chemistry Group, 2014).

A relatively good agreement (within a factor 2) is obtained with the experimental SOA yields in the majority of cases when using EVAPORATION vapour pressures. Underestimations are found for the experiments at the highest temperatures (Griffin et al., 1999), in line with the noted trend for dark ozonolysis. For the LEAK experiments, M_O is underestimated by the model (Fig. 4.4), but this can to a large degree be explained by the fact that β-pinene consumption was also underestimated (Figs. 4.4a and 4.4c). Overestimations can be seen for one experiment of Griffin et al. (1999), for Ng et al. (2006) and for the low NO_x experiment in the LEAK chamber (TROPOS, Leipzig Atmospheric Chemistry Group, 2014) (see Fig. 4.11). In this last experiment, OH exposure was considerable (2.3×10^7 molecules cm^{-3} h). The overestimation has very probably similar reasons as the overestimates for α-pinene SOA ageing experiments, which will be discussed in Chapter 5. The sensitivity tests RBA and RBB lead to reductions in SOA yield. This confirms that some of the multi-functional compounds in the ring-opening branch of the recent mechanism of Vereecken and Peeters (2012) are an important source of SOA.

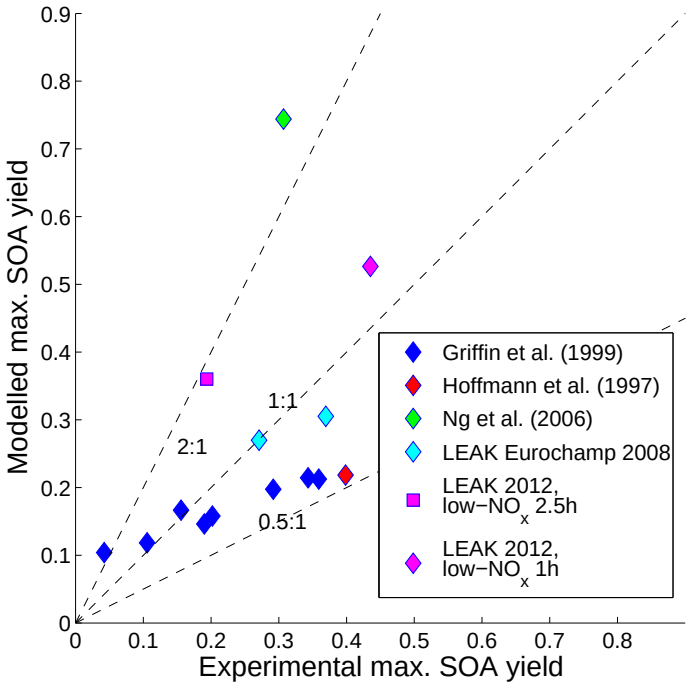

FIGURE 4.10: Simulated versus measured SOA yields for β-pinene photooxidation experiments.

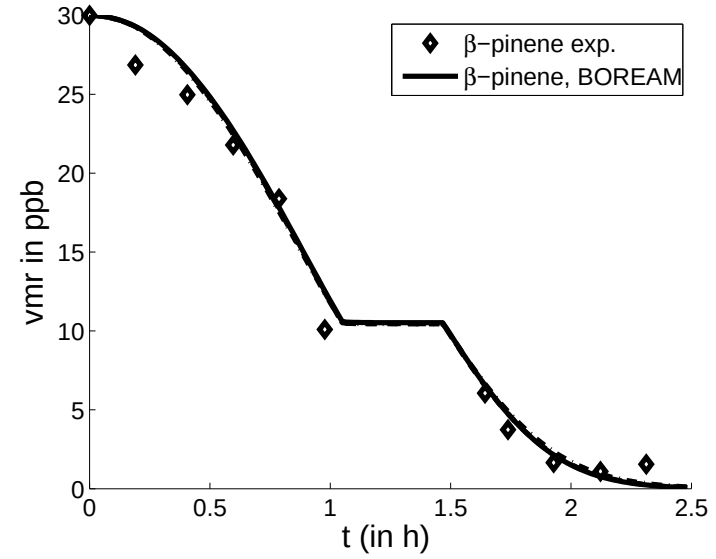

(A) β-pinene

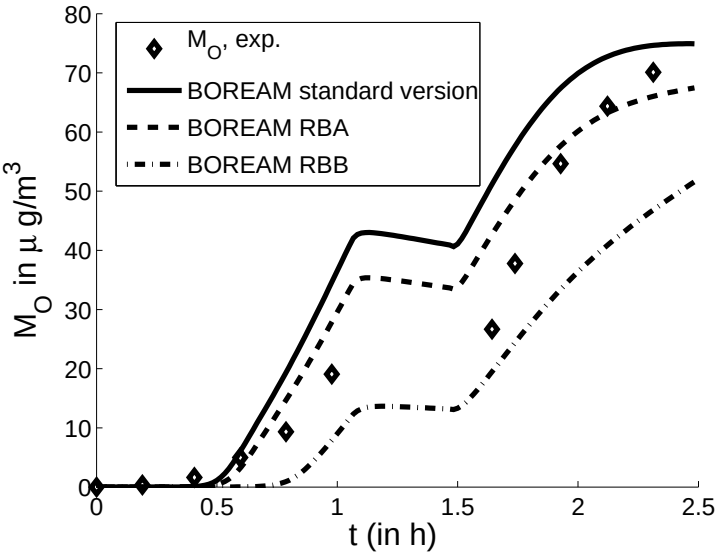

(B) SOA

FIGURE 4.11: β-pinene and SOA for the low-NO_x OH-initiated oxidation experiment performed in the Leipzig Aerosol Chamber (LEAK) on 13/08/2012 (TROPOS, Leipzig Atmospheric Chemistry Group, 2014). H_2O_2 photolysis was used as an OH source, with a flux of about 1.9 ppb of H_2O_2 per minute. The radiation is provided by 254 nm UV lamps, whose intensity was chosen in order to match β-pinene decay in the BOREAM simulations. The evolution of β-pinene suggests that OH-production was interrupted for about 25 minutes after the first hour. BOREAM simulations are performed with the standard mechanism, and with test mechanisms RBA and RBB.

4.6 Discussion and conclusions on the BOREAM simulations of β-pinene oxidation experiments

The recent state-of-the-art mechanisms of Nguyen et al. (2009a) and Vereecken and Peeters (2012), based on quantum-chemical calculations, were introduced into BOREAM and tested in simulations of β-pinene oxidation. The effect of variations of key reaction rates was investigated. BOREAM simulations show that variation of the branching of **actBPINOH1** towards **R1OO** and **BPINOH1** has an important impact on ozone formation and β-pinene decay. The test RBB, which uses branching fractions from the MCMv3.2, leads to a strong overestimation of ozone formation, contrary to the study of Pinho et al. (2007). This shows that other primary or secondary reactions contribute to the stronger ozone formation compared to Pinho et al. (2007). Variations of the uncertain branching towards bi-peroxy radicals in the ozonolysis mechanism, of the β-pinene ozonolysis rate and of uncertain experimental conditions, such as the radiative flux, all have large effects on ozone formation. Currently, no single mechanism achieves a satisfactory match with all experimental data.

The modelling of SOA in dark ozonolysis and photooxidation experiments of β-pinene presented here is the first study in which a reasonable agreement (of the order of a factor of two) is obtained with a detailed model, without having to resort to adjustment of estimated saturated vapour pressures of products by an artificial factor, as was necessary in Griffin et al. (1999) and Jenkin (2004). This is partly due to the use of an up-to-date vapour pressure estimation method (EVAPORATION), to mechanistic changes in the primary chemistry, and to a more complete secondary chemistry. As in the case of α-pinene, the temperature sensitivity of SOA yields is found to be exaggerated in the model, leading to serious underestimations at the highest temperatures. Products formed in the biradical mechanism contribute significantly to SOA formation in ozonolysis experiments, and the branching fraction change from 8 to 70% for the ring-opening of compound **actBPINOH1** leads to roughly a doubling of modelled SOA yields for photooxidation SOA.

The mechanistic tests are by no means complete, but they do show an important sensitivity to uncertainties of reaction rates and product distributions. Further experimental studies and calculations are clearly needed to narrow down these mechanistic uncertainties.

Chapter 5

Photochemical ageing of α-pinene secondary organic aerosol

In this Chapter, BOREAM is used to investigate the effect of prolonged photochemical oxidation of α-pinene products on SOA, a process known as SOA ageing. After a short presentation of the available experimental evidence and of the need for an improved representation in models, the treatment of SOA ageing in BOREAM is investigated, by means of extensive comparisons with relevant laboratory data. Conclusions on how well the model is able to reproduce SOA concentrations during the ageing phase are drawn.

5.1 Experimental evidence and model representations of SOA ageing

The properties of ambient organic aerosol have been observed to differ markedly from those of SOA formed in short-duration smog chamber experiments. This difference is best expressed in terms of O to C ratios and effective saturation concentration C_i^* (Donahue et al., 2006). Whereas freshly made SOA is mostly made of so-called semi-volatile oxidised organic aerosol (SV-OOA), with O to C ratios lying between 0.3 and 0.6, and C_i^* lying between 10^{-2} and $10^2\,\mu\mathrm{g\,m^{-3}}$ (corresponding to a saturated vapour pressure between 8.6×10^{-10} and 8.6×10^{-6} Torr, using formula 4 of Donahue et al. (2006) with $T = 298$ K and $M_i = 215$ g/mol), an important fraction of ambient SOA is made of so-called low-volatile oxidised organic aerosol (LV-OOA), with O to C ratios above 0.6 and C_i^* below $10^{0.5}\mu\mathrm{g\,m^{-3}}$ (i.e. corresponding to a saturated vapour pressure below 2.7×10^{-7} Torr) (Jimenez et al., 2009).

The transformation of fresh SOA, corresponding mostly to SV-OOA, into LV-OOA (Jimenez et al., 2009) has been observed during the MILAGRO campaign, for example, where recently formed SOA within the Mexico mega-city area was shown to consist mainly of SV-OOA, whereas SOA in air masses advected away from the city was found to be partly of the LV-OOA type (Jimenez et al., 2009). Jimenez et al. (2009) showed that in several long-term smog chamber experiments, with various organic aerosol sources (α-pinene SOA, squalane POA, diesel combustion exhaust or woodburning smoke), long-term OH exposure leads to a strong increase of the LV-OOA and SV-OOA contributions, while in the case of α-pinene, SV-OOA was for a large part converted into LV-OOA (Jimenez et al., 2009, Fig. 2). Importantly, it was also shown that ageing induces significant changes in the aerosol's properties, such as its hygroscopicity, which is found to generally increase due to photochemical ageing (Jimenez et al., 2009). This process therefore strongly impacts the ability of aerosol particles to serve as cloud condensation nuclei, and hence their role in cloud formation and properties, which in turn influences climate.

The increase in O to C ratio and decrease in volatility during SOA ageing is brought about by chemical reactions taking place in both the gas and aerosol phase. Those reactions tend to increase the number of functional groups per molecule, while leading to shorter carbon chains through decomposition, or longer carbon chains through oligomerisation.

For example, H-abstraction by OH from an aliphatic carbon leads (upon O_2 addition) to a peroxy radical, which under low-NO_x conditions can react with HO_2 or other peroxy radicals, leading to the formation of a hydroperoxide, alcohol, ketone or alkoxy radical. In the first three cases, the oxidation by OH has led to an increased functionalisation of the molecule. High-NO_x reactions of peroxy radicals tend to lead to higher yields of alkoxy radicals, although nitrates or peroxy nitrates can also be formed. Decomposition of alkoxy radicals leads to shorter carbon chains and thus might increase volatility, while H-shift isomerisation often leads to an extra alcohol group plus a new peroxy radical group, thus contributing to a decrease in volatility. It should be noted that in the case of H-abstraction from a carbon with an α-functionality, such as hydroperoxide, alcohol or nitrate, this function can be replaced by a carbonyl group. Attack of OH on a carbonyl group can lead to an acyl peroxy radical. The latter can either react with NO_2, forming a PAN function, with HO_2, partly forming carboxylic and peroxy acids, or with NO, leading to acyl alkoxy radicals, which generally eliminate CO_2.

As can be seen from the above summary, the chemistry following reaction with OH is complex, and depends strongly on the concentration of NO_x, HO_x and RO_2, and on various product branching ratios, such as those of the alkoxy radicals. At least during a first ageing stage, oxidation by OH should on average decrease volatility and increase O

to C ratios. In most cases, oxidation by OH competes with photolysis, which generally forms more volatile compounds, although the combined effect of photolysis and oxidation by OH can have diverse impacts, as will be seen in this chapter (also in Chapter 6).

As was shown in Chapter 3, BOREAM is able to predict SOA concentrations relatively well for smog chamber studies lasting at most a few hours, with the majority of calculated SOA yields falling within a factor of two of experimental yields. A large number of studies have derived SOA parameterisations based on such short smog chamber experiments, making use of two or several-product models (see Section 6.5 for an overview), including the approach known as the volatility basis set (VBS) model (Stanier et al., 2008, Jimenez et al., 2009).

Such parameter models have been used in global modelling studies to estimate global SOA formation from biogenic or anthropogenic sources (Pye and Seinfeld, 2010, Farina et al., 2010). However, it has become clear that parameter models adjusted based on short-duration smog chamber experiments are inappropriate in real atmospheric conditions, the main reason being that the typical atmospheric lifetime of aerosol particles is of the order of several days, i.e. more than 10 times longer than the typical duration of most smog chamber experiments, with dry and wet deposition being the main loss processes for particles. Model estimates of global average aerosol lifetimes range between 3 to 7 days, with most estimates around 6 days (Kristiansen et al., 2012, Spracklen et al., 2011, Textor et al., 2006). With day-time concentrations of OH of the order of several 10^6 cm^{-3} (see Chapter 6), the typical OH-exposure is of the order of 2×10^8 h cm^{-3} (assuming 6 days of 12 hours of exposure to on average 3×10^6 cm^{-3} of OH).

Several parameter models have been extended in order to include the effect of SOA ageing, for example through a reaction of lumped reaction products with OH, which results in lower volatility compounds. For example, based on diesel exhaust aerosol ageing experiments, Robinson et al. (2007) adjusted a 1-dimensional VBS including a reaction with OH (of rate 4×10^{-11} cm^{-3} s^{-1}) which lowers the product volatility by one order of magnitude. Grieshop et al. (2009) and the global modelling study of Pye and Seinfeld (2010) used similar schemes, although no OH ageing was applied to biogenic SOA.

Although certainly an improvement over parameterisations ignoring ageing effects altogether, the above mentioned implementations remain very simplistic. Since they are based on a limited number of experiments, they might not be applicable to other types of organic aerosol and other conditions (high or low NO_x, temperature, radiation). Moreover, as will be seen in Chapter 6, the effects of photolysis can be as important as the impact of oxidation by OH. In order to address the complexity of SOA ageing,

a series of papers presented the development of a two-dimensional VBS model (Jimenez et al., 2009, Donahue et al., 2011b, Chacon-Madrid et al., 2012, Donahue et al., 2012), in which the products are differentiated not only by their volatility (as in the 1-D VBS model), but also by their O to C ratio. Molecules with high carbon number and little oxygen content can indeed have a similar volatility but a very different reactivity or hygroscopicity as molecules with less carbons and more oxygens. The 2-D VBS has some similarity to the generic species system used in BOREAM, except that the generic system is based on volatility and carbon number, and has some additional chemical complexity. Another difference is that the generic chemistry is only a supplement to the explicit chemistry in BOREAM, whereas the 2-dimensional VBS is used to model the entire SOA evolution.

Aiming at a better understanding of SOA ageing processes, several experimental groups have recently conducted α-pinene SOA experiments in which OH exposure approaches atmospheric conditions. The next section describes simulations of these experiments with our detailed model BOREAM. Donahue et al. (2012) studied such experiments of the MUCHACHAS campaign using the 2-D VBS model, and obtained a good agreement, but it should be reminded that the VBS reactions were adjusted to the results of similar ageing experiments. Another point is that in several experiments, the very large and uncertain wall losses were adjusted in order to obtain a better agreement with the model. As far as we know it is not proven that the 2-D VBS model is able to predict SOA yields accurately over a wide range of atmospheric conditions.

5.2 Ageing experiments for α-pinene SOA

5.2.1 Ozonolysis followed by photooxidative ageing

A number of recent α-pinene SOA ageing studies (Henry and Donahue, 2012, Tritscher et al., 2011, Salo et al., 2011, Donahue et al., 2012, Yasmeen et al., 2012, Qi et al., 2012) made use of similar experimental protocols. In a first phase, α-pinene undergoes dark ozonolysis. In a second phase, an OH source is introduced, most often together with radiation (UV or solar-like), in order to mimic the effects of photooxidative ageing in the real atmosphere. In this way, the impact of ageing is broadly separated from the condensation of primary products. In most of these studies, no OH-scavenger was used, and a considerable fraction of α-pinene was oxidised by OH (sometimes between 20 and 40%). Furthermore, the primary products underwent reaction with OH during the first phase of the experiments.

An overview of the modelled experiments is given in Table 5.1. The latest model version was used, which was specifically extended to better represent SOA ageing. Besides OH formation due to ozone photolysis, an additional OH source was usually introduced, either abruptly or through a constant influx. A precise description of the setup was often not given, however, and most experiments did not report real-time measurement of the concentration of the OH source compounds. In some cases the photolysis rates were also uncertain. These uncertainties on the OH source and on radiation can have substantial effects on both gas phase chemistry and SOA formation.

The modelled total OH exposure is given in Table 5.1, as well as the ratio of the SOA mass yields in the model and the experiments, at the end of the initial phase, i.e. prior to photooxidative ageing or ageing through a dark OH source ($Y_{\mathrm{i,mod.}}/Y_{\mathrm{i,exp.}}$). The impact of ageing during the subsequent phase is quantified in the last three columns of Table 5.1 with the increase (or in some cases decrease) in SOA yield during the photooxidation phase of the experiment.

5.2.1.1 Experiments of Henry and Donahue (2012)

The α-pinene smog chamber experiments of Henry and Donahue (2012) were performed in the Carnegie Mellon University (CMU) 12 m^3 smog chamber. Besides a base-case experiment in which no ageing took place, three ageing experiments were conducted, using different OH sources.

In experiment 2, H_2O_2 was added during the dark ozonolysis phase, when H_2O_2 scavenged part of the produced OH-radicals, before producing OH through photolysis after the lights were switched on after one hour. The precise amount of added H_2O_2 was not given by Henry and Donahue (2012), but the decay of tracer species was used to infer an OH radical concentration of the order of 10^6 cm^{-3} after one hour of photooxidation. In the standard BOREAM simulation, a relatively low flux of 5 ppb/h of H_2O_2 is found to be sufficient to reach 1.15×10^6 cm^{-3} after 1 hour, as the photolysis of O_3 and the enhanced photolysis of carbonyl hydroperoxides also contribute significantly to OH production. It should be noted that using this H_2O_2 flux, the resulting OH levels are different from the ones given in Henry and Donahue (2012) when we test alternative photolysis rates for organic compounds.

In experiment 3, HONO photolysis led to about [OH] = 10^7 cm^{-3} during the first hour, and about 2×10^6 cm^{-3} afterwards. The authors indicate that VOC/NO_x was less than 1 throughout the experiment. When about 14 ppb of HONO is injected, together with 10 ppb of NO (which slightly suppresses formation of OH), both indicated OH and NO_x levels can be approached in the simulation.

TABLE 5.1: Dark ozonolysis initiated photooxidative ageing of α-pinene SOA, simulated with the BOREAM model (SOA ageing v7). $Y_{\mathrm{i,mod.}}$ and $Y_{\mathrm{i,exp.}}$ are the SOA yields prior to the ageing phase of the experiment, ΔY_{a} is the yield increase during the ageing phase.

Exp.	VOC (ppb)	OH source (ppb)	T (K)	$j(NO_2)$ (10^{-3} s^{-1})	OH exposure 10^7h/cm^3	$\frac{Y_{\mathrm{i,mod.}}}{Y_{\mathrm{i,exp.}}}$	ΔY_{a} exp.	ΔY_{a} mod.	$\frac{\Delta Y_{\mathrm{a,mod.}}}{\Delta Y_{\mathrm{a,exp.}}}$
Henry and Donahue (2012)									
2[a,e]	38	H_2O_2	295	3.0[d]	0.78	0.88	-0.136	0.045	-0.32
3[b,e]	25	HONO	295	3.0[d]	1.40	1.02	-0.008	0.178	-21
4[c,e]	26	TME,O_3	295	3.0[d]	1.53	0.87	0.64	0.198	0.31
Tritscher et al. (2011)									
4[g]	10	O_3,HONO	294	2.0[f]	4.2	0.43	0.28	0.37	1.3
5[h]	10	O_3,HONO	294	2.0[f]	4.0	1.0	0.23	0.45	1.9
7[i]	40	O_3,HONO,NO	294	2.0[f]	2.5	0.66	0.164	0.37	2.3
14[j]	10	O_3,TME	294	2.0[f]	6.5	0.50	0.32	0.60	1.9
Salo et al. (2011)									
08-14	33	O_3,TME	293	dark	6.1	0.99	-0.063	0.36	-5.7
Yasmeen et al. (2012)									
E0208	252	O_3	297	4.2	1.07	1.66	-0.141	0.028	-0.20
Qi et al. (2012)									
1037A	80	57.3 NO	300	3.0	0.76	0.29	0.012	0.035	2.8
1037B	80	O_3	298	3.0	0.72	0.29	0.055	0.013	0.23
1038A	100	2000 H_2O_2	300	3.0	1.48	0.25	0.073	0.154	2.1
1074A	100	20 N_2O_5	300	3.0	0.79	0.55	0.070	0.063	0.89

[a] $[O_3]_i$ = 620 ppb. During the 1st hour, 5 ppb of H_2O_2 is added through a constant flux in the simulation, together with water vapour, leading to 20% RH. UV is applied after 1 h.

[b] $[O_3]_i$ = 700 ppb. After 2 h, UV is applied, and 14 ppb HONO and 10 ppb NO were added. Dry air was used, which, following the study Pathak et al. (2007) of the same group, corresponded to RH below 10% (5% is assumed in the model).

[c] $[O_3]_i$ = 400 ppb. After 2 h, O_3 is increased to 2 ppm and 5 ppb of TME is added, and during hour 3 and 4, an additional 18 ppb of TME is added through a constant flux. After 4 h, UV is applied. RH = 5% was assumed.

[d] For the UV-light, the spectrum given by Presto et al. (2005b) (Fig. 2) was used to calculate photolysis rates, which were scaled according to $j(NO_2) = 3 \times 10^{-3}\,s^{-1}$, given by Henry and Donahue (2012).

[e] Experimental SOA yields were corrected for wall losses, using the assumption that wall-deposited particles continue to participate in aerosol/gas phase partitioning.

[f] The radiation intensity spectrum for the Xenon arc lamps was not given above a wavelength of 350 nm in Paulsen et al. (2005) (Fig. 3), therefore it was supplemented above 350 nm with that of a similar Xenon-arc lamp, used in the CESAM chamber (Wang et al., 2011). The spectrum was scaled in order to match the estimated $j(NO_2)$ given by Paulsen et al. (2005).

[g] $[O_3]_i$ = 200 ppb. In BOREAM it is assumed that during the hour prior to photooxidation, 20 ppb of HONO was added to exp. 4 through a continuous flux. RH = 50% for all experiments of Tritscher et al. (2011).

[h] $[O_3]_i$ = 300 ppb. During the hour prior to photooxidation, 12.5 ppb of HONO was added to exp. 5 through a continuous flux. Lights were switched off for about 2 h during photooxidation.

[i] $[O_3]_i$ = 250 ppb. The HONO flux is assumed to be the same as for exp. 4, but an additional flux of 50 ppb of NO is added during the 5th hour.

[j] $[O_3]_i$ = 650 ppb. The TME influx is assumed to start after 4 hours, and equal to 6.6 ppb/h, and continue throughout the experiment. Light is switched on over 2 periods during photooxidation.

[k] $[O_3]_i$ = 300 ppb was chosen. From about 2 hours and 15 minutes until 14 hours into the experiment, TME was added with a flux of 21 ppb h^{-1}, together with an additional injection of 400 ppb of O_3.

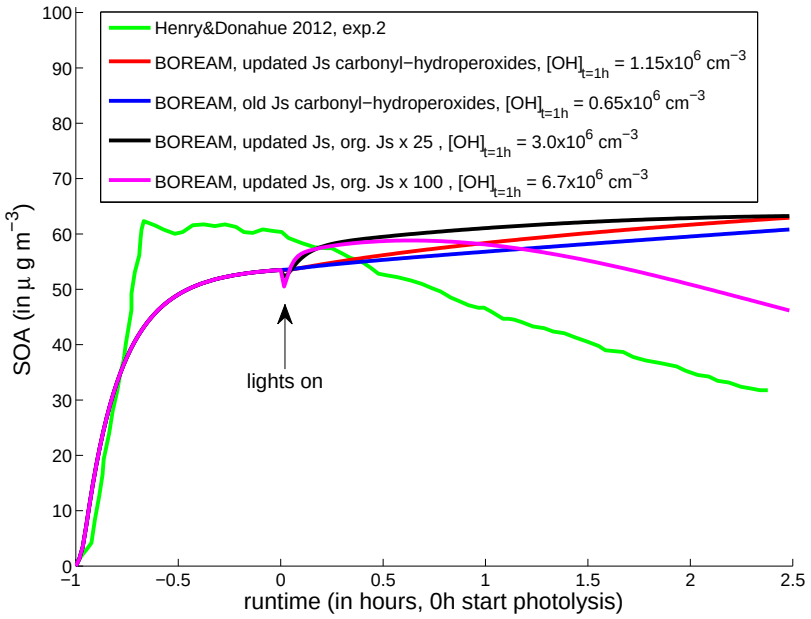

FIGURE 5.1: Experimental vs. simulated SOA mass concentrations for experiment 2 in Henry and Donahue (2012). Four sets of photolysis rates were tested. In red, the simulation accounting for the enhancement effect of interactions between carbonyl chromophores and oxygenated functional groups such as hydroperoxide is shown. In blue, the simulation excludes this effect. In black and magenta, all photolysis rates of organic species have been increased by a factor of 25 or 100, respectively. The simulated OH radical concentration after 1 hour is also indicated.

In experiment 4, after 2 hours of dark ozonolysis, ageing was initiated in the dark by adding tetramethyl ethene (TME), which yields OH upon reaction with ozone. The quantity of TME added was not specified. The adopted input of TME and O_3 in the simulation, described in Table 5.1, leads to OH-levels around 2.5×10^6 cm^{-3} after 0 and 1 hour of photooxidation, close to the value estimated by Henry and Donahue (2012). After 4 hours, UV-lamps were switched on for the remainder of the experiment.

The SOA concentration is relatively well simulated by BOREAM during the dark ozonolysis phase for all three experiments (Fig. 5.1, Fig. 5.2, Fig. 5.3 and Table 5.1). At the start of the photooxidative ageing, the observed SOA concentration started decreasing in experiment 2. This behaviour was not found in the standard simulation, where a small increase of the SOA yield was predicted instead. In experiment 3, when the lights were turned on, SOA-levels underwent an increase during the first half hour, which is well reproduced by the model. After half an hour, experimental SOA levels started decreasing, whereas simulated SOA levels kept increasing until the end of the experiment. In the fourth experiment, SOA levels increased in both experiment and simulation after the

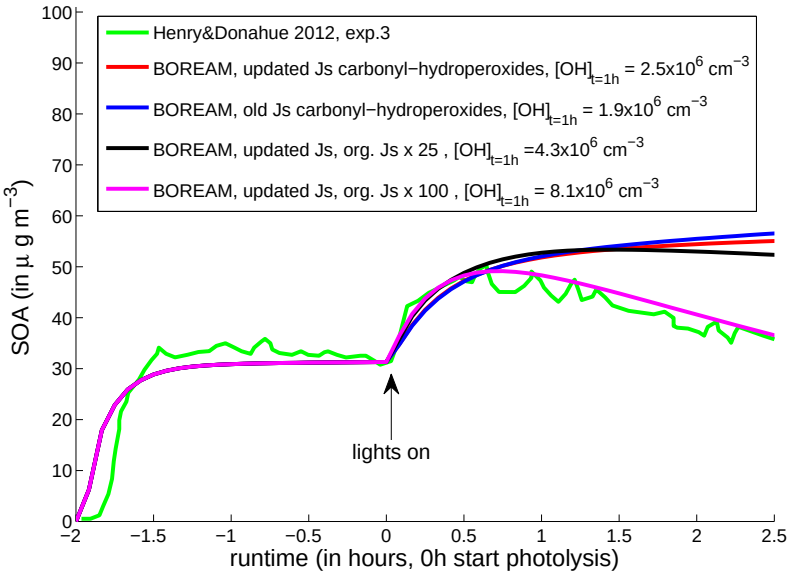

FIGURE 5.2: Experimental vs. simulated SOA mass concentrations, for experiment 3 in Henry and Donahue (2012). Simulations are as described for Fig. 5.1.

start of dark TME ageing, but the experimental increase was about three times as high as the simulated increase.

In order to investigate the possible reasons for the inability of the model to reproduce the SOA decrease induced by photooxidative ageing in the presence of light, we performed a number of sensitivity tests. In a first test, we turned off the increasing effect of the carbonyl-hydroperoxide interaction on the photolysis rate. This change has an almost negligible effect on SOA, although it leads to a much lower OH concentration in experiment 2, by a factor of about 2. This indicates that in the standard case a substantial amount of OH-radicals are produced from the photolysis of carbonyl hydroperoxides. In two further tests, the photolysis rates of organic compounds were drastically increased, by a factor of 25 or 100, although such increases are not expected to be realistic for most compounds. This leads to substantially higher OH levels. Only for the 100-fold increase of photolysis rates is the observed SOA decay reproduced in experiments 2 and 3. This points towards a possible strong underestimation of the impact of photolysis on SOA. However, the strong overestimation of OH in this case (by a factor of 6 for experiment 2 and 3.25 for experiment 3) shows that the applied increase is unrealistic. When applying the 100-fold increase of photolysis rates, the OH concentrations remain strongly overestimated even when no OH precursor such as H_2O_2 or HONO is introduced, therefore it was not possible in these tests to reconcile [OH] and SOA decay.

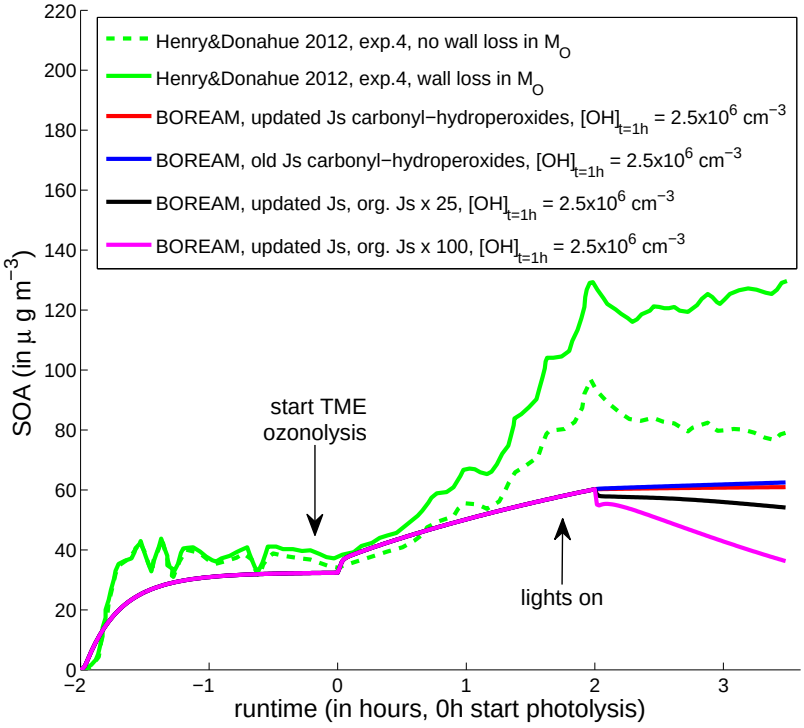

FIGURE 5.3: Experimental vs. simulated SOA mass concentrations, for experiment 4 in Henry and Donahue (2012). Experimental SOA masses were corrected for particle wall losses as reported in Henry and Donahue (2012), either under the hypothesis of wall-deposited particles not further participating in partitioning (dashed green line), or wall deposited particles participating in gas-particle partitioning (solid green line). Simulations are as described for Fig. 5.1.

5.2.1.2 Experiments of Tritscher et al. (2011)

The experiments described in Tritscher et al. (2011) were performed in the 27 m^3 fluorinated ethylene propylene (FEP, or Teflon) smog chamber of the Paul Scherrer Institute (PSI). The initial α-pinene (either 10 or 40 ppb) first underwent dark ozonolysis for 5 hours, followed by an SOA ageing phase, which usually also lasted about 5 hours. For the SOA ageing, either the chamber was exposed to near-solar spectrum light from 4 Xenon arc lamps (Paulsen et al., 2005), causing photolysis of ozone or HONO to produce OH radicals, or dark TME ozonolysis was used as OH source. Four experiments for which detailed time series of SOA levels were given in Tritscher et al. (2011) were modeled with BOREAM. Metzger et al. (2008) found that for smog chamber experiments in the PSI chamber, a number of heterogeneous wall reactions had to be taken into account in order to reconcile observations and modelling results for certain gas phase species. Tests of the PSI SOA ageing experiments with BOREAM indicate that the use of the wall model of Metzger et al. (2008) only has a minor impact on SOA concentrations,

TABLE 5.2: Measured vs. experimental [OH] in Tritscher et al. (2011)

	[OH] (in 10^6 cm^{-3}) after 2 h of ageing		after 4 h of ageing[a]	
	exp.	mod.	exp.	mod.
Experiment 4	10.0	6.5	8.0	5.8
Experiment 5	6.8	7.1	–[b]	–
Experiment 7	4.2	3.6	3.5	2.8
Experiment 14	3.0	3.0	–[b]	–

[a] Except for Experiment 4, where [OH] after 3 h of ageing is given.
[b] Not measured.

and only affects OH concentrations near the end of the ageing experiment, and therefore does not present a large source of uncertainty.

Tritscher et al. (2011) added 20 ppb of 3-pentanol shortly before the start of the OH-initiated ageing phase, as an OH tracer (instead, 2-butanol was added in the present BOREAM simulations, as 3-pentanol is not treated in the current BOREAM version – the reaction rate with OH of 2-butanol only being about 15% lower than that of 3-pentanol, according to Atkinson et al. (2006) and Lendar et al. (2013)). The deduced OH concentrations are used to constrain the OH source in the simulations. HONO was introduced one hour before photooxidation was started, and reached a peak of 15–20 ppb. Note that the implemented wall reactions of Metzger et al. (2008) lead to a production of about 5 ppb of HONO before the ageing phase. When lights were turned on, HONO concentrations started to decrease through photolysis, and it was assumed that no further HONO was added. In experiment 7, 50–80 ppb of NO was added together with HONO. For experiment 14, it was assumed that TME was added continuously, beginning from the 5th hour of the experiment, and the flux was chosen in order to match the measured OH concentration after 2 hours of ageing, equal to 3×10^6 particles cm^{-3}. For experiment 4, OH concentrations remained underestimated by BOREAM when using a HONO concentration of the order indicated by Tritscher et al. (2011), but for the other modelled experiments, a good agreement could be reached (see Table 5.2).

Experimental SOA masses were wall-loss corrected, based on a fitting to an exponential decay (which assumes a constant SOA mass wall loss rate) (Paulsen et al., 2005). Therefore, this assumption may not account for partitioning of vapours to wall-deposited particles. Possible gas phase partitioning to the teflon walls was not discussed by Tritscher et al. (2011), and was not considered in the simulations.

As seen in Fig. 5.4 and Table 5.1, during the dark ozonolysis phase, in three out of four experiments, SOA concentrations are strongly underestimated (see $Y_{\mathrm{i,mod.}}/Y_{\mathrm{i,exp.}}$ in Table 5.1). In contrast, the increase in SOA mass yield during the SOA ageing phase is

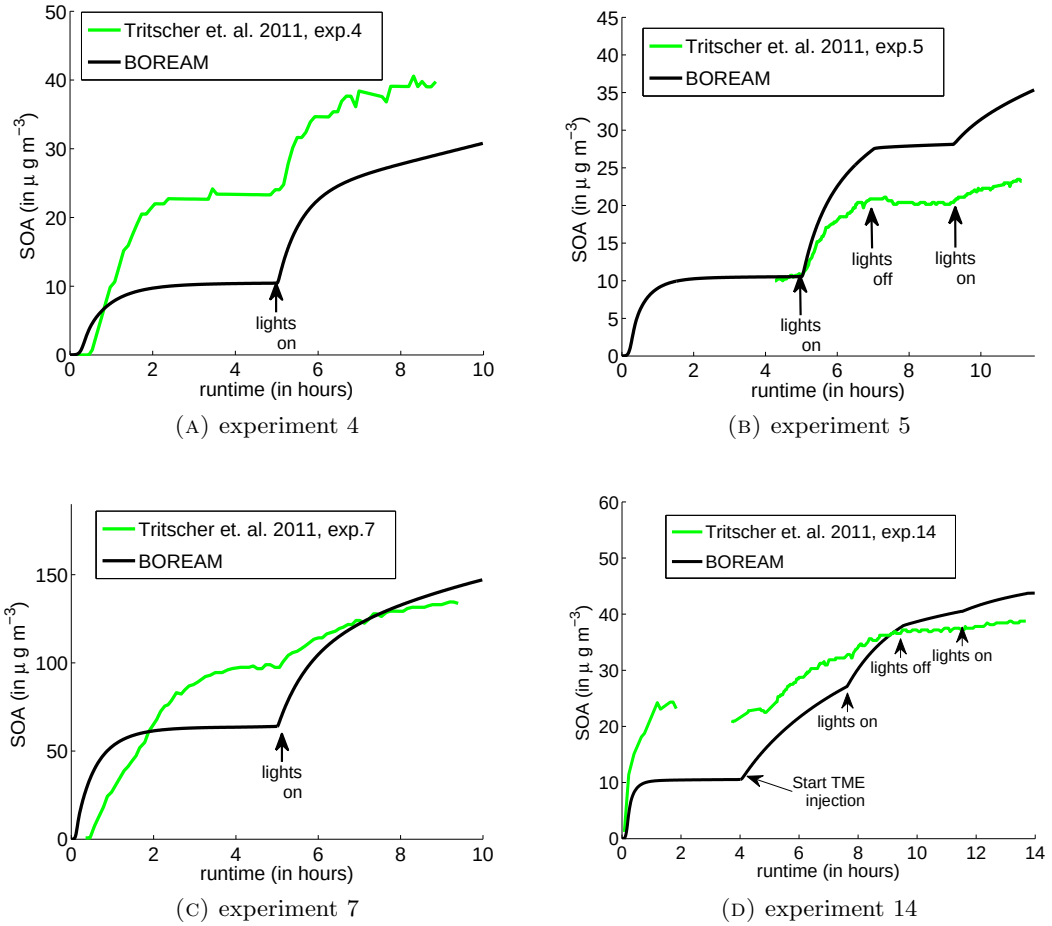

(A) experiment 4 (B) experiment 5

(C) experiment 7 (D) experiment 14

FIGURE 5.4: Experimental and BOREAM SOA mass concentrations for experiments 4, 5, 7 and 14 in Tritscher et al. (2011). A dark ozonolysis phase is followed by photooxidative HONO ageing (experiments 4, 5 and 7) or TME ageing (experiment 14).

in all cases much larger in the model than in the experiment, by a factor between 1.3 and 2.3.

The experimental estimates of the O to C ratios are compared with model estimates in Fig. 5.5. As explained in Section 2.3, generic species (which make up between 25% and 50% of the SOA near the end of the experiments, see Fig. 5.11) are a large source of uncertainty for the modelled O to C ratios. The O to C ratio of explicit species (in blue in Fig. 5.5) can be considered as a lower limit of the O to C ratio for the modelled SOA, since the generic fraction is more aged and is therefore expected to have a higher O to C ratio than the explicit species. The difference between the O to C ratios including or excluding generic compounds is relatively small (a few percent), except for the last part of experiment 14. The O to C ratios are slightly overestimated compared to the experimental values in the dark ozonolysis phase (about 0.45 compared to 0.40).

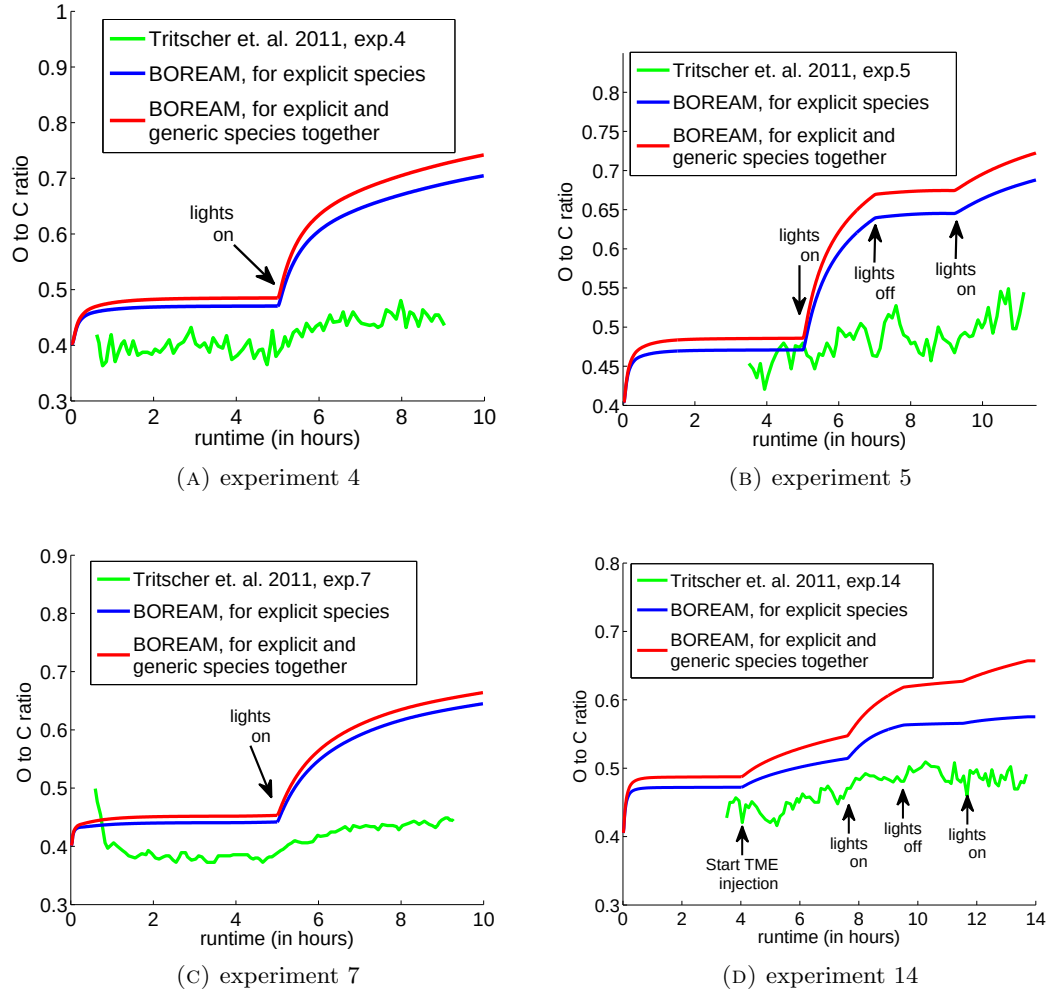

(A) experiment 4 (B) experiment 5

(C) experiment 7 (D) experiment 14

FIGURE 5.5: Experimental vs. simulated O/C ratios for experiments 4, 5, 7 and 14 in Tritscher et al. (2011).

However, once photooxidative SOA ageing starts, the simulated O to C ratios increase strongly to values of about 0.6–0.75 at the end of the experiment, whereas observations suggest a very modest increase, to about 0.45 (Fig. 5.5).

Fig. 5.6 shows the abundance of each functional group per molecule in the SOA during Exp. 7, based on the modelled concentrations of explicit compounds. The contribution of generic species are not included here, although they make up about 25% of the SOA near the end of this experiment.

The most abundant groups, in descending order, are the alcohol, ketone, hydroperoxide, PAN, carboxylic acid, aldehyde, nitrate and peroxy acid groups. The number of alcohol, hydroperoxide, carboxylic acid and aldehyde groups per molecule slightly decreases during the HONO photolysis ageing phase. In contrast, the number of PAN and nitrate groups strongly increases, which can be explained by the fact that around the start of

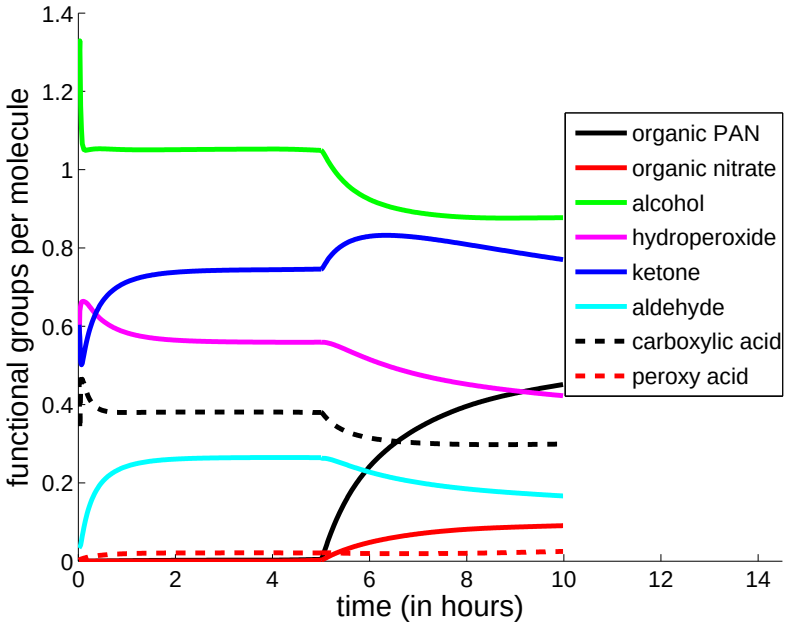

FIGURE 5.6: Time evolution of the average functional group composition of explicit species in the SOA for experiment 7 of Tritscher et al. (2011).

photooxidative ageing, 50 ppb of NO was added in addition to HONO. Since the PAN and nitrate groups contain a high number of oxygens (5 and 3, respectively), their increase compensates the decrease in the other oxygenated groups, and leads to the overall increase in O to C ratio shown in Fig. 5.5.

5.2.1.3 Experiments of Salo et al. (2011)

The study of Salo et al. (2011) describes a number of smog chamber SOA ageing experiments in the AIDA chamber (Karlsruhe Institute of Technology) and in the SAPHIR chamber (Forschungzentrum Jülich). A BOREAM simulation of experiment SOA08-14 (AIDA) is performed, for which time series of the observed suspended SOA mass in the chamber are given. In this experiment, dark ozonolysis during 2 hours was followed by a dark ageing phase, using TME ozonolysis as an OH source, with an OH concentration estimated to range between 2 and $3.5 \times 10^6\,\mathrm{cm}^{-3}$ (between 2.5 and $6 \times 10^6\,\mathrm{cm}^{-3}$ in the simulation).

Of importance is the fact that gas phase carboxylic acids were observed to be lost to the aluminium wall of the AIDA chamber, with an apparently irreversible deposition rate between 1.8 to 3.8×10^{-4} s^{-1} (Salo et al., 2011). Shown in Fig. 5.7 are SOA concentrations simulated without those gas phase wall losses (in blue) and with the low or high estimates of the wall loss rate, applied to carboxylic and peroxy acids (in red

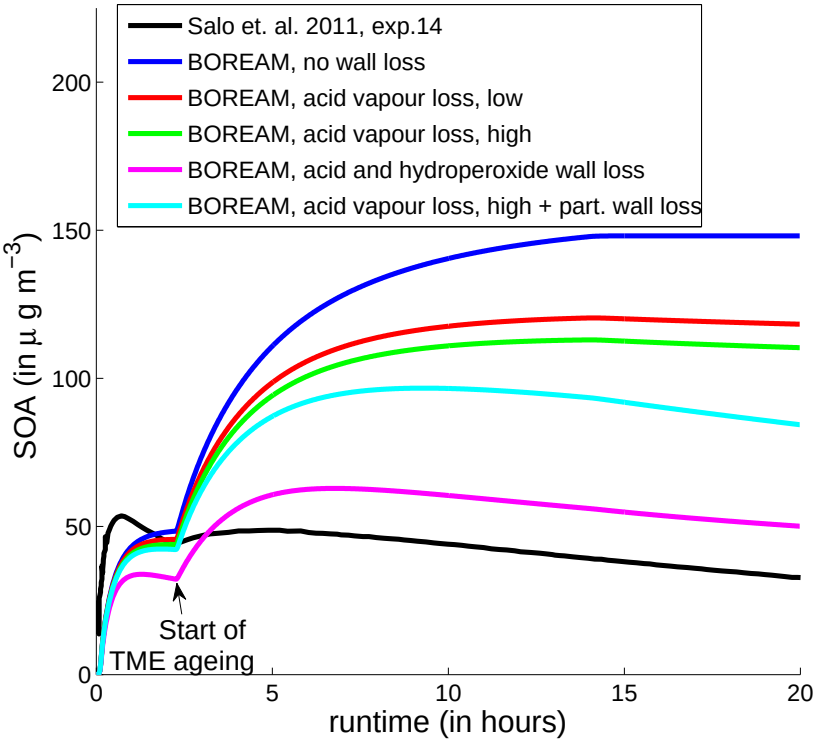

FIGURE 5.7: Experimental and modelled SOA for experiment 14 in the AIDA chamber in Salo et al. (2011).

and green). During the dark ozonolysis phase, modelled SOA is slightly underestimated. In all three cases, however, SOA is strongly overestimated during the photooxidation phase. An additional test in which also hydroperoxides are assumed to be deposited with the same rate leads to a strong reduction in the modelled SOA, more in line with the experimental SOA, although still higher. It should be noted that the gas phase wall loss rate of hydroperoxides in the AIDA chamber is unknown.

In another simulation, the wall loss of aerosol particles is also taken into account. Particle wall loss was modelled based on the diameter dependent wall loss ($1.1 \times 10^5\,\mathrm{s}^{-1}$ for 50 nm, and $1.9 \times 10^{-6}\,\mathrm{s}^{-1}$ for 200 nm) reported for the AIDA chamber (Salo et al., 2011). Those values were used to adjust a diameter-dependent particle wall loss rate, following assumptions discussed in Section 2.4.4. In this case, the vapour wall loss turns out to be more important than the particle wall loss (Fig. 5.7).

Donahue et al. (2012) obtained a good agreement of their 2-D VBS model with the experimental data (see their Fig. S4), but this required the assumption that wall-adsorbed organic vapours quickly became the dominant carbon reservoir. In their simulation, 50% of organic material was already deposited to the wall after 2 hours, i.e. at the start of

the ageing phase, and 80% or organic material was wall-deposited from the gas phase after 7 hours, whereas particle phase deposition was assumed to be negligible. The true effects of wall losses are difficult to estimate, given that the chemical composition in the gas phase was not determined experimentally, and gas phase deposition velocities are available only for a small number of carboxylic acid compounds. A reliable interpretation of experiments for which wall losses are potentially very important would require the determination of gas phase deposition rates for a number of different representative compounds, in order to determine how structure influences deposition. Nevertheless, the model results appear to be consistent with the hypothesis of an overestimation of SOA formation due to ageing.

5.2.1.4 Experiments of Yasmeen et al. (2012)

In Yasmeen et al. (2012), two experiments with similar conditions were performed, one of which (E0208) was simulated with BOREAM. Initial α-pinene concentrations were higher than in the previously discussed experiments (Table 5.1). The arc-lights of the CESAM chamber (Wang et al., 2011) were switched on after one hour of dark ozonolysis, in order to produce OH radicals by photolysis of ozone and other compounds. No extra OH source was introduced.

Figure 5.8 shows that, in contrast with the underestimations found in the simulations of experiments by Tritscher et al. (2011) and Qi et al. (2012), the simulated SOA in the dark ozonolysis phase is overestimated by a factor of about 1.7. One possible reason for this difference could be the higher initial α-pinene concentration. During the photooxidation phase, simulated SOA slightly increases, while experimental SOA starts decreasing already during the dark ozonolysis phase. A test for the effects of particle wall losses using estimated particle wall losses for the CESAM chamber leads to only a minor difference with the simulation without wall losses. Vapour phase wall losses were not accounted for, by lack of data for this process in the CESAM smog chamber, which has stainless-steel walls. However, given the evidence that vapour wall losses can be important for Teflon chambers (Matsunaga and Ziemann, 2010) and the noted importance of this process in the aluminium AIDA chamber, one can speculate that gas phase wall losses might be non-negligible also in this case. This could explain the clear SOA decline prior to photolysis, when strong volatilisation of SOA is not expected. During the ageing phase, the observed SOA continues decreasing, while the combined effect of OH oxidation and photolysis leads to a small SOA increase in the model.

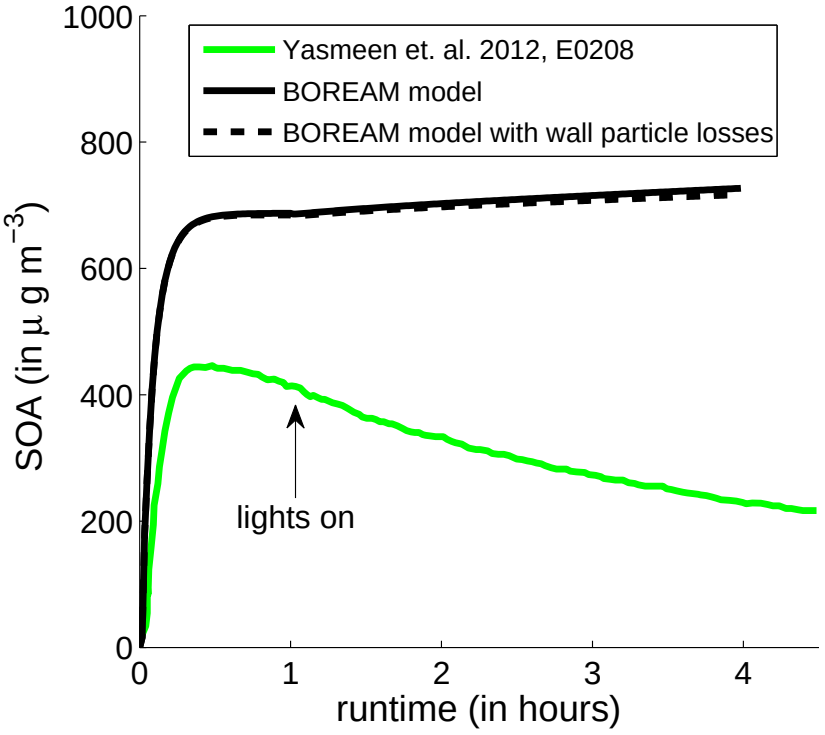

FIGURE 5.8: Experimental SOA (corrected for dilution, but not for wall losses), compared with simulated SOA, with and without particle wall losses, for experiment E0208 of Yasmeen et al. (2012).

5.2.1.5 Experiments of Qi et al. (2012)

The experiments in Qi et al. (2012) were conducted in the 90 m^3 Teflon University of California Riverside environmental chamber (Carter et al., 2005). The BOREAM simulations of the dark ozonolysis phase of the four simulated experiments indicate an underestimation of SOA by a factor 2 to 4 (Table 5.1). This is somewhat unexpected, given that for the dark ozonolysis experiments of Cocker III et al. (2001), which were performed by the same research group, although in a different chamber, simulated SOA concentrations agreed more closely (see Section 3.1.1). One difference is the absence of OH scavengers in Qi et al. (2012), so that OH formed by α-pinene ozonolysis can react with α-pinene and its oxidation products. After this phase, UV-lights were switched on, and four different OH sources were used to produce OH radicals. As seen in Table 5.1, the SOA yield change due to this photooxidative ageing is poorly reproduced by the model, which however does not show any systematic over- or underestimation. Interpretation is difficult, since simulations and measurements already strongly differ at the start of the ageing phase.

TABLE 5.3: OH-initiated photooxidative ageing of α-pinene SOA, simulated with the BOREAM model (SOA ageing v7).

Exp.	VOC (ppb)	OH source (ppb)	T (K)	$j(NO_2)$ (10^{-3} s^{-1})	OH exposure 10^7h cm^{-3}	M_O exp. μg m^{-3}	M_O mod. μg m^{-3}	$M_{O,mod.}/M_{O,exp.}$
Ng et al. (2007a),Valorso et al. (2011)								
1	13.8	4000 H_2O_2[a]	298	4.0	2.3	28.8	43.6	1.51
3	13.1	10^4 H_2O_2, 198 NO	296	4.0	3.3	16.0	31.5	2.0
4	12.6	500 HONO,NO[b]	299	4.0	2.8	4.9	8.1	1.65
Eddingsaas et al. (2012a)[c]								
1	45.0	750 H_2O_2[d]	296	4.0[f]	2.3	66.8	139.	2.1
2	50.1	140 HONO[e]	296	4.0	1.6	20.0	53.7	2.7
3	48.5	750 H_2O_2[d]	298	4.0	2.1	76.6	133.	1.7
4	52.4	125 HONO[e]	296	4.0	1.5	37.2	50.1	1.35
5	46.9	850 H_2O_2[d]	298	4.0	2.3	72.9	136.	1.87
6	45.4	180 HONO[e]	296	4.0	1.7	39.6	44.5	1.12
7	19.8	4000 H_2O_2[d]	298	4.0	3.0	40.1	76.2	1.90
8	38.9	225 CH_3ONO[e]	296	4.0	2.0	51.9	49.1	0.95
9	46.8	3000 H_2O_2[d]	298	4.0	2.5	71.6	155.0	2.16
10	47.9	120 CH_3ONO[e]	296	4.0	2.0	60.3	59.0	0.98
11	46.8	3000 H_2O_2[d]	298	4.0	2.3	70.4	155.	2.2
12	43.7	200 CH_3ONO[e]	296	4.0	1.7	42.6	55.6	1.31
13	45.0	2000 H_2O_2[d]	298	4.0	2.1	63.5	139.	2.2
14	44.9	250 CH_3ONO[e]	296	4.0	1.9	54.0	65.8	1.22

[a] Initially 4 ppb O_3, 350 ppt NO, 350 ppt NO_2 plus 5 ppt/min NO_x off-gassing (50/50 NO and NO_2) [b] 475 ppb NO, 463 ppb NO_2. An extra unknown OH source was introduced, as in Valorso et al. (2011), of $1.8{\cdot}10^9$ cm^{-3}s^{-1} [c] OH source is injected at start, with initial conditions adjusted so as to match the OH-exposure given in Fig. 3 of Eddingsaas et al. (2012a)
[d] Initial NO and NO_2 chosen to be 0.35 ppb. [e] Only the initial sum of HONO or CH_3ONO and NO_x was measured (800 ppb). We assume 5 ppb of NO_2.
[f] Not given in Eddingsaas et al. (2012a), but based on similar experiment in Valorso et al. (2011).

5.2.2 Prolonged photooxidative ageing

5.2.2.1 Experiments of Ng et al. (2007a)

The experiments of Ng et al. (2007a) (with additional data and modelling by Valorso et al., 2011) were already discussed in Chapter 3. Here we use the extended version of BOREAM, found to give similar yields as in Chapter 3. In Fig. 5.9 and Table 5.3, the SOA yields are compared for the low, intermediate and high-NO_x experiments 1, 3 and 4. Experimental SOA yields were corrected for particle wall losses according to Ng et al. (2007a). As can be seen, in all three cases BOREAM overestimates the SOA yield by about a factor 1.5 to 2. Compared to the results with the version of Chapter 3, in Fig. 3.6, the overestimation for the low-NO_x experiment decreased, while for the high-NO_x experiment the overestimation becomes slightly stronger in the more extended model version. Sensitivity tests excluding aerosol photolysis lead to higher SOA yields, by about 10% in Exp. 1 and by a few percent in Exp. 4. In most cases, the GECKO-A model

overestimated the observed SOA even more (Fig. 5.9). Differences in applied SARs, in vapour pressure estimation and in the primary mechanism, and the use of a generic chemistry mechanism in BOREAM might explain these differences. These simulations are, to our knowledge, the only other published results of a detailed chemical SOA model for α-pinene SOA ageing experiments. The comparison suggests that the SOA overestimations frequently found by BOREAM for SOA ageing studies are not unique to BOREAM.

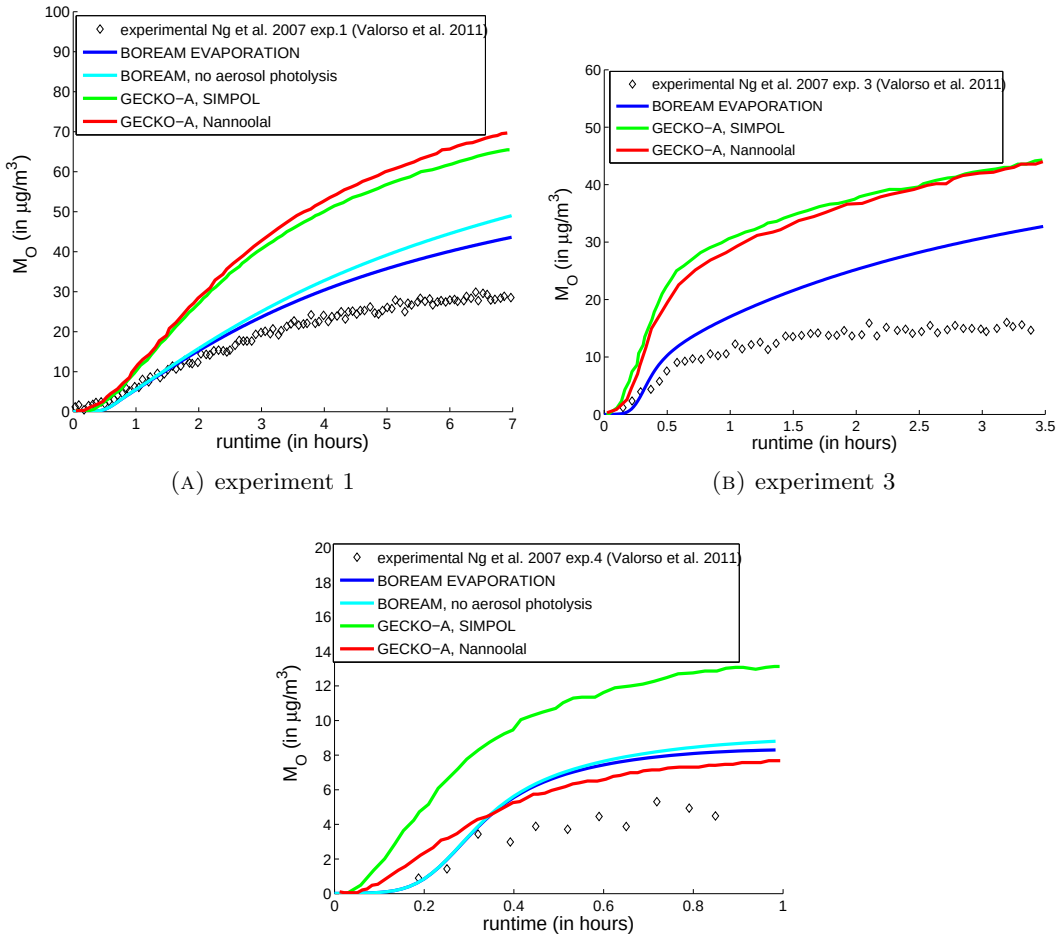

(A) experiment 1

(B) experiment 3

(C) experiment 4

FIGURE 5.9: Experimental and BOREAM SOA mass concentrations for exps. 1, 3, and 4 in Ng et al. (2007a) and Valorso et al. (2011). The simulations with GECKO-A are from Valorso et al. (2011), using vapor pressures from either SIMPOL (Pankow and Asher, 2008) or the method of Nannoolal et al. (2008).

5.2.2.2 Experiments of Eddingsaas et al. (2012a)

In Eddingsaas et al. (2012b) and Eddingsaas et al. (2012a) the formation of gas phase products and SOA in a number of photooxidation experiments under low-, intermediate-

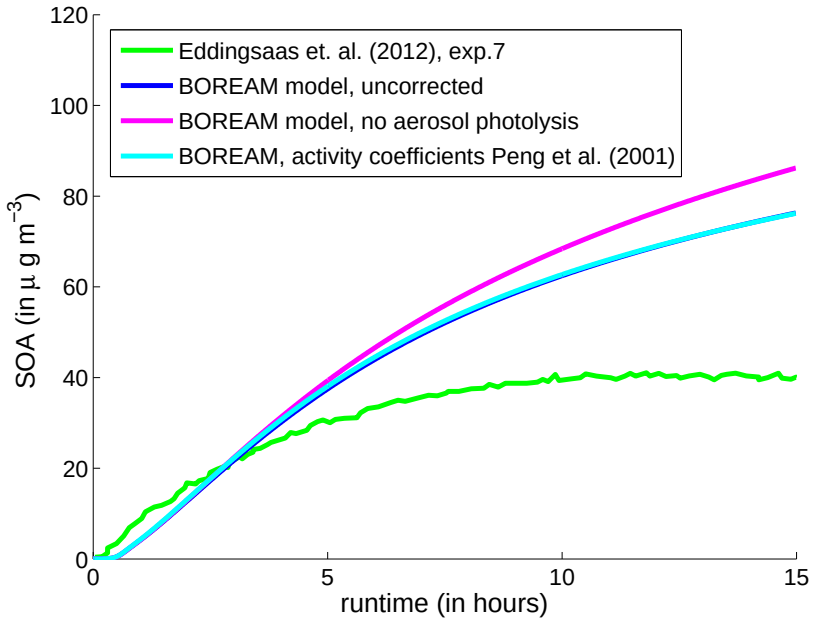

FIGURE 5.10: Modelled vs. simulated SOA concentrations for experiment 7 of Eddingsaas et al. (2012a).

and high-NO_x conditions was investigated. Gas phase measurements were discussed in Section 3.3.1

The influx of the OH precursors HONO, CH_3ONO or H_2O_2 were adjusted in the simulations in order to match the given α-pinene concentration profiles or OH exposures. Overestimates of SOA yields by a factor between about 1 to 2.5 are found. The overestimates are generally strongest when H_2O_2 is used, while when CH_3ONO is used, the agreement is best. Fig. 5.10 shows the low-NO_x Exp.7, with an overestimate of SOA by a factor 2 near the end of the experiment. A model simulation without aerosol photolysis shows a moderate increase of SOA formation, while a simulation using a different activity coefficient method (Peng et al., 2001) shows no difference.

5.3 Discussion of model performance in reproducing aged SOA

The comparisons presented in the previous sections show a consistent pattern of model overestimation of SOA during photooxidative ageing. The only exception is the dark TME ageing experiment of Henry and Donahue (2012), in which the model strongly underestimates the SOA increase due to ageing. For most modelled experiments, however, the overestimation factor is situated roughly between 1 and 2.5 (also found by the

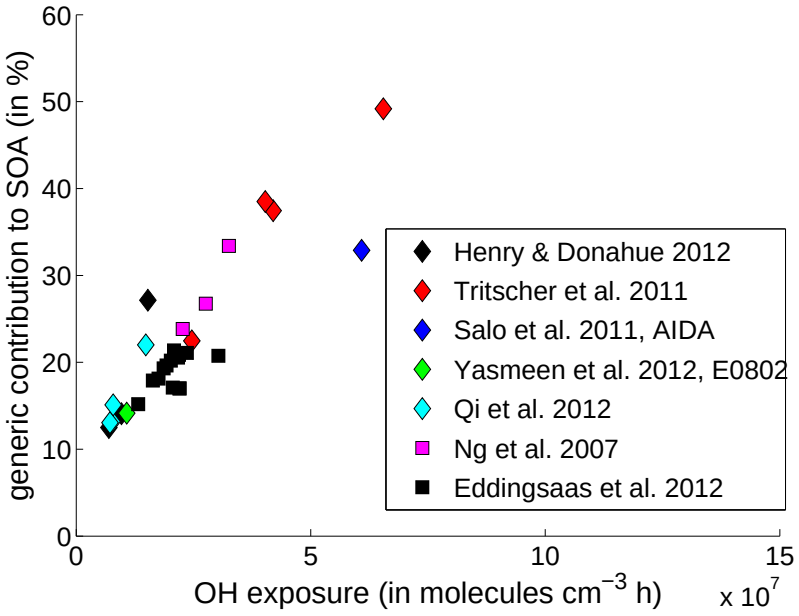

FIGURE 5.11: The fraction of SOA comprised by generic species at the end of the modelled SOA ageing experiments, versus OH exposure.

GECKO-A model for Ng et al. (2007a) by Valorso et al. (2011)). For experiments 1 and 2 of Henry and Donahue (2012), and the modelled experiments of Salo et al. (2011) and Yasmeen et al. (2012), SOA increases in the simulations during the ageing phase, while the measured SOA decreases.

Particle loss to the walls might be underestimated in some cases, possibly contributing to this discrepancy, although it can certainly not explain the strong overestimations noted in the first hours in some experiments, when the cumulative amount of wall-deposited aerosol cannot be high. Similarly, although generic species do make up a large fraction (up to 50%) of SOA at the end of strong ageing experiments (Fig. 5.11), they are still relatively unimportant in the first ageing stage of the experiment, when already strong SOA overestimates have been found. Although it has its weaknesses, the generic chemistry implemented in BOREAM therefore cannot be blamed for the general overestimation pattern. Other possible causes for the model overestimates are briefly discussed below.

Another factor contributing to the overall uncertainty is the generally neglected loss of gas-phase compounds towards Teflon or other walls. Except for one smog chamber (AIDA) chamber, the loss rates of gas phase species are unknown. As discussed in Section 2.4.4, Matsunaga and Ziemann (2010) provided evidence that in their Teflon chamber, species with saturated vapour pressures in the range of those found in SOA might partition for a large fraction towards the wall, and do so in a short time frame (20 minutes).

If confirmed for the presently modelled ageing experiments, this process could explain a large fraction of the model overestimate.

The large discrepancy noted for O to C ratios for Tritscher et al. (2011) suggests that there is a significant difference in chemical composition between the simulated and observed aerosol in these chambers, provided that measurement issues (e.g. decomposition of less stable functional groups, such as hydroperoxide or PAN) do not play a role. The higher level of oxygenation in the simulated SOA leads to lower average saturated vapour pressures, and thus could explain the higher SOA concentrations.

Another possibility is that some destruction processes of multifunctional species, such as photolysis, are underrepresented. This is also suggested by the inability of the model to reproduce the SOA decrease upon irradiation observed in experiments 2 and 3 of Henry and Donahue (2012). Tests of simulations without photolysis of aerosol species lead to a moderate increase of the model SOA overestimate (for Ng et al. (2007a) and Eddingsaas et al. (2012a)), showing that this process contributes to the decomposition of functional groups. The implementation of aerosol photolysis is among the most uncertain and simplified parts of BOREAM, as it makes use of the same photolysis rates as for the gas phase, and it is assumed to produce gas phase species. For molecular products, this is not critical, as they are expected to partition rapidly between the aerosol and gas phase. However, the radicals produced from aerosol photolysis are expected to react in the SOA. Although there have been some compilations of reaction rates of alkyl, alkoxy and peroxy radicals in the liquid phase (Hendry et al., 1974, Neta et al., 1990, Denisov and Afanasev, 2005, von Sonntag, 2006), until now very few atmospheric models have investigated this chemistry in the SOA, except Chen et al. (2011), who considered radical reactions as a possible pathway towards oligomers. There are indications that radical propagation reactions in the SOA could also lead to the destruction of functional groups. Hiatt et al. (1964), for example, studied the photolysis of tert-butyl hydroperoxide in the liquid phase, and observed that for every hydroperoxide group which photolysed, an estimated additional 7 to 10 hydroperoxide groups were lost. This is brought about by the fact that the produced alkoxy and OH radical can abstract an H-atom from other hydroperoxides, inducing further loss of functional groups. Additionally, through H-abstraction by radicals in the SOA, alkyl radicals can be formed, which after reaction with O_2 might form peroxy radicals. These might exhibit different reactivity than in the gas phase. For example, in the liquid phase the cross-reactions with other peroxy-radicals could be favoured over reactions with HO_2 or NO_x, and the branching ratios of the cross-reactions might favour formation of alkoxy radicals, which could partially decompose, continuing the radical propagation. However, further studies are needed to estimate the possible impact of radical propagation in the aerosol phase. Ruehl et al.

(2013) found a strong influence of radical propagation within SOA consisting of alkanes undergoing heterogeneous OH oxidation.

A further possibility is that physical properties of the aerosol might inhibit partitioning towards the SOA. The aerosol can in some circumstances take on a highly viscous semi-solid state at low temperatures (Zobrist et al., 2008) or in certain inorganic/organic aerosol mixtures in which phase separation takes place (Shiraiwa et al., 2013b). Cappa and Wilson (2011) reported slower than expected evaporation of semi-volatile compounds in SOA upon heating, and suggested that mass transfer inhibition due to high viscosity might be the cause, although they acknowledged that a lower than expected volatility of the SOA could be an alternative explanation. Experiments on α-pinene SOA by Saleh et al. (2013) found that equilibration time scales upon heating were fast (minutes to at most half an hour), corresponding to a mass accommodation coefficient of the order of 0.1, which suggests that there was no highly viscous state inhibiting equilibration. Additionally, Robinson et al. (2013) found fast mixing of toluene and α-pinene SOA at the time scale of 1 minute, suggesting high diffusivity. No measurements on the state of the SOA have been reported in the SOA ageing studies discussed in this chapter.

5.4 Conclusions

BOREAM simulations of a large number of α-pinene SOA ageing experiments show that the model in many cases overestimates SOA upon ageing, often by a factor of two or higher. These results are in line with earlier model simulations of ageing experiments (Valorso et al., 2011). The difficult representation of wall losses of aerosols and possibly gas phase compounds obscures the quantitative comparison between model and experiment, but the relatively early onset of model overestimation in some experiments suggests that misrepresented wall losses are not the only cause of the mismatch. Also, during the ageing phase there is a large model overestimation of O to C ratios in the case of Tritscher et al. (2011), indicating a discrepancy between measured and modelled composition. Additionally, for experiments 1 and 2 of Henry and Donahue (2012), SOA simulations are not able to reproduce the experimental SOA decrease during photooxidative ageing. The reasons for the model overestimates could not be determined with certainty. Besides the above mentioned misrepresentation of wall losses, missing pathways in the gas phase chemistry, the possibly limited applicability of SARs to reactions of poly-oxygenated compounds in which H-bonding might play a critical role, or a misrepresentation of the chemistry of radicals formed in the aerosol could all contribute to the discrepancies.

Chapter 6

Parameterising secondary organic aerosol from monoterpenes using a detailed model

In this chapter, we present a parameter model for α-pinene SOA involving the formation of 10 condensable products, taking into account the impact of temperature, type of oxidant, NO_x-regime and photochemical ageing on SOA yields. The effect of water uptake is also treated. Due to its small size, this parameterisation is easily implementable in three-dimensional regional or global chemistry transport models. The parameterisation is based on simulations with the detailed BOREAM model. The use of a box model makes it possible to cover a wide range of photochemical conditions. The parameterisation is designed to reproduce the SOA yields at equilibrium, when the production of condensable products is balanced by losses due to deposition and photochemical degradation, after typically two weeks. A similar approach was adopted recently in Xia et al. (2011), in which a reduced mechanism consisting in a volatility basis set with further ageing reactions was designed, based on simulations with the detailed MCM mechanism for α-pinene (Saunders et al., 2003). Another reduced-size model designed to reproduce SOA production of a larger model (in this case the MCM v3.1) is the Common Representative Intermediates mechanism for both anthropogenic and biogenic VOC oxidation and SOA formation (Utembe et al., 2009).

In Sect. 6.1 the parameter model is presented, and the adjustment of its parameters is described in Sect. 6.2. In Sect. 6.4 the sensitivity of the parameterised SOA to changes in NO_x, HO_x and radiation levels is investigated, and the parameterisation is evaluated against the full model in simulations of ambient conditions at 17 different locations around the globe, using oxidant, radiation and meteorological fields from a global

chemistry-transport model. Section 6.5 presents a comparison with previous parameterisations. Finally, in Sect. 6.6, the treatment of water uptake is discussed.

6.1 Parameter model

In contrast to previous mechanism reduction studies (e.g. Xia et al., 2009), which aimed at reproducing the impact of the precursor VOC not only on SOA formation but also on the concentrations of oxidants and several key gaseous compounds, we limit the scope of our parameterisation to SOA formation as modelled by BOREAM in typical atmospheric conditions. For this purpose, we adopt the commonly used two-product model first applied by Odum et al. (1996), except that the parameters are obtained from box model simulations with BOREAM, and that the parameterisation accounts for the dependence of SOA yields on the nature of the oxidant (OH, O_3 or NO_3) and on the abundance of NO. This leads us to consider five different scenarios: OH-oxidation and ozonolysis, both for low and high-NO_x, and high-NO_x NO_3-oxidation. It is found that in each case two condensable products suffice to parameterise SOA-formation, thus leading to a model containing in total 10 condensable products.

In the original two-product model, oxidation of the SOA precursor leads to the immediate formation of two surrogate compounds, with mass-stoichiometric coefficients (α_i) and partitioning constants ($K_{p,i}$) adjusted in order to reproduce a set of experimental SOA yields, through the equation

$$Y = \sum Y_i = M_O \sum \frac{\alpha_i K_{p,i}}{1 + K_{p,i} \cdot M_O} \tag{6.1}$$

where Y is the SOA mass yield. Note that the molar stoichiometric coefficients α'_i can be derived from the mass-stoichiometric coefficients and the ratio of the molar mass of the precursor and the organic aerosol: $\alpha'_i = \mathrm{MW}_{\alpha\text{-pinene}}/\mathrm{MW}_{\mathrm{OA}} \cdot \alpha_i$.

In order to account for the large influence of the NO_x-regime on SOA yields (see for example Presto et al. (2005b) or Capouet et al. (2008)), the VOC oxidation product can be taken to be a peroxy radical ("PRAPOH1" and "PRAPO31", Table 6.1), which upon reaction with NO or HO_2, leads to a set of condensable products with stoichiometric and partitioning coefficients adjusted against experiments conducted under high or low NO conditions respectively. This system, adopted by Henze et al. (2008) to parameterise NO_x-dependence of SOA yields for aromatic compounds, is also used here, although modified with the introduction of an additional peroxy radical ("PRAPOH2" or "PRAPO32" in Table 6.1), in order to better reproduce the NO_x-dependence of the yields at intermediate NO levels, as described in more detail in Sect. 6.4.1. The reduced mechanism

TABLE 6.1: Chemical mechanism of the parameter model.

APIN + OH $\rightarrow$ PRAPOH1
PRAPOH1 + $HO_2 \rightarrow (1-\beta_{OH}).\alpha'_1$ APOHL1 + $(1-\beta_{OH}).\alpha'_2$ APOHL2 + β_{OH} PRAPOH2
PRAPOH1 + NO (or + NO_3) $\rightarrow \alpha'_3$ APOHH1 + α'_4 APOHH2 + NO_2
PRAPOH2 + $HO_2 \rightarrow \alpha'_1$ APOHL1 + α'_2 APOHL2
PRAPOH2 + NO (or + NO_3) $\rightarrow \alpha'_3$ APOHH1 + α'_4 APOHH2 + NO_2
APIN + $O_3 \rightarrow$ PRAPO31
PRAPO31 + $HO_2 \rightarrow (1-\beta_{O_3}).\alpha'_5$ APO3L1 + $(1-\beta_{O_3}).\alpha'_6$ APO3L2 + β_{O_3} PRAPO32
PRAPO31 + NO (or + NO_3) $\rightarrow \alpha'_7$ APO3H1 + α'_8 APO3H2 + NO_2
PRAPO32 + $HO_2 \rightarrow \alpha'_5$ APO3L1 + α'_6 APO3L2
PRAPO32 + NO (or + NO_3) $\rightarrow \alpha'_7$ APO3H1 + α'_8 APO3H2 + NO_2
APIN + $NO_3 \rightarrow \alpha'_9$ APNO31 + α'_{10} APNO32
APOHL1 + h$\nu \rightarrow$
APOHL2 + h$\nu \rightarrow$
...

of our parameterisation is presented in Table 6.1. We made the assumption that under low-NO_x conditions, the oxidation of α-pinene would be dominated by the reactions with OH and ozone. Therefore, SOA formation due to oxidation by NO_3 is parameterised in the high-NO_x case only. Although the cross-reactions of peroxy radicals are ignored in the reduced mechanism, their role is taken into account in the full BOREAM model. This simplification is not expected to cause large errors, except in the case of very high VOC loadings. Additionally, for each condensable product a pseudo-photolysis reaction is introduced, which accounts for chemical processing of the condensable products, as will be explained in more detail in the next section. The parameterisation includes a total of 21 equations and 10 condensable products.

6.2 Scenarios for full model runs

The parameter model is fitted to full BOREAM model simulations conducted under five scenarios, each corresponding to one pair of products. We limit the oxidation of α-pinene to one oxidant, by turning off the reactions with the other two main oxidants. All oxidants, however, are allowed to react with the oxidation products of α-pinene. For the high-NO_x scenario we adopt a concentration of 100 ppb of NO_2, while for the low-NO_x scenario we take 1 ppt of NO_2.

In order to mimic real atmospheric conditions, where SOA is composed of a mix of fresh and aged material, subject to wet and dry deposition, we conduct BOREAM simulations including a sustained emission of α-pinene, as well as a sink of gaseous and particulate

compounds due to dilution and deposition. Adopting a sink term corresponding to a lifetime of 6 days, typical for organic aerosols (see for example Farina et al., 2010), as well as prescribed diurnal cycles for the photolysis rates and for the concentrations of OH, HO_2, O_3, α-pinene and NO_2, the system approaches a quasi-steady-state in about 12 days (see the black curve in Figs. 6.1a and 6.1b). The noontime photolysis rates are calculated by assuming a 20° zenith angle. Their diurnal variation is assumed to follow a $\sin^2$ function zeroing at 5 AM and 7 PM LT, corresponding to summertime conditions at mid-latitudes. The concentrations of OH and HO_2 are kept constant during the night, at 2×10^5 and 10^8 cm^{-3}, respectively, whereas their noontime (maximum) values are set to 10^7 and 2×10^9 cm^{-3}, respectively. These values are in the range of concentrations reported from field measurements, e.g. Hofzumahaus et al. (2009) in the Pearl River Delta, Martinez et al. (2003) around Nashville, and Martinez et al. (2010) in the Surinam rainforest.

Ozone concentrations are also prescribed, and follow a diurnal cycle. For high-NO_x scenarios or when O_3 is the main oxidant, the night-time concentrations are assumed to be 15 ppb, and during the day they follow the diurnal cycle, reaching a maximum value of 60 ppb. In low-NO_x conditions, and when OH is the oxidant, ozone concentrations typical of unpolluted areas are chosen with 5 ppb at night and 15 ppb at the daytime maximum. A series of runs with increasing VOC concentrations is then performed, in order to cover a range of organic aerosol loadings between about 0.1 and 50–100 μg/m^3, at seven temperatures between 273 K and 303 K, with steps of 5 K. Water uptake to the aerosol phase is suppressed in these runs. The additional SOA formation due to water uptake will be parameterised through activity coefficients, as documented in Sect. 6.6. When SOA has reached an equilibrium state in the full model OH-oxidation scenarios, SOA typically keeps varying diurnally with a maximum value in the afternoon, a few hours after both α-pinene and OH concentrations have reached a peak value. Later on SOA concentrations go down due to photochemical losses, deposition and the weakening of photochemical production.

For each simulation, the quasi-steady state SOA mass yield is calculated from the model results on the 13th day of the simulation, with $Y = \Delta[\mathrm{OA}]_{\mathrm{prod.}}/\Delta[\alpha\text{-pinene}]$, where $\Delta[\alpha\text{-pinene}]$ is the amount of α-pinene oxidised during one day, and $\Delta[\mathrm{OA}]_{\mathrm{prod.}}$ represents the amount of condensable products produced from this amount of oxidised α-pinene which contributes to the SOA. Assuming equilibrium, $\Delta[\mathrm{OA}]_{\mathrm{prod.}}$ should equal $\Delta[\mathrm{OA}]_{\mathrm{lost}}$, the amount of organic aerosol which is lost due to mainly two processes. A first sink is the loss through deposition/dilution during one day, which equals the daily averaged aerosol concentration divided by the deposition lifetime in days.

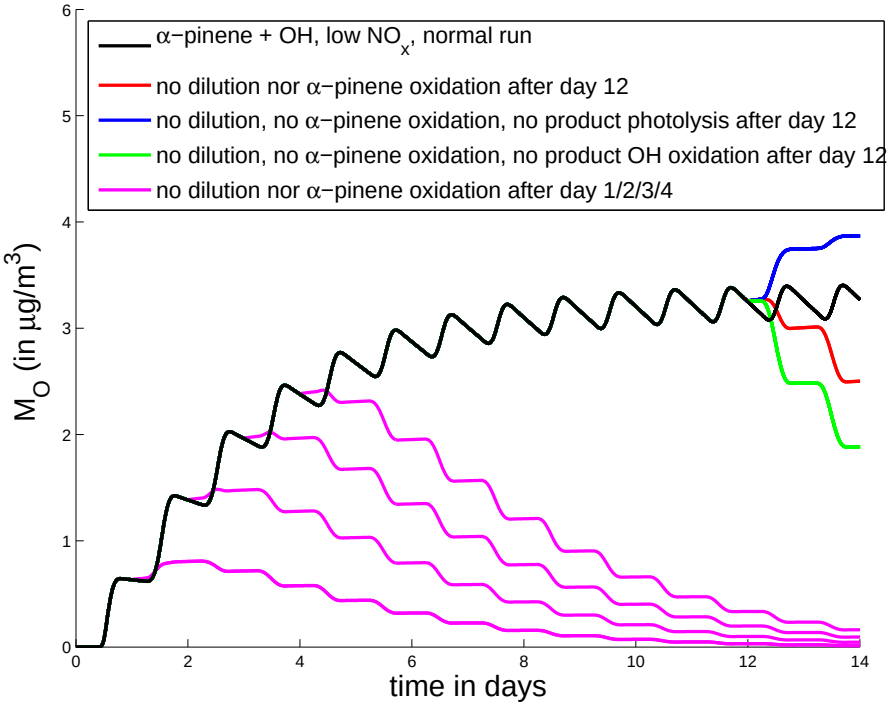

(A) low-NO_x OH-oxidation (273 K)

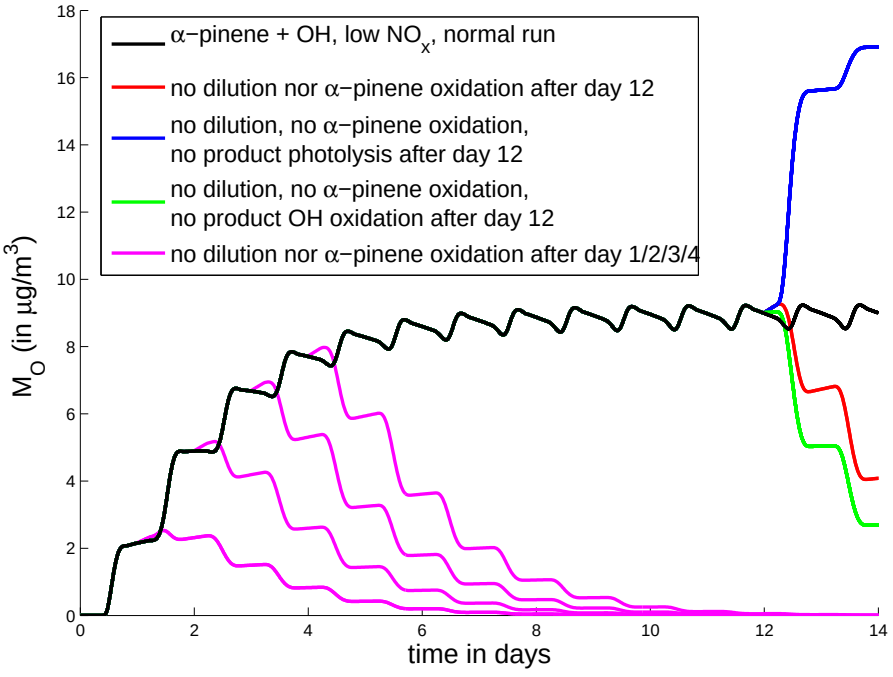

(B) high-NO_x OH-oxidation (273 K)

FIGURE 6.1: Full BOREAM model SOA mass loading M_O, for the low-NO_x and high-NO_x OH-oxidation scenario, at 273 K, as a function of time (black). α-pinene concentrations undergo a diurnal variation between 0.002 ppb at night and 0.01 ppb as the maximum during the day for low-NO_x, and between 0.02 and 0.1 ppb for high-NO_x. When M_O has reached a stable equilibrium level, a number of tests are conducted, starting after day 12, to estimate the impact of photochemical reactions on the condensable products without further α-pinene oxidation and product deposition. Similar tests show the effect of photochemical reactions at earlier points in the ageing scenario, starting after 1, 2, 3 or 4 days (magenta).

A second important contribution is the degradation of the condensable products due to photochemical reactions and photolysis. This includes the oxidation and photolysis of gaseous products at equilibrium with the SOA components, as well as the photolysis of particulate compounds. Simulations with the full BOREAM model in which, starting from day 13, both α-pinene oxidation and product deposition/dilution are switched off, show that the combined effect of photolysis and reactions with oxidants leads to a decrease of SOA concentrations, both under low and high-NO_x conditions (see the red curves in Figs. 6.1a and 6.1b). This result might seem contrary to the finding (e.g. Donahue et al., 2005, Tritscher et al., 2011) that photochemical ageing generally increases SOA concentrations. In the laboratory experiments reported by Lambe et al. (2011), using UV lamps, SOA yields for α-pinene photooxidation were observed to first increase with increasing OH exposure time (from 20% to 40%), but after reaching a maximum value, SOA yields began decreasing to about 25%, when photochemical ageing was continued. It was hypothesised by the authors that this decrease could be due to the fragmentation of semivolatile compounds into smaller, more volatile compounds, becoming more important than further functionalisation.

However, in the present simulations SOA material is already photochemically aged at the onset of the test. Tests in which only photolysis reactions or only OH reactions take place after day 12 show that, taken separately, these processes have a decreasing respectively increasing effect on the SOA levels. When these reactions take place together, their combined effect is to decrease the SOA concentration. It also is apparent from the tests shown in Figs. 6.1a and 6.1b that, especially at high-NO_x, superimposing the separate effects of photolysis and OH reactions on SOA concentrations does not reproduce exactly the combined effect of photolysis and OH reactions acting simultaneously on SOA products. We have performed similar tests for the effect of photochemical reactions on SOA concentrations when α-pinene oxidation and deposition of products have been turned off after an earlier time period than 12 days, as shown on Figs. 6.1a and 6.1b. For low-NO_x, when α-pinene oxidation/deposition is turned off after 1 or 2 days of ageing, there is first a slight increase in SOA concentration due to the reactions with OH and photolysis of the remaining oxidation products. However, when α-pinene oxidation/deposition is turned off after 4 days of α-pinene oxidation, the material is more aged. In this case a slight decrease in SOA is obtained due to the combined effect of photochemical reactions on the oxidation products. For high-NO_x, the combined photochemical reactions and photolysis leads to a decrease in SOA even when α-pinene oxidation and deposition are shut down after 2 days.

We estimate the net amount of SOA lost during one day due to photochemical processes, which we will call the photochemical OA loss, $[\mathrm{OA}]_{\mathrm{pl}}$. The correct SOA yield is then $(\Delta[\mathrm{OA}]_{\mathrm{dep.}} + \Delta[\mathrm{OA}]_{\mathrm{pl}})/\Delta[\alpha\text{-pinene}]$. Note that it would have been possible to

neglect the photochemical OA loss and define a yield based solely on the estimated deposition loss. In such case, the only sink of the (gaseous+particulate) semi-volatile products in the parameterisation is deposition. Although such model would be able to match the SOA concentration of the full model at equilibrium, it would underestimate the SOA concentrations before the onset of this equilibrium, when the photochemical production of condensable compounds greatly exceeds the losses . Using the above formula for calculating the SOA yield, the additional production must be balanced in the parameterisation by an additional sink besides deposition. We therefore incorporate a pseudo-photolysis reaction of the condensable products in the parameter model, with a photorate J_{pl} which is adjusted based on the amount of photochemically lost material, estimated from full BOREAM model runs. For each scenario, the same photolysis rate is applied to both condensable compounds of the two-product model, in the gaseous and in the particulate phases. The procedure for estimating $[\mathrm{OA}]_{\mathrm{pl}}$ and the temperature-dependent fitting of the photorates for each oxidation scenario is described in more detail in Appendix C, Section C.1. Since our model scenarios used maximum photolysis rates calculated assuming a 20° solar zenith angle, extrapolation of the SOA photolysis rate to any radiative condition is made by scaling the retrieved maximum photorate with the photolysis rate of higher aldehydes: $J_{\mathrm{pl}} = f_{\mathrm{pl,max}} \cdot J_{\mathrm{ald}}$ with $f_{\mathrm{pl,max}} = J_{\mathrm{pl,max}}/J_{\mathrm{ald,max}}$ where $J_{\mathrm{pl,max}}$ and $J_{\mathrm{ald,max}}$ are the pseudo-photolysis rate of SOA and the photolysis rate of higher aldehydes, respectively, at the maximum 20° solar zenith angle in our model scenarios. For each of the 5 oxidation scenarios considered, we then derive a temperature-dependent fit for the functions $f_{\mathrm{pl,max}}$ (Table C.1 in Appendix C).

In order to take the temperature sensitivity of the yields into account, $Y(M_O)$ curves are obtained at seven temperatures between 273 K and 303 K. We assume the following temperature dependence for the partitioning constant:

$$K_{p,i}(T) = K_{p,i}(T_r)\,\frac{T}{T_r}\exp\left(\frac{\Delta H_i}{R}\left(\frac{1}{T}-\frac{1}{T_r}\right)\right)\frac{\mathrm{MW}}{\mathrm{MW_{ref}}} \tag{6.2}$$

in which the reference temperature $T_r = 298$ K, ΔH_i represents the enthalpy of vaporisation and $\mathrm{MW_{ref}}$ is the reference average molar mass of the molecules in the SOA. This approach (Eq. 6.2) was followed by Saathoff et al. (2009) for obtaining temperature-dependent coefficients for α-pinene dark ozonolysis experiments over a wide range of temperatures.

The values for $\mathrm{MW_{ref}}$ are chosen per oxidation scenario, at a temperature of 298 K and for an α-pinene concentration leading to an equilibrium SOA concentration around 2.5 $\mu\mathrm{gm}^{-3}$. In simulations with the full model at other temperatures and α-pinene concentrations, MW varies by not more than roughly 5% from this reference value. In the full model the average MW of SOA is calculated based on the molecular masses of the

TABLE 6.2: Fitted parameters for the 10 condensable products in the temperature-dependent parameter model (5 scenarios considered).

Scenario	Product	α_i^0	α_i^1	$K_{p,i}$(298 K) ($m^3 \mu g^{-1}$)	ΔH_i (kJ mol^{-1})	MW_{ref} (g mol^{-1})
α-pinene + OH,	APOHL1	0.621	-0.01229	5.4786	103.2	218.4
low-NO_x	APOHL2	0.347	-0.01532	0.1284	20.25	218.4
α-pinene + OH,	APOHH1	0.134	-0.0284	0.6769	82.9	252.6
high-NO_x	APOHH2	0.295	-0.0300	0.01300	35.8	252.6
α-pinene + O_3,	APO3L1	0.566	-0.0143	6.18	87.6	214.7
low-NO_x	APO3L2	0.326	-0.01637	0.0152	77.9	214.7
α-pinene + O_3,	APO3H1	0.1195	-0.0342	0.557	81.9	237.6
high-NO_x	APO3H2	0.505	-0.01312	0.00888	61.5	237.6
α-pinene + NO_3,	APNO31	0.0336	-0.0657	1.043	157.7	246.9
high-NO_x	APNO32	0.252	-0.01258	0.00580	116.2	246.9

explicit species and on estimates for the generic species classes. Equation 6.2 can be rewritten as $K_{p,i}(T) = A_i \cdot T \cdot \exp(\frac{B_i}{T})$, where A_i and B_i are the fitting parameters. For the mass stoichiometric coefficient, a temperature dependence of the form

$$\alpha_i(T) = \alpha_i^0 \exp(\alpha_i^1 (T - T_r)) \tag{6.3}$$

is assumed. The parameterisations are obtained by minimising the relative difference between the full model yields and the yields calculated using Eq. 6.1. In Table 6.2, the fitted parameters for the ten products considered are given.

6.3 Parameter adjustment results

We compare the evolution of M_O over time between the full model and the parameter model until quasi-steady state in the previously described scenario simulations. The parameter adjustment focussed on achieving a reasonable agreement over the range of 0.5–20 $\mu g m^{-3}$ for M_O. We show the time evolution of SOA in simulations for OH oxidation under low-NO_x and high-NO_x conditions, and an example for oxidation by NO_3, in Fig. 6.2. In these three cases, the parameter model approaches the full model SOA levels near the end of the simulations, when an equilibrium state is reached. Over the whole range of the time evolution, the parameter model's skill at reproducing SOA concentrations is more variable. For the low-NO_x OH oxidation shown here, the time evolution can be considered satisfactory. However, for the oxidation by NO_3, it is not found possible to achieve an accurate time evolution, as shown in the example in Fig. 6.2, featuring significant underestimations during the first days.

In order to provide a measure of how well both models agree in these simulations, we define a deviation factor equal to $\exp(|\log(\overline{M_{O,p}}/\overline{M_{O,f}})|)$, where $\overline{M_{O,p}}$ and $\overline{M_{O,f}}$ are the

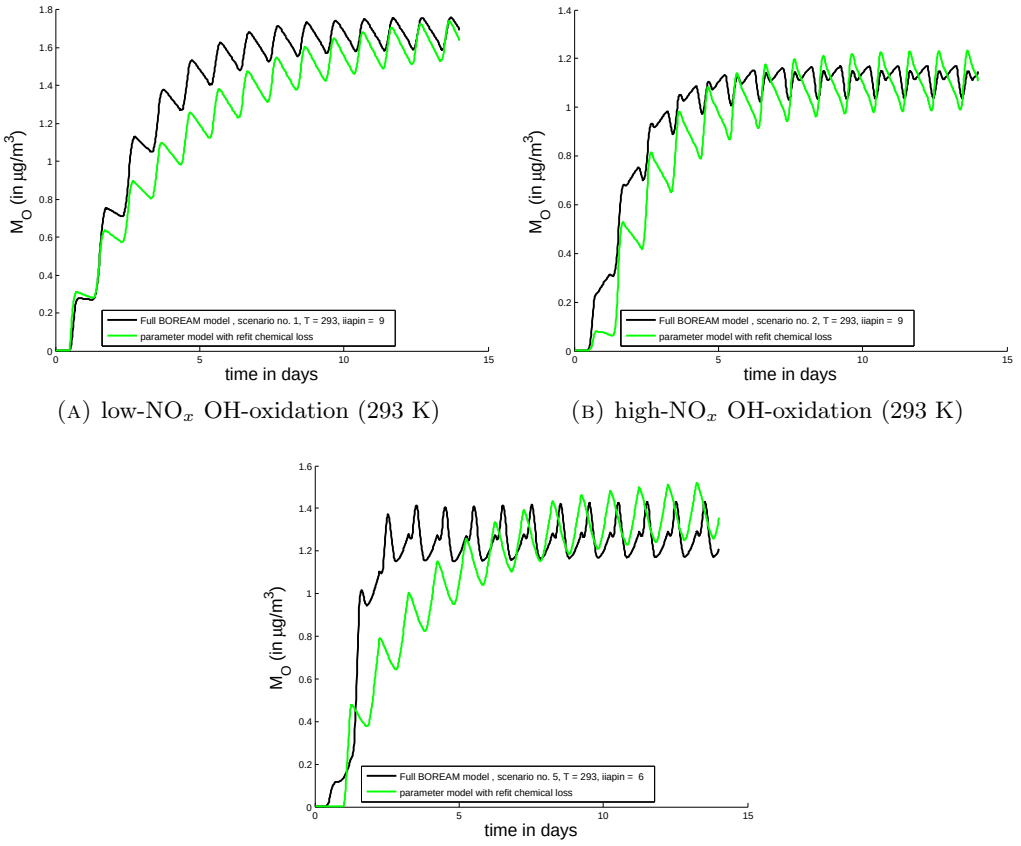

(A) low-NO_x OH-oxidation (293 K)

(B) high-NO_x OH-oxidation (293 K)

(C) high-NO_x NO_3-oxidation (293 K)

FIGURE 6.2: Time evolution of M_O for three examples of the simulations of α-pinene oxidation. The full model results are given in black and the parameter model results in green.

daily averaged M_O concentrations in the parameterisation and in the full model, respectively. The values of this deviation factor are summarised in Table C.2 in Appendix C. To compare SOA yields between full and reduced model at SOA equilibrium, we also calculate a net SOA yield at equilibrium, using the formula $Y_{\text{net}} = \Delta[\text{OA}]_{\text{dep.}}/\Delta[\alpha\text{-pinene}]$. In this way only the net amount of OA produced is considered, equal to the amount lost to deposition over one day near equilibrium. We show plots of Y_{net} versus M_O near SOA equilibrium for the five scenarios and the seven temperatures considered (Fig. 6.3).

As can be seen from the SOA deviation factors, agreement is good in the large majority of cases, both during SOA build-up and at SOA equilibrium. For the highest temperatures, and especially in the NO_3-oxidation case, it is found more difficult to obtain a good agreement over the whole time period of the SOA build-up in the scenarios. In a few cases at low M_O concentrations (below 0.5 μgm^{-3}) and at high temperatures, SOA concentrations are strongly underestimated during the build-up of the SOA (explaining the number of deviations larger than a factor 2 in Table C.2 in Appendix C), although

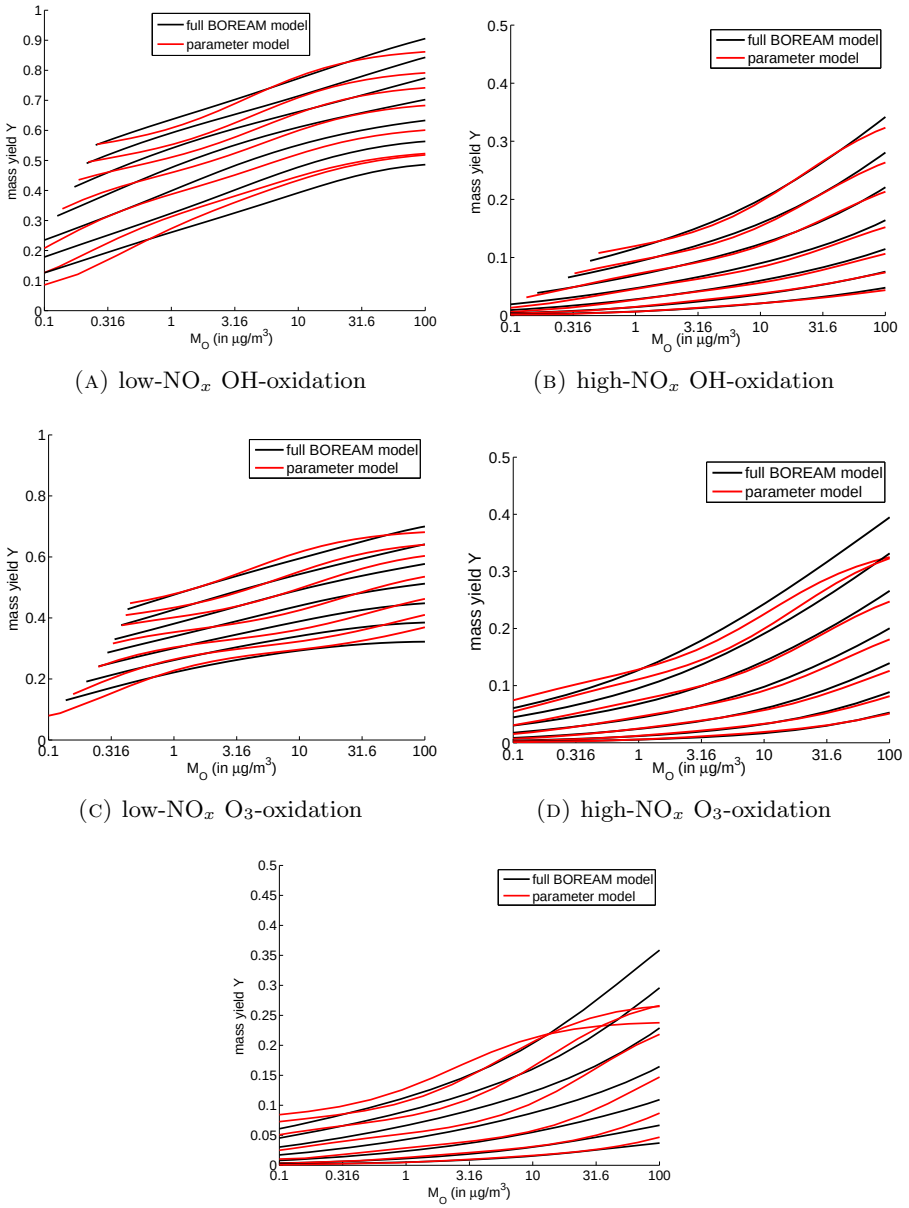

(A) low-NO_x OH-oxidation

(B) high-NO_x OH-oxidation

(C) low-NO_x O_3-oxidation

(D) high-NO_x O_3-oxidation

(E) high-NO_x NO_3-oxidation

FIGURE 6.3: Fitted (red) and full model (black) net equilibrium SOA mass yields as functions of the organic aerosol mass loading M_O, for the different scenarios. The seven curves are obtained at temperatures ranging from 0 to 30°C, by steps of 5°C, the highest temperature corresponding to the lowest curve.

by the time the SOA reaches an equilibrium concentration both models agree better (Fig.6.3).

Figure 6.4 shows the parameterised (dashed lines) and full model (full lines) $Y(M_O)$ curves at 298 K between 0 and 20 μg m^{-3}. The yields in both low-NO_x scenarios are about a factor 10 higher than the high-NO_x yields. The reduction of SOA yields at high-NO_x has been observed in several previous experimental studies, such as Presto et al.

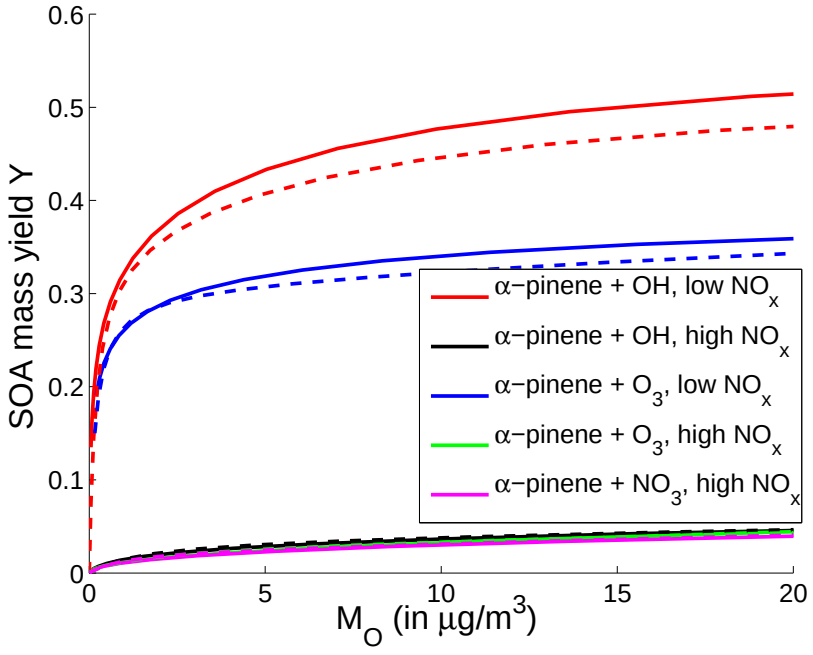

FIGURE 6.4: Net SOA mass yields near SOA equilibrium in the full model (solid lines) and parameter model (dashed lines) at 298 K for the five α-pinene oxidation scenarios, as functions of organic aerosol mass loading.

(2005a). The yields for the OH-oxidation of α-pinene are found to be somewhat higher than for ozonolysis at low NO_x. The yield curves for the high-NO_x scenarios lie close to each other, and their maximum in this range is about 3–4%.

6.4 Sensitivity of the parameterised yields to model assumptions

Since photochemical conditions in the atmosphere might differ from the conditions assumed for the parameterisation, in this subsection we investigate the sensitivity of the parameterised yields to key parameters and assumptions.

6.4.1 NO_x dependence

The NO_x dependence of the parameterised model is based on full model runs at very high and very low NO_x levels. As seen in Table 6.1, the parameterisation involves two peroxy radicals (PRAPOH1 and PRAPOH2) upon α-pinene oxidation by OH, and two peroxy radicals (PRAPO31 and PRAPO32) upon α-pinene ozonolysis. A simpler parameterisation similar to the scheme used in Henze et al. (2008), in which only one peroxy radical

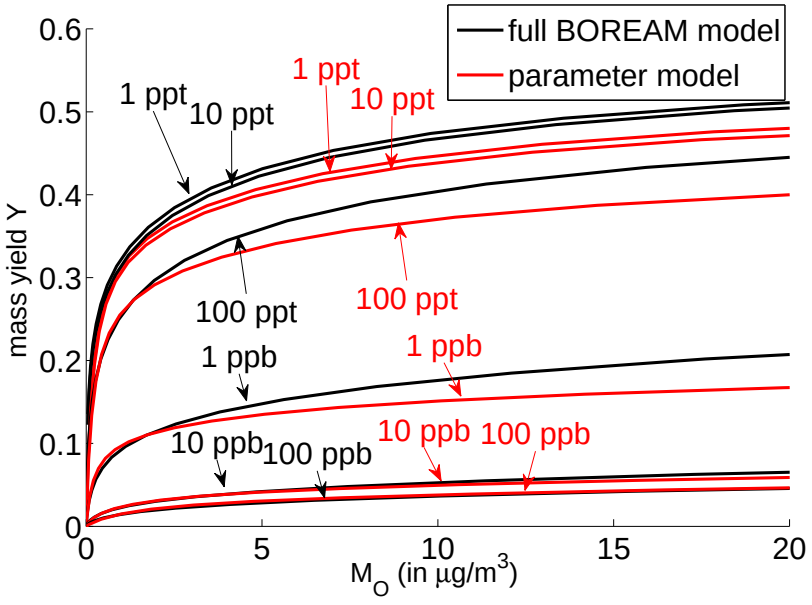

FIGURE 6.5: Net SOA mass yields near SOA equilibrium calculated by the full (black) and parameterised (red) model at NO_2 levels between 1 ppt and 100 ppb, for OH-oxidation of α-pinene (at 298 K).

was produced (i.e. when the branching ratios β_{OH} and β_{O_3} towards the second-generation peroxy radicals PRAPOH2 and PRAPO32 are zero), has been tested, but was found to lead to significant SOA overestimates at intermediate NO_x levels. This can partly be explained by the fact that the peroxy radicals reacting with HO_2 in the parameter model would in that case immediately yield highly condensable low-NO_x products, which in the full model correspond to products formed only after several subsequent reactions of peroxy radicals with HO_2, for example hydroxy dihydroperoxides. In the full model, however, a reaction with HO_2 can be followed by a reaction with NO at intermediate NO_x, leading to the formation of a much more volatile product in the full BOREAM model.

The introduction of the second generation peroxy radicals PRAPOH2 and PRAPO32, produced with a fitted branching ratio $\beta_i(T)$ from the reactions of the first peroxy radicals with HO_2, as seen in Table 6.1, results in a redistribution between high and low-NO_x products, and to an improved agreement between full and parameter model at intermediate NO_x levels for both OH and ozone oxidation. It was not found necessary to introduce such a branching to a second peroxy radical for the reaction of the first generation peroxy radicals with NO. The temperature dependent fitted function for both β_{OH} and β_{O_3} is $4.286 \cdot 10^{-4} \cdot T^2 - 0.2181 \cdot T + 27.53$ for the range 278 K to 303 K, while outside this range the function remains constant at the values it has at the edge of the fitting range.

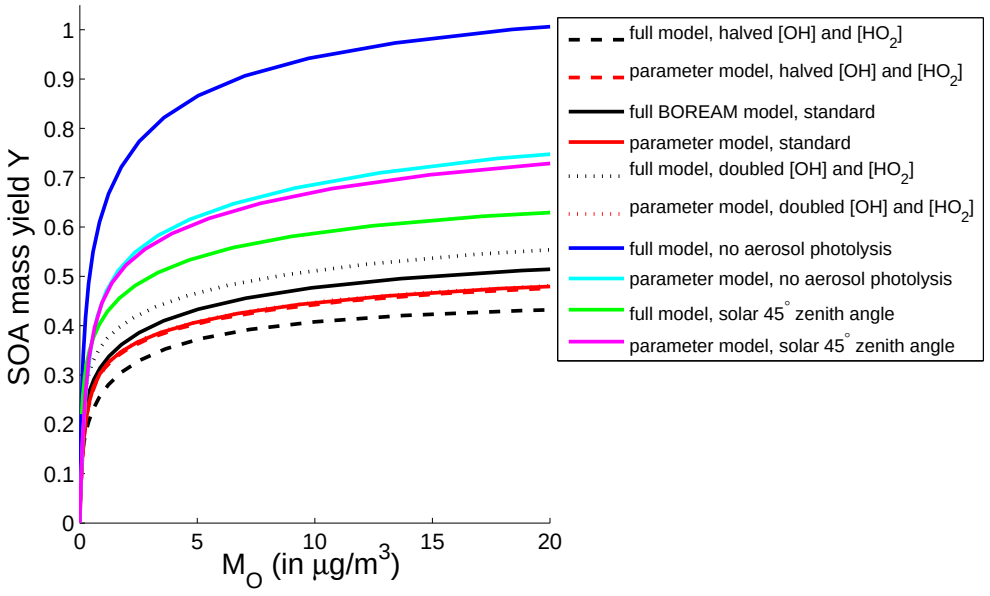

FIGURE 6.6: Net SOA yields calculated for the OH-oxidation of α-pinene at low-NO_x scenario, at 298 K, for sensitivity tests with the full model and the parameter model for variations in OH and HO_2 concentrations, solar zenith angle and absence of particulate phase photolysis. These equilibrium SOA yields are obtained after 12 days into the photochemical ageing scenario.

We have checked the agreement of full and parameter model at intermediate-NO_x levels at different temperatures. The curves of the net mass yields Y_{net} near SOA equilibrium, as defined in the previous Section 6.3, versus M_O can be seen in Fig. 6.5 and Figs. C.3e to C.3d in Appendix C.

6.4.2 Importance of aerosol photolysis for SOA ageing

Aerosol photolysis has only little impact for the simulation of the experiments described in Table 3.3, which lasted only a few hours. Aerosol photolysis has, however, a potentially major impact on SOA yields after prolonged ageing. In the full model simulations, described in Sect. 6.2, turning off aerosol photolysis leads to a near doubling of the SOA yields, in particular for the oxidation of α-pinene by OH under low-NO_x conditions, with SOA mass yields reaching values of around 100% (Fig. 6.6, blue curve).

This strong sensitivity of SOA yields to aerosol photolysis is caused by the fact that most condensable species reside predominantly in the aerosol phase after several days of ageing. When photolysis of the aerosol phase species is ignored, only the small fraction of these condensable species left in the gas phase can undergo further reactions (photolysis or oxidation by OH). The more volatile species, residing mostly in the gas phase, are oxidised in part to low-volatility compounds, which can partition to the aerosol phase, where they are shielded from further oxidation. This process will over time lead to an

accumulation of very condensable oxidation products in the SOA. Aerosol photolysis can partly revolatilise these condensable species, except those which do not contain any photolabile chromophore. Ignoring aerosol photolysis will therefore likely lead to unrealistically high SOA yields in models, although large uncertainties exist, regarding the rates of aerosol phase photolysis reactions, and the further chemistry of the photolysis products. Further experimental work is clearly desirable. The curve for the SOA loadings in a parameter model simulation in which particulate phase photolysis is ignored has been included (cyan curve). In this case there is also an increase in SOA concentration. However, this increase in SOA is smaller than the one observed in the full model. The parameter model has not been designed to reproduce the case without aerosol photolysis, and it is therefore not expected to reproduce full model results in the absence of aerosol photolysis. The results in Fig. 6.6 are referring to equilibrium net SOA yields, obtained after 12 days of the ageing scenario.

In a second sensitivity test, the solar zenith angle used in the calculation of photorates is increased from 20° to 45° (but the prescribed oxidant levels are kept identical). This leads to an increase of SOA yields in the full model (solid green curve), e.g. from 0.48 to 0.59 at $M_O = 10\ \mu g\,m^{-3}$. This increase is overestimated by the parameter model (at about 0.68, solid magenta curve). This discrepancy is due to the fact that, as was mentioned in Sect. 6.2, the parameter model has not been explicitly fitted to match the full model for various radiation spectra.

The impact of other possible particulate phase chemistry reactions such as oligomerisation is difficult to estimate. We acknowledge that such reactions could be important for long-term ageing and this topic clearly requires further investigation.

6.4.3 Influence of assumed OH and HO_2 concentrations

OH and HO_2 play an important role in SOA formation, especially at low NO_x, since their concentrations determine the formation of hydroperoxides and other oxygenated species. As seen in Fig. 6.6, the SOA yields increase only slightly from 0.48 to 0.51 for $M_O = 10\ \mu g\,m^{-3}$ in the full model (dotted black line), when the OH and HO_2 concentrations are doubled.

Halving the OH and/or HO_2 levels leads to a comparatively larger change. E.g. at $M_O = 10\ \mu g\,m^{-3}$, the SOA yield at low-NO_x is reduced from 0.48 to 0.41 when both the OH and HO_2 concentrations are halved in the full model (dashed black line). In contrast, the net SOA mass yields of the parameter model (in red) are not sensitive to these variations, as expected, since there is no direct impact of OH and HO_2 concentrations on the properties of condensable products in the parameter model. In conclusion, the

use of a fixed diurnal profile for OH and HO_2 in the model calculations introduces an uncertainty in the parameterised SOA formation rate, estimated to be typically of the order of 10–15%.

6.4.4 Sensitivity to generic chemistry parameters in BOREAM

Sensitivity tests were conducted to evaluate the impact of several key parameters related to OH reactions and photolysis of the generic species, similar to those shown in Fig. 3.6, but here applied to the long-term SOA ageing scenarios, as shown in Fig. 6.7.

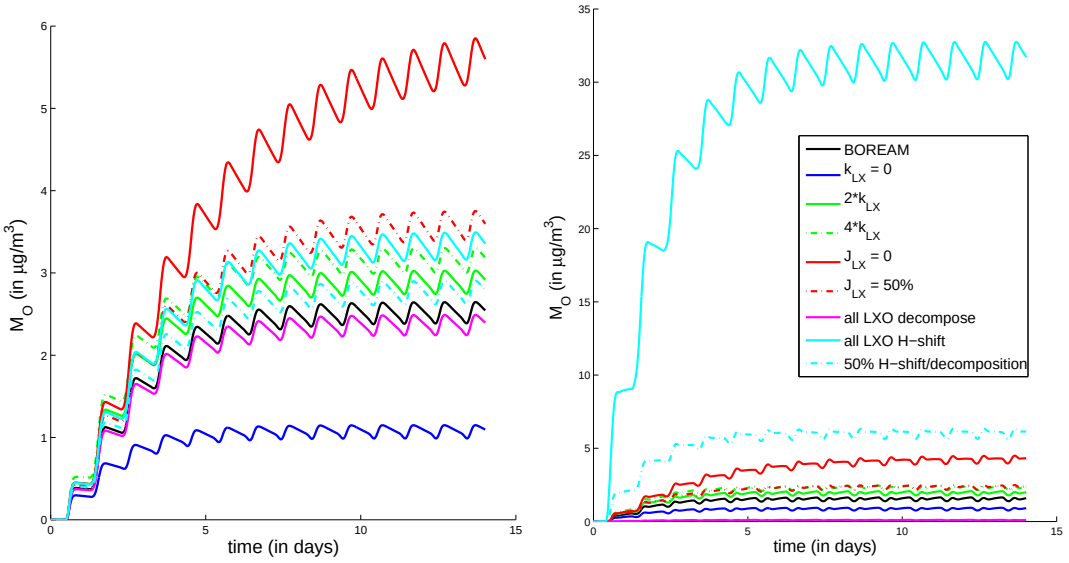

(A) low-NO_x OH-oxidation scenario (B) high-NO_x OH-oxidation scenario

FIGURE 6.7: Sensitivity tests for SOA yields to the assumed reaction constant with OH of the generic part of generic species classes, k_{LX}, to the J-value j_{LXALD} of this generic part and to the branching ratios of generic alkoxy radicals, similar to the tests shown in Fig. 3.6, for OH oxidation under (a) low (left panel) and (b) high-NO_x conditions (right).

As seen in Fig. 6.7, a significant decrease in SOA (factor of 2) is observed when k_{LX}, the OH-reaction rate of generic species (excluding the reactivity associated with the explicitly represented functional group), is set to zero (see the blue curve). If by contrast k_{LX} would be twice or four times higher than the assumed standard value in BOREAM then only a moderate increase in SOA is found (green solid and dash-dotted curves). Setting the j-value j_{LXALD} (used to represent part of the photolysis rate of generic species, corresponding to the photo-rate of an aldehyde) to zero leads to a significant increase (factor 2–3) in SOA (red), although a more plausible reduction of j_{LXALD} by 50 percent leads to a more moderate increase of about 30% (red dash-dotted line). Sensitivity to the assumed alkoxy radical branching between H-shift isomerisation and

decomposition is found to be moderate for the OH low-NO_x scenario (magenta and cyan). By contrast, for the OH high-NO_x scenario, sensitivity to the alkoxy radical branching parameters for the generic species is found to be strong. In the unrealistic case where all generic alkoxy radicals would undergo H-shift isomerisation, a very strong increase in simulated SOA concentration is found (cyan solid line). Setting the branching ratio to 50 percent H-shift isomerisation still leads to more than a doubling of SOA yields. We can conclude that at high-NO_x, uncertainty on SOA concentrations simulated by the BOREAM model is considerable due to the uncertainty on parameters related to alkoxy radicals in the generic chemistry. Note that even in a fully explicit mechanism the uncertainty on the structure activity relationships for alkoxy radical reactions is often considerable (Vereecken and Peeters, 2010).

6.4.5 Comparison of full and parameter model for simulations based on ambient conditions

In order to test the ability of the parameter model to reproduce the SOA loadings calculated by the full BOREAM model under ambient conditions, simulations are performed in which the previously investigated sensitivities (to mass loading, temperature, NO_x-regime, oxidant levels and applied radiation) are probed using more realistic atmospheric scenarios. The global chemistry transport model IMAGESv2 (e.g. Stavrakou et al., 2012) was used to obtain time series of temperature, α-pinene emission rates and the concentrations of important atmospheric species over 5 months (from May until September) at 17 selected locations around the globe (see Table C.3 in Appendix C for an overview). The IMAGESv2 output is vertically averaged over the tropospheric column (weighted by the gas phase α-pinene product concentrations) and applied in the box models. OA from other sources than the monoterpenes (primary organic aerosol and SOA from isoprene, aromatics, sesquiterpenes and small dicarbonyls) was also modelled in these IMAGESv2 simulations, using parameterisations from the literature (Stavrakou et al., 2009, 2012). This additional OA also contributes to the total absorbing organic mass in our box model simulations. In the box model, monoterpene SOA concentrations are taken to be zero at the start of the month. Water uptake is ignored.

The level of agreement between full and parameter model differs for the different locations, depending on atmospheric conditions. An overall view of the parameter model skill is provided by Fig. 6.8, where the daily averaged values M_O due to α-pinene in the parameter model ($\overline{M_{O,p,i}}$) are represented against the corresponding values in the full model ($\overline{M_{O,f,i}}$). We calculate an averaged relative difference factor per location using $\sum |\overline{M_{O,p,i}} - \overline{M_{O,f,i}}| / \sum \overline{M_{O,f,i}}$. Similarly we calculate an averaged bias factor using $\sum \left(\overline{M_{O,p,i}} - \overline{M_{O,f,i}}\right) / \sum \overline{M_{O,f,i}}$. For most locations agreement is quite good, as can be

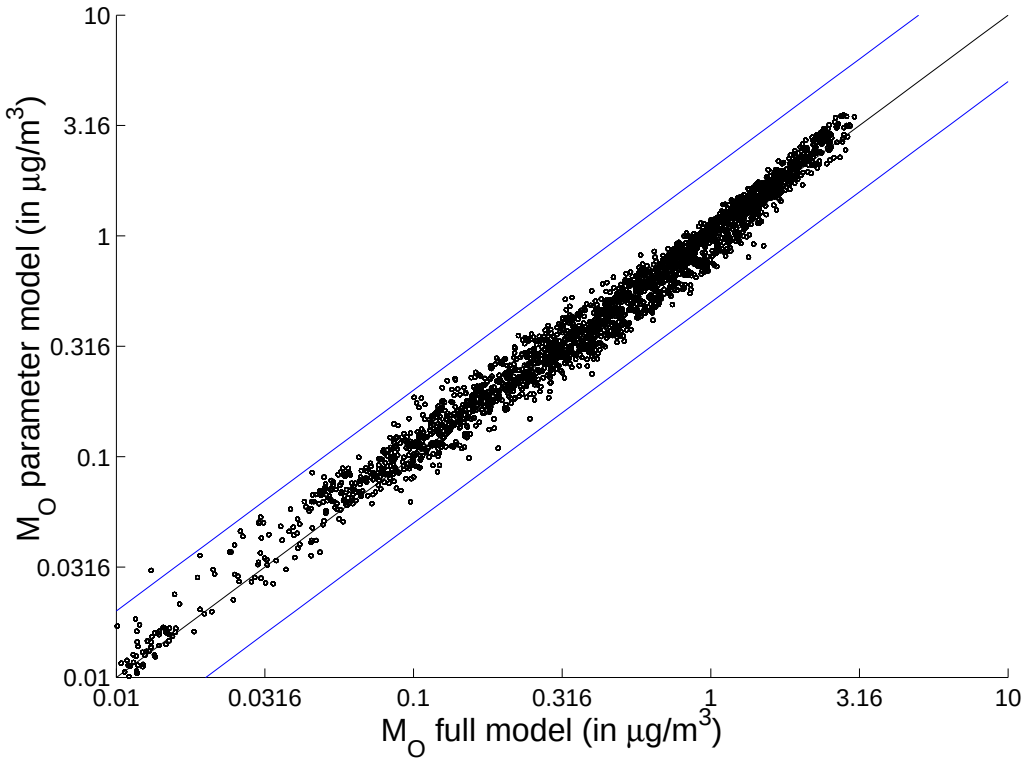

FIGURE 6.8: Daily averaged α-pinene M_O parameter model values versus full BOREAM model values for 17 locations during 5 months, using ambient data simulated with the global CTM IMAGESv2. The blue lines indicate the region of agreement to within a factor two.

seen in Figs. 6.8 and 6.9, and Table C.3 and Fig. C.4 in Appendix C. The largest deviations are found for Queensland, where there is on average an overestimation of about 25%, and for Finland and the Pearl River Delta, where the parameter model SOA concentrations are on average about 20 percent too low. These deviations are probably partly caused by the fact that the fitting procedure was not always entirely successful in matching SOA formation at all times and for all photochemical conditions (Section 6.3). A second cause of error is that the parameter fitting did not consider possible impacts of variations in atmospheric conditions, such as variable radiation or concentrations of oxidants (Subsections 6.4.2 and 6.4.3). In most other locations, such as for example The United States, Belgium and Peru, agreement is better; on average over all locations the deviation is about 11%, with only little bias. Given the large uncertainties associated with SOA model estimates, this level of agreement between parameter and full model seems satisfactory.

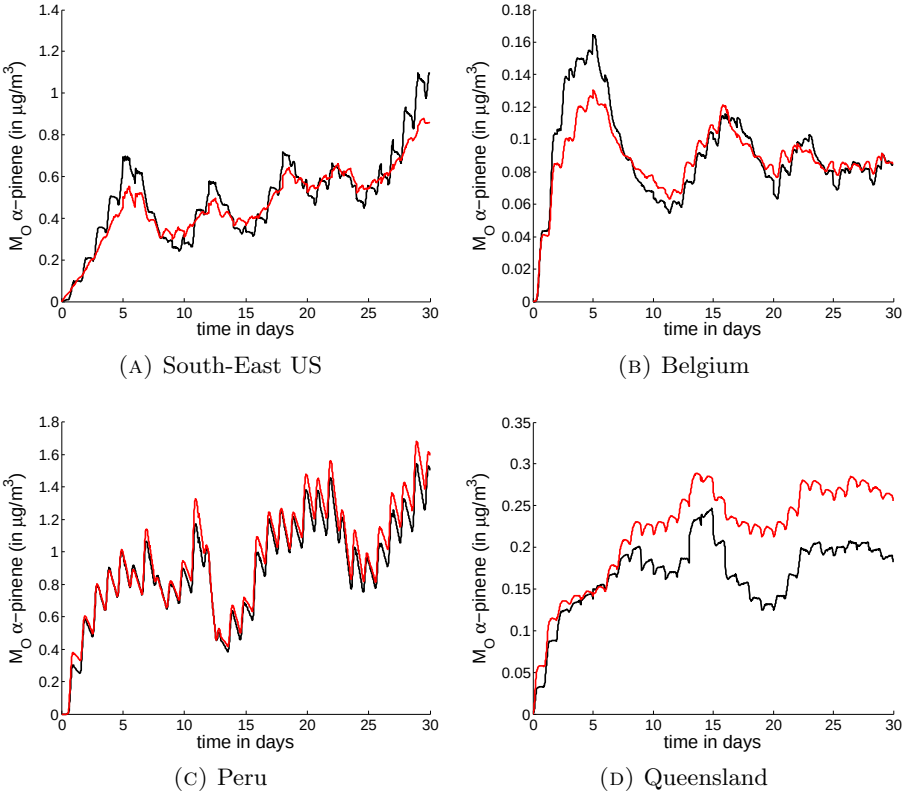

(A) South-East US (B) Belgium

(C) Peru (D) Queensland

FIGURE 6.9: Example of time evolution of α-pinene SOA in the full BOREAM model (black) versus the parameter model (red) for simulations based on atmospheric conditions simulated with the CTM IMAGESv2, shown here for the month of July.

TABLE 6.3: Parameterisations for α-pinene SOA based on smog chamber experiments. VBS = Volatility Basis Set. 2P = 2-product model.

Study	Type	Oxidant	NO_x depend.	T depend.	Radiation
Odum et al. (1996)[a]	2P	OH, O_3	no (interm. NO_x)	no ($\pm$321 K)	solar
Griffin et al. (1999)	2P	O_3[d]	no (low NO_x)	no (308 K)	dark
Cocker III et al. (2001)	2P	O_3[d]	no (low NO_x)	no (301 K)	dark
Presto et al. (2005a)	2P	O_3[d]	yes (low/high NO_x)	no (295 K)	dark/UV
Saathoff et al. (2009)	2P	O_3[d]	no (low NO_x)	yes	dark
Pye et al. (2010)[b]	VBS	O_3[d]	yes (low/high NO_x) $Y_{\mathrm{h.\,NO}_x} = \frac{1}{2} Y_{\mathrm{l.\,NO}_x}$	no (298 K)	dark
Farina et al. (2010)[c]	VBS	OH, O_3	yes (low/high NO_x)	no	blacklight

[a] based on Hoffmann et al. (1997)
[b] based on Shilling et al. (2008)
[c] based on Hoffmann et al. (1997), Ng et al. (2006), Ng et al. (2007a)
[d] including an OH-scavenger

6.5 Comparison with parameterised models based on experimental yields

A non-exhaustive overview of parameterisations for SOA formation from α-pinene based on smog chamber studies is given in Table 6.3. Figure 6.10 compares the SOA yield

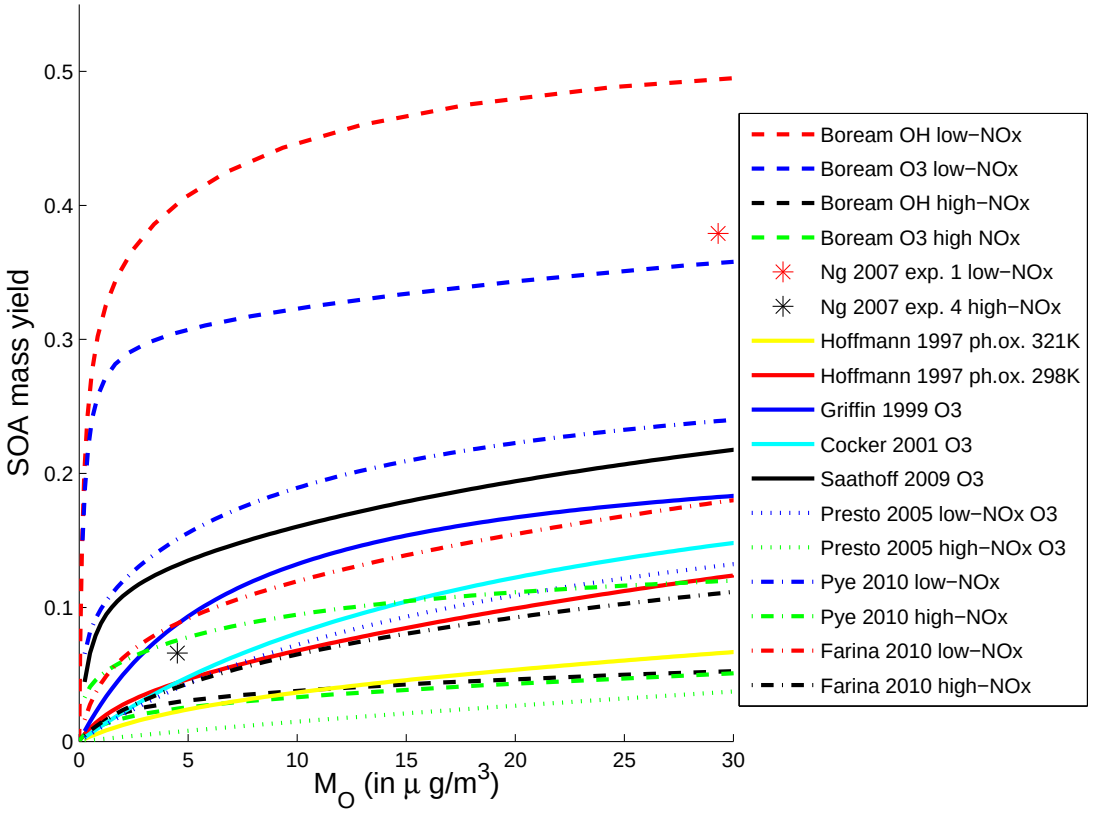

FIGURE 6.10: Comparison of previously derived SOA mass yield curves from other studies, based on smog chamber experiments, with parameterisations based on the BOREAM model (four scenarios, dashed lines). Also shown are the measured experimental yields of experiments 1 and 4 in Ng et al. (2007a).

curves for these studies with the parameterisation obtained with BOREAM. The reference temperature is taken to be 298 K, to allow for proper comparison. For those experimental parameterisations which do not contain an explicit temperature dependence, we adjusted the partitioning equilibrium constants by use of Eq. 6.2, assuming a value for $\Delta H_{\mathrm{vap}}/R$ of 5000 K, although it should be noted that a large uncertainty exists for the enthalpy of vaporisation of SOA (Stanier et al., 2008). For the parameterisation of Hoffmann et al. (1997) this adjustment nearly doubles the SOA yield, but for most other parameterisations the difference is less important.

Figure 6.10 shows a very large variation between the different parameterisations based on experiments, stressing the large impact of experimental conditions on the SOA yields. Most experimental SOA yield curves fall between the high yields of the low-NO_x BOREAM results and the low yields for the high-NO_x scenario. Low-NO_x BOREAM-based yields are considerably higher than those for the experimental studies, partly due to the fact that ageing has a larger impact in our model scenarios. These assume an average lifetime of 6 days for the gas and aerosol species, much longer than the duration of the smog chamber experiments, which typically last several hours. Moreover, in most

ozonolysis studies, OH scavengers were used, which limits the extent of further ageing which the primary products can undergo. In our low-NO_x model scenario, the continuous exposure of products to OH and HO_2 is responsible for much of the increase in functionalisation (with for example additional hydroperoxide groups as a result) and decrease in volatility of the oxidation products. In shorter experiments, or in experiments without OH, this process will be limited, and SOA yields remain lower.

By contrast, for the high-NO_x parameterisation based on BOREAM, SOA yields are lower than in most parameterisations from other studies based on high-NO_x photooxidation experiments. In the BOREAM simulations of photooxidation at high-NO_x, the reaction with NO forms mostly alkoxy radicals, and some nitrates or peroxy acyl nitrates (PANs) as side products. The alkoxy radicals can in some cases decompose, which leads to smaller carbon chains or to a loss of oxygenated functional groups, increasing volatility. This explains the large difference found between high and low-NO_x yields, and also why ageing over a long time period of two weeks under high-NO_x conditions might lead to lower SOA yields than seen in high-NO_x photooxidation experiments of shorter duration (several hours). As an illustration, the high-NO_x experimental yield of Ng et al. (2007a) experiment 4 is shown in Fig. 6.10. This yield is higher than in the BOREAM scenario for photooxidation at high-NO_x. It should be noted that in the simulation of this experiment, the full BOREAM model calculated SOA yields were slightly overestimated (Fig. 3.5, Fig. 3.6). One exception is the high-NO_x case of Presto et al. (2005a) in which even lower yields were found. This last experiment was a dark ozonolysis experiment with an OH scavenger, resulting in only first generation products, which are generally less condensable than more aged products.

Experimental SOA parameterisations for α-pinene have been used in several global modelling studies, where they are generally used to represent SOA from the monoterpene family. Pye et al. (2010) used a NO_x-dependent parameterisation, for which the low-NO_x yield is based on the study of Shilling et al. (2008), which consisted of dark ozonolysis experiments with addition of an OH scavenger. The absence of OH can partly explain their lower yield compared to BOREAM. Farina et al. (2010) used a NO_x-dependent parameterisation of a 4-product volatility basis set, based on the studies of Hoffmann et al. (1997), Ng et al. (2006) and Ng et al. (2007a). Their high-NO_x yields lie somewhat lower than the high-NO_x experimental yields of Ng et al. (2007a) and the temperature-adjusted parameterisation of Hoffmann et al. (1997). Their low-NO_x curve is considerably lower than the low-NO_x experimental yield of Ng et al. (2007a), and the low-NO_x BOREAM yield curve.

6.6 Treatment of water uptake and water activity

In Compernolle et al. (2009), the UNIFAC method for activity coefficient calculation, as implemented by Hansen et al. (1991), was extended to include missing atmospherically relevant functional groups, such as the hydroperoxide, peroxy-acid, nitrate and peroxy acyl nitrate groups. This method was applied in all BOREAM simulations presented in this study. However, water uptake was not considered in these simulations, although it is expected to increase the total number of molecules in the absorbing phase, and therefore also the partitioning to the particulate phase of organic semi-volatile compounds.

These effects are included in our parameterisation through the introduction of an activity coefficient for water, γ_{H_2O}, and a pseudo-activity coefficient for the organic species in SOA, γ_{Org}. Both parameters are estimated from BOREAM simulations including water uptake, conducted at a temperature of 288 K and at relative humidity values ranging between 0 and 99.9%.

As a simplification, the SOA is treated as a binary mixture of water and one organic pseudo-compound, which represents the entire organic fraction of the SOA. The overall pseudo-activity coefficient γ_{Org} accounts for the non-ideality effects which the added water exerts on the organic compounds, whereas the non-ideality effects among organic compounds are implicitly accounted for in the parameterisation without water uptake.

Figure 6.11 shows the resulting dependence of the water activity coefficient on relative humidity. At relatively low relative humidity (typically below 60%), the water activity coefficient is lower than 1, leading to an increased water concentration in SOA, compared to the ideal case, in which the relative molecular water concentration would be equal to the relative humidity. γ_{H_2O} reaches a maximum of 1.08 for the low-NO_x scenario at 92% RH. At higher RH values, γ_{H_2O} decreases towards a value of 1 at 100% RH. This is expected, as the organic fraction becomes very small, causing non-ideality effects of the organic fraction to become negligible.

Two methods are used to derive the pseudo-activity coefficient γ_{Org} for the organic fraction. In the first method, γ_{Org} is obtained from the modelled activity coefficient and molecular fraction of water in SOA. Indeed, for a binary mixture, when the molar fraction and activity coefficient for one component are known, the Gibbs-Duhem relationship at constant temperature and pressure (Poling et al., 2001)

$$x_1 \left(\frac{\partial \ln \gamma_1}{\partial x_1} \right)_{T,P} = x_2 \left(\frac{\partial \ln \gamma_2}{\partial x_2} \right)_{T,P} \tag{6.4}$$

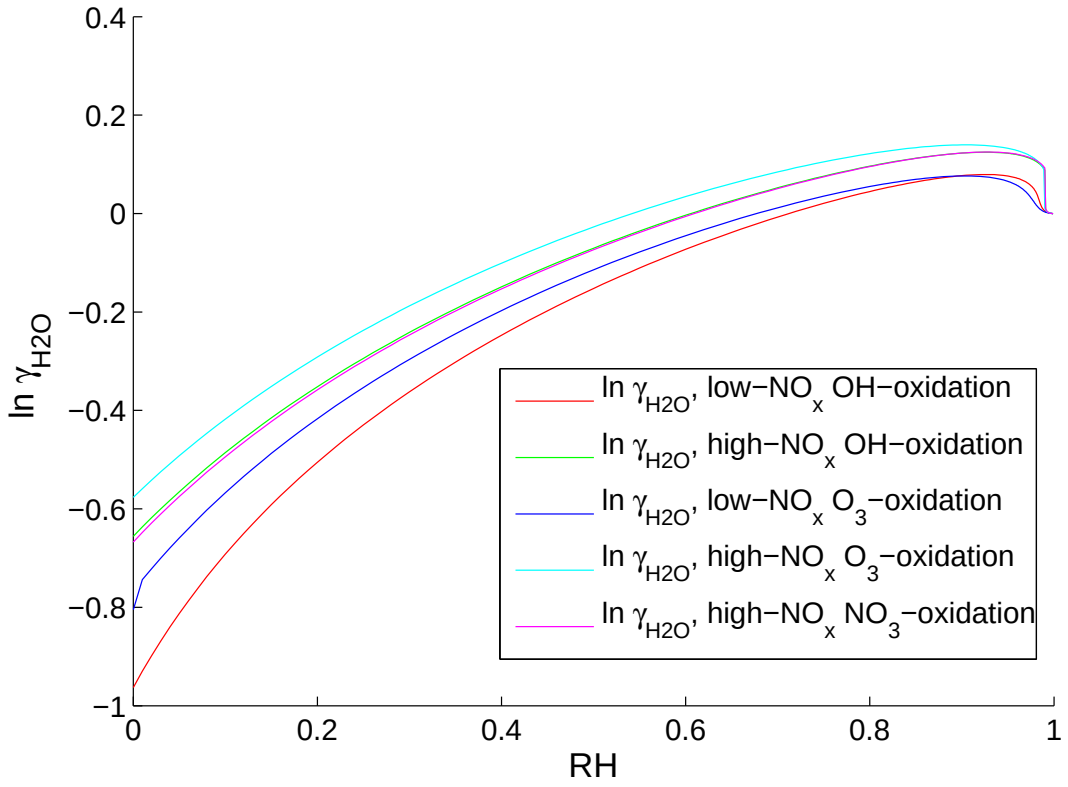

FIGURE 6.11: The activity coefficient of water in function of RH, for the five oxidation scenarios (at 288 K).

might be used to derive the activity coefficient of the other component through an integration. At $x_1 = 0$, the activity coefficient of the second component is 1, and $\ln \gamma_2 = 0$. We can then integrate Eq. 6.4 from $x_1 = 0$ to any x_1 (Olander, 2007):

$$\int_{\ln \gamma_2(x_1=0)}^{\ln \gamma_2(x_1)} d \ln \gamma_2 = \ln \gamma_2 = - \int_{\ln \gamma_1(x_1=0)}^{\ln \gamma_1(x_1)} \frac{x_1}{1 - x_1} \, d \ln \gamma_1 \tag{6.5}$$

Taking water and the organic fraction to be component 1 and 2, $\gamma_2 = \gamma_{\mathrm{Org}}$ can be obtained by the numerical evaluation of the integral on the right-hand side of Eq. 6.5, with γ_1 and x_1 provided by BOREAM model simulations.

Comparing simulated M_O values including water for the parameter model and the full model (Fig. 6.13), a good agreement is found for the low-NO_x OH-oxidation. For the other oxidation scenarios, however, the use of the Gibbs-Duhem γ_{Org} leads to larger deviations above 80% RH. Therefore, for high-NO_x conditions a direct optimisation of γ_{Org} was performed instead, at 160 RH values between 0 and 100%, which minimises the difference in M_O between full and parameterised model (shown in Fig. 6.12). As can be seen in Fig. 6.13, these values lead to an excellent agreement of the SOA yields for the high-NO_x scenario. Tabulated values for $\gamma_{\mathrm{H_2O}}$ and γ_{Org} for the oxidation scenarios can be found in Tables C.4 and C.5 of Appendix C. Sensitivity tests in which the activity

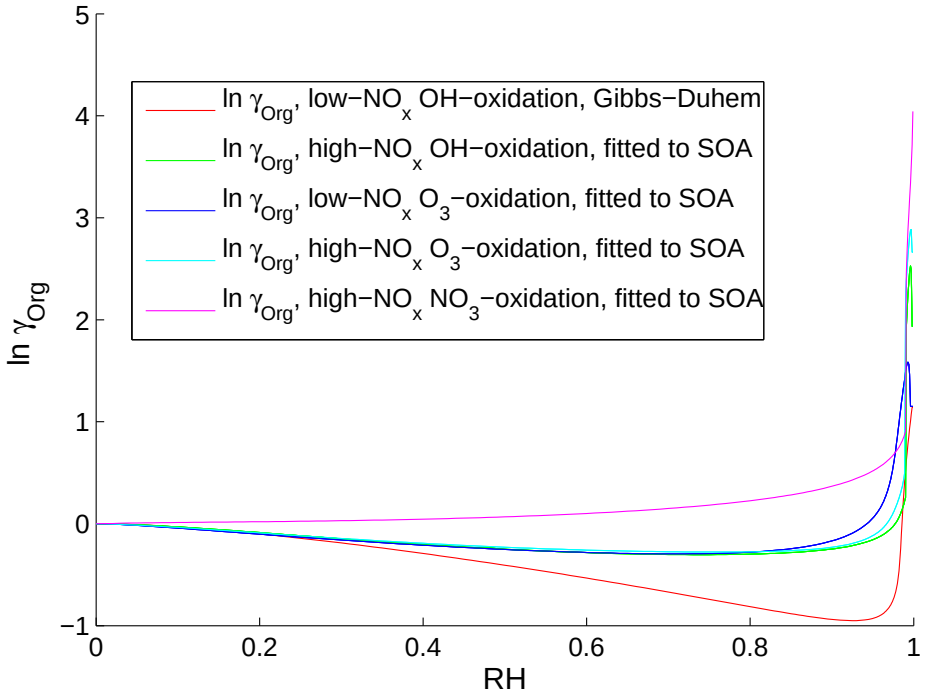

FIGURE 6.12: The pseudo-activity coefficient γ_{Org}, which accounts for the non-ideality effects of water on the organic fraction (at 288 K). For low-NO_x OH-oxidation it is derived based on the Gibbs-Duhem equation (red curve). For the other scenarios, the use of this γ_{Org} based on Gibbs-Duhem does not always lead to a satisfactory agreement between full BOREAM SOA yields and the parameterisation. Therefore, γ_{Org} values derived by a direct fitting in order to optimise M_O agreement between full BOREAM and parameter model are used (other curves).

coefficients are given constant values (1 or 1.1 for γ_{H_2O}, and 1 for the organic species) show that at high RH the use of these constant values for the γ can lead to important discrepancies (Fig. 6.13).

Extrapolation to intermediate NO_x levels of the above parameterisation for water uptake and water activity can be performed as follows. The values of $\gamma_{\mathrm{Org},i}$ for each oxidation scenario are assigned to the corresponding condensable products. γ_{H_2O} is extrapolated based on the mass fraction of products corresponding to oxidation scenario i in the SOA, r_i, using $\gamma_{H_2O} = \prod (\gamma_{H_2O,i})^{r_i}$. We have performed simulations at intermediate NO_x (100 ppt and 1 ppb NO_2), see Section C.5 in the Appendix, showing that the agreement between full and parameter model is good.

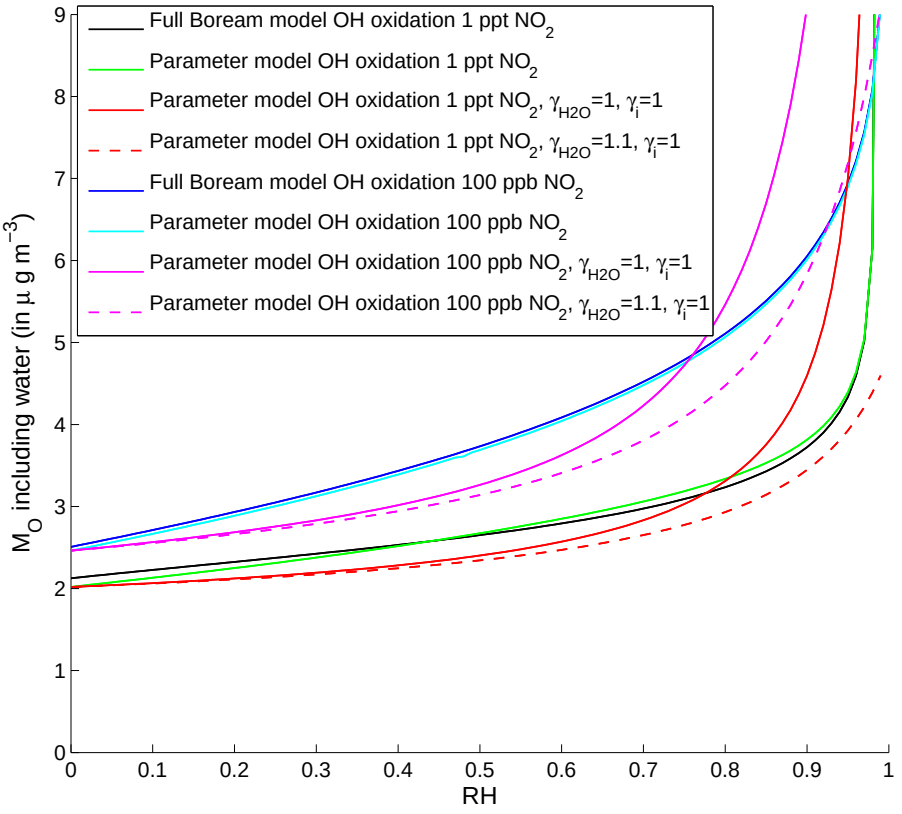

FIGURE 6.13: The impact of relative humidity (RH) on total absorbing mass M_O (including water), for the full model in the case of OH-oxidation at low-NO_x (black) and high-NO_x (blue), at 288 K. Note that the applied α-pinene concentration was higher in the case of the high-NO_x simulation shown here. The parameter model results are given in green for low NO_x and cyan for high NO_x. Two sensitivity tests illustrate the model discrepancy resulting from the use of constant values for the activity coefficients in the parameter model.

6.7 Conclusions

BOREAM has been used to design and adjust an SOA parameterisation for use in large-scale atmospheric models. Simulations were performed with BOREAM for low- and high-NO_x conditions, using a prescribed diurnal cycle for radiation, oxidants and α-pinene, and accounting for the deposition of gas phase and particulate compounds. The equilibrium SOA mass concentrations, reached typically after about 12 days, were used to constrain the parameters for each oxidation scenario. In order to take into account the revolatilisation of condensable products due to photochemical processes, a pseudo-photolysis reaction has been applied to the condensable products in the parameter model. The SOA parameterisation is shown to reproduce the full BOREAM model

results reasonably well in the majority of cases at all NO_x levels. A decrease of SOA mass yields is found for increasing NO_x concentrations in the full model, which is generally well reproduced by the parameter model.

The SOA mass yields are relatively insensitive to variations of the concentrations of OH and HO_2 adopted in the simulations. Increasing radiation intensity reduces SOA mass yields considerably, however (at similar oxidant levels). The photolysis of aerosol phase species has a large impact on the SOA mass yields in atmospheric conditions, since it is found to reduce SOA yields by a factor of about 2 after several days of ageing in the low-NO_x OH-initiated oxidation scenario. Particulate phase photolysis is therefore a large factor of uncertainty which warrants further experimental studies.

The low-NO_x SOA mass yields in our model are considerably higher (up to 50% mass yield for low-NO_x OH-oxidation) than in previously published SOA parameterisations based on smog chamber experiments. This is largely due to the fact that these smog chamber experiments were not conducted at the very low NO_x concentrations used in our model, and generally did not allow for much photochemical ageing, in contrast with the simulations performed here. The simulated high-NO_x SOA yields, on the other hand, are found to be lower than in most experimental parameterisations.

Box model simulations under ambient conditions, as generated by a global chemistry-transport model, were conducted with the full and parameter model. Agreement between parameter and full model is found to be about around 10% overall, with only a small minority of cases where deviations exceed 20%, which is a satisfactory result given other larger uncertainties in connection with SOA models.

The parameterisation of water uptake involves an RH-dependent activity coefficient for water, γ_{H_2O}, and an overall pseudo-activity coefficient γ_{Org}, which accounts for the non-ideality effects which the added water exerts on the organic compounds. Use of these adjusted activity coefficients in the parameterised model leads to a good agreement with the full model for all relative humidities, for both low, intermediate and high-NO_x simulations.

The parameterisation for secondary organic aerosol from α-pinene obtained in this chapter accounts for the influence of temperature, NO_x-regime, the impact of long-term photochemical ageing and water uptake, which was generally not the case for parameter models based on experiments, usually due to lack of sufficient data. It should be acknowledged that large uncertainties remain in the full BOREAM model, e.g. with respect to the photolysis of SOA and the further generation chemistry. Further model validation against long-term ageing experiments under various NO_x conditions is desirable, as would be model intercomparison with other new SOA models (for example

Valorso et al., 2011, Utembe et al., 2009, Xia et al., 2011, or other studies making use of the VBS approach). For wider application in SOA modelling it would also be necessary to extend this approach to other SOA precursors, and address the interaction with other types of aerosol components which might be present, such as primary organic aerosol or inorganic components.

Chapter 7

Conclusions

7.1 Main results

In this study, we presented the (further) development of BOREAM, a detailed model describing the oxidation and subsequent aerosol formation of α- and β-pinene, two important biogenic volatile organic compounds. The model has been brought in line with the latest knowledge on kinetic rates and thermodynamic properties. The primary oxidation mechanism of α-pinene was updated, and for β-pinene, a new oxidation mechanism was implemented, based on recent theoretical studies. New SARs were considered for e.g. reactions of alkenes with ozone or NO_3, and for unimolecular decomposition and H-shift isomerisation of alkoxy radicals. The enhancement of photolysis rates due to interactions of carbonyl chromophores with hydroperoxide or nitrate groups is tentatively taken into account. The photolysis of compounds in the aerosol phase is also considered, albeit still in a simplified way.

In order to address the challenge of modelling long-term SOA ageing, the chemical mechanism has been greatly extended, using automatic mechanism generation. In an iterative procedure, the number of explicit compounds has been increased so that generic species (i.e. lumped species defined by a volatility class, carbon number and an explicit functional group) make up only a minor fraction of simulated SOA in most situations. At the same time, this approach keeps the size of the mechanism (about 90,000 reactions and 10,000 species) manageable for the model solver. Interestingly, the modelled SOA yields were not strongly affected by the mechanism extension, indicating that the generic chemistry approach is a valid compromise, and that the BOREAM predictions for SOA should not differ much from the results of a fully explicit model.

BOREAM is found to reproduce the measured SOA yields in α-pinene dark ozonolysis and photooxidation experiments to within a factor of two or less in most cases. There are exceptions, however, as model overestimations of up to an order of magnitude are found for dark ozonolysis at high temperature ($> 30°C$), in particular when initial VOC concentrations are low. The strong decrease of the modelled yields with temperature contrasts with the much weaker temperature dependence exhibited by the observations. The choice of the saturated vapour pressure estimation methods can have a strong impact on SOA yields at high temperature, but no tested method can bring the SOA temperature dependence of the model in line with the observations. The model performance in terms of temperature dependence is improved when additional ozonolysis pathways are assumed to form highly condensable products, with formation pathways which could possibly be temperature-dependent.

Even though BOREAM relies on the most recent SARs and theoretical or experimental rates, serious discrepancies are found between modelled and observed SOA composition. For the low-NO_x photooxidation experiment of Eddingsaas et al. (2012a), the gas phase formation of hydroperoxide products and pinonaldehyde can be reproduced qualitatively, but the model predicts large concentrations of hydroperoxides in the SOA, which most experimental studies have not yet been able to confirm. On the other hand, many experimental studies have identified SOA tracer species, such as terpenylic acid or MBTCA, containing one or more carboxylic acid group. No viable explanation could be found for their relatively large observed yields, which suggests that possibly important pathways in the oxidation of α-pinene remain to be discovered. Some of these tracers might account for part of the very condensable compounds invoked to explain the higher-than-modelled yields in high temperature dark ozonolysis experiments. It should be reminded though, that the total amount of identified SOA species still make up only a small fraction of the total SOA.

Uncertainties in key reaction rates in the new β-pinene mechanism in BOREAM have been shown to have a large impact on modelled gas phase chemistry and SOA. For example, possible errors regarding the fate of specific radicals in the OH-initiated oxidation mechanism, such as for the prompt ring opening of the main alkyl radical formed upon OH-addition, are found to have an important impact on ozone formation and β-pinene decay. Use of branching fractions from the widely used MCMv3.2 mechanism leads to a strong overestimation of ozone formation, contrary to the study of Pinho et al. (2007). Variations of the uncertain branching towards bi-peroxy radicals in the ozonolysis mechanism, of the β-pinene ozonolysis rate and of uncertain experimental conditions, such as the radiative flux, all have large effects on ozone formation. Currently, we have to conclude that no single mechanism achieves a satisfactory match with all experimental data.

BOREAM is the first detailed model which shows a reasonable agreement (of the order of a factor two) with measured SOA yields in β-pinene dark ozonolysis and photooxidation experiments, without having to resort to adjustment of estimated saturated vapour pressures. As for α-pinene, the temperature sensitivity of SOA yields from dark ozonolysis is found to be too high in the model. Products formed in the biradical mechanism potentially make a large contribution to SOA in ozonolysis experiments, and the branching fraction change from 8 to 70% for the ring-opening of the alkyl radical formed in the main OH-addition channel, proposed by Vereecken and Peeters (2012), leads to roughly a doubling of modelled SOA yields for photooxidation.

The photochemical ageing of SOA, a process believed to be of great importance for the evolution of ambient aerosols, has received much attention through dedicated smog chamber experiments conducted in several laboratories. BOREAM is found to overestimate SOA upon ageing in many cases, often by a factor of two or higher. These results are in line with earlier model simulations of ageing experiments using an explicit mechanism (Valorso et al., 2011). The difficult representation of wall losses of aerosols and gas phase compounds obscures the comparison between model and experiment, but the relatively early onset of model overestimation in some experiments suggests that this specific issue is not the only cause of the mismatch. During the ageing phase, the model also strongly overestimates the O to C ratios measured in experiments by Tritscher et al. (2011). Results for dark OH ageing are less clear, with both a strong model underestimation in one series of experiments (Henry and Donahue, 2012), and a model overestimate in the case of Tritscher et al. (2011). BOREAM could not reproduce the observed SOA decrease due to photooxidative ageing in experiments by Henry and Donahue (2012), for reasons yet unclear. The strong role of wall losses in SOA ageing experiments, but also missing pathways, the limited applicability of SARs to chemical reactions of poly-oxygenated compounds, or a misrepresentation of the chemistry of radicals formed in the aerosol could all contribute to the discrepancies.

BOREAM has been used to design and adjust an SOA parameterisation for use in large-scale atmospheric models, aimed at reproducing the concentrations of aged SOA. Simulations were performed with BOREAM for low- and high-NO_x conditions, at different temperatures, using a prescribed diurnal cycle for radiation, oxidants and α-pinene, and accounting for the deposition of gas phase and particulate compounds. The equilibrium SOA mass concentrations, reached typically after about 12 days, were used to constrain the parameters for each oxidation scenario. In order to take into account the revolatilisation of condensable products due to photochemical processes, a pseudo-photolysis reaction of the condensable products has been introduced in the parameter model. The SOA mass yields are relatively insensitive to variations of OH and HO_2 in the simulations, but increasing radiation intensity reduces SOA mass yields considerably. The

photolysis of aerosol phase species has a large impact on the SOA mass yields in atmospheric conditions, since it is found to reduce SOA yields by a factor of about 2 after several days of ageing in the low-NO_x OH-initiated oxidation scenario.

A parameterisation of water uptake involving an RH-dependent activity coefficient for water and an overall pseudo-activity coefficient for the non-ideality effects of the added water on the organic compounds has also been developed.

The SOA parameterisation was validated by comparisons with the full BOREAM model in a series of box model simulations under ambient conditions, as generated by a global chemistry-transport model. Overall, agreement is found to be good, with deviations in SOA typically around 10% on average, with only a small minority of cases where deviations exceed 20%. This result is satisfactory, given the other larger uncertainties associated with SOA modelling.

7.2 Perspectives

Better parameterisations for biogenic secondary organic aerosols can contribute to a reduction of the uncertainties in chemical transport, air quality, weather and climate models, and improve our understanding of the global problems of human-induced climate change and the impact of atmospheric particulate matter. More insight into the formation of SOA from α- and β-pinene, two major organic compounds emitted by vegetation, is an important step towards that goal, and this has prompted a multitude of experimental and theoretical studies in the last 25 years.

The level of agreement achieved by BOREAM in the simulation of α- and β-pinene oxidation experiments (a factor of two in many cases) is a marked improvement over a number of previous studies. BOREAM is found to be appropriate to interpret smog chamber experiments, including those with extensive SOA ageing. However, large uncertainties remain, as testified by substantial model/measurement deviations found in a number of cases.

Further experimental and theoretical studies will be needed to close this gap in our understanding of SOA formation and composition.

In particular, the chemistry of the aerosol phase has remained largely unexplored. Kinetic rates for oligomerisation reactions remain unavailable. In this study, we show the potential importance of photolysis of SOA compounds. Furthermore, the chemistry of the radicals produced in this process has not yet received much attention.

The recent finding that atmospheric biogenic SOA can be enhanced through anthropogenic pollution shows the potential importance of interactions between SOA and other aerosol types. It will be important to extend the model for such interactions. Furthermore, possible impacts of aerosol viscosity and phase separation might have to be addressed.

The interpretation of smog chamber data for SOA ageing is seriously complicated by losses of both organic vapours and particles to the chamber walls, an issue which has been largely overlooked by both experimentalists and modellers in the past. As many parameterisations used in large scale models are based on SOA yields from smog chambers which might not correctly account for these wall losses, the risk is that a large fraction of potential SOA is missed in such models. Much more effort will be needed to quantify these loss processes in dedicated experiments. Models should attempt to represent these processes more thoroughly, and preferably on a physical basis, with the help of kinetic and thermodynamic data obtained from experiments.

Direct intercomparison of SOA models (for example Valorso et al., 2011, Utembe et al., 2009, Xia et al., 2011, Donahue et al., 2012) has rarely been undertaken, and would be useful in order to better estimate model uncertainty.

The SOA parameterisation derived from the full BOREAM model has already been implemented in the global model IMAGES (Tsigaridis et al., 2014). The predicted SOA yields of IMAGES are among the highest which global models predict, in part due to the high SOA yields calculated by BOREAM for monoterpenes under low-NO_x conditions. However, there are indications that the global model overestimates biogenic SOA, compared to measurements. This could be expected, given the finding that the BOREAM model tends to overestimate SOA from long-term ageing in smog chamber experiments. A temporary solution is therefore to scale down the biogenic SOA production in the global model (Stavrakou et al., 2013), to bring it more in line with ambient measurements. However, if detailed models can be improved, based e.g. on the suggestions above, then the parameterisation method proposed in this work might be applied to enable a more accurate modeling of SOA loadings in large scale models.

Appendix A

Generic chemistry

A.1 Generic Chemistry: Description

A.1.1 Generic species

The generic chemistry system was introduced in Capouet et al. (2008), and further extended in Ceulemans et al. (2010). Generic species are defined by their carbon number (from 10 down to 6) and by one explicit functional group. The generic species are further subdivided into 11 volatility classes. Each class represents lumped organic compounds, which have a "parent compound" (the molecule resulting from replacement of the explicit functional group by one or more hydrogen atoms) with a saturated liquid vapour pressure $p^0_{\mathrm{L,parent}}$ falling within the volatility class range. For the highest volatility class, indicated by the letter "a", $p^0_{\mathrm{L,parent}} > 10^{-1}$ Torr at 298 K. Class "b" contains species with 10^{-1} Torr $> p^0_{\mathrm{L,parent}} > 10^{-1.5}$ Torr, etc., and for class "k", $p^0_{\mathrm{L,parent}} < 10^{-5.5}$ Torr.
In our notation a generic species name consists of the prefix "LX", the carbon number, the vapour pressure class symbol and the explicit functional group. In total there are 55 classes (5 carbon numbers times eleven vapour pressure classes), besides the generic products with less than 6 carbon atoms, which are not considered for SOA formation, and lumped into a special generic class (with prefix "SX").
The vapour pressure of a (non-radical) generic species is determined by the contribution of its explicit group (see Table A.1), and the representative volatility class vapour pressure $p^0_{\mathrm{L,LX}}$, which at 298 K is equal to the geometric mean of the volatility class range for classes "b"-"j", $10^{-0.75}$ Torr for class "a", and $10^{-5.75}$ Torr for class "k". The temperature dependence of $p^0_{\mathrm{L,LX}}$ is estimated based on Makar (2001).

Table A.1: Overview of generic species.

Generic species	Explicitly represented group	$\Delta \log_{10} p^0_{\mathrm{group}}$ (Capouet and Müller, 2006)	Note
LX10eOOH	hydroperoxide	$-2.9942 + 0.0332(T - 298)$	
LX10eOH	alcohol	$-2.0374 + 0.0124(T - 298)$	
LX10eCHO	aldehyde	$-0.8937 + 0.0124(T - 298)$	a
LX10eCAR	keto-aldehyde	$-1.787 + 0.0248(T - 298)$	a
LX10eKET	ketone	$-0.8937 + 0.0124(T - 298)$	
LX10ePAN	peroxy acyl nitrate	$-2.5372 + 0.0113(T - 298)$	a,b
LX10eONO2	nitrate	$-1.6711 + 0.0063(T - 298)$	
LX10eCOOH	carboxylic acid	$-3.2516 + 0.0075(T - 298)$	a
LX10eCOOOH	peroxy acid	$-3.2516 + 0.0075(T - 298)$	a
LX10eO	alkoxy radical		
LX10eO2	peroxy radical		
LX10e03	acyl peroxy radical		

[a] The carbons in this explicit group are already accounted for in the implicit part of the species.
[b] The contribution of the PAN group in Capouet and Müller (2006) has been reduced in the current version of BOREAM. Uncertainty is very high, however, as vapour pressures for only one compound have been experimentally determined.

A.1.2 Generic reactions

In the following tables, the reactions for one category of generic species are listed. The reaction rates and products are based on the reaction rates and product distributions for similar explicit compounds.

A.1.2.1 Photolysis of molecular generic species

TABLE A.2: Photolysis of molecular generic species: illustration for LX10e.

Reactants	Products	Reaction rate	Note
LX10eOOH + $h\nu$	→ LX10eO + OH	2 j(LXCH3OOH)	a,b
LX10eOOH + $h\nu$	→ LX8aOOH + CH_3CHO	j(LXALD)	c
LX10eOH + $h\nu$	→ LX10cO + OH	j(LXCH3OOH)	b
LX10eOH + $h\nu$	→ LX8aOH + CH_3CHO	j(LXALD)	c
LX10eCHO + $h\nu$	→ LX8cO2 + R2R + CH_3CHO	$0.8 \cdot j$(ALD)	a,d
	→ LX9dO2 + R2R + CO	$0.2 \cdot j$(ALD)	
LX10eCHO + $h\nu$	→ LX10aO + OH	j(LXCH3OOH)	b
LX10eCHO + $h\nu$	→ LX8aCHO + CH_3CHO	j(LXALD)	c
LX10eCAR + $h\nu$	→ LX8eKET + CH_3CHO	$0.8 \cdot j$(ALD)	a
	→ LX9fO2 + R2R + CO	$0.2 \cdot j$(ALD)	
LX10eCAR + $h\nu$	→ LX7dKET + CH_3CHO	$0.8 \cdot j$(keto)	
	→ LX8eO2 + R2R + CH_3CO	$0.2 \cdot j$(keto)	
LX10eCAR + $h\nu$	→ LX10cO + OH	j(LXCH3OOH)	b
LX10eCAR + $h\nu$	→ LX8aCOOOH + CH_3CHO	j(LXALD)	c
LX10eKET + $h\nu$	→ LX8cO2 + R2R + CH_3CHO	$0.8 \cdot j$(keto)	a,d
LX10eKET + $h\nu$	→ LX8cO2 + R2R + CH_3CO_3 + RO3	$0.2 \cdot j$(keto)	
LX10eKET + $h\nu$	→ LX10aO + OH	j(LXCH3OOH)	b
LX10eKET + $h\nu$	→ LX8aKET + CH_3CHO	j(LXALD)	c
LX10ePAN + $h\nu$	→ LX10eO3 + NO_2 + RO3	$0.8 \cdot j$(ppn)	a
LX10ePAN + $h\nu$	→ LX10eO2 + NO_3 + R2R	$0.2 \cdot j$(ppn)	
LX10ePAN	→ LX10eO3 + NO_2 + RO3	k_{PAN}	a
LX10ePAN + $h\nu$	→ LX10eO + OH + NO_2	j(LXCH3OOH)	b
LX10ePAN + $h\nu$	→ LX8aPAN + CH_3CHO	j(LXALD)	c
LX10eONO2 + $h\nu$	→ LX10eO + NO_2	j(nitu)	a
LX10eONO2 + $h\nu$	→ LX10aO + OH + NO_2	j(LXCH3OOH)	b
LX10eONO2 + $h\nu$	→ LX8bONO2 + CH_3CHO	j(LXALD)	c
LX10eCOOH + $h\nu$	→ LX10eO + OH	j(LXCH3OOH)	b
LX10eCOOH + $h\nu$	→ LX8aCOOH + CH_3CHO	j(LXALD)	c
LX10eCOOOH + $h\nu$	→ LX9dO2 + R2R + CO_2 + OH	j(peracid)	a
LX10eCOOOH + $h\nu$	→ LX10eO + OH	j(LXCH3OOH)	b
LX10eCOOOH + $h\nu$	→ LX8aCOOH + CH_3CHO	j(LXALD)	c

[a] The j-values for photolysis of the explicitly represented groups and the product distributions follow Capouet et al. (2004) and Capouet et al. (2008).

[b],[c] Photolysis of the implicit part of the molecule, assumed to proceed as for a compound containing one hydroperoxide group (b) and one aldehyde group (c). For classes "a" to "d", the j-values are halved, due to expected lower functionalisation.

[b] Photolysis of a hydroperoxide group in the implicit part of the compound, resulting in an alkoxy radical and OH.

[c] Aldehyde photolysis in the implicit part is assumed to follow the Norrish-type II reaction, which leads to an alkene and acetaldehyde (see Paulson et al., 2006). This results in removal of 2 carbons and the aldehyde group from the implicit part of the generic species, increasing volatility (here from class "e" to "a").

[d] For explicit aldehyde and ketone photolysis, branching ratios of 0.8 for Norrish-type II reaction (leading to an alkene and acetaldehyde), and 0.2 for the radical channel are assumed. In the first case, the alkene is then assumed to quickly react with OH or ozone, yielding a peroxy radical.

A.1.2.2 Reactions of molecular generic species

TABLE A.3: Reactions of generic molecular species: illustration for LX10e. R2R and RO3 are peroxy radical counters (see Capouet et al., 2004).

Reactants	Products	Reaction rate	Note
LX10eOOH + OH	→ LX10eCHO + OH	k_{seth}	a
LX10eOOH + OH	→ LX10kO2 + R2R	0.4 k_{LX}	g
	→ LX10iO3 + RO3	0.3 k_{LX}	h
	→ LX10eCHO + OH	0.3 k_{LX}	i
LX10eOH + OH	→ LX10eCHO + HO_2	k_{seth}	b
LX10eOH + OH	→ LX10iO2 + R2R	0.4 k_{LX}	g
	→ LX10gO3 + RO3	0.3 k_{LX}	h
	→ LX10cCHO + OH	0.3 k_{LX}	i
LX10eCHO + OH	→ LX10eO3 + RO3	k_{carb}	c
LX10eCHO + NO_3	→ LX10eO3 + RO3 + HNO_3	$k_{\mathrm{NO_3}}$	d
LX10eCHO + OH	→ LX10gO2 + R2R	0.4 k_{LX}	g
	→ LX10eO3 + RO3	0.3 k_{LX}	h
	→ LX10aCHO + OH	0.3 k_{LX}	i
LX10eCAR + OH	→ LX10gO3 + RO3	k_{carb}	c
LX10eCAR + NO_3	→ LX10gO3 + RO3 + HNO_3	$k_{\mathrm{NO_3}}$	d
LX10eCAR + OH	→ LX10iO2 + R2R	0.4 k_{LX}	g
	→ LX10gO3 + RO3	0.3 k_{LX}	h
	→ LX10cCHO + OH	0.3 k_{LX}	i
LX10eKET + OH	→ LX10gO2 + R2R	0.4 k_{LX}	g
	→ LX10eO3 + RO3	0.3 k_{LX}	h
	→ LX10aCHO + OH	0.3 k_{LX}	i
LX10ePAN + OH	→ LX10kO2 + R2R + NO_2	0.4 k_{LX}	g
	→ LX10iO3 + RO3 + NO_2	0.3 k_{LX}	h
	→ LX10eCHO + OH + NO_2	0.3 k_{LX}	i
LX10eONO2 + OH	→ LX10eCHO + NO_2	0.07 k_{seth}	e
LX10eONO2 + OH	→ LX10hO2 + R2R + NO_2	0.4 k_{LX}	g
	→ LX10fO3 + RO3 + NO_2	0.3 k_{LX}	h
	→ LX10bCHO + OH + NO_2	0.3 k_{LX}	i
LX10eCOOH + OH	→ LX9dO2 + R2R + CO_2	$k_{\mathrm{H-abst.ROH}}$	f,j
LX10eCOOH + OH	→ LX10kO2 + R2R	0.4 k_{LX}	g
	→ LX10iO3 + RO3	0.3 k_{LX}	h
	→ LX10eCHO + OH	0.3 k_{LX}	i
LX10eCOOOH + OH	→ LX10eO3 + H_2O + RO3	$k_{\mathrm{H-abst.ROOH}}$	f,j
LX10eCOOOH + OH	→ LX10kO2 + R2R	0.4 k_{LX}	g
	→ LX10iO3 + RO3	0.3 k_{LX}	h
	→ LX10eCHO + OH	0.3 k_{LX}	i

[a],[b] $k_{\mathrm{seth}} = 5.32\times10^{-12}\,\mathrm{cm^3\,molecules^{-1}\,s^{-1}}$, based on the rate recommended by Neeb (2000) for abstraction of a secondary H from the α-carbon, bearing an -OH or -OOH group. H-abstraction from oxygen atoms is ignored.

[c] H-abstraction from the -CHO group: $k_{\mathrm{carb}} = 16.9\times10^{-12}\,\mathrm{cm^3\,molecules^{-1}\,s^{-1}}$, based on measurements reported by Atkinson et al. (2006) and Schurath and Naumann (2003).

[d] $k_{\mathrm{NO_3}} = 1.67\,\exp(-1460/T)10^{-12}\,\mathrm{cm^3\,molecules^{-1}\,s^{-1}}$ (Atkinson et al., 2006).

[e] based on Neeb (2000).

[f] based on Neeb (2000), for abstraction of an H attached to a single oxygen ($k_{\mathrm{H-abst.ROH}} = 0.8\times10^{-12}\,\mathrm{cm^3\,molecules^{-1}\,s^{-1}}$) or to a peroxy group ($k_{\mathrm{H-abst.ROOH}} = 2.0\times10^{-12}\,\mathrm{cm^3\,molecules^{-1}\,s^{-1}}$).

[g] H-abstraction from an implicit aliphatic carbon, leading to a peroxy radical.

[h] H-abstraction from an implicit aldehydic carbon, leading to an acyl peroxy radical.

[i] H-abstraction from an implicit carbon bearing an α-hydroperoxide function, leading to a carbonyl and an OH radical.

[g] to [i]: For OH-reactions with the implicit part of the generic compound; $k_{\mathrm{LX}} = 8.0\times10^{-12}\,\mathrm{cm^3\,molecules^{-1}\,s^{-1}}$. The branching ratios of the reaction pathways described in notes [g] to [i] depend on the presence of functional groups in the parent structure, and therefore also on its vapour pressure (as vapour pressure and functionalisation are correlated). We assume these branching ratios have the values (0.6,0.2,0.2) for classes "a" to "c", (0.4,0.3,0.3) for classes "d"–"g" and (0.2,0.4,0.4) for classes "h"–"k".

A.1.2.3 Generic alkoxy radical reactions

TABLE A.4: Reactions of generic alkoxy radicals: illustration with the radical LX10eO.

Reactants	Products	Branching ratios	Note
LX10eO + O_2	→ LX10eCHO + HO_2	0.15	a,g
LX10eO	→ LX9dO2 + R2R + CH_2O	0.3	b,f,g
	→ LX9bO3 + RO3 + CH_2O	0.1	f
	→ LX9aCHO + OH + CH_2O	0.1	f
LX10eO	→ LX9aO2 + R2R + HCOOH	0.05	c,g
LX10eO	→ LX7aO2 + R2R + acetone	0.10	d,g
LX10eO	→ LX10iO2 + R2R	0.12	e,f,g
	→ LX10gO3 + RO3	0.04	f
	→ LX10cCHO + OH	0.04	f

[a] Assumed branching ratio for reaction with O_2.
[b] We consider three types of decomposition, with the most common being of the type $RCH_2O^\bullet \rightarrow R^\bullet + CH_2O$.
[c] This decomposition follows $RCH(OH)O^\bullet \rightarrow R^\bullet + HCOOH$.
[d] This decomposition reaction follows $R(CH3CO^\bullet CH3) \rightarrow R^\bullet$ + acetone .
[e] H-shift isomerisation, as in $RCH_2CH_2CH_2CH_2O^\bullet \rightarrow RC^\bullet HCH_2CH_2CH_2OH$.
[f] An alkyl radical is produced. Alkyl radicals without an α-functionality react with O_2, forming peroxy radicals. However, alkyl radicals bearing an α-aldehyde function generate acyl alkoxy radicals, and in case of a possible α-hydroperoxide, the radical becomes an aldehyde + OH. The assumed branching ratios for these three possible pathways are $(0.6, 0.2, 0.2)$ for classes "e" to "k" and $(0.8, 0.1, 0.1)$ for classes "a" to "d".
[g] The branching ratios depend on the vapour pressure class (see Table A.5).

TABLE A.5: Branching ratios for generic alkoxy radicals depending on their vapour pressure class.

Alkoxy radical reaction pathway	class a–c	class d–g	class h–k
Reaction with O_2	0.20	0.15	0.05
CH_2O elimination	0.40	0.5	0.65
HCOOH elimination	0.05	0.05	0.05
Acetone elimination	0.05	0.10	0.15
H-shift isomerisation	0.30	0.2	0.10

Decomposition is more likely for the more chemically functionalised species (see for example Vereecken and Peeters, 2009). Therefore, the assumed branching ratios for decomposition increase with decreasing vapour pressure, since we assume an inverse correlation between number of functional groups present and vapour pressure.

A.1.2.4 Generic peroxy radical reactions

TABLE A.6: Reactions of generic peroxy radicals: illustration with radical LX10eO2.

Reactants	Products	Reaction rate	Note
LX10eO2 + NO	→ LX10eO + NO_2 - R2R	0.9 $\cdot k_{NO,RO_2}$	a,b
LX10eO2 + NO	→ LX10eONO2 - R2R	0.1 $\cdot k_{NO,RO_2}$	a,b
LX10eO2 + NO_3	→ LX10eO + NO_2 - R2R	k_{NO_3,RO_2}	a,c
LX10eO2 + HO_2	→ LX10eOOH - R2R	k_{HO_2,RO_2}	a,d
LX10eO2 + R3R	→ 0.70 LX10eO + 0.30 LX10eCHO	$k_{R2R,R3R}$	a
LX10eO2 + R3O	→ 0.70 LX10eO + 0.30 LX10eCHO	$k_{R2R,R3O}$	a
LX10eO2 + R3H	→ 0.70 LX10eO + 0.30 LX10eCHO	$k_{R2R,R3H}$	a
LX10eO2 + R2R	→ 0.50 LX10eO + 0.25 LX10eCHO + 0.25 LX10eOH	$k_{R2R,R2R}$	a
LX10eO2 + R2O	→ 0.50 LX10eO + 0.25 LX10eCHO + 0.25 LX10eOH	$k_{R2R,R3R}$	a
LX10eO2 + R2H	→ 0.50 LX10eO + 0.25 LX10eCHO + 0.25 LX10eOH	$k_{R2R,R2H}$	a
LX10eO2 + R1R	→ 0.50 LX10eO + 0.25 LX10eCHO + 0.25 LX10eOH	$k_{R2R,R1R}$	a
LX10eO2 + R1H	→ 0.50 LX10eO + 0.25 LX10eCHO + 0.25 LX10eOH	$k_{R2R,R1H}$	a
LX10eO2 + RO3	→ LX10eO	$r_{oxyr} \cdot k_{RO_2,RO_3}$	a,e,f
LX10eO2 + RO3	→ LX10eCHO	$r_{acid} \cdot k_{RO_2,RO_3}$	a,e,f

[a] Peroxy radicals are grouped into 9 classes according to their functionality, and their cross reactions are then treated using a system of peroxy radical class counters (Capouet et al., 2004). Generic peroxy radicals are assumed to behave as the so-called R2R-class, which contains secondary peroxy radicals without α- or β-functional groups. The cross-reaction rates $k_{R2R,R3R}$, etc., can be calculated using Table 2 and Eq. 3 in Capouet et al. (2004), and the product distributions follow Table 1 in Capouet et al. (2004).
[b] $k_{NO,RO_2} = 2.54 \times 10^{-12} \exp(360/T)$ cm^3 molecule^{-1}s^{-1} (Saunders et al., 2003). The estimated alkyl nitrate yield is 0.1 (see Capouet et al., 2004).
[c] $k_{NO_3,RO_2} = 2.3 \times 10^{-12}$ cm^3 molecule^{-1}s^{-1} (based on $C_2H_5O_2$ in Atkinson et al., 2006).
[d] $k_{HO_2,RO_2} = 2.72 \times 10^{-13} \exp(1250/T)$ cm^3 molecule^{-1}s^{-1} (Saunders et al., 2003).
[e] For the cross-reactions between peroxy radicals and acyl peroxy radicals the rate constant $k_{RO_2,RO_3} = 1.0 \times 10^{-11}$ cm^3 molecule^{-1}s^{-1} is used (Capouet et al., 2004).
[f] The branching ratios of the alkoxy radical channel and the molecular channel are given by $r_{acid} = 1/(1 + 2.2 \cdot 10^6 \exp(-3280/T))$ and $r_{oxyr} = 1 - r_{acid}$.

A.1.2.5 Generic acyl peroxy radical reactions

TABLE A.7: Reactions of generic acyl peroxy radicals: illustration with acyl peroxy radical LX10eO3.

Reactants	Products	Reaction rate	Note
LX10eO3 + NO	→ CO_2 + 0.60 LX9dO2 + 0.60 R2R + 0.20 LX9bO3 + 0.20 RO3 + 0.20 LX9aCHO + 0.20 OH + NO_2 - RO3	k_{NO,RO_3}	a,g
LX10eO3 + NO_2	→ LX10ePAN - RO3	k_{NO_2,RO_3}	b
LX10eO3 + NO_3	→ CO_2 + 0.60 LX9dO2 + 0.60 R2R + 0.20 LX9bO3 + 0.20 RO3 + 0.20 LX9aCHO + 0.20 OH + NO_2 - RO3	k_{NO_3,RO_3}	c,g
LX10eO3 + HO_2	→ LX10eCOOH + O_3 - RO3	$0.13 \cdot k_{HO_2,RO_3}$	d
LX10eO3 + HO_2	→ LX10eCOOOH + O_2 - RO3	$0.41 \cdot k_{HO_2,RO_3}$	d
LX10eO3 + HO_2	→ CO_2 + 0.60 LX9dO2 + 0.60 R2R + 0.20 LX9bO3 + 0.20 RO3 + 0.20 LX9aCHO + 0.20 OH + OH - RO3	$0.46 \cdot k_{HO_2,RO_3}$	d,g
LX10eO3 + R3R	→ CO_2 + 0.60 LX9dO2 + 0.60 R2R + 0.20 LX9bO3 + 0.20 RO3 + 0.20 LX9aCHO + 0.20 OH	k_{RO_2,RO_3}	e,g
LX10eO3 + R3O	→ CO_2 + 0.60 LX9dO2 + 0.60 R2R + 0.20 LX9bO3 + 0.20 RO3 + 0.20 LX9aCHO + 0.20 OH	k_{RO_2,RO_3}	g
LX10eO3 + R3H	→ CO_2 + 0.60 LX9dO2 + 0.60 R2R + 0.20 LX9bO3 + 0.20 RO3 + 0.20 LX9aCHO + 0.20 OH	k_{RO_2,RO_3}	g
LX10eO3 + R2R	→ CO_2 + 0.60 LX9dO2 + 0.60 R2R + 0.20 LX9bO3 + 0.20 RO3 + 0.20 LX9aCHO + 0.20 OH	$r_{oxyr} \cdot k_{RO_2,RO_3}$	g
LX10eO3 + R2R	→ LX10eCOOH	$r_{acid} \cdot k_{RO_2,RO_3}$	
LX10eO3 + R2O	→ CO_2 + 0.60 LX9dO2 + 0.60 R2R + 0.20 LX9bO3 + 0.20 RO3 + 0.20 LX9aCHO + 0.20 OH	$r_{oxyr} \cdot k_{RO_2,RO_3}$	g
LX10eO3 + R2O	→ LX10eCOOH	$r_{acid} \cdot k_{RO_2,RO_3}$	
LX10eO3 + R2H	→ CO_2 + 0.60 LX9dO2 + 0.60 R2R + 0.20 LX9bO3 + 0.20 RO3 + 0.20 LX9aCHO + 0.20 OH	$r_{oxyr} \cdot k_{RO_2,RO_3}$	g
LX10eO3 + R2H	→ LX10eCOOH	$r_{acid} \cdot k_{RO_2,RO_3}$	
LX10eO3 + R1R	→ CO_2 + 0.60 LX9dO2 + 0.60 R2R + 0.20 LX9bO3 + 0.20 RO3 + 0.20 LX9aCHO + 0.20 OH	$r_{oxyr} \cdot k_{RO_2,RO_3}$	g
LX10eO3 + R1R	→ LX10eCOOH	$r_{acid} \cdot k_{RO_2,RO_3}$	
LX10eO3 + R1O	→ CO_2 + 0.60 LX9dO2 + 0.60 R2R + 0.20 LX9bO3 + 0.20 RO3 + 0.20 LX9aCHO + 0.20 OH	$r_{oxyr} \cdot k_{RO_2,RO_3}$	g
LX10eO3 + R1O	→ LX10eCOOH	$r_{acid} \cdot k_{RO_2,RO_3}$	
LX10eO3 + R1H	→ CO_2 + 0.60 LX9dO2 + 0.60 R2R + 0.20 LX9bO3 + 0.20 RO3 + 0.20 LX9aCHO + 0.20 OH	$r_{oxyr} \cdot k_{RO_2,RO_3}$	g
LX10eO3 + R1H	→ LX10eCOOH	$r_{acid} \cdot k_{RO_2,RO_3}$	
LX10eO3 + RO3	→ CO_2 + 0.60 LX9dO2 + 0.60 R2R + 0.20 LX9bO3 + 0.20 RO3 + 0.20 LX9aCHO + 0.20 OH	k_{self,RO_3}	f

[a] $k_{NO,RO_3} = 6.7 \times 10^{-12} \exp(340/T)$ cm^3 molecules^{-1} s^{-1}, based on $C_2H_5CO(O_2)$ (Atkinson et al., 2006).

[b] k_{NO_2,RO_3} is calculated using the high-pressure limit of the Troe-expression for the $CH_3C(O)O_2 + NO_2$ reaction (see Capouet et al. (2004) and references therein), which in this case is $1.2 \cdot 10^{-11}(T/300)^{-0.9}$ cm^3 molecules^{-1} s^{-1} (Atkinson et al., 2006).

[c] $k_{NO_3,RO_3} = 4.3 \times 10^{-12}$ cm^3 molecules^{-1} s^{-1} based on $CH_3CO(O_2)$(Saunders et al., 2003).

[d] The product distribution is based on $CH_3C(O)O_2 + HO_2$ Jenkin et al. (2007). The reaction rate $k_{HO_2,RO_3} = 5.2 \times 10^{-13} \exp(983/T)$ cm^3 molecules^{-1} s^{-1} is used (see Capouet et al., 2004).

[e] For the cross-reactions between peroxy radicals and acyl peroxy radicals the rate constant $k_{RO_2,RO_3} = 1.0 \times 10^{-11}$ cm^3 molecules^{-1} s^{-1} is used (Capouet et al., 2004).

[f] For the self-reactions of acyl peroxy radicals, $k_{self,RO_3} = 1.5 \times 10^{-11}$ cm^3 molecules^{-1} s^{-1} is used (Capouet et al., 2004).

[g] In these reactions an acyl alkoxy radical is produced, which decomposes into an alkyl radical and CO_2. Treatment of alkyl radicals follows note f in Table A.4 .

Appendix B

Additional BOREAM Model validation

We present a comparison of measured time series for α-pinene, ozone and NO_x with simulations performed with the full BOREAM model. First we show simulations for a low-NO_x experiment (1) and a high-NO_x experiment (4) from Ng et al. (2007a). The time series and discussion of some aspects concerning the simulations are given in Valorso et al. (2011). Initial concentrations for important species for which measurements were not available were optimised in order to obtain good agreement for observed α-pinene decay. For three experiments from Carter (2000) we compare the quantity $D(O_3-NO) = ([O_3] - [O_3]_{\text{initial}}) - ([NO] - [NO]_{\text{initial}})$, which is an indication for the strength of ozone production.

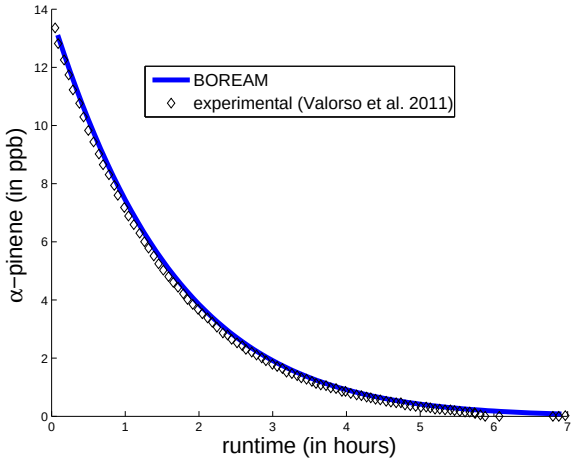

(A) α-pinene

FIGURE B.1: Measured and simulated α-pinene for experiment 1 of Ng et al. (2007a).

TABLE B.1: Initial settings for concentrations of VOC and inorganic compounds in the experiments 1 and 4 from Ng et al. (2007a), discussed in Valorso et al. (2011). Optimised initial values and wall sources differ slightly from those in Valorso et al. (2011)

Initial settings	Exp. 1	Exp. 4
Available measurements		
Temperature	298 K	299 K
Relative humidity	5.3%	3.3%
[α-pinene]	13.8 ppb	12.6 ppb
[O_3]	4 ppb	not available
[NO]	not available	475 ppb
[NO_2]	not available	463 ppb
Model settings for unmeasured parameters		
[O_3]	measured value	0 ppb
[NO]	0.35 ppb	measured value
[NO_2]	0.35 ppb	measured value
[H_2O_2]	1250 ppb	0 ppb
[HONO]	0 ppb	1000 ppb
$j(NO_2)$	$3.3 \times 10^{-1}\,\mathrm{min}^{-1}$	$4.2 \times 10^{-1}\,\mathrm{min}^{-1}$
$j(H_2O_2)$	$1.35 \times 10^{-4}\,\mathrm{min}^{-1}$	$1.7 \times 10^{-4}\,\mathrm{min}^{-1}$
NO wall source	0.5 ppt min^{-1}	none
NO_2 wall source	0.5 ppt min^{-1}	none
Unknown OH source	none	$1.8 \times 10^{9}\,\mathrm{cm}^{-3}\,\mathrm{s}^{-1}$
Aerosol wall loss	$1.0{\times}10^{-5}$ s^{-1}	$1.0 \times 10^{-5}\mathrm{s}^{-1}$

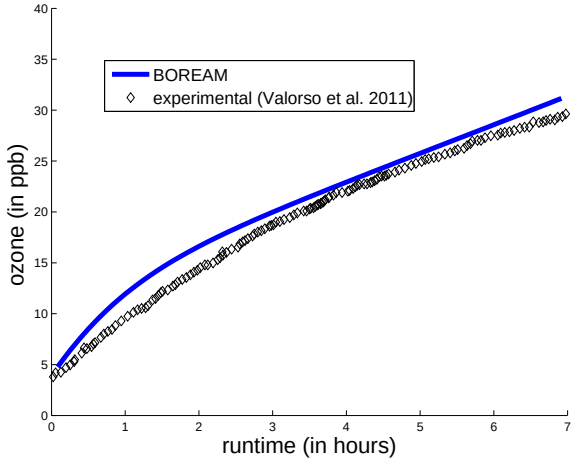

(A) ozone

FIGURE B.2: Measured and simulated ozone concentrations for experiment 1 of Ng et al. (2007a).

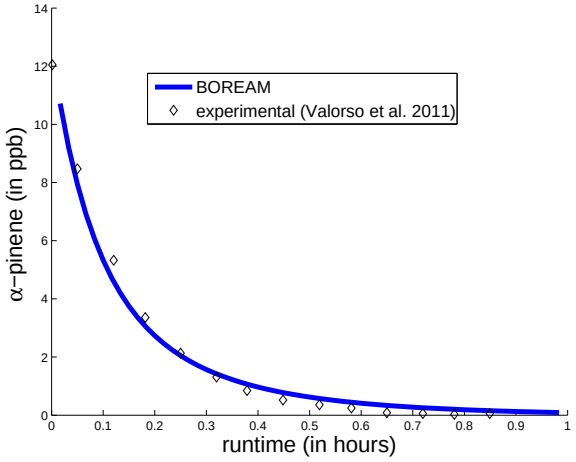

FIGURE B.3: Measured and simulated α-pinene concentrations for experiment 4 of Ng et al. (2007a).

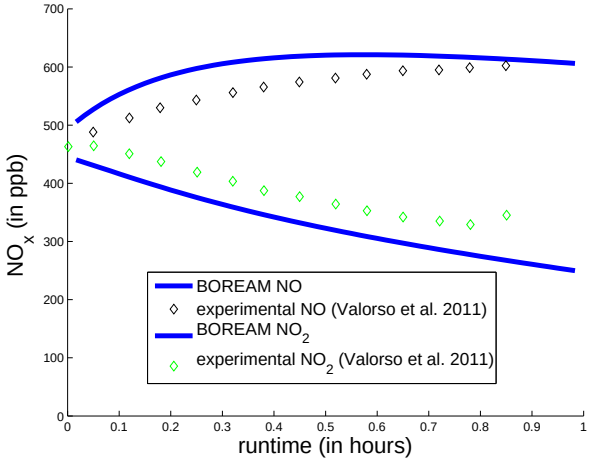

FIGURE B.4: Measured and simulated NO and NO_2 concentrations for experiment 4 of Ng et al. (2007a).

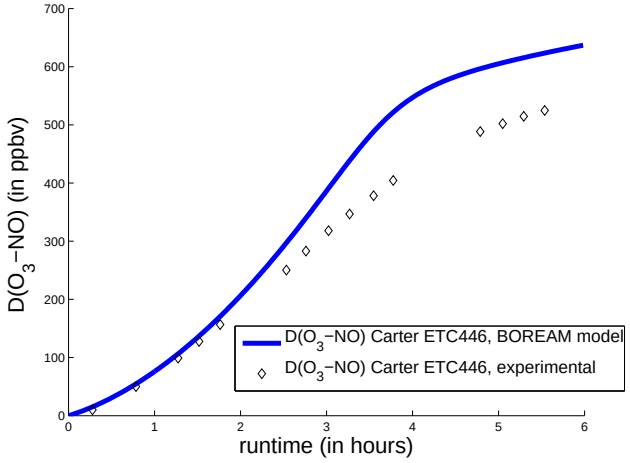

(A) experiment 446

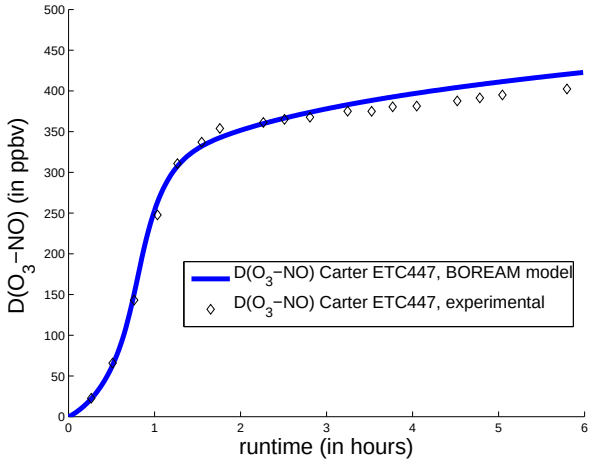

(B) experiment 447

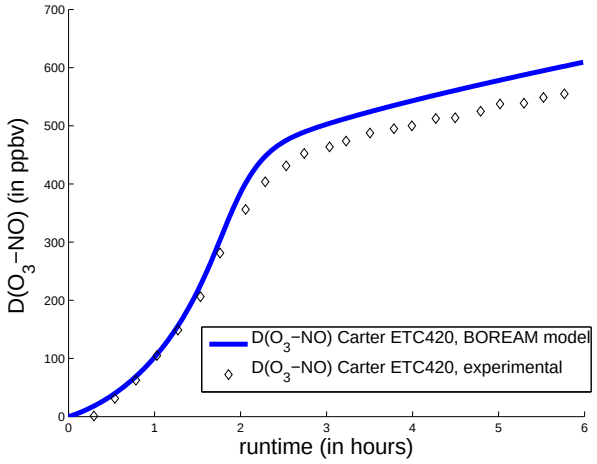

(C) experiment 420

FIGURE B.5: Measured and simulated $D(\mathrm{O_3} - \mathrm{NO}) = ([\mathrm{O_3}] - [\mathrm{O_3}]_{\mathrm{initial}}) - ([\mathrm{NO}] - [\mathrm{NO}]_{\mathrm{initial}})$ (in ppb) for experiments ETC446, 447 and 420 of Carter (2000).

Appendix C

SOA parameterisation

C.1 Fitting procedure for the photochemical SOA loss

For each oxidation scenario and each temperature, the sensitivity calculations illustrated in Fig. 6.1 in Section 6.2 were used to estimate the amount of organic aerosol lost due to photochemical processing at SOA equilibrium, $[\mathrm{OA}]_{\mathrm{pl}}$, for the simulation at an α-pinene concentration which leads to an SOA concentration of around 2.5 $\mu\mathrm{gm}^{-3}$. The maximum (noontime) photochemical loss rate is fitted to reproduce the condensable material lost during one day at SOA equilibrium. We use the formula

$$[\mathrm{OA}]_{\mathrm{pl}} = \int_{\mathrm{day13}} J_{\mathrm{pl,max}} \cdot S(t) \cdot [\mathrm{OA}](t) dt \tag{C.1}$$

where $S(t)$ denotes the diurnal shape factor (between 0 and 1) adopted for all photolysis rates in the box model calculations. For the NO_3-oxidation scenario at high temperatures, it turns out that the estimated values of $[\mathrm{OA}]_{\mathrm{pl}}$ are too large. Therefore in such cases, an additional correction factor was applied. At α-pinene concentrations differing from those of the above fitting , we then insert the derived $J_{\mathrm{pl,max}}$ in formula C.1, which together with the simulated SOA concentration $[\mathrm{OA}](t)$ allows us to deduce the value of $[\mathrm{OA}]_{\mathrm{pl}}$ for that α-pinene concentration. This $[\mathrm{OA}]_{\mathrm{pl}}$ is then used to calculate the SOA yield according to formula $([\mathrm{OA}]_{\mathrm{dep.}} + [\mathrm{OA}]_{\mathrm{pl}})/\Delta[\alpha\text{-pinene}]$.

The retrieved yield parameters and SOA photolysis rates are inserted in the parameter model, which is then used to simulate the 5 oxidation scenarios at varying temperatures and α-pinene concentrations. At this stage a final optimization of $J_{\mathrm{pl,max}}$ is performed in order to improve the agreement of the time evolution of M_O between full and parameter model in the range of atmospherically relevant M_O concentrations. We then perform a fitting of $J_{\mathrm{pl,max}}$ as a function of temperature for each of the 5 scenarios. From these

maximum photolysis rates, the j-values J_{pl} for the photochemical loss rates can be obtained as explained in Chapter 6. The parameters for the polynomial fittings for the factors $f_{\mathrm{pl,max}}$ are given and graphically represented below for each of the five oxidation scenarios.

TABLE C.1: Polynomial coefficients for the temperature dependent fitting $f_{\mathrm{pl,max}} = \sum_{i=0}^{5} a_i (T - 273)^i$.

	low-NO_x, OH	high-NO_x, OH	low-NO_x, O_3	high-NO_x, O_3	high-NO_x, NO_3
a_5	$-4.146 \cdot 10^{-8}$	$3.316 \cdot 10^{-7}$	$6.577 \cdot 10^{-8}$	$-2.646 \cdot 10^{-7}$	$3.536 \cdot 10^{-8}$
a_4	$1.959 \cdot 10^{-6}$	$-2.291 \cdot 10^{-5}$	$-5.243 \cdot 10^{-6}$	$2.116 \cdot 10^{-5}$	$-2.732 \cdot 10^{-6}$
a_3	$-1.962 \cdot 10^{-5}$	$5.544 \cdot 10^{-4}$	$1.4078 \cdot 10^{-4}$	$-6.161 \cdot 10^{-4}$	$5.830 \cdot 10^{-5}$
a_2	$-7.746 \cdot 10^{-5}$	$-4.917 \cdot 10^{-3}$	$-1.375 \cdot 10^{-3}$	$8.637 \cdot 10^{-3}$	$2.975 \cdot 10^{-4}$
a_1	$1.483 \cdot 10^{-3}$	$1.555 \cdot 10^{-2}$	$2.452 \cdot 10^{-3}$	$-4.354 \cdot 10^{-2}$	$-1.902 \cdot 10^{-2}$
a_0	$7.292 \cdot 10^{-2}$	$2.268 \cdot 10^{-1}$	$1.293 \cdot 10^{-1}$	$3.187 \cdot 10^{-1}$	$1.649 \cdot 10^{-1}$

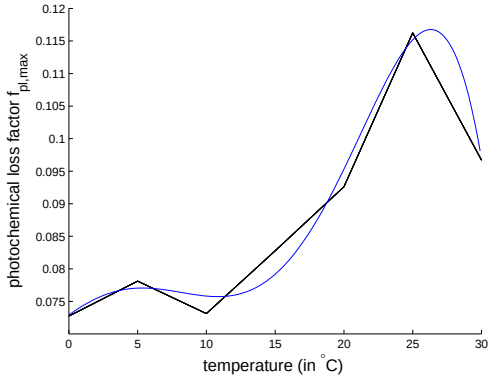

FIGURE C.1: Temperature dependent fit (in blue) in the low-NO_x OH oxidation case for the photochemical loss factor $f_{\mathrm{pl,max}}$, which allows calculation of the J-value for the photochemical loss reaction in the parameter model through $J_{\mathrm{pl}} = f_{\mathrm{pl,max}} \cdot J_{\mathrm{ald}}$.

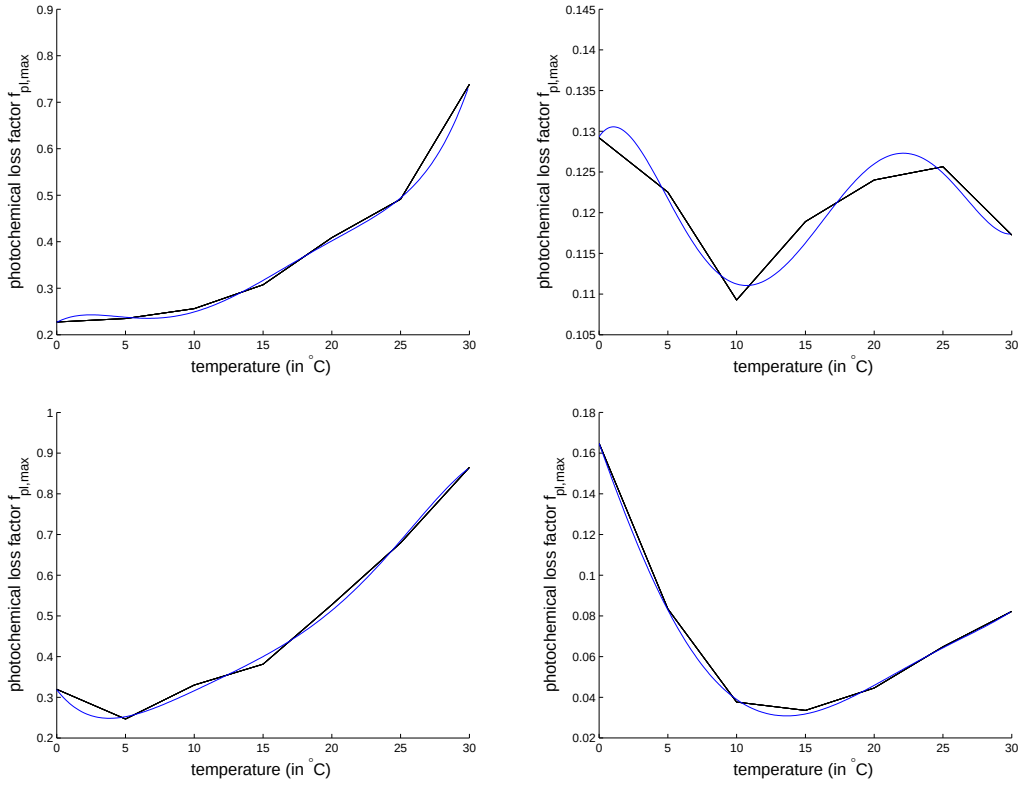

FIGURE C.2: $f_{\mathrm{pl,max}}$ (in blue) for the high-NO_x OH oxidation (upper left), low-NO_x O_3 oxidation (upper right), high-NO_x O_3 oxidation (lower left), and high-NO_x NO_3 oxidation (lower right).

C.2 SOA parameterisation agreement with full model

In the following Table we evaluate the level of agreement between the full and the parameter model for the 5 oxidation scenarios, which were simulated at 7 temperatures and at a number of different α-pinene concentrations. In each simulation SOA build-up was simulated over 14 day. Simulations for which the maximum M_O reached did not fall in the range 0.5–20 μgm^{-3} were not considered. The following table provides the percentage of simulated days satisfying a given level of agreement, using a deviation factor defined as $\exp(|\log(\overline{M_{O,p}}/\overline{M_{O,f}})|)$.

TABLE C.2: Percentage of days for which the model deviation factor falls within the range 1 to 1.25 (first part), or exceeds a factor 2 (second part).

Scenario	273 K	278 K	283 K	288 K	293 K	298 K	303 K
low-NO_x, OH	98.2	97.3	94.6	91.7	85.7	84.5	81.2
high-NO_x, OH	95.5	95.0	93.5	87.9	80.1	89.3	78.6
low-NO_x, O_3	98.2	98.2	97.6	91.1	83.3	76.8	80.4
high-NO_x, O_3	92.9	83.6	94.4	92.1	88.9	85.7	57.1
high-NO_x, NO_3	86.7	80.4	73.5	70.4	64.3	68.4	53.1
low-NO_x, OH	0	0	0	0	0	1.8	5.8
high-NO_x, OH	0	0	0.6	2.9	5.6	5.4	16.3
low-NO_x, O_3	0	0	0	0	0	1.2	3.6
high-NO_x, O_3	2.1	2.1	0	0.8	3.2	6.1	7.1
high-NO_x, NO_3	3.1	2.7	2.0	1.0	5.1	11.2	27.6

Fig. C.3e compares the full and parameterised model yields at various NO_x levels for the ozonolysis scenario. Figs. C.3a to C.3d compare the full and parameter model for SOA formed under OH-oxidation at intermediate-NO_x and at temperatures between 273 K and 303 K.

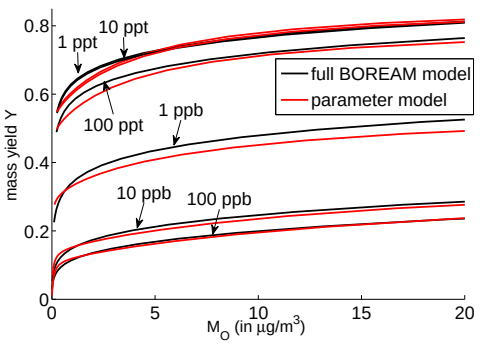

(A) For OH as the oxidant, at 273 K.

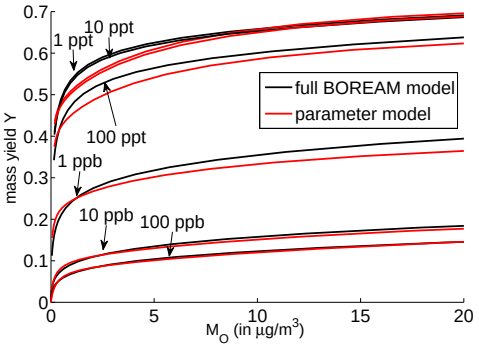

(B) For OH as the oxidant, at 283 K.

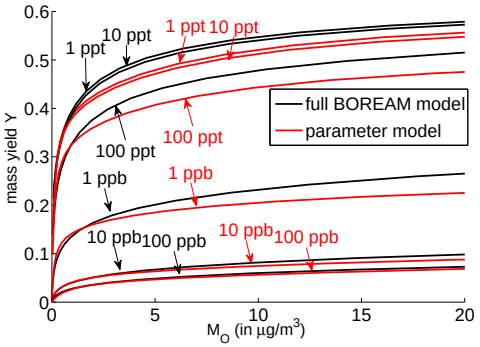

(C) For OH as the oxidant, at 293 K.

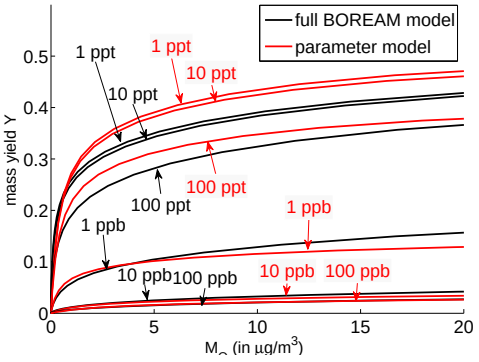

(D) For OH as the oxidant, at 303 K.

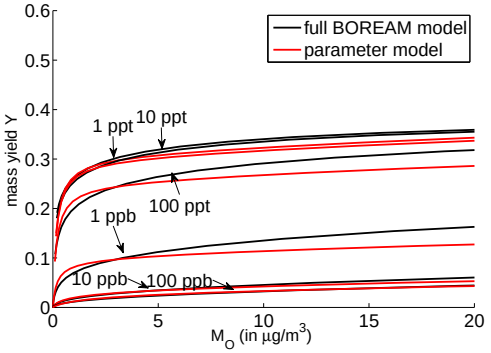

(E) For O_3 as the oxidant, at 298 K.

FIGURE C.3: Net SOA yields near SOA equilibrium calculated by the full (black) and parameterised (red) model at various NO_2 levels, for OH as the oxidant of α-pinene, at different temperatures, and for ozone as the oxidant, at 298 K.

C.3 Full BOREAM and parameter model for ambient conditions based on IMAGESv2

Table C.3 provides an overview of the conditions and model results for the 17 locations considered, during the months of May until September. Fig. C.4 displays the temporal dependence of the modelled α-pinene SOA concentrations in the parameter model and the full BOREAM model, for the month of July, at the locations for which these plots are not shown in the main article.

TABLE C.3: Average temperature ($\overline{T}$), NO_x concentration ($\overline{[NO_x]}$), concentration of organic aerosol excluding α-pinene SOA ($\overline{[OA_{other}]}$), concentration of α-pinene SOA calculated using BOREAM ($\overline{M_{O,f}}$) in the simulations based on IMAGESv2 output. The values are tropospheric averages weighted by the α-pinene oxidation product concentrations in the gas phase. The last two columns provide the averaged deviation and bias, expressed relatively to the average concentration in the full model simulation (see Sect. 3.4.5 in the main article for the used formulas).

Location	$\overline{T}$ (in K)	$\overline{[NO_x]}$ (in ppt)	$\overline{[OA_{other}]}$ (in μg m^{-3})	$\overline{M_{O,f}}$ α-pinene (in μg m^{-3})	average deviation	average bias
Surinam	278.7	53	1.2	1.70	0.16	0.15
South-East US	283.1	381	3.0	1.43	0.098	-0.036
Russia	269.8	142	0.65	0.64	0.093	-0.024
North-West US	271.8	390	0.81	0.37	0.12	-0.026
Mexico	278.	301	1.85	0.45	0.086	0.037
Peru	275.8	48	1.41	1.07	0.071	0.068
South-Brazil	265.9	122	0.68	0.11	0.16	0.011
Benin	278.4	185	2.02	0.77	0.067	-0.044
Congo	279.8	119	4.0	1.54	0.044	0.002
Belgium	267.1	648	0.77	0.084	0.092	0.018
Finland	271.3	323	0.75	0.44	0.18	-0.18
Pearl River Delta	274.0	752	2.07	0.79	0.19	-0.19
Beijing	278.6	723	1.56	0.26	0.084	-0.049
India, coastal	278.6	156	1.67	0.008	0.11	-0.037
Siberia	266.7	84	1.57	0.62	0.12	0.11
Borneo	280.0	127	2.14	1.00	0.11	0.10
Queensland	268.4	98	0.52	0.26	0.24	0.24
Overall				0.68	0.11	0.021

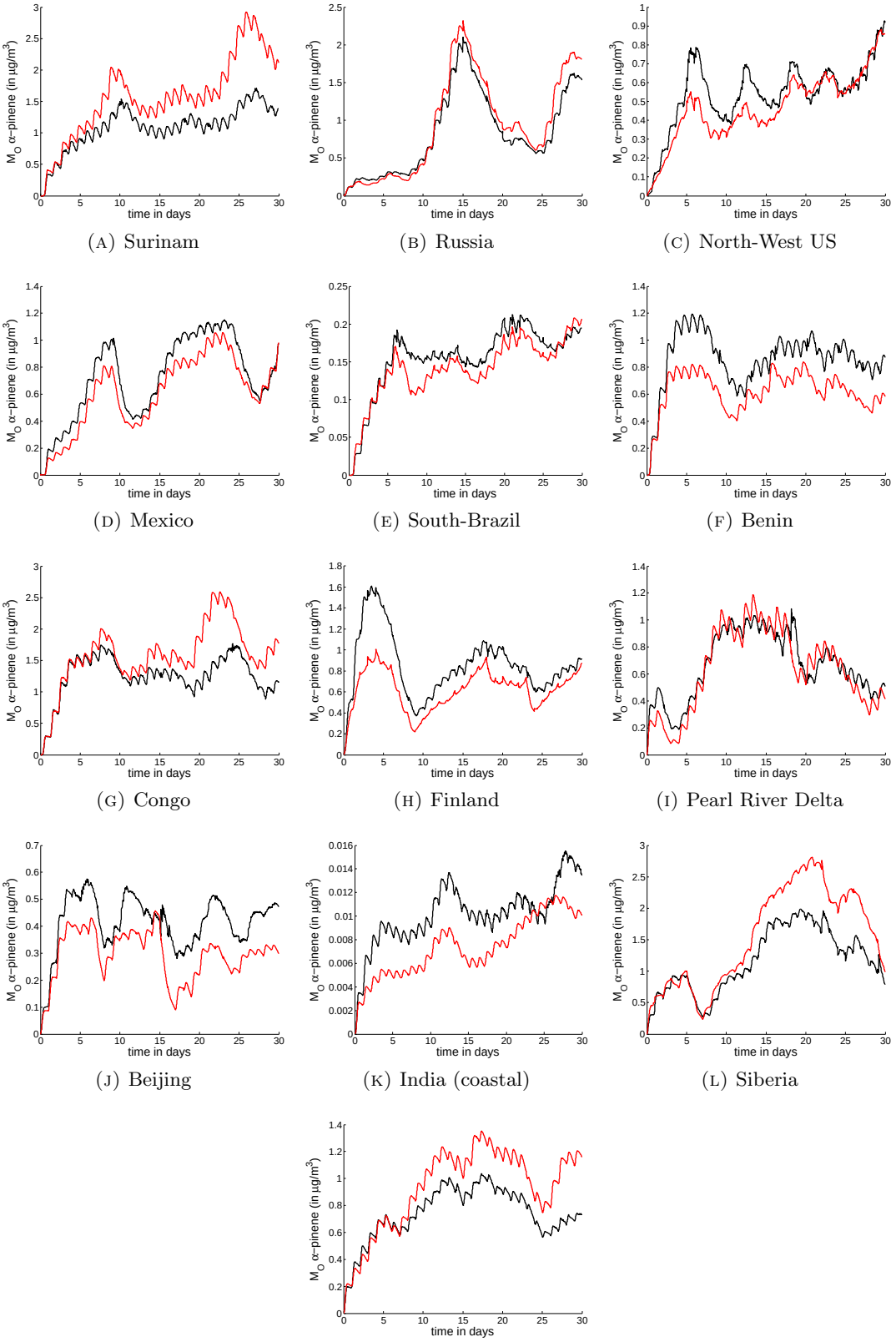

(A) Surinam (B) Russia (C) North-West US

(D) Mexico (E) South-Brazil (F) Benin

(G) Congo (H) Finland (I) Pearl River Delta

(J) Beijing (K) India (coastal) (L) Siberia

(M) Borneo

FIGURE C.4: Example of time evolution of α-pinene SOA in the full BOREAM model (black) versus the parameter model (red) for simulations based on atmospheric conditions simulated with the CTM IMAGESv2, shown here for the month of July.

C.4 Parameterised activity coefficients for the 10-product model

γ_{H_2O} (activity coefficient of water, Table C.4) and γ_{Org} (pseudo-activity coefficient of the organic SOA fraction, Table C.5) are given at RH-values from 0 up to 99% for the five scenarios considered.

TABLE C.4: Activity coefficient γ_{H_2O} for water

RH (in %)	γ_{H_2O} OH low-NO_x	γ_{H_2O} OH high-NO_x	γ_{H_2O} O_3 low-NO_x	γ_{H_2O} O_3 high-NO_x	γ_{H_2O} NO_3 high-NO_x
0.0	0.3816	0.5191	0.4470	0.5191	0.5131
5.0	0.4437	0.5682	0.5172	0.5682	0.5626
10.0	0.5004	0.6151	0.5669	0.6151	0.6099
15.0	0.5534	0.6602	0.6141	0.6602	0.6552
20.0	0.6033	0.7034	0.6591	0.7034	0.6988
25.0	0.6508	0.7451	0.7022	0.7451	0.7408
30.0	0.6961	0.7854	0.7435	0.7854	0.7813
35.0	0.7394	0.8242	0.7831	0.8242	0.8204
40.0	0.7810	0.8616	0.8210	0.8616	0.8580
45.0	0.8208	0.8976	0.8573	0.8976	0.8943
50.0	0.8589	0.9321	0.8920	0.9321	0.9291
55.0	0.8953	0.9652	0.9249	0.9652	0.9625
60.0	0.9298	0.9966	0.9560	0.9966	0.9942
65.0	0.9625	1.0262	0.9851	1.0262	1.0241
70.0	0.9930	1.0537	1.0119	1.0537	1.0520
75.0	1.0209	1.0789	1.0359	1.0789	1.0775
80.0	1.0458	1.1010	1.0564	1.1010	1.1000
85.0	1.0663	1.1190	1.0720	1.1190	1.1185
90.0	1.0801	1.1308	1.0794	1.1308	1.1307
95.0	1.0792	1.1302	1.0676	1.1302	1.1310
96.0	1.0745	1.1270	1.0589	1.1270	1.1280
97.0	1.0659	1.1217	1.0441	1.1217	1.1231
98.0	1.0460	1.1125	1.0194	1.1125	1.1146
99.0	1.0052	1.0924	1.0032	1.0924	1.0971

TABLE C.5: Pseudo-activity coefficient γ_{Org} for impact of water on the organic fraction

RH (in %)	γ_{Org} OH low-NO_x	γ_{Org} OH high-NO_x	γ_{Org} O_3 low-NO_x	γ_{Org} O_3 high-NO_x	γ_{Org} NO_3 high-NO_x
0.0	1.0000	1.0000	1.0000	1.0000	1.0000
5.0	0.9908	0.9958	0.9940	0.9958	0.9956
10.0	0.9688	0.9844	0.9796	0.9844	0.9840
15.0	0.9391	0.9677	0.9589	0.9677	0.9668
20.0	0.9047	0.9467	0.9336	0.9467	0.9454
25.0	0.8672	0.9225	0.9049	0.9225	0.9207
30.0	0.8280	0.8958	0.8738	0.8958	0.8934
35.0	0.7876	0.8670	0.8408	0.8670	0.8641
40.0	0.7469	0.8367	0.8066	0.8367	0.8334
45.0	0.7061	0.8053	0.7716	0.8053	0.8015
50.0	0.6656	0.7732	0.7362	0.7732	0.7689
55.0	0.6257	0.7405	0.7005	0.7405	0.7358
60.0	0.5867	0.7077	0.6651	0.7077	0.7026
65.0	0.5486	0.6750	0.6300	0.6750	0.6695
70.0	0.5118	0.6427	0.5958	0.6427	0.6369
75.0	0.4765	0.6113	0.5628	0.6113	0.6051
80.0	0.4435	0.5816	0.5323	0.5816	0.5751
85.0	0.4138	0.5550	0.5062	0.5550	0.5481
90.0	0.3913	0.5353	0.4916	0.5353	0.5278
95.0	0.3950	0.5376	0.5304	0.5376	0.5282
96.0	0.4086	0.5460	0.5703	0.5460	0.5358
97.0	0.4403	0.5620	0.6687	0.5620	0.5502
98.0	0.5552	0.5947	1.0274	0.5947	0.5793
99.0	1.6851	0.6944	1.9288	0.6944	0.6604

C.5 Comparison of the RH-dependence parameterisation at intermediate NO_x

The following figure compares the full BOREAM model and the parameterisation for total SOA mass concentration (including water) as a function of relative humidity (RH) at 2 intermediate NO_x levels. Also shown are results for 2 sensitivity tests for which activity coefficients are constant and equal to 1 (ideality). This assumption leads to significant discrepancies at higher RH values .

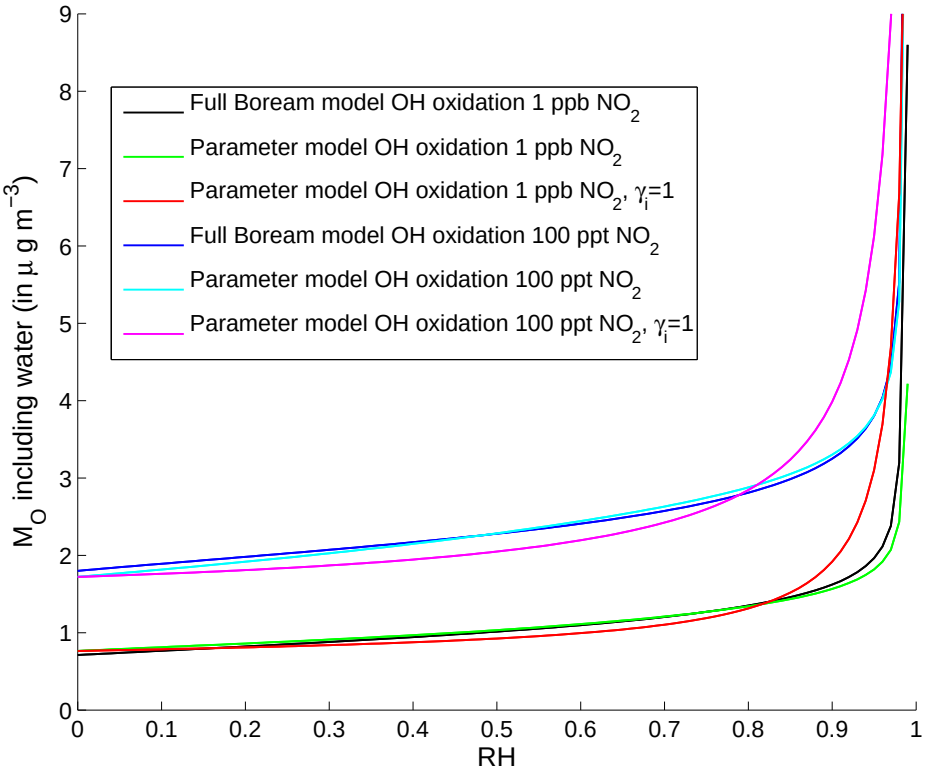

FIGURE C.5: Parameterised and full model SOA mass loading M_O (including water) in function of RH, at 100 ppt and 1 ppb NO_2 for the OH-oxidation scenario (at 288 K). Also shown are results for 2 sensitivity tests for which activity coefficients are constant and equal to 1 (ideality).

Bibliography

Adachi, K. and Buseck, P. R. (2008). Internally mixed soot, sulfates, and organic matter in aerosol particles from Mexico City. *Atmos. Chem. Phys.*, 8(21):6469–6481.

Alvarado, A., Arey, J., and Atkinson, R. (1998). Kinetics of the gas-phase reactions of OH and NO_3 radicals and O_3 with the monoterpene reaction products pinonaldehyde, caronaldehyde and sabinaketone. *J. Atmos. Chem.*, 31(3):281–297.

Andreae, M. O. (2007). Aerosols before pollution. *Science*, 315(5808):50–51.

Anglada, J. M., González, J., and Torrent-Sucarrat, M. (2011). Effects of the substituents on the reactivity of carbonyl oxides. A theoretical study on the reaction of substituted carbonyl oxides with water. *Phys. Chem. Chem. Phys.*, 13(28):13034.

Arey, J., Aschmann, S., Kwok, E., and Atkinson, R. (2001). Alkyl nitrate, hydroxyalkyl nitrate, and hydroxycarbonyl formation from the NO_x-air photooxidations of C5-C8 n-alkanes. *J. Phys. Chem. A*, 105(6):1020–1027.

Arey, J., Atkinson, R., and Aschmann, S. M. (1990). Product study of the gas-phase reactions of monoterpenes with the OH radical in the presence of NO_x. *J. Geophys. Res.*, 95(D11):18539.

Atkinson, R. (1994). *Gas-Phase Tropospheric Chemistry of Organic Compounds*. National Institute of Standards and Technology.

Atkinson, R. (2007a). Gas-phase tropospheric chemistry of organic compounds: a review. *Atmos. Environ.*, 41, Supplement(0):200–240.

Atkinson, R. (2007b). Rate constants for the atmospheric reactions of alkoxy radicals: An updated estimation method. *Atmos. Environ.*, 41(38):8468–8485.

Atkinson, R. and Aschmann, S. M. (1993). Atmospheric chemistry of the monoterpene reaction products nopinone, camphenilone, and 4-acetyl-1-methylcyclohexene. *J. Atmos. Chem.*, 16:337–3448.

Atkinson, R., Aschmann, S. M., and Pitts, J. N. (1986). Rate constants for the gas-phase reactions of the OH radical with a series of monoterpenes at 294 ± 1 K. *Int. J. Chem. Kinet.*, 18(3):287–299.

Atkinson, R., Baulch, D. L., Cox, R. A., Crowley, J. N., Hampson, R. F., Hynes, R. G., Jenkin, M. E., Rossi, M. J., Troe, J., and IUPAC Subcommittee (2006). Evaluated kinetic and photochemical data for atmospheric chemistry: Volume II - gas phase reactions of organic species. *Atmos. Chem. Phys.*, 6(11):3625–4055.

Auld, J. and Hastie, D. R. (2011). Investigation of organic nitrate product formation during hydroxyl radical initiated photo-oxidation of β-pinene. *Atmos. Environ.*, 45(1):26–34.

Aumont, B., Camredon, M., Mouchel-Vallon, C., La, S. Y., Ouzebidour, F., Valorso, R., Lee-Taylor, J., and Madronich, S. (2013). Modeling the influence of alkane molecular structure on secondary organic aerosol formation. *Faraday Discuss.*, 165:105–122.

Aumont, B., Szopa, S., and Madronich, S. (2005). Modelling the evolution of organic carbon during its gas-phase tropospheric oxidation: development of an explicit model based on a self generating approach. *Atmos. Chem. Phys.*, 5:2497–2517.

Ausloos, P. (1961). Intramolecular rearrangements. II. Photolysis and Radiolysis of 4-methyl-2-hexanone. *J. Phys. Chem.*, 65(9):1616–1618.

Baldwin, P. J., Canosa-Mas, C. E., Frey, H. M., and Walsh, R. (1987). The photochemistry of cyclobutyl methyl ketone. Part 1. Room-temperature results and the general mechanism. *Journal Cover:J. Chem. Soc., Faraday Trans. 2*, 83:1049–1058.

Barnes, I., Becker, K. H., and Zhu, T. (1993). Near UV absorption spectra and photolysis products of difunctional organic nitrates: Possible importance as NO_x reservoirs. *J. Atmos. Chem.*, 17(4):353–373.

Bell, M. L., Davis, D. L., and Fletcher, T. (2003). A retrospective assessment of mortality from the London smog episode of 1952: The role of influenza and pollution. *Environ. Health Perspect.*, 112(1):6–8.

Berndt, T., Böge, O., and Stratmann, F. (2003). Gas-phase ozonolysis of α-pinene gaseous products and particle formation. *Atmos. Environ.*, 37:3933–3945.

Böge, O. (2009). β-pinene 07/03/2008 and 28/04/2008 photo-oxidation experiments at the LEAK chamber: experimental records in the Eurochamp database. `http://projects.tropos.de/eurochamp/LEAK_2008_03_07/cover.html`.

Bonn, B., Korhonen, H., Petäjä, T., Boy, M., and Kulmala, M. (2007). Understanding the formation of biogenic secondary organic aerosol from α-pinene in smog chamber studies: role of organic peroxy radicals. *Atmos. Chem. Phys. Disc.*, 7:3901–3939.

Bowman, F. M., Odum, J. R., Seinfeld, J. H., and Pandis, S. N. (1997). Mathematical model for gas-particle partitioning of secondary organic aerosols. *Atmos. Environ.*, 31(23):3921–3931.

Breitmaier, E. (2006). *Terpenes*. Wiley-V C H Verlag Gmbh.

Britannica online (2013a). *"Naval Stores"*. `http://www.britannica.com/EBchecked/topic/406872/naval-stores`.

Britannica online (2013b). *"Turpentine"*. `http://www.britannica.com/EBchecked/topic/610397/turpentine`.

Burkholder, J. B., Talukdar, R. K., Ravishankara, A. R., and Solomon, S. (1993). Temperature dependence of the HNO_3 UV absorption cross sections. *J. Geophys. Res.*, 98(D12):22937.

Calogirou, A., Jensen, N. R., Nielsen, C. J., Kotzias, D., and Hjorth, J. (1999). Gas-phase reactions of nopinone, 3-isopropenyl-6-oxo-heptanal, and 5-methyl-5-vinyltetrahydrofuran-2-ol with OH, NO_3, and ozone. *Environ. Sci. Technol.*, 33(3):453–460.

Calvert, J. G., Mellouki, A., Orlando, J., Pilling, M., and Wallington, T. (2011). *The mechanisms of atmospheric oxidation of the oxygenates*, chapter Ketenes. Oxford University Press.

Camredon, M., Hamilton, J. F., Alam, M. S., Wyche, K. P., Carr, T., White, I. R., Monks, P. S., Rickard, A. R., and Bloss, W. J. (2010). Distribution of gaseous and particulate organic composition during dark α-pinene ozonolysis. *Atmos. Chem. Phys.*, 10:2893–2917.

Capouet, M. (2005). *Modeling the oxidation of α-pinene and the related aerosol formation in laboratory and atmospheric conditions*. PhD thesis, Université Libre de Bruxelles, Faculté des Sciences.

Capouet, M. and Müller, J.-F. (2006). A group contribution method for estimating the vapour pressures of α-pinene oxidation products. *Atmos. Chem. Phys.*, 6:1455–1467.

Capouet, M., Müller, J.-F., Ceulemans, K., Compernolle, S., Vereecken, L., and Peeters, J. (2008). Modeling aerosol formation in α-pinene photo-oxidation experiments. *J. Geophys. Res.*, 113(D02308):D02308.

Capouet, M., Peeters, J., Nozière, B., and Müller, J.-F. (2004). α-pinene oxidation by OH: simulations of laboratory experiments. *Atmos. Chem. Phys.*, 4:2285–2311.

Cappa, C. D. and Wilson, K. R. (2011). Evolution of organic aerosol mass spectra upon heating: implications for OA phase and partitioning behavior. *Atmos. Chem. Phys.*, 11(5):1895–1911.

Carlton, A. G., Bhave, P. V., Napelenok, S. L., Edney, E. O., Sarwar, G., Pinder, R. W., Pouliot, G. A., and Houyoux, M. (2010). Model representation of secondary organic aerosol in CMAQv4.7. *Environ. Sci. Technol.*, 44:8553–8560.

Carlton, A. G. and Turpin, B. J. (2013). Particle partitioning potential of organic compounds is highest in the Eastern US and driven by anthropogenic water. *Atmos. Chem. Phys.*, 13(20):10203–10214.

Carter, W. P., W., Cocker III, D., Fitz, D., Malkina, I., Bumiller, K., Sauer, C., Pisano, J., Bufalino, C., and Song, C. (2005). A new environmental chamber for evaluation of gas-phase chemical mechanisms and secondary aerosol formation. *Atmos. Environ.*, 39(40):7768–7788.

Carter, W. P. L. (2000). Documentation of the SAPRC-99 chemical mechanism for VOC reactivity assessment, final report to California Air Resources Board, contracts 92-329 and 95-308. Technical report, Air Pollut. Res. Cent. for Environ. Res. and Technol., Univ. of California, Riverside, California.

Ceulemans, K., Compernolle, S., and Müller, J.-F. (2012). Parameterising secondary organic aerosol from α-pinene using a detailed oxidation and aerosol formation model. *Atmos. Chem. Phys.*, 12(12):5343–5366.

Ceulemans, K., Compernolle, S., Peeters, J., and Müller, J.-F. (2010). Evaluation of a detailed model of secondary organic aerosol formation from α-pinene against dark ozonolysis experiments. *Atmos. Environ.*, 44(40):5434–5442.

Chacon-Madrid, H. J., Henry, K. M., and Donahue, N. M. (2013). Photo-oxidation of pinonaldehyde at low NO_x: from chemistry to organic aerosol formation. *Atmos. Chem. Phys.*, 13(6):3227–3236.

Chacon-Madrid, H. J., Murphy, B. N., Pandis, S. N., and Donahue, N. M. (2012). Simulations of smog-chamber experiments using the two-dimensional volatility basis set: Linear oxygenated precursors. *Environ. Sci. Technol.*, 46:11179–11186.

Chen, J. J. and Griffin, R. J. (2005). Modeling secondary organic aerosol formation from oxidation of α-pinene, β-pinene, and *d*-limonene. *Atmos. Environ.*, 39(40):7731–7744.

Chen, Q., Liu, Y., Donahue, N. M., Shilling, J. E., and Martin, S. T. (2011). Particle-phase chemistry of secondary organic material: modeled compared to measured O:C and H:C elemental ratios provide constraints. *Environ. Sci. Technol.*, 45:4763–4770.

Chylek, P. and Geldart, D. J. W. (1997). Water vapor dimers and atmospheric absorption of electromagnetic radiation. *Geophys. Res. Lett.*, 24:2015–2018.

Claeys, M., Graham, B., Vas, G., Wang, W., Vermeylen, R., Pashynska, V., Cafmeyer, J., Guyon, P., Andreae, M. O., Artaxo, P., and Maenhaut, W. (2004). Formation of secondary organic aerosols through photooxidation of isoprene. *Science*, 303:1173–1176.

Claeys, M., Iinuma, Y., Szmigielski, R., Surratt, J. D., Blockhuys, F., Van Alsenoy, C., Böge, O., Sierau, B., Gómez-González, Y., Vermeylen, R., Van der Veken, P., Shahgholi, M., Chan, A. W. H., Herrmann, H., Seinfeld, J. H., and Maenhaut, W. (2009). Terpenylic acid and related compounds from the oxidation of α-pinene: Implications for new particle formation and growth above forests. *Environ. Sci. Technol.*, 43:6976–6982.

Cocker III, D. R., Clegg, S. L., Flagan, R. C., and Seinfeld, J. H. (2001). The effect of water on gas-particle partitioning of secondary organic aerosol. Part I: α-pinene/ozone system. *Atmos. Environ.*, 35:6049–6072.

Compernolle, S., Ceulemans, K., and Müller, J.-F. (2009). Influence of non-ideality on condensation to aerosol. *Atmos. Chem. Phys.*, 9:1325–1337.

Compernolle, S., Ceulemans, K., and Müller, J.-F. (2011). EVAPORATION: a new vapour pressure estimation method for organic molecules including non-additivity and intramolecular interactions. *Atmos. Chem. Phys.*, 11(18):9431–9450.

Crump, J. G., Flagan, R. C., and Seinfeld, J. H. (1982). Particle wall loss rates in vessels. *Aerosol Sci. Technol.*, 2(3):303–309.

da Silva Rodriguez-Corrêa, K. C., de Lima, J. C., and Fett-Neto, A. G. (2012). Pine oleoresin: tapping green chemicals, biofuels, food protection, and carbon sequestration from multipurpose trees. *Food and Energy Security*, 1:87–93.

Dash, M. R. and Rajakumar, B. (2013). Experimental and theoretical rate coefficients for the gas phase reaction of β-pinene with OH radical. *Atmos. Environ.*, 79:161–171.

Davis, E. M. and Croteau, R. (2000). *Biosynthesis*, volume 209 of *Topics in Current Chemistry*, chapter Cyclyzation Enzymes in the Biosynthesis of Monoterpenes, Sesquiterpenes, and Diterpenes, pages 53–95. Springer-Verlag.

Davis, M. E., Tapscott, C., and Stevens, P. S. (2005). Measurements of the kinetics of the OH-initiated oxidation of β-pinene: Radical propagation in the OH plus β-pinene plus O_2 plus NO reaction system. *Int. J. Chem. Kinet.*, 37(9):522–531.

Daylight Inc. (2008). *SMARTS Tutorial*. DAYLIGHT Inc. `http://www.daylight.com/dayhtml_tutorials/languages/smarts/index.html`.

Demarcke, M., Müller, J.-F., Schoon, N., Van Langenhove, H., Dewulf, J., Joó, E., Steppe, K., Šimpraga, M., Heinesch, B., and Aubinet, M. (2010). History effect of light and temperature on monoterpenoid emissions from Fagus sylvatica L. *Atmos. Environ.*, 44(27):3261–3268.

Denisov, E. T. and Afanasev, I. B. (2005). *Oxidation and antioxidants in organic chemistry and biology*. CRC Press.

Dillon, T. J. and Crowley, J. N. (2008). Direct detection of OH formation in the reactions of HO_2 with CH_3COO_2 and other substituted peroxy radicals. *Atmos. Chem. Phys.*, 8:4877–4889.

Docherty, K. S. and Ziemann, P. J. (2003). Effects of stabilized Criegee intermediate and OH radical scavengers on aerosol formation from reactions of β-pinene with O_3. *Aerosol Sci. Technol.*, 37:877–891.

Donahue, N. M., Drozd, G. T., Epstein, S. A., Presto, A. A., and Kroll, J. H. (2011a). Adventures in ozoneland: down the rabbit-hole. *Phys . Chem. Chem. Phys .*, 13:10848–10857.

Donahue, N. M., Epstein, S. A., Pandis, S. N., and Robinson, A. L. (2011b). A two-dimensional volatility basis set: 1. Organic-aerosol mixing thermodynamics. *Atmos. Chem. Phys.*, 11(7):3303–3318.

Donahue, N. M., Hartz, K. E. H., Chuong, B., Presto, A. A., Stanier, C. O., Rosenhorn, T., Robinson, A. L., and Pandis, S. N. (2005). Critical factors determining the variation in SOA yields from terpene ozonolysis: A combined experimental and computational study. *Faraday Discuss.*, 130:295–309.

Donahue, N. M., Henry, K. M., Mentel, T. F., Kiendler-Scharr, A., Spindler, C., Bohn, B., Brauers, T., Dorn, H. P., Fuchs, H., Tillmann, R., Wahner, A., Saathoff, H., Naumann, K.-H., Möhler, O., Leisner, T., Müller, L., Reinnig, M.-C., Hoffmann, T., Salo, K., Hallquist, M., Frosch, M., Bilde, M., Tritsher, T., Barmet, P., Praplan, A. P., DeCarlo, P. F., Dommen, J., Prévôt, A. S. H., and Baltensperger, U. (2012). Aging of biogenic secondary organic aerosol via gas-phase OH radical reactions. *Proc. Nat. Acad. Sci.*, 109:13503–13508.

Donahue, N. M., Robinson, A. L., Stanier, C. O., and Pandis, S. N. (2006). Coupled partitioning, dilution and chemical aging of semivolatile organics. *Environ. Sci. Technol.*, 40:26352643.

Dueck, T. A., de Visser, R., Poorter, H., Persijn, S., Gorissen, A., de Visser, W., Schapendonk, A., Verhagen, J., Snel, J., Harren, F. J. M., and et al. (2007). No evidence for substantial aerobic methane emission by terrestrial plants: a ^{13}C-labelling approach. *New Phytologist*, 175(1):29–35.

Eddingsaas, N. C., Loza, C. L., Yee, L. D., Chan, M., Schilling, K. A., Chhabra, P. S., Seinfeld, J. H., and Wennberg, P. O. (2012a). α-pinene photooxidation under controlled chemical conditions — Part 2: SOA yield and composition in low- and high-NO_x environments. *Atmos. Chem. Phys.*, 12(16):7413–7427.

Eddingsaas, N. C., Loza, C. L., Yee, L. D., Seinfeld, J. H., and Wennberg, P. O. (2012b). α-pinene photooxidation under controlled chemical conditions — Part 1: Gas-phase composition in low- and high-NO_x environments. *Atmos. Chem. Phys.*, 12(14):6489–6504.

Eisenreich, W., Bacher, A., Arigoni, D., and Rohdich, F. (2004). Biosynthesis of isoprenoids via the non-mevalonate pathway. *Cell. Mol. Life Sci.*, 61:1401–1426.

Engelhart, G. J., Hildebrandt, L., Kostenidou, E., Mihalopoulos, N., Donahue, N. M., and Pandis, S. N. (2011). Water content of aged aerosol. *Atmos. Chem. Phys.*, 11:911–920.

EUROCHAMP - EU 7th FP Infrastructure Initiative (2014). EUROCHAMP-2 database. Online. `http://eurochamp-database.es/disclaimer.html`.

European Union (2008). Directive 2008/50/EC of the European Parliament and of the Council of 21 May 2008 on ambient air quality and cleaner air for Europe. *Official Journal of the European Union*, L152:1–44.

Fan, J., Zhao, J., and Zhang, R. (2005). Theoretical study of OH addition to α-pinene and β-pinene. *Chem. Phys. Lett.*, 411(1-3):1–7.

Fantechi, G., Vereecken, L., and Peeters, J. (2002). The OH-initiated atmospheric oxidation of pinonaldehyde: Detailed theoretical study and mechanism construction. *Phys. Chem. Chem. Phys.*, 4(23):5795–5805.

Farina, S. C., Adams, P. J., and Pandis, S. N. (2010). Modeling global secondary organic aerosol formation and processing with the volatility basis set: Implications for anthropogenic secondary organic aerosol. *J. Geophys. Res.*, 115:D09202.

Fenske, J. D., Kuwata, K. T., Houk, K. N., and Paulson, S. E. (2000). OH radical yields from the ozone reaction with cycloalkenes. *J. Phys. Chem. A*, 104:7246–7254.

Fredenslund, A., Jones, R. L., and Prausnitz, J. M. (1975). Group-contribution estimation of activity coefficients in nonideal liquid mixtures. *AIChE J.*, 21:1086–1099.

Fry, J. L., Kiendler-Scharr, A., Rollins, A. W., Wooldridge, P. J., Brown, S. S., Fuchs, H., Dubé, W., Mensah, A., dal Maso, M., Tillmann, R., Dorn, H.-P., Brauers, T., and Cohen, R. C. (2009). Organic nitrate and secondary organic aerosol yield from NO_3 oxidation of β-pinene evaluated using a gas-phase kinetics/aerosol partitioning model. *Atmos. Chem. Phys.*, 9(4):1431–1449.

Fuller, E. N., Ensley, K., and Giddings, J. C. (1969). Diffusion of halogenated hydrocarbons in helium. The effect of structure on collision cross sections. *J. Phys. Chem.*, 73(11):3679–3685.

Gardner, E. P., Sperry, P. D., and Calvert, J. G. (1987). Photodecomposition of acrolein in oxygen-nitrogen mixtures. *J. Phys. Chem.*, 91(7):1922–1930.

Gaschen, A., Lang, D., Kalberer, M., Savi, M., Geiser, T., Gazdhar, A., Lehr, C.-M., Bur, M., Dommen, J., Baltensperger, U., and et al. (2010). Cellular responses after exposure of lung cell cultures to secondary organic aerosol particles. *Environ. Sci. Technol.*, 44(4):1424–1430.

Gershenzon, J. and Dudareva, N. (2007). The function of terpene natural products in the natural world. *Nat. Chem. Biol.*, 3:408–414.

Geyer, A. (2000). *The role of the nitrate radical in the boundary layer — observations and modeling studies*. PhD thesis, Heidelberg.

Geyer, A., Alicke, B., Ackermann, R., Martinez, M., Harder, H., Brune, W., di Carlo, P., Williams, E., Jobson, T., Hall, S., Shetter, R., and Stutz, J. (2003). Direct observations of daytime NO_3: Implications for urban boundary layer chemistry. *J. Geophys. Res.-Atmos.*, 108(D12).

Gill, K. J. and Hites, R. A. (2002). Rate constants for the gas-phase reactions of the hydroxyl radical with isoprene, α- and β-pinene, and limonene as a function of temperature. *J. Phys. Chem. A*, 106(11):2538–2544.

Grieshop, A. P., Logue, J. M., Donahue, N. M., and Robinson, A. L. (2009). Laboratory investigation of photochemical oxidation of organic aerosol from wood fires 1: measurement and simulation of organic aerosol evolution. *Atmos. Chem. Phys.*, 9(4):1263–1277.

Griffin, R. J. (2013). The sources and impacts of tropospheric particulate matter. *Nature Education Knowledge*, 4:1.

Griffin, R. J., Flagan, R. C., and Seinfeld, J. H. (1999). Organic aerosol formation from the oxidation of biogenic hydrocarbons. *J. Geophys. Res.*, 104:3555–3567.

Grosjean, D., Williams, E. L., Grosjean, E., Andino, J. M., and Seinfeld, J. H. (1993). Atmospheric oxidation of biogenic hydrocarbons: reaction of ozone with β-pinene, *d*-limonene and trans-caryophyllene. *Environ. Sci. Technol.*, 27(13):2754–2758.

Guenther, A. (2013). Biological and chemical diversity of biogenic volatile organic emissions into the atmosphere. *ISRN Atmospheric Sciences*, 2013:1–27.

Guenther, A. B., Jiang, X., Heald, C. L., Sakulyanontvittaya, T., Duhl, T., Emmons, L. K., and Wang, X. (2012). The Model of Emissions of Gases and Aerosols from Nature version 2.1 (MEGAN2.1): an extended and updated framework for modeling biogenic emissions. *Geosci. Model Dev.*, 5:1471–1492.

Guerreiro, C., de Leeuw, F., and Foltescu, V. (2013). Air quality in Europe — 2013 report. Technical report, European Environment Agency's (EEA) Topic Centre for Air and Climate Change Mitigation (ETC/ACM).

Haagen-Smit, A. J. (1952). Chemistry and physiology of Los Angeles smog. *Ind. Eng. Chem.*, 44(6):1342–1346.

Hallquist, M., Wangberg, I., and Ljungstrom, E. (1997). Atmospheric fate of carbonyl oxidation products originating from α-pinene and $\Delta(3)$-carene: Determination of rate of reaction with OH and NO_3 radicals, UV absorption cross sections, and vapor pressures. *Environ. Sci. Technol.*, 31:3166–3172.

Hallquist, M., Wangberg, I., Ljungstrom, E., Barnes, I., and Becker, K.-H. (1999). Aerosol and product yields from NO_3 radical-initiated oxidation of selected monoterpenes. *Environ. Sci. Technol.*, 33(4):553–559.

Hallquist, M., Wenger, J. C., Baltensperger, U., Rudich, Y., Simpson, D., Claeys, M., Dommen, J., Donahue, N. M., George, C., Goldstein, A. H., Hamilton, J. F., Herrmann, H., Hoffmann, T., Iinuma, Y., Jang, M., Jenkin, M. E., Jimenez, J. L., Kiendler-Scharr, A., Maenhaut, W., McFiggans, G., Mentel, T. F., Monod, A., Prévôt, A. S. H., Seinfeld, J. H., Surratt, J. D., Szmigielski, R., and Wildt, J. (2009). The formation, properties and impact of secondary organic aerosol: current and emerging issues. *Atmos. Chem. Phys.*, 9:5155–5236.

Haneke, K. E. and Masten, S. (2002). Turpentine (turpentine oil, wood turpentine, sulfate turpentine, sulfite turpentine) [8006-64-2] review of toxicological literature. Technical report, National Institute of Environmental Health Sciences.

Hansen, A. M. K., Kristensen, K., Nguyen, Q. T., Zare, A., Cozzi, F., Nøjgaard, J. K., Skov, H., Brandt, J., Christensen, J. H., Ström, J., and et al. (2014). Organosulfates and organic acids in arctic aerosols: speciation, annual variation and concentration levels. *Atmos. Chem. and Phys.*, 14(15):7807–7823.

Hansen, H. K., Rasmussen, P., Fredenslund, A., Schiller, M., and Gmehling, J. (1991). Vapor-liquid equilibria by UNIFAC group contribution. 5. Revision and extension. *Ind. Eng. Chem. Res.*, 30:2352–2355.

Hansen, J., Sato, M., Kharecha, P., and von Schuckmann, K. (2011). Earth's energy imbalance and implications. *Atmos. Chem. Phys.*, 11(24):13421–13449.

Hasson, A. S., Tyndall, G. S., and Orlando, J. J. (2004). A product yield study of the reaction of HO_2 radicals with ethyl peroxy ($C_2H_5O_2$), acetyl peroxy ($CH_3C(O)O_2$), and acetonyl peroxy ($CH_3C(O)CH_2O_2$) radicals. *J. Phys. Chem. A*, 108(28):5979–5989.

Hasson, A. S., Tyndall, G. S., Orlando, J. J., Singh, S., Hernandez, S. Q., Campbell, S., and Ibarra, Y. (2012). Branching ratios for the reaction of selected carbonyl-containing peroxy radicals with hydroperoxy radicals. *J. Phys. Chem. A*, 116(24):6264–6281.

Hatakeyama, S., Izumi, K., Fukuyama, T., and Akimoto, H. (1989). Reactions of ozone with α-pinene and β-pinene in air: yields of gaseous and particulate products. *J. Geophys. Res.*, 94:13013–13024.

Heaton, K. J., Dreyfus, M. A., Wang, S., and Johnston, M. V. (2007). Oligomers in the early stage of biogenic secondary organic aerosol formation and growth. *Environ. Sci. Technol.*, 41:6129–6136.

Hendry, D. G., Mill, T., Piszkiewicz, L., Howard, J. A., and Eigenmann, H. K. (1974). A critical review of H-atom transfer in the liquid phase: chlorine atom, alkyl, trichloromethyl, alkoxy and alkylperoxy radicals. *J. Phys. Chem. Ref. Data.*, 4:937–978.

Hennigan, C. J., Miracolo, M. A., Engelhart, G. J., May, A. A., Presto, A. A., Lee, T., Sullivan, A. P., McMeeking, G. R., Coe, H., Wold, C. E., and et al. (2011). Chemical and physical transformations of organic aerosol from the photo-oxidation of open biomass burning emissions in an environmental chamber. *Atmos. Chem. Phys.*, 11(15):7669–7686.

Henry, K. M. and Donahue, N. M. (2012). Photochemical aging of α-pinene secondary organic aerosol: Effects of OH radical sources and photolysis. *J. Phys. Chem. A*, 116:5932–5940.

Henze, D. K., Seinfeld, J. H., Ng, N. L., Kroll, J. H., Fu, T.-M., Jacob, D. J., and Heald, C. L. (2008). Global modeling of secondary organic aerosol formation from aromatic hydrocarbons: high- vs. low-yield pathways. *Atmos. Chem. Phys.*, 8(9):2405–2420.

Hewitt, C. N., editor (1999). *Reactive hydrocarbons in the atmosphere*. Associated Press.

Hiatt, R., Clipsham, J., and Visser, T. (1964). The induced decomposition of tert-butyl hydroperoxide. *Can. J. Chem.*, 42(12):2754–2757.

Hildebrandt, L., Donahue, N. M., and Pandis, S. N. (2009). High formation of secondary organic aerosol from the photo-oxidation of toluene. *Atmos. Chem. Phys.*, 9(9):2973–2986.

Hildebrandt, L., Kostenidou, E., Mihalopoulos, N., Worsnop, D. R., Donahue, N. M., and Pandis, S. N. (2010). Formation of highly oxygenated organic aerosol in the atmosphere: Insights from the Finokalia Aerosol Measurement Experiments. *Geophys. Res. Lett.*, 37:L23801.

Hoffmann, T., Odum, J. R., Bowman, F., Collins, D., Klockow, D., Flagan, R. C., and Seinfeld, J. H. (1997). Formation of organic aerosols from the oxidation of biogenic hydrocarbons. *J. Atmos. Chem.*, 26:189–222.

Hofzumahaus, A., Rohrer, F., Lu, K., Bohn, B., Brauers, T., Chang, C.-C., Fuchs, H., Holland, F., Kita, K., Kondo, Y., Li, X., Lou, S., Shao, M., Zeng, L., Wahner, A., and Zhang, Y. (2009). Amplified trace gas removal in the troposphere. *Science*, 324(5935):1702–1704.

Horie, O. and Moortgat, G. K. (1992). Reactions of $CH_3C(O)O_2$ radicals with CH_3O_2 and HO_2 between 263 and 333 K. A product study. *Faraday Trans.*, 88(22):3305.

Horowitz, A. and Calvert, J. G. (1982). Wavelength dependence of the primary processes in acetaldehyde photolysis. *J. Phys. Chem.*, 86:3105–3114.

Horowitz, A., Meller, R., and Moortgat, G. K. (2001). The UV-VIS absorption cross sections of the α-dicarbonyl compounds: pyruvic acid, biacetyl and glyoxal. *J. Photochem. Photobiol. A: Chemistry*, 146(1-2):19–27.

Hoyle, C., Boy, M., Donahue, N. M., Fry, J. L., Glasius, M., Guenther, A., Hallar, A. G., Huff Hartz, K., Petters, M. D., Petäjä, T., Rosenoern, T., and Sullivan, A. P. (2011). A review of the anthropogenic influence on biogenic secondary organic aerosol. *Atmos. Chem. Phys.*, 11:321–343.

Iinuma, Y., Böge, O., Gnauk, T., and Herrmann, H. (2004). Aerosol-chamber study of the α-pinene/O_3 reaction: influence of particle acidity on aerosol yields and products. *Atmos. Environ.*, 38:761–773.

Iinuma, Y., Müller, C., Berndt, T., Böge, O., Claeys, M., and Herrmann, H. (2007). Evidence for the existence of organosulfates from β-pinene ozonolysis in ambient secondary organic aerosol. *Environ. Sci. Technol.*, 41:6678–6683.

IPCC (2013). *Climate Change 2013: The physical science basis. Contribution of Working Group I to the Fifth assessment report of the Intergovernmental Panel on Climate Change*, chapter Summary for policymakers, pages 3–29. Cambridge University Press, Cambridge, United Kingdom and New York, NY, USA. `http://www.climatechange2013.org/images/report/WG1AR5_SPM_FINAL.pdf`.

IPCC (2014). *Climate Change 2014: Impacts Adaptation and Vulnerability. Part A: Global and Sectoral Aspects. Contribution of Working Group II to the Fifth Assessment Report of the Intergovernmental Panel on Climate Change*, chapter Summary for policymakers, pages 1–32. Cambridge University Press, Cambridge, United Kingdom and New York, NY, USA. `http://ipcc-wg2.gov/AR5/images/uploads/WG2AR5_SPM_FINAL.pdf`.

IPCC, Working group I (2014). IPCC fifth assessmens report: Climate change 2013: The physical science basis. Technical report, IPCC.

IUPAC (2011). The IUPAC International Chemical Identifier (InChI). `http://www.iupac.org/home/publications/e-resources/inchi.html`.

IUPAC (2014). Evaluated kinetic data. Online. `http://iupac.pole-ether.fr`.

Jacobson, M. Z. (2002). *Atmospheric pollution : history, science and regulation.* Cambridge University Press.

Jang, M., Czoschke, N. M., Lee, S., and Kamens, R. M. (2002). Heterogeneous atmospheric aerosol production by acid-catalyzed particle-phase reactions. *Science*, 298(5594):814–817.

Jaoui, M. and Kamens, R. M. (2003). Mass balance of gaseous and particulate products from β-pinene/O_3/air in the absence of light and β-pinene/NO_x/air in the presence of natural sunlight. *J. Atmos. Chem.*, 45(2):101–141.

Jenkin, M. (2004). Modelling the formation and composition of secondary organic aerosol from α- and β-pinene ozonolysis using MCM v3. *Atmos. Chem. Phys.*, 4:1741–1757.

Jenkin, M. E., Hurley, M. D., and Wallington, T. J. (2007). Investigation of the radical product channel of the $CH_3C(O)O_2$ + HO_2 reaction in the gas phase. *Phys. Chem. Chem. Phys.*, 9:3149–3162.

Jenkin, M. E., Saunders, S. M., and Pilling, M. J. (1997). The tropospheric degradation of volatile organic compounds: a protocol for mechanism development. *Atmos. Environ.*, 31:81–104.

Jenkin, M. E., Shallcross, D. E., and Harvey, J. N. (2000). Development and application of a possible mechanism for the generation of cis-pinic acid from the ozonolysis of α- and β-pinene. *Atmos. Environ.*, 34(18):2837–2850.

Jenkin, M. E., Wyche, K. P., Evans, C. J., Carr, T., Monks, P. S., Alfarra, M. R., Barley, M. H., McFiggans, G. B., Young, J. C., and Rickard, A. R. (2012). Development and chamber evaluation of the MCM v3.2 degradation scheme for β-caryophyllene. *Atmos. Chem. Phys.*, 12(11):5275–5308.

Jiang, L., Wang, W., and Xu, Y.-S. (2009). Theoretical investigation of the NO_3 radical addition to double bonds of limonene. *Int. J. Mol. Sci.*, 10(9):3743–3754.

Jimenez, J. L., Canagaratna, M. R., Donahue, N. M., Prévôt, A. S. H., Zhang, Q., Kroll, J. H., DeCarlo, P. F., Allan, J. D., Coe, H., Ng, N. L., and et al. (2009). Evolution of organic aerosols in the atmosphere. *Science*, 326:1525 – 1529.

Jorand, F., Kerhoasb, L., Heissc, A., Einhornb, J., and Sahetchian, K. (2000). Determination of the ultra violet absorption cross section of hexyl-ketohydroperoxides in solution in acetonitrile. *J. of Photochem. Photobiol. A*, 134:119–125.

Kahnt, A. (2012). *Semivolatile compounds from atmospheric monoterpene oxidation.* PhD thesis, Fakultät für Chemie und Mineralogie, Universität Leipzig.

Kamens, R., Jang, M., Chien, C.-J., and Leach, K. (1999). Aerosol formation from the reaction of α-pinene and ozone using a gas-phase kinetics-aerosol partitioning model. *Environ. Sci. Technol.*, 33:1430–1438.

Kamens, R. and Jaoui, M. (2001). Modeling aerosol formation from α-pinene + NO_x in the presence of natural sunlight using gas-phase kinetics and gas-particle partitioning theory. *Environ. Sci. Technol.*, 35:1394–1405.

Kerdouci, J., Picquet-Varrault, B., and Doussin, J.-F. (2010). Prediction of rate constants for gas-phase reactions of nitrate radical with organic compounds: A new structure-activity relationship. *Chem. Phys. Chem.*, 11:3909–3920.

Keywood, M., Varutbangkul, V., Bahreini, R., Flagan, R., and Seinfeld, J. (2004). Secondary organic aerosol formation from the ozonolysis of cycloalkenes and related compounds. *Environ. Sci. Technol.*, 38(15):4157–4164.

Khamaganov, V. G. and Hites, R. A. (2001). Rate constants for the gas-phase reactions of ozone with isoprene, α- and β-pinene, and limonene as a function of temperature. *J. Phys. Chem. A*, 105(5):815–822.

Kim, H., Barkey, B., and Paulson, S. E. (2010). Real refractive indices of α- and β-pinene and toluene secondary organic aerosols generated from ozonolysis and photo-oxidation. *J. Geophys. Res.*, 115(D24):D24212.

Kirschke, S., Bousquet, P., Ciais, P., Saunois, M., Canadell, J. G., Dlugokencky, E. J., Bergamaschi, P., Bergmann, D., Blake, D. R., Bruhwiler, L., and et al. (2013). Three decades of global methane sources and sinks. *Nature Geoscience*, 6(10):813–823.

Kostenidou, E., Lee, B.-H., Engelhart, G. J., Pierce, J. R., and Pandis, S. N. (2009). Mass spectra deconvolution of low, medium, and high volatility biogenic secondary organic aerosol. *Environ. Sci. Technol.*, 43:4884–4889.

Kristensen, K., Cui, T., Zhang, H., Gold, A., Glasius, M., and Surratt, J. D. (2014). Dimers in α-pinene secondary organic aerosol: effect of hydroxyl radical, ozone, relative humidity and aerosol acidity. *Atmos. Chem. Phys.*, 14(8):4201–4218.

Kristensen, K., Enggrob, K. L., King, S. M., Worton, D. R., Platt, S. M., Mortensen, R., Rosenoern, T., Surratt, J. D., Bilde, M., Goldstein, A. H., and et al. (2013). Formation and occurrence of dimer esters of pinene oxidation products in atmospheric aerosols. *Atmos. Chem. Phys.*, 13(7):3763–3776.

Kristiansen, N. I., Stohl, A., and Wotawa, G. (2012). Atmospheric removal times of the aerosol-bound radionuclides ^{137}Cs and ^{131}I measured after the Fukushima Dai-ichi nuclear accident - a constraint for air quality and climate models. *Atmos. Chem. Phys.*, 12(22):10759–10769.

Kroll, J. H., Ng, N. L., Murphy, S. M., Flagan, R. C., and Seinfeld, J. H. (2006). Secondary organic aerosol formation from isoprene photooxidation. *Environ. Sci. Technol.*, 40:1869–1877.

Kwok, E. S. C. and Atkinson, R. (1995). Estimation of hydroxyl radical reaction rate constants for gas-phase organic compounds using a structure-reactivity relationship: An update. *Atmos. Environ.*, 29:1685–1695.

Laing, A. and Evans, J.-L. (2011). *Introduction to Tropical Meteorology*. The COMET Program, 2nd edition edition. `http://www.goes-r.gov/users/comet/tropical/textbook_2nd_edition/index.htm`.

Lambe, A. T., Ahern, A. T., Williams, L. R., Slowik, J. G., Wong, J. P. S., Abbatt, J. P. D., Brune, W. H., Ng, N. L., Wright, J. P., Croasdale, D. R., Worsnop, D. R.,

Davidovits, P., and Onasch, T. B. (2011). Characterization of aerosol photooxidation flow reactors: heterogeneous oxidation, secondary organic aerosol formation and cloud condensation nuclei activity measurements. *Atmos. Meas. Tech.*, 4:445–461.

Larsen, B. R., Di Bella, D., Glasius, M., Winterhalter, R., Jensen, N. R., and Hjorth, J. (2001). Gas-phase OH oxidation of monoterpenes: Gaseous and particulate products. *J. Atmos. Chem.*, 38(3):231–276.

Laval-Szopa, S. (2003). *Développement d'une chaîne automatique d'écriture de schémas chimiques explicites et réduits adaptés à l'étude de la pollution photooxydante aux différentes échelles (Development of an automatic tool for the writing of explicit and reduced chemical schemes suited to the study of photooxidative pollution at different scales)*. PhD thesis, Laboratoire inter-universitaire des systèmes atmosphèriques (LISA) CNRS : UMR7583 INSU Université Denis Diderot - Paris VII Université Paris XII Val de Marne 61 Av du général de Gaulle 94010 CRETEIL CEDEX France.

Leather, K. E., McGillen, M. R., and Percival, C. J. (2010). Temperature-dependent ozonolysis kinetics of selected alkenes in the gas phase: an experimental and structur-eactivity relationship (SAR) study. *Phys. Chem. Chem. Phys.*, 12:2935–2943.

Lee, B.-H., Pierce, J. R., Engelhart, G. J., and Pandis, S. N. (2011). Volatility of secondary organic aerosol from the ozonolysis of monoterpenes. *Atmos. Environ.*, 45(14):2443–2452.

Lelieveld, J. and Crutzen, P. J. (1991). The role of clouds in tropospheric photochemistry. *J. Atmos. Chem.*, 12:229–267. 10.1007/BF00048075.

Lendar, M., Aissat, A., Cazaunau, M., Daële, V., and Mellouki, A. (2013). Absolute and relative rate constants for the reactions of OH and Cl with pentanols. *Chem. Phys. Lett.*, 582:38–43.

Lewis, P. J., Bennett, K. A., and Harvey, J. N. (2005). A computational study of the atmospheric oxidation of nopinone. *Phys. Chem. Chem. Phys.*, 7(8):1643–1649.

Lin, G., Penner, J. E., Sillman, S., Taraborrelli, D., and Lelieveld, J. (2012). Global modeling of SOA formation from dicarbonyls, epoxides, organic nitrates and peroxides. *Atmos. Chem. Phys.*, 12(10):4743–4774.

Ma, Y. et al. (2007). Organic acid formation in the gas-phase ozonolysis of α-pinene. *Phys. Chem. Chem. Phys.*, 9:5084–5087.

Ma, Y. and Marston, G. (2008). Multifunctional acid formation from the gas-phase ozonolysis of β-pinene. *Phys. Chem. Chem. Phys.*, 10:6115 – 6126.

Madronich, S. (1993). *Environmental Effects of Ultraviolet Radiation*, chapter UV radiation in the natural and perturbed atmosphere, pages 17–69. Lewis, Boca Raton, Florida.

Madronich, S. and Calvert, J. G. (1990). Permutation reactions of organic peroxy radicals in the troposphere. *J. Geophys. Res.*, 95:5697–5715.

Makar, P. A. (2001). The estimation of organic gas vapour pressure. *Atmos. Environ.*, 35:961–974.

Mang, S. A., Henricksen, D. K., Bateman, A. P., Andersen, M. P. S., Blake, D. R., and Nizkorodov, S. A. (2008). Contribution of carbonyl photochemistry to aging of atmospheric secondary organic aerosol. *J. Phys. Chem. A*, 112:8337–8344.

Martin, D. M., Gershenzon, J., and Bohlmann, J. (2003). Induction of volatile terpene biosynthesis and diurnal emission by methyl jasmonate in foliage of Norway spruce. *Plant Physiol.*, 132:1586–1599.

Martinez, M., Harder, H., Kovacs, T. A., Simpas, J. B., Bassis, J., Lesher, R., Brune, W. H., Frost, G. J., Williams, E. J., Stroud, C. A., Jobson, B. T., Roberts, J. M., Hall, S. R., Shetter, R. E., Wert, B., Fried, A., Alicke, B., Stutz, J., Young, V. L., White, A. B., and Zamora, R. J. (2003). OH and HO_2 concentrations, sources, and loss rates during the Southern Oxidants Study in Nashville, Tennessee, summer 1999. *J. Geophys. Res.*, 108:4617.

Martinez, M., Harder, H., Kubistin, D., Rudolf, M., Bozem, H., Eerdekens, G., Fischer, H., Klüpfel, T., Gurk, C., Königstedt, R., Parchatka, U., Schiller, C. L., Stickler, A., Williams, J., and Lelieveld, J. (2010). Hydroxyl radicals in the tropical troposphere over the suriname rainforest: airborne measurements. *Atmos. Chem. Phys.*, 10(8):3759–3773.

Martinez, R. D., Buitrago, A. A., Howell, N. W., Hearn, C. H., and Joens, J. A. (1992). The near U.V. absorption spectra of several aliphatic aldehydes and ketones at 300 K. *Atmos. Environ. Part A. General Topics*, 26(5):785–792.

Matsunaga, A. and Ziemann, P. J. (2010). Gas-wall partitioning of organic compounds in a Teflon film chamber and potential effects on reaction product and aerosol yield measurements. *Aerosol Sci. Technol.*, 44(10):881–892.

Matthews, J., Sinha, A., and Francisco, J. S. (2005). The importance of weak absorption features in promoting tropopsheric radical production. *Proc. Nat. Acad. Sci.*, 102:7449–7452.

McDonald, J. D., Doyle-Eisele, M., Campen, M. J., Seagrave, J., Holmes, T., Lund, A., Surratt, J. D., Seinfeld, J. H., Rohr, A. C., and Knipping, E. M. (2010). Cardiopulmonary response to inhalation of biogenic secondary organic aerosol. *Inhalation Toxicol.*, 22(3):253–265.

McGillen, M. R., Archibald, A. T., Carey, T., Leather, K. E., Shallcross, D. E., Wenger, J. C., and Percival, C. J. (2011). Structure-activity relationship (SAR) for the prediction of gas-phase ozonolysis rate coefficients: an extension towards heteroatomic unsaturated species. *Phys. Chem. Chem. Phys.*, 13:2842–2849.

McGillen, M. R., Carey, T. J., Archibald, A. T., Wenger, J. C., Shallcross, D. E., and Percival, C. J. (2008). Structure-activity relationship (SAR) for the gas-phase ozonolysis of aliphatic alkenes and dialkenes. *Phys. Chem. Chem. Phys.*, 10:1757.

McMillan, G. R., Calvert, J. G., and Pitts, J. N. (1964). Detection and lifetime of enol-acetone in the photolysis of 2-pentanone vapor. *J. Am. Chem. Soc.*, 86(18):3602–3605.

McMurry, P. H. and Grosjean, D. (1985). Gas and aerosol wall losses in Teflon film smog chambers. *Environ. Sci. Technol.*, 19(12):1176–1182.

Mellouki, A. and Mu, Y. (2003). On the atmospheric degradation of pyruvic acid in the gas phase. *J. Photochem. Photobiol. A: Chemistry*, 157:295–300.

Metzger, A., Dommen, J., Gaeggeler, K., Duplissy, J., Prévôt, A. S. H., Kleffmann, J., Elshorbany, Y., Wisthaler, A., and Baltensperger, U. (2008). Evaluation of 1,3,5 trimethylbenzene degradation in the detailed tropospheric chemistry mechanism, MCMv3.1, using environmental chamber data. *Atmos. Chem. Phys.*, 8(21):6453–6468.

Meyer, N. K., Duplissy, J., Gysel, M., Metzger, A., Dommen, J., Weingartner, E., Alfarra, M. R., Prévôt, A. S. H., Fletcher, C., Good, N., McFiggans, G., Jonsson, A. M., Hallquist, M., Baltensperger, U., and Ristovski, Z. D. (2009). Analysis of the hygroscopic and volatile properties of ammonium seeded and unseeded SOA particles. *Atmos. Chem. Phys.*, 9:721–732.

Miller, B., Oschinski, C., and Zimmer, W. (2001). First isolation of an isoprene synthase gene from poplar and successful expression of the gene in Escherichia coli. *Planta*, 213:483–487.

Montenegro, A., Ishibashi, J. S., Lam, P., and Li, Z. (2012). Kinetics study of reactions of α-pinene and β-pinene with hydroxyl radical at 1-8 Torr and 240-340 K using the relative rate/discharge flow/mass spectrometry method. *J. Phys. Chem. A*, 116:12096–12103.

Mukhopadhyay, A., Mukherjee, M., Ghosh, A. K., and Chakraborty, T. (2011). UV photolysis of α-cyclohexanedione in the gas phase. *J. Phys. Chem. A*, 115(26):7494–7502.

Müller, J.-F., Peeters, J., and Stavrakou, T. (2014). Fast photolysis of carbonyl nitrates from isoprene. *Atmos. Chem. Phys.*, 14:2497–2508.

Müller, J.-F., Stavrakou, T., Wallens, S., De Smedt, I., Van Roozendael, M., Potosnak, M. J., Rinne, J., Munger, B., Goldstein, A., and Guenther, A. B. (2008). Global isoprene emissions estimated using MEGAN, ECMWF analyses and a detailed canopy environment model. *Atmos. Chem. Phys.*, 8(5):1329–1341.

Müller, L., Reinng, M.-C., Naumann, K. H., Saathoff, H., Mentel, T. F., Donahue, N. M., and Hoffmann, T. (2012). Formation of 3-methyl-1,2,3-butanetricarboxylic acid via gas phase oxidation of pinonic acid - a mass spectrometric study of SOA aging. *Atmos. Chem. Phys.*, 12:1483–1496.

Myhre, G., Myhre, C. E. L., Samset, B. H., and Storelvmo, T. (2013). Aerosols and their relation to global climate and climate sensitivity. *Nature Education Knowledge*, 4:7.

Myrdal, P. B. and Yalkowsky, S. H. (1997). Estimating pure component vapor pressures of complex organic molecules. *Ind. Eng. Chem. Res.*, 36:2494–2499.

Nannoolal, Y., Rarey, J., and Ramjugernath, D. (2008). Estimation of pure component properties: Part 3. Estimation of the vapor pressure of non-electrolyte organic compounds via group contributions and group interactions. *Fluid Phase Equilib.*, 269:117–133.

Nannoolal, Y., Rarey, J., Ramjugernath, D., and Cordes, W. (2004). Estimation of pure component properties: Part 1. Estimation of the normal boiling point of non-electrolyte organic compounds via group contributions and group interactions. *Fluid Phase Equilib.*, 226:45–63.

Neeb, P. (2000). Structure-reactivity based estimation of the rate constants for hydroxyl radical reactions with hydrocarbons. *J. Atmos. Chem.*, 35:295–315.

Neta, P., Huie, R. E., and Ross, A. B. (1990). Rate constants for reactions of peroxyl radicals in fluid solutions. *J. Phys. Chem. Ref. Data*, 19(2):413–513.

Ng, N. L., Chhabra, P. S., Chan, A. W. H., Surratt, J. D., Kroll, J. H., Kwan, A. J., McCabe, D. C., Wennberg, P. O., Sorooshian, A., Murphy, S. M., Dalleska, N. F., Flagan, R. C., and Seinfeld, J. H. (2007a). Effect of NO_x level on secondary organic

aerosol (SOA) formation from the photooxidation of terpenes. *Atmos. Chem. Phys.*, 7(19):5159–5174.

Ng, N. L., Kroll, J. H., Chan, A. W. H., Chhabra, P. S., Flagan, R. C., and Seinfeld, J. H. (2007b). Secondary organic aerosol formation from m-xylene, toluene, and benzene. *Atmos. Chem. Phys.*, 7:3909–3922.

Ng, N. L., Kroll, J. H., Keywood, M. D., Bahreini, R., Varutbangkul, V., Flagan, R. C., Seinfeld, J. H., Lee, A., and Goldstein, A. H. (2006). Contribution of first- versus second-generation products to secondary organic aerosols formed in the oxidation of biogenic hydrocarbons. *Environ. Sci. Technol.*, 40:2283–2297.

Nguyen, T. L., Peeters, J., and Vereecken, L. (2009a). Theoretical study of the gas-phase ozonolysis of β-pinene ($C_{10}H_{16}$). *Phys. Chem. Chem. Phys.*, 11:5643–5656.

Nguyen, T. L., Winterhalter, R., Moortgat, G., Kanawati, B., Peeters, J., and Vereecken, L. (2009b). The gas-phase ozonolysis of β-caryophyllene ($C_{15}H_{24}$). part II: A theoretical study. *Phys. Chem. Chem. Phys.*, 11:4173–4183.

Nisbet, R., Fisher, R., Nimmo, R., Bendall, D., Crill, P., Gallego-Sala, A., Hornibrook, E., López-Juez, E., Lowry, D., Nisbet, P., and et al. (2009). Emission of methane from plants. *P. Roy. Soc. B-Biol. Sci.*, 276(1660):1347–1354.

Nozière, B., Barnes, I., and Becker, K. H. (1999). Product study and mechanisms of the reactions of α-pinene and of pinonaldehyde with OH radicals. *J. Geophys. Res.-Atmos.*, 104:23645–23656.

O'Boyle, N. (2012). Towards a universal SMILES representation - a standard method to generate canonical SMILES based on the InChI. *J. Cheminform.*, 4:22.

O'Boyle, N., Banck, M., James, C., Morley, C., Vandermeersch, T., and Hutchison, G. (2011). Open Babel: An open chemical toolbox. *J Cheminform.*, 3:33.

Odum, J. R., Hoffmann, T., Bowman, F., Collins, D., Flagan, R. C., and Seinfeld, J. H. (1996). Gas/particle partitioning and secondary organic aerosol yields. *Environ. Sci. Technol.*, 30:2580–2585.

Olander, D. (2007). *General Thermodynamics*. CRC Press.

Orlando, J. J. and Tyndall, G. S. (2012). Laboratory studies of organic peroxy radical chemistry: an overview with emphasis on recent issues of atmospheric significance. *Chem. Soc. Rev.*, 41(19):6294–6317.

Orlando, J. J., Tyndall, G. S., and Wallington, T. J. (2003). The atmospheric chemistry of alkoxy radicals. *Chem. Rev.*, 103:4657–4690.

Osbourne, A. E. and Lanzotti, V., editors (2009). *Plant-derived Natural Products*. Springer-Verlag.

Pan, X., Underwood, J. S., Xing, J.-H., Mang, S. A., and Nizkorodov, S. A. (2009). Photodegradation of secondary organic aerosol generated from limonene oxidation by ozone studied with chemical ionization mass spectrometry. *Atmos. Chem. Phys.*, 9:3851–3865.

Pankow, J. F. (1994). An absorption model of gas/particle partitioning of organic compounds in the atmosphere. *Atmos. Environ.*, 28:185–188.

Pankow, J. F. and Asher, W. E. (2008). SIMPOL.1: a simple group contribution method for predicting vapor pressures and enthalpies of vaporization of multifunctional organic compounds. *Atmos. Chem. Phys.*, 8:2773–2796.

Park, S. H., Kim, H. O., Han, Y. T., Kwon, S. B., and Lee, K. W. (2001). Wall loss rate of polydispersed aerosols. *Aerosol Sci. Technol.*, 35(3):710–717.

Pathak, R., Donahue, N. M., and Pandis, S. N. (2008). Ozonolysis of β-pinene: Temperature dependence of secondary organic aerosol mass fraction. *Environ. Sci. Technol.*, 42:5081–5086.

Pathak, R. K., Stanier, C. O., Donahue, N. M., and Pandis, S. N. (2007). Ozonolysis of α-pinene at atmospherically relevant concentrations: Temperature dependence of aerosol mass fractions (yields). *J. Geophys. Res.-Atmos.*, 112(D03201):D03201.

Paulot, F., Crounse, J. D., Kjaergaard, H. G., Kroll, J. H., Seinfeld, J. H., and Wennberg, P. O. (2009). Isoprene photooxidation: new insights into the production of acids and organic nitrates. *Atmos. Chem. Phys.*, 9(4):1479–1501.

Paulsen, D., Dommen, J., Kalberer, M., Prévôt, A. S. H., Richter, R., Sax, M., Steinbacher, M., Weingartner, E., and Baltensperger, U. (2005). Secondary organic aerosol formation by irradiation of 1,3,5-trimethylbenzene/NO_x/H_2O in a new reaction chamber for atmospheric chemistry and physics. *Environ. Sci. Technol.*, 39(8):2668–2678.

Paulson, S. E., Liu, D.-L., and Orzechowska, G. E. (2006). Photolysis of heptanal. *J. Org. Chem.*, 71:6403–6408.

Peeters, J., Boullart, W., Pultau, V., Vandenberk, S., and Vereecken, L. (2007). Structure-activity relationship for the addition of OH to (poly)alkenes: Site-specific and total rate constants. *J. Phys. Chem. A*, 111(9):1618–1631.

Peeters, J. and Müller, J.-F. (2010). HO_x radical regeneration in isoprene oxidation via peroxy radical isomerisations. II: experimental evidence and global impact. *Phys. Chem. Chem. Phys.*, 12(42):14227–14235.

Peeters, J. and Nguyen, T. (2012). Unusually fast 1,6-H shifts of enolic hydrogens in peroxy radicals: formation of the first-generation C2 and C3 carbonyls in the oxidation of isoprene. *J. Phys. Chem. A*, 116:6134–6141.

Peeters, J., Nguyen, T. L., and Vereecken, L. (2009). HO_x radical regeneration in the oxidation of isoprene. *Phys. Chem. Chem. Phys.*, 11:5935–5939.

Peeters, J., Vereecken, L., and Fantechi, G. (2001). The detailed mechanism of the OH-initiated atmospheric oxidation of α-pinene: a theoretical study. *Phys. Chem. Chem. Phys.*, 3:5489 – 5504.

Peng, C., Chan, M. N., and Chan, C. K. (2001). The hygroscopic properties of dicarboxylic and multifunctional acids: Measurements and UNIFAC predictions. *Environ. Sci. Technol.*, 35(22):4495–4501.

Petrovič, V., Ducman, V., and Škapin, S. D. (2012). Determination of the photocatalytic efficiency of TiO_2 coatings on ceramic tiles by monitoring the photodegradation of organic dyes. *Ceramics International*, 38(2):1611–1616.

Pfaffenberger, L., Barmet, P., Slowik, J. G., Praplan, A. P., Dommen, J., Prévôt, A. S. H., and Baltensperger, U. (2013). The link between organic aerosol mass loading and degree of oxygenation: an α-pinene photooxidation study. *Atmos. Chem. Phys.*, 13(13):6493–6506.

Pierce, J. R., Engelhart, G. J., Hildebrandt, L., Weitkamp, E. A., Pathak, R. K., Donahue, N. M., Robinson, A. L., Adams, P. J., and Pandis, S. N. (2008). Constraining particle evolution from wall losses, coagulation, and condensation-evaporation in smog-chamber experiments: Optimal estimation based on size distribution measurements. *Aerosol Sci. Technol.*, 42(12):1001–1015.

Pinho, P., Pio, C., and Jenkin, M. (2005). Evaluation of isoprene degradation in the detailed tropospheric chemical mechanism, MCM v3, using environmental chamber data. *Atmos. Environ.*, 39(7):1303–1322.

Pinho, P. G., Pio, C. A., Carter, W. P. L., and Jenkin, M. E. (2007). Evaluation of α- and β-pinene degradation in the detailed tropospheric chemistry mechanism, MCM v3.1, using environmental chamber data. *J. Atmos. Chem.*, 57(2):171–202.

Plum, C. N., Sanhueza, E., Atkinson, R., Carter, W. P. L., and Pitts, J. N. (1983). Hydroxyl radical rate constants and photolysis rates of α-dicarbonyls. *Environ. Sci. Tech.*, 17(8):479–484.

Poling, B. E., Prausnitz, J. M., and O'Connell, J. P. (2001). *The properties of gases and liquids*. McGraw-Hill.

Pope, C. A., Ezzati, M., and Dockery, D. W. (2009). Fine-particulate air pollution and life expectancy in the united states. *New Engl. J. Med.*, 360(4):376–386.

Pope III, C. A. (2011). Health effects of particulate matter air pollution. EPA Wood Smoke Health Effects Webinar `http://www.epa.gov/burnwise/pdfs/PMHealthEffects-Pope.pdf`.

Praplan, A. P., Barmet, P., Dommen, J., and Baltensperger, U. (2012). Cyclobutyl methyl ketone as a model compound for pinonic acid to elucidate oxidation mechanisms. *Atmos. Chem. Phys.*, 12(22):10749–10758.

Presto, A., Huff Hartz, K., and Donahue, N. (2005a). Secondary organic aerosol production from terpene ozonolysis. 2. Effect of NO_x concentration. *Environ. Sci. Technol.*, 39:7046–7054.

Presto, A. A., Huff Hartz, K. E., and Donahue, N. M. (2005b). Secondary organic aerosol production from terpene ozonolysis. 1. Effect of UV radiation. *Environ. Sci. Technol.*, 39:7036–7045.

Pye, H. O. T., Chan, A. W. H., Barkley, M. P., and Seinfeld, J. H. (2010). Global modeling of organic aerosol: the importance of reactive nitrogen (NO_x and NO_3). *Atmos. Chem. Phys.*, 10:11261–11276.

Pye, H. O. T. and Seinfeld, J. H. (2010). A global perspective on aerosol from low-volatility organic compounds. *Atmos. Chem. Phys.*, 10:4377–4401.

Qi, L., Nakao, S., and Cocker, D. R. (2012). Aging of secondary organic aerosol from α-pinene ozonolysis: Roles of hydroxyl and nitrate radicals. *J. Air Waste Manag. Assoc.*, 62(12):1359–1369.

Raatikainen, T. and Laaksonen, A. (2005). Application of several activity coefficient models to water-organic-electrolyte aerosols of atmospheric interest. *Atmos. Chem. Phys.*, 5:2475–2495.

Reda, I. and Andreas, A. (2008). Solar position algorithm for solar radiation application. technical report NREL/TP-560-34302. Technical report, National Renewable Energy Laboratory (NREL).

Reinnig, M.-C., Warnke, J., and Hoffmann, T. (2009). Identification of organic hydroperoxides and hydroperoxy acids in secondary organic aerosol formed during the ozonolysis of different monoterpenes and sesquiterpenes by on-line analysis using atmospheric pressure chemical ionization ion trap mass spectrometry. *Rapid Commun Mass Spectrom*, 23:1735–1741.

Roberts, J. M. (2005). Measurement of the Henry's law coefficient and first order loss rate of PAN in *n*-octanol. *Geophys. Res. Lett.*, 32:L08803.

Robinson, A. L., Donahue, N. M., Shrivastava, M. K., Weitkamp, E. A., Sage, A. M., Grieshop, A. P., Lane, T. E., Pierce, J. R., and Pandis, S. N. (2007). Rethinking organic aerosols: Semivolatile emissions and photochemical aging. *Science*, 315(5816):1259–1262.

Robinson, E. S., Saleh, R., and Donahue, N. M. (2013). Organic aerosol mixing observed by single-particle mass spectrometry. *J. Phys. Chem. A*, 117(51):13935–13945.

Rohr, A. C. (2013). The health significance of gas- and particle-phase terpene oxidation products: A review. *Environment International*, 60:145–162.

Roldin, P., Eriksson, A. C., Nordin, E. Z., Hermansson, E., Mogensen, D., Rusanen, A., Boy, M., Swietlicki, E., Svenningsson, B., Zelenyuk, A., and Pagels, J. (2014). Modelling non-equilibrium secondary organic aerosol formation and evaporation with the aerosol dynamics, gas- and particle-phase chemistry kinetic multi-layer model ADCHAM. *Atmos. Chem. Phys. Disc.*, 14:769–869.

Romero, M., Blitz, M., Head, D., Pilling, M., Price, B., Seakins, P., and Wang, L. (2005). Photolysis of methylethyl, diethyl and methylvinyl ketones and their role in the atmospheric HO_x budget. *Faraday Discuss.*, 130:73–88.

Rowley, D. M., Lesclaux, R., Lightfoot, P. D., Nozière, B., Wallington, T. J., and Hurley, M. D. (1992). Kinetic and mechanistic studies of the reactions of cyclopentylperoxy and cyclohexylperoxy radicals with hydroperoxy radical. *J. Phys. Chem.*, 96(12):4889–4894.

Roy, V. (2009). sunposition.m (matlab m-file). Online (Matlab Central). `http://www.mathworks.com/matlabcentral/fileexchange/4605-sunposition-m`.

Ruehl, C. R., Nah, T., Isaacman, G., Worton, D. R., Chan, A. W. H., Kolesar, K. R., Cappa, C. D., Goldstein, A. H., and Wilson, K. R. (2013). The influence of molecular structure and aerosol phase on the heterogeneous oxidation of normal and branched alkanes by OH. *J. Phys. Chem. A*, 117(19):3990–4000.

Ryzhkov, A. B. and Ariya, P. A. (2004). A theoretical study of the reactions of parent and substituted Criegee intermediates with water and the water dimer. *Phys. Chem. Chem. Phys.*, 6:5042 – 5050.

Saathoff, H., Naumann, K.-H., Möhler, O., Jonsson, Å. M., Hallquist, M., Kiendler-Scharr, A., Mentel, T. F., Tillmann, R., and Schurath, U. (2009). Temperature dependence of yields of secondary organic aerosols from the ozonolysis of α-pinene and limonene. *Atmos. Chem. Phys.*, 9:1551–1577.

Saleh, R., Donahue, N. M., and Robinson, A. L. (2013). Time scales for gas-particle partitioning equilibration of secondary organic aerosol formed from α-pinene ozonolysis. *Environ. Sci. Technol.*, 47:5588–5594.

Salo, K., Hallquist, M., Jonsson, Å. M., Saathoff, H., Naumann, K.-H., Spindler, C., Tillmann, R., Fuchs, H., Bohn, B., Rubach, F., Mentel, T. F., Müller, L., Reinnig, M., Hoffmann, T., and Donahue, N. M. (2011). Volatility of secondary organic aerosol during OH radical induced ageing. *Atmos. Chem. Phys.*, 11(21):11055–11067.

Sander, S. P., Abbatt, J., Barker, J. R., Burkholder, J. B., Friedl, R. R., Golden, D. M., Huie, R. E., Kolb, C. E., Kurylo, M. J., Moortgat, G. K., Orkin, V. L., , and Wine, P. H. (2011). Chemical kinetics and photochemical data for use in atmospheric studies - evaluation number 17. Technical report, Jet Propulsion Laboratory, California Institute of Technology, Pasadena, California.

Sander, S. P., Friedl, R. R., Golden, D. M., Kurylo, M. J., Moortgat, G. K., Keller-Rudek, H., Wine, P. H., Ravishankara, A. R., Kolb, C. E., Molina, M. J., Finlayson-Pitts, B. J., Huie, R. E., and Orkin, V. L. (2006). Chemical kinetics and photochemical data for use in atmospheric studies - evaluation number 15. Technical report, Jet Propulsion Laboratory, California Institute of Technology, Pasadena, California.

Sandu, A., Daescu, D. N., and Carmichael, G. R. (2003). Direct and adjoint sensitivity analysis of chemical kinetic systems with KPP: Part I-Theory and software tools. *Atmos. Environ.*, 37:5083–5096.

Sandu, A. and Sander, R. (2006). Technical note: Simulating chemical systems in Fortran90 and Matlab with the Kinetic PreProcessor KPP-2.1. *Atmos. Chem. Phys.*, 6(1):187–195.

Saunders, S. M., Jenkin, M. E., Derwent, R. G., and Pilling, M. J. (2003). Protocol for the development of the Master Chemical Mechanism, MCM v3 (Part A): tropospheric degradation of non-aromatic volatile organic compounds. *Atmos. Chem. Phys.*, 3:161–180. `http://mcm.leeds.ac.uk/MCM`.

Scala, A. A. and Ballan, D. G. (1972). Vacuum ultraviolet photolysis of cyclohexanone. *J. Phys. Chem.*, 76(5):615–620.

Schurath, U. and Naumann, K.-H. (2003). Chemical Mechanism Develoment (CMD), EUROTRAC-2 subproject, final report. Technical report, Int. Sci. Secr.t, GSF-Natl. Res. Cent. for Environ. and Health, Munich, Germany.

Seinfeld, J. H. and Pandis, S. N. (2006). *Atmospheric Chemistry and Physics*. John Wiley & Sons, Inc.

Shilling, J. E., Chen, Q., King, S. M., Rosenoern, T., Kroll, J. H., Worsnop, D. R., McKinney, K. A., and Martin, S. T. (2008). Particle mass yield in secondary organic aerosol formed by the dark ozonolysis of α-pinene. *Atmos. Chem. Phys.*, 8:2073–2088.

Shiraiwa, M., Yee, L. D., Schilling, K. A., Loza, C. L., Craven, J. S., Zuend, A., Ziemann, P. J., and Seinfeld, J. H. (2013a). Size distribution dynamics reveal particle-phase chemistry in organic aerosol formation. *Proc. Nat. Acad. Sci.*, 110(29):11746–11750.

Shiraiwa, M., Zuend, A., Bertram, A., and Seinfeld, J. H. (2013b). Gas-particle partitioning of atmospheric aerosols: Interplay of physical state, non-ideal mixing and morphology. *Phys. Chem. Chem. Phys.*, 15:11441–11453.

Smith, J. D., Kroll, J. H., Cappa, C. D., Che, D. L., Liu, C. L., Ahmed, M., Leone, S. R., Worsnop, D. R., and Wilson, K. R. (2009). The heterogeneous reaction of hydroxyl radicals with sub-micron squalane particles: a model system for understanding the oxidative aging of ambient aerosols. *Atmos. Chem. Phys.*, 9:3209–3222.

Song, C. et al. (2007). Effect of hydrophobic primary organic aerosols on secondary organic aerosol formation from ozonolysis of α-pinene. *Geophys. Res. Lett.*, 34(L20803):doi:10.1029/2007GL030720.

Spracklen, D. V., Jimenez, J. L., Carslaw, K. S., Worsnop, D. R., Evans, M. J., Mann, G. W., Zhang, Q., Canagaratna, M. R., Allan, J., Coe, H., McFiggans, G., Rap, A., and Forster, P. (2011). Aerosol mass spectrometer constraint on the global secondary organic aerosol budget. *Atmos. Chem. Phys.*, 11(23):12109–12136.

Stanier, C. O., Donahue, N., and Pandis, S. N. (2008). Parameterization of secondary organic aerosol mass fractions from smog chamber data. *Atmos. Environ.*, 42:2276–2299.

Stavrakou, T., Müller, J.-F., Boersma, K. F., van der A, R. J., Kurokawa, J., Ohara, T., and Zhang, Q. (2013). Key chemical NOx sink uncertainties and how they influence top-down emissions of nitrogen oxides. *Atmos. Chem. Phys.*, 13(17):9057–9082.

Stavrakou, T., Müller, J.-F., De Smedt, I., Van Roozendael, M., van der Werf, G. R., Giglio, L., and Guenther, A. (2009). Evaluating the performance of pyrogenic and biogenic emission inventories against one decade of space-based formaldehyde columns. *Atmos. Chem. Phys.*, 9:1037–1060.

Stavrakou, T., Müller, J.-F., Peeters, J., Razavi, A., Clarisse, L., Clerbaux, C., Coheur, P.-F., Hurtmans, D., De Mazière, M., Vigouroux, C., Deutscher, N. M., Griffith, D. W. T., Jones, N., and Paton-Walsh, C. (2012). Satellite evidence for a large source of formic acid from boreal and tropical forests. *Nature Geoscience*, 5:26–30.

Steinemann, A. C., MacGregor, I. C., Gordon, S. M., Gallagher, L. G., Davis, A. L., Ribeiro, D. S., and Wallace, L. A. (2011). Fragranced consumer products: Chemicals emitted, ingredients unlisted. *Environmental Impact Assessment Review*, 31:328–333.

Suarez-Bertoa, R., Picquet-Varrault, B., Tamas, W., Pangui, E., and Doussin, J.-F. (2012). Atmospheric fate of a series of carbonyl nitrates: Photolysis frequencies and OH-oxidation rate constants. *Environ. Sci. Technol.*, 46(22):12502–12509.

Sun, Q., X, J., and et al (2005). Long-term air pollution exposure and acceleration of atherosclerosis and vascular inflammation in an animal model. *JAMA*, 294(23):3003.

Surratt, J., Gómez-González, Y., Chan, A. W., Vermeylen, R., Shahgholi, M., Kleindienst, T., Edney, E., Offenberg, J., Lewandowski, M., Jaoui, M., Maenhaut, W., Claeys, M., Flagan, R., and Seinfeld, J. (2008). Organosulfate formation in biogenic secondary organic aerosol. *J. Phys. Chem. A*, 112:8345–8378.

Surratt, J. D., Chan, A. W. H., Eddingsaas, N. C., Chan, M., Loza, C. L., Kwan, A. J., Hersey, S. P., Flagan, R. C., Wennberg, P. O., and Seinfeld, J. H. (2010). Reactive intermediates revealed in secondary organic aerosol formation from isoprene. *Proc. Nat. Acad. Sci.*, 107(15):6640–6645.

Surratt, J. D., Kroll, Jesse, H., Kleindienst, T. E., Edney, E. O., Claeys, M., Sorooshian, A., Ng, N. L., Offenberg, J. H., Lewandowski, M., Flagan, R. C., and Seinfeld, J. H. (2007). Evidence for organosulfates in secondary organic aerosol. *Environ. Sci. & Technol.*, 41:517–527.

Szmigielski, R., Surratt, J. D., Gómez-González, Y., Van der Veken, P., Kourtchev, I., Vermeylen, R., Blockhuys, F., Jaoui, M., Kleindienst, T. E., Lewandowski, M., Offenberg, J. H., Edney, E. O., Seinfeld, J. H., Maenhaut, W., and Claeys, M. (2007). 3-methyl-1,2,3-butanetricarboxylic acid: An atmospheric tracer for terpene secondary organic aerosol. *Geophys. Res. Lett.*, 34(24):L24811.

Tadic, J., Juranic, I., and Moortgat, G. K. (2001a). Photooxidation of n-hexanal in air. *Molecules*, 6:287–299.

Tadic, J., Juranic, I., and Moortgat, G. K. (2001b). Pressure dependence of the photooxidation of selcted carbonyl compounds in air: n-butanal and n-pentanal. *J. Photochem. Photobiol. A*, 143:169–179.

Tadic, J., Xu, L., Houk, K. N., and Moortgat, G. K. (2011). Photooxidation of n-octanal in air: Experimental and theoretical study. *J. Org. Chem.*, 76:1614–1620.

Takekawa, H., Minoura, H., and Yamazaki, S. (2003). Temperature dependence of secondary organic aerosol formation by photo-oxidation of hydrocarbons. *Atmos. Environ.*, 37:3413 – 3424.

Textor, C., Schulz, M., Guibert, S., Kinne, S., Balkanski, Y., Bauer, S., Berntsen, T., Berglen, T., Boucher, O., Chin, M., and et al. (2006). Analysis and quantification of the diversities of aerosol life cycles within AeroCom. *Atmos. Chem. Phys.*, 6(7):1777–1813.

Tillmann, R. et al. (2010). Influence of relative humidity and temperature on the the production of pinonaldehyde and OH radicals from the ozonolysis of α-pinene. *Atmos. Chem. Phys.*, 10:3129–3173.

Tobias, H. and Ziemann, P. (2001). Kinetics of the gas-phase reactions of alcohols, aldehydes, carboxylic acids, and water with the C13 stabilized Criegee intermediate formed from ozonolysis of 1-tetradecene. *J. Phys. Chem. A*, 105:6129–6135.

Tolocka, M. P. et al. (2006). Chemistry of particle inception and growth during α-pinene ozonolysis. *Environ. Sci. Technol.*, 40:1843–1848.

Tritscher, T., Dommen, J., DeCarlo, P. F., Gysel, M., Barmet, P. B., Praplan, A. P., Weingartner, E., Prévôt, A. S. H., Riipinen, I., Donahue, N. M., and et al. (2011). Volatility and hygroscopicity of aging secondary organic aerosol in a smog chamber. *Atmos. Chem. Phys.*, 11(22):11477–11496.

TROPOS, Leipzig Atmospheric Chemistry Group (2014). Data for SOA in β-pinene low-NO_x photo-oxidation experiment at LEAK of 13/08/2012. (personal communication, Ariane Kahnt, 2014).

Tsigaridis, K., Daskalakis, N., Kanakidou, M., Adams, P. J., Artaxo, P., Bahadur, R., Balkanski, Y., Bauer, S. E., Bellouin, N., Benedetti, A., and et al. (2014). The AeroCom evaluation and intercomparison of organic aerosol in global models. *Atmos. Chem. Phys. Disc.*, 14(5):6027–6161.

Tsigaridis, K. and Kanakidou, M. (2007). Secondary organic aerosol importance in the future atmosphere. *Atmos. Environ.*, 41:4682–4692.

Tsigaridis, K., Krol, M., Dentener, F. J., Balkanski, Y., Lathière, J., Metzger, S., Hauglustaine, D. A., and Kanakidou, M. (2006). Change in global aerosol composition since preindustrial times. *Atmos. Chem. Phys.*, 6:5143–5162.

Tyndall, G. S., Cox, R. A., Granier, C., Lesclaux, R., Moortgat, G. K., Pilling, M. J., Ravishankara, A. R., and Wallington, T. J. (2001). Atmospheric chemistry of small organic peroxy radicals. *J. Geophys. Res.*, 106(D11):12157–12182.

Utembe, S. R., Watson, L. A., Shallcross, D. E., and Jenkin, M. E. (2009). A Common Represetative Intermediates (CRI) mechanism for VOC degradation. Part 3: development of a secondary organic aerosol module. *Atmos. Environ.*, 43:1982–1990.

Valavanidis, A., Fiotakis, K., and Vlachogianni, T. (2008). Airborne particulate matter and human health: Toxicological assessment and importance of size and composition of particles for oxidative damage and carcinogenic mechanisms. *J. Environ. Sci. Health, Part C*, 26(4):339–362.

Valorso, R., Aumont, B., Camredon, M., Raventos-Duran, T., Mouchel-Vallon, C., Ng, N. L., Seinfeld, J. H., Lee-Taylor, J., and Madronich, S. (2011). Explicit modelling of SOA formation from α-pinene photooxidation: sensitivity to vapour pressure estimation. *Atmos. Chem. Phys.*, 11:68956910.

Vereecken, L. and Francisco, J. S. (2012). Theoretical studies of atmospheric reaction mechanisms in the troposphere. *Chem. Soc. Rev.*, 41:6259–6293.

Vereecken, L., Müller, J.-F., and Peeters, J. (2007). Low-volatility poly-oxygenates in the OH-initiated atmospheric oxidation of α-pinene: impact of non-traditional peroxyl radical chemistry. *Phys. Chem. Chem. Phys.*, 9:5241–5248.

Vereecken, L. and Peeters, J. (2002). Enhanced H-atom abstraction from pinonaldehyde, pinonic acid, pinic acid, and related compounds: theoretical study of C-H bond strengths. *Phys. Chem. Chem. Phys.*, 4(3):467–472.

Vereecken, L. and Peeters, J. (2004). Nontraditional (per)oxy ring-closure paths in the atmospheric oxidation of isoprene and monoterpenes. *J. Phys. Chem. A*, 108(24):5197–5204.

Vereecken, L. and Peeters, J. (2009). Decomposition of substituted alkoxy radicals — part 1: a generalized structure-activity relationship for reaction barrier heights. *Phys. Chem. Chem. Phys.*, 11:9062–9074.

Vereecken, L. and Peeters, J. (2010). A structure-activity relationship for the rate coefficient of H-migration in substituted alkoxy radicals. *Phys. Chem. Chem. Phys.*, 12:12608–12620.

Vereecken, L. and Peeters, J. (2012). A theoretical study of the OH-initiated gas-phase oxidation mechanism of β-pinene ($C_{10}H_{16}$): first generation products. *Phys . Chem. Chem. Phys .*, 14:3802–3815.

Verwer, J. G. (1994). Gauss-Seidel iteration for stiff ODEs from chemical kinetics. *SIAM J. Sci. Comput*, 15:1243–1250.

Verwer, J. G., Blom, J. G., van Loon, M., and Spee, E. J. (1996). A comparison of stiff ODE solvers for atmospheric chemistry problems. *Atmos. Environ.*, 30(1):49–58.

Vickers, C. E., Gershenzon, J., Lerdau, M. T., and Loreto, F. (2009). A unified mechanism of action for volatile isoprenoids in plant abiotic stress. *Nat. Chem. Biol.*, 5(5):283–291.

Virtanen, A., Joutsensaari, J., Koop, T., Kannosto, J., Yli-Pirilä, P., Leskinen, J., Mäkelä, J. M., Holopainen, J. K., Pöschl, U., Kulmala, M., Worsnop, D. R., and Laaksonen, A. (2010). An amorphous solid state of biogenic secondary organic aerosol particles. *Nature*, 467(7317):824–827.

Volkamer, R., Ziemann, P. J., and Molina, M. J. (2009). Secondary organic aerosol formation from acethylene (C_2H_2): seed effect on SOA yields due to organic photochemistry in the aerosol aqueous phase. *Atmos. Chem. Phys.*, 9:1907–1928.

von Hessberg, C., von Hessberg, P., Pöschl, U., Bilde, M., O. Nielsen, J., and Moortgat, G. K. (2009). Temperature and humidity dependence of secondary organic aerosol yield from the ozonolysis of β-pinene. *Atmos. Chem. Phys.*, 9:3593–3599.

von Sonntag, C. (2006). *Free-radical-induced DNA damage and its repair*. Springer.

Walser, M. L., Park, J., Gomez, A. L., Russell, A. R., and Nizkorodov, S. A. (2007). Photochemical aging of secondary organic aerosol particles generated from the oxidation of d-limonene. *J. Phys. Chem. A*, 111(10):1907–1913.

Wang, J., Doussin, J. F., Perrier, S., Perraudin, E., Katrib, Y., Pangui, E., and Picquet-Varrault, B. (2011). Design of a new multi-phase experimental simulation chamber for atmospheric photosmog, aerosol and cloud chemistry research. *Atmos. Meas. Tech.*, 4(11):2465–2494.

Wang, S. and Hao, J. (2012). Air quality management in China: Issues, challenges, and options. *J. Environ. Sci. (China)*, 24(1):2–13.

Weininger, D. (1988). SMILES, a chemical language and information system. 1. Introduction to methodology and encoding rules. *J. Chem. Inf. Comput. Sci.*, 28(1):31–36.

Weininger, D., Weininger, A., and Weininger, J. L. (1989). SMILES. 2. Algorithm for generation of unique SMILES notation. *J. Chem. Inf. Model.*, 29(2):97–101.

WHO (2014a). Burden of disease from ambient air pollution for 2012. Technical report, World Health Organization.

WHO (2014b). Burden of disease from household air pollution for 2012. Technical report, World Health Organization.

WHO-Europe (2013). Review of evidence on health aspects of air pollution - REVIHAAP project technical report. Technical report, World Health Organisation.

Wild, D. J. (2009). Grand challenges for cheminformatics. *J. Cheminformatics*, 1(1):1.

Winer, A. M., Lloyd, A. C., Darnall, K. R., and Pitts, J. N. (1976). Relative rate constants for the reaction of the hydroxyl radical with selected ketones, chloroethenes, and monoterpene hydrocarbons. *J. Phys. Chem.*, 80(14):1635–1639.

Winterhalter, R., Jensen, N., Magneron, I., Wirtz, K., Mellouki, W., Yujing, M., Tadic, J., Horowitz, A., Moortgat, G., and Hjorth, J. (2001). Studies of the photolysis of pyruvic acid: Products and mechanism. In *Proceedings of the EUROTRAC Symposium 2000*.

Wisthaler, A., Jensen, N. R., Winterhalter, R., Lindinger, W., and Hjorth, J. (2001). Measurements of acetone and other gas phase product yields from the OH-initiated oxidation of terpenes by proton-transfer-reaction mass spectrometry (PTR-MS). *Atmos. Environ.*, 35(35):6181–6191.

Wolf, J. L., Richters, S., Pecher, J., and Zeuch, T. (2011). Pressure dependent mechanistic branching in the formation pathways of secondary organic aerosol from cyclic-alkene gas-phase ozonolysis. *Phys . Chem. Chem. Phys* ., 13(23):10952.

Xia, A. G., Michelangeli, D. V., and Makar, P. A. (2008). Box model studies of the secondary organic aerosol formation under different HC/NO_x conditions using the subset of the Master Chemical Mechanism for α-pinene oxidation. *J. Geophys. Res.*, 113(D10301):D10301.

Xia, A. G., Michelangeli, D. V., and Makar, P. A. (2009). Mechanism reduction for the formation of secondary organic aerosol for integration into a 3-dimensional regional air quality model: α-pinene oxidation system. *Atmos. Chem. Phys.*, 9:4341–4362.

Xia, A. G., Stroud, C. A., and Makar, P. A. (2011). Development of a simple unified volatility-based scheme (SUVS) for secondary organic aerosol formation using genetic algorithms. *Atmos. Chem. Phys.*, 11:6185–6205.

Yasmeen, F., Szmigielski, R., Vermeylen, R., Gomez-Gonzalez, Y., Surratt, J. D., Chan, A. W. H., Seinfeld, J. H., Maenhaut, W., and Claeys, M. (2011). Mass spectrometric characterization of isomeric terpenoic acids from the oxidation of α-pinene, β-pinene, *d*-limonene, and δ-3-carene in fine forest aerosol. *J. Mass Spectrom.*, 46(4):425–442.

Yasmeen, F., Vermeylen, R., Maurin, N., Perraudin, E., Doussin, J.-F., and Claeys, M. (2012). Characterisation of tracers for aging of α-pinene secondary organic aerosol using liquid chromatography/negative ion electrospray ionisation mass spectrometry. *Environ. Chem.*, 9:236–246.

Yu, J., Cocker, D. R., Griffin, R. J., Flagan, R. C., and Seinfeld, J. H. (1999a). Gas-phase ozone oxidation of monoterpenes: gaseous and particulate products. *J. Atmos. Chem.*, 34:207–258.

Yu, J., Flagan, R. C., Seinfeld, J. H., and Blanchard, P. (1999b). Observation of gaseous and particulate products of monoterpene oxidation in forest atmospheres. *Geophys. Res. Lett.*, 26:1145–1148.

Zhang, S.-H., Shaw, M., Seinfeld, J. H., and Flagan, R. C. (1992). Photochemical aerosol formation from α-pinene and β-pinene. *J. Geophys. Res.*, 97(D18):20,717–20,729.

Zhao, P. S., Dong, F., He, D., Zhao, X. J., Zhang, X. L., Zhang, W. Z., Yao, Q., and Liu, H. Y. (2013). Characteristics of concentrations and chemical compositions for PM2.5 in the region of Beijing, Tianjin, and Hebei, China. *Atmos. Chem. Phys.*, 13(9):4631–4644.

Ziemann, P. J. and Atkinson, R. (2012). Kinetics, products, and mechanisms of secondary organic aerosol formation. *Chem. Soc. Rev.*, 41(19):6582.

Zobrist, B., Marcolli, C., Pedernera, D. A., and Koop, T. (2008). Do atmospheric aerosols form glasses? *Atmos. Chem. Phys.*, 8(17):5221–5244.